Final report: DOE-UMICH-02645

LOW TEMPERATURE COMBUSTION CHEMISTRY AND FUEL COMPONENT INTERACTIONS

FINAL REPORT

Federal Agency and Organization Element to Which Report is Submitted	Office of Science, Basic Energy Sciences Department of Energy
Federal Grant Number	DE-FE002645
Project Title	Low Temperature Combustion Chemistry and Fuel Component Interactions
PI Name	Margaret S. Wooldridge
PI Title	Arthur F. Thurnau Professor Departments of Mechanical and Aerospace Engineering
PI Contact Information	Department of Mechanical Engineering University of Michigan 2350 Hayward Street Ann Arbor, Michigan 48109-2125
Submission Date	February 7, 2017
DUNS Number	073133571
Recipient Organization:	The Regents of the University of Michigan Ann Arbor, Michigan 48109
Project/Grant Period:	6/15/13-1/14/17
Reporting Period End Date:	1/14/17
Report Submission Date:	2/24/17
Report Term:	FINAL REPORT
Signature of Submitting Official	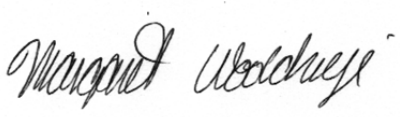

DISCLAIMER

Low Temperature Combustion Chemistry And Fuel Component Interactions

FINAL REPORT

Abstract

Recent research into combustion chemistry has shown that reactions at "low temperatures" (700 – 1100 K) have a dramatic influence on ignition and combustion of fuels in virtually every practical combustion system. A powerful class of laboratory-scale experimental facilities that can focus on fuel chemistry in this temperature range is the rapid compression facility (RCF), which has proven to be a versatile tool to examine the details of fuel chemistry in this important regime. An RCF was used in this project to advance our understanding of low temperature chemistry of important fuel compounds. We show how factors including fuel molecular structure, the presence of unsaturated C=C bonds, and the presence of alkyl ester groups influence fuel auto-ignition and produce variable amounts of negative temperature coefficient behavior of fuel ignition. We report new discoveries of synergistic ignition interactions between alkane and alcohol fuels, with both experimental and kinetic modeling studies of these complex interactions. The results of this project quantify the effects of molecular structure on combustion chemistry including carbon bond saturation, through low temperature experimental studies of esters, alkanes, alkenes, and alcohols.

Keywords: Ethanol, hexene, isomers, combustion kinetics, ignition,

Table of Contents

Executive Summary

The objective of the project was to develop quantitative understanding of the effects of molecular structure and fuel component interactions at conditions relevant to modern and next-generation combustion systems. Auto-ignition delay times and stable intermediate species measurements were made using the unique state-of-the-art experimental at the University of Michigan (UM). A rapid compression facility (RCF) was used to the measure ignition properties of several fuel compounds over a range of state and mixture conditions. Stable intermediate species measurements were used to provide quantitative and detailed understanding the reaction pathways important in the different fuel systems. The results were compared with model predictions which used elementary reaction mechanisms that represent the state-of-current understanding of combustion chemistry. The specific fuels studied included ethanol, methyltrans3hexenoate, n-heptane, n-butanol, 1-hexene, trans-2-hexene, trans-3-hexene, cis-2-hexene, cis-3-hexene and blends of n-butanol/n-heptane and ethanol/iso-octane. Details of the results of each study are provided in the associated journal articles (provided as appendices to this report), and highlights of the hexene isomer, studies are reported here. In the UM RCF ignition study of the three linear isomers of hexene, we measured the reactivity of the isomers and validated the reaction rate rules used to create reaction mechanisms of these unsaturated hydrocarbons. We found the predictive understanding was unequal for the different isomers based on the location of the double bond, with the 1- and 2-trans hexenes well represented by current reaction theory, and the 3-trans hexene less well understood. This is particularly relevant as alkenes are critical to soot formation mechanisms and as components of conventional and unconventional fossil fuels. In our ethanol study, we found excellent predictive agreement between experimental data and model predictions for ignition delay time and for most intermediate species. However, the model predictions are based on semi-empirical reaction rate theory for the most important reaction of $C_2H_5OH + HO_2$. The experimental results provide a basis for improving and validating *ab initio* reaction rates for $C_2H_5OH + HO_2$. We also revisited n-butanol ignition to understand the impact of new *ab initio* calculations of key elementary reactions on the measurements of intermediate species we made previously. The results highlight how global reactivity of n-butanol is very well understood, and advances in *ab initio* rate coefficient calculations are reducing empiricism and improving predictive accuracy of key intermediate reaction pathways. Overall, the results of this DOE project demonstrate how a

combination of global and detailed reaction parameters like ignition delay time and corresponding species time histories identify divergence in the reaction chemistry and focus research efforts on which key reactions need further investigation.

Project Objectives

The objective of this work was to improve the understanding of important features of combustion chemistry at the low temperatures and moderate pressures where reaction chemistries remain uncertain. There is a clear deficiency in the understanding of some intermediate steps of ignition for hydrocarbon and oxygenated hydrocarbon fuels at conditions that are important for modern combustion applications. Understanding structural effects is particularly important as transportation fuels are increasing in complexity due to changes in fossil and non-fossil fuel feed stocks. If the role of fuel structure on the key characteristics of combustion, such as octane numbers and octane sensitivity, can be quantitatively determined, changes in fuel composition can be quickly understood based on sound scientific results.

Towards the goals of successfully integrating sustainable fuels and improving our understanding of fossil and alternative fuels, the project objectives were:

1. to develop accurate and quantitative databases on the effects of fuel structure (with particular focus on carbon saturation) and multi-component fuels on the reaction chemistry of ignition, fuel decomposition and pollutant formation;
2. to validate the predicted trends via studies progressing in chemical structure and fuel components,
3. to cooperatively develop reaction mechanisms which accurately reproduce the observed experimental behaviors.

Technical Approach

The technical approach used to meet the project objectives was a combination of experimental and modeling efforts. All experiments were conducted using the University of Michigan (UM) rapid compression facility (RCF). The UM RCF is an innovative and robust experimental apparatus that can be used to isolate reaction kinetics by creating uniform conditions over a broad range of temperatures (T = 500-3000 K) and pressures (P = 0.5-60 atm). A detailed description of the UM RCF, including performance characteristics, can be found in Donovan et al. [1]. As shown schematically in **Fig. 1**, the UM RCF is basically a free-piston/cylinder device where the compression process can be considered adiabatic and isentropic [1]. During an experiment, the core region of the test gas mixture is sealed within the test chamber and the cooler gases along the wall of the RCF are sealed within the shoulder region of the convergent section and the sabot (i.e. free piston). This exclusive design of the UM RCF sabot and test section allows long test times (> 50 ms with excellent uniformity have been demonstrated [1]) that are required for studies that cover a large range of fuels, mixture compositions, T and P conditions and which apply gas-sampling.

The test section of the UM RCF is equipped with multiple instrumentation ports, including two optical ports for laser access, a pressure transducer port, and gas-sampling ports (end wall). The test section is equipped with a piezoelectric transducer (Kistler 6041AX4) and charge amplifier (Kistler 5010B) for pressure measurements, and an uncoated polycarbonate (Lexan R) end wall is used to provide optical access to the test manifold. The large size of the polycarbonate end wall allows the entire test volume to be imaged using a high-speed color digital video camera (Vision Research, Phantom V711, 800×600 pixel SR-CMOS 48 bit color array, capable of recording at 160 kHz). The camera array records RGB color images. A fast 50 mm lens (f/0.95 Navitar TV Lens) and c-mount extension tube are used with the camera to optimize the capture of available light emission.

An example of the excellent homogeneity that can be obtained in the UM RCF is shown in the end-view imaging sequences of **Fig. 2** of *n*-butanol/air ignition. As seen in the images, the mixture reacts and ignites uniformly throughout the test chamber. Such uniformity is critical for gas-sampling and speciation measurements. An additional benefit of the RCF is that the reactant mixtures are created externally using a dedicated mixing tank and manifold. Accurate mixtures are made manometrically using the partial pressures of each component of the test gas mixture.

Therefore mixing uncertainties are eliminated, and the fuel reaction chemistry can be isolated in UM RCF experiments without complications from mixture preparation.

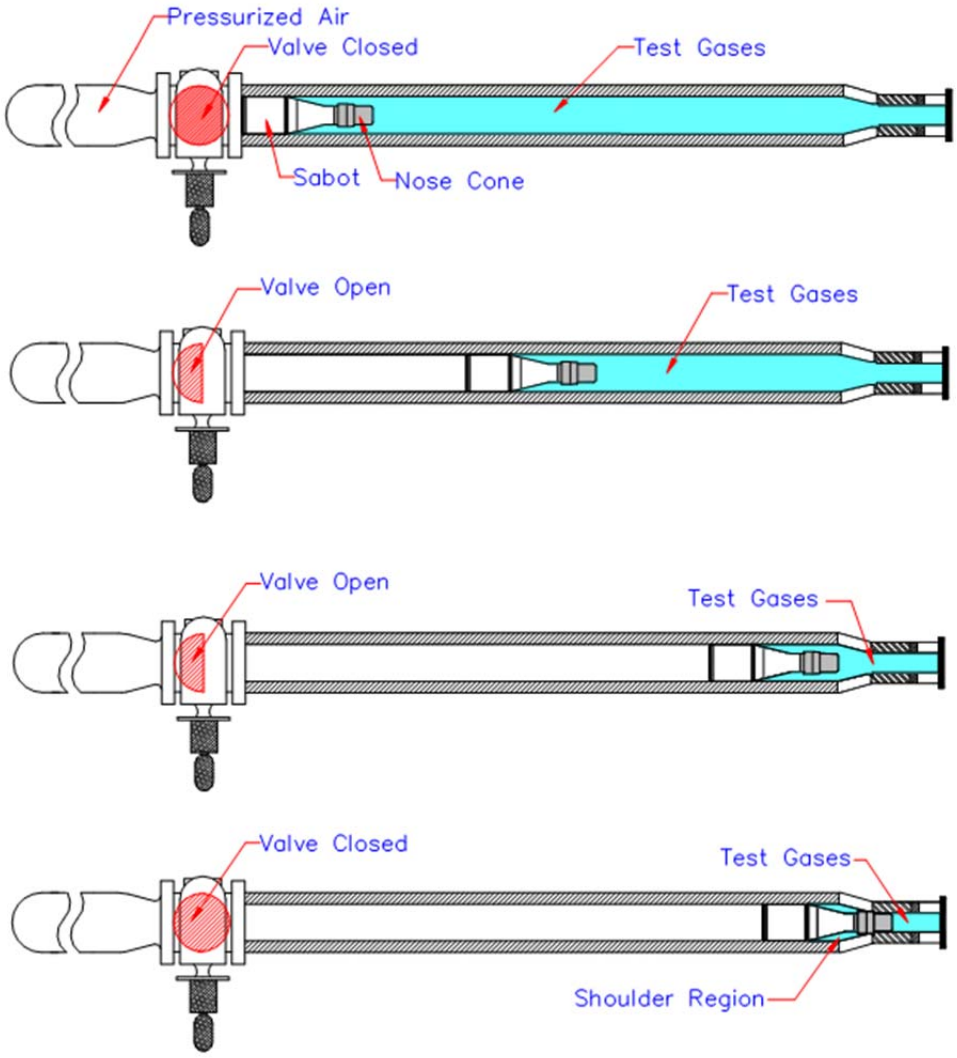

Fig. 1. Schematic of the UM-RCF in operation, where the panels progress from the a) top to d) bottom. a) Driven section is charged with the test gas mixture prior to start of test. Driver section is charged with high-pressure air. b) Hydraulic valve is opened and high-pressure gas from the driver section propels the sabot down the length of the driven section. c) Sabot travels down the length of the driven section, compressing the test gas mixture ahead of the sabot. d) Sabot is lodged in the extension section, trapping the test gas mixture within the test manifold. The annular region of the test gas mixture, which includes most of the fluid disturbances caused by the travel of the sabot down the length of the driven section, is trapped in the shoulder region [1].

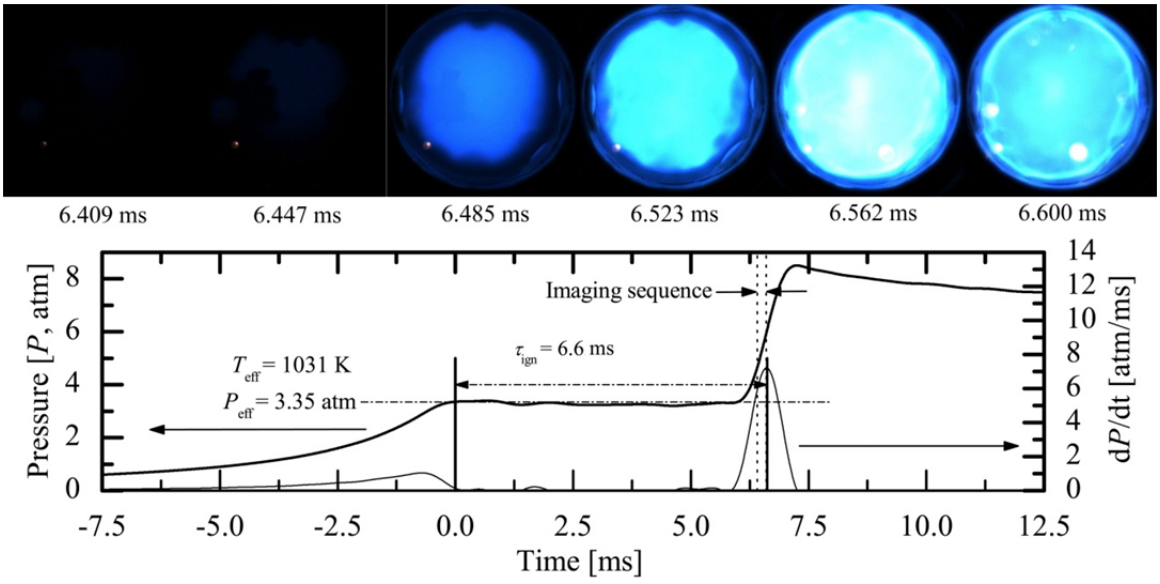

Fig. 2. Results from a typical n-butanol ignition experiment with P_{eff} = 3.35 atm, T_{eff} = 1031 K, ϕ = 1, inert/O_2 = 5.64 and τ_{ign} = 6.6 ms [2**Error! Bookmark not defined.**]. The lower panel shows the pressure (P) and the rate of pressure rise (dP/dt) in the test section. End of compression is set as time t = 0 ms. The upper panel shows the corresponding still images (end view), acquired at 26,000 fps, of the chemiluminescence during ignition (no color adjustment).

For each experiment with single stage ignition, the ignition delay time (τ_{ign}) was determined using the pressure time-history, and defined as the time from the maximum pressure at the end of compression, P_{max}, to the time of the maximum rate of pressure rise, dP/dt_{max}. This definition for τ_{ign} is illustrated in **Fig. 2.** The temperature and pressure for each ignition experiment were defined as the time integrated pressure during the ignition delay period, P_{eff}, and the corresponding temperature, T_{eff}, was determined using isentropic compression equations and the known composition of the reactant mixture. An advantage of the UM RCF is that the definitions for τ_{ign}, P_{eff} and T_{eff} have been demonstrated as robust and accurate for the core (i.e. adiabatic) region of the test section and allow direct comparison with shock tube data and other experimental and modeling kinetics studies [1,3].

For the speciation experiments, the UM RCF was equipped with a rapid gas sampling system that allowed gas chromatography (GC) to be applied to identify and quantify a broad range of stable intermediate species, including hydrocarbons, oxygenates and permanent gases. The gas sampling system consisted of four sampling probe systems. Each sampling system included a fast-acting solenoid valve (custom modified Festo MHE2-MS1H-3/2G-M7-K), vacuum isolation valves, a vacuum pump, and a sample chamber (4.5±0.5 mL). The sample chambers were equipped with a septum port (low-bleed septa, VICI Valco) for gas extraction

and a pressure sensor. The sampling probes (2 mm inner diameter) were installed on the RCF end wall. The open end of the probe extended approximately 10 mm into the RCF test section, beyond the thermal boundary layer near the end wall. A piezoresistive pressure sensor (Kistler 4045A2) and a piezoresitive amplifier (Kistler 4618A0) were used to record the pressure in the sampling chamber. The vacuum pump was used to evacuate the sampling tank before each experiment. Representative gas samples were acquired at targeted time intervals by triggering the fast acting valves using two digital delay/pulse generators (Stanford Research Systems Model DG535). The samples were then analyzed using three GCs (two Perkin Elmer Autosystems and one Perkin Elmer Clarus 500) equipped with thermal conductivity and flame ionization detectors which were used to identify and quantify the species present during ignition. We also recently added a GC mass spectrometry system (GC MS, Perkin Elmer Arnel Clarus 680 GC, SQ8T MS) to our diagnostic capabilities to further improve the fidelity of the species measurements.

Results

Results - Ignition Chemistry of the Linear Hexene Isomers

A brief summary of the results and discoveries of the recent UM RCF study of the three linear hexene isomers [4] is presented here. Experiments were conducted using the UM RCF to determine ignition delay times from pressure time histories. Stoichiometric ($\phi = 1.0$) mixtures at dilution levels of buffer gas:O_2 = 7.5 (mole basis) were investigated at an average pressure of 11 atm and temperatures from 837-1086 K. The measured ignition delay times are presented in **Fig. 3**. The UM RCF data are highlighted in the inset of **Fig. 3** and show the three hexene isomers exhibited virtually identical reactivity (within the uncertainty of the measurements) at the conditions studied. The UM RCF data filled the void between previous higher temperature (Mehl *et al.* [5]), and lower temperature (Vanhove *et al.* [6]) hexene ignition studies, and agree well with the trends indicated by the previous studies.

Fast gas sampling and gas chromatography were used to measure 13 stable intermediate species formed during the ignition delay period of each hexene isomer at a temperature of ~900 K. **Figures 4-6** present the results for the hexenes, propene, and propanal, respectively, where the time scales are normalized to the ignition delay time, i.e. $t/\tau_{ign} = 0$ corresponds to the end of compression and $t/\tau_{ign} = 1$ corresponds to autoignition. The data highlight differences, both expected and unexpected, in the reaction pathways of the three hexene isomers. The results were modeled using a gasoline surrogate reaction mechanism from Lawrence Livermore National Laboratory (LLNL) [7], which contained a sub-mechanism for the trans-hexene isomers. The model predictions are shown in **Figs. 3-6** as the solid lines. The initial conditions and compositions for the 0-D, isometric, adiabatic CHEMKIN simulations were the average conditions of the fast gas sampling experiments, nominally P = 11 atm, T = 900 K, $\phi = 1.0$, O_2 = 11.6%, molar ratio of buffer gas:O_2 = 7.5. The reactivity of the hexene isomers was well captured by the reaction mechanism and supported the current understanding that at higher temperatures (>~850 K) the ignition delay times of the isomers are virtually identical and exhibit Arrhenius dependence on temperature. As seen in **Fig. 4**, agreement between the experimental data and the model was excellent (within 20% for the majority of the time history of the hexenes). At later times (t/τ_{ign} >~0.9), the model over-predicted the rate of consumption of trans-3-hexene. For the majority of the ignition delay period (t/τ_{ign} <~0.9), the hexene concentrations and the measured stable intermediates accounted for >80% of the carbon initially in the test

mixtures, indicating good capture of the carbon balance and representation of the overall reaction pathways.

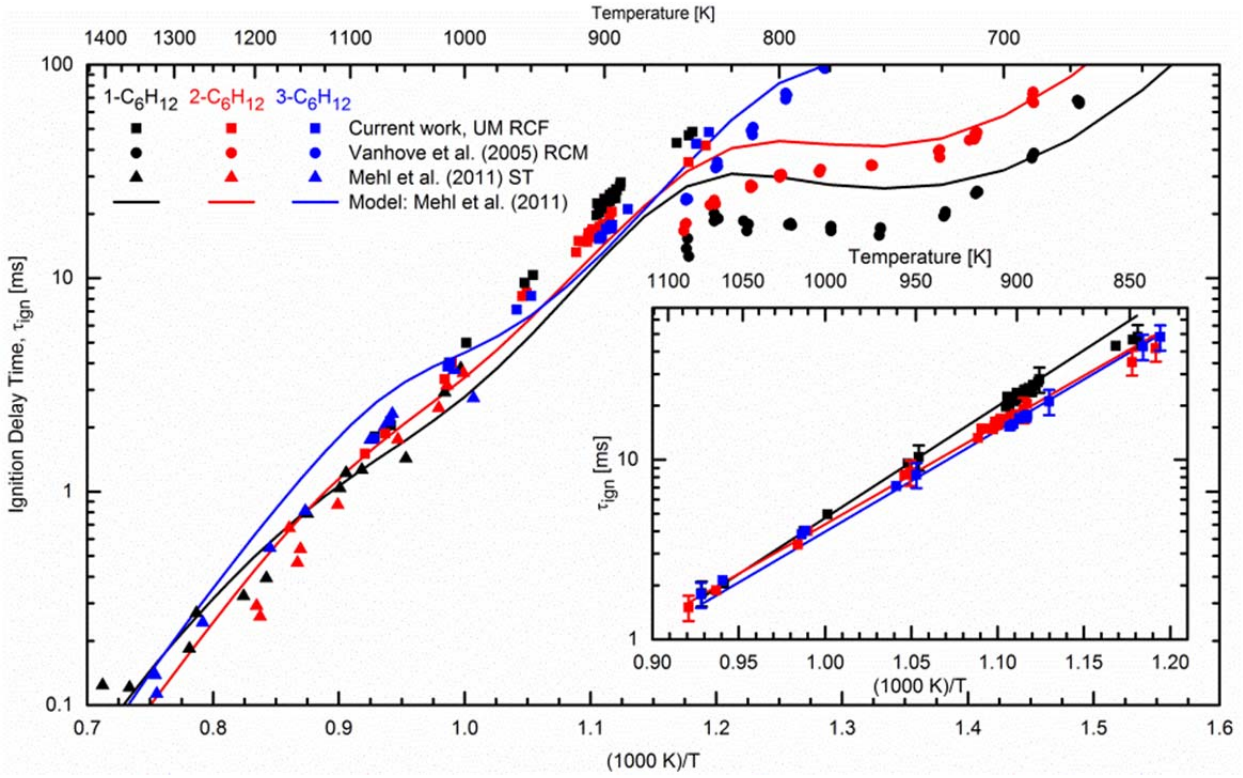

Fig. 3. From Wagnon et al. [4], comparison of UM RCF results with previous ignition studies of the three linear hexene isomers. Predicted results for ignition delay time using the LLNL mechanism by Mehl *et al.* [7] are shown as the solid lines in the main figure and linear regressions to the UM RCF data are shown in the inset. All experimental data were normalized to $\phi = 1$, inert:$O_2 = 7.5$, and P = 11 atm.

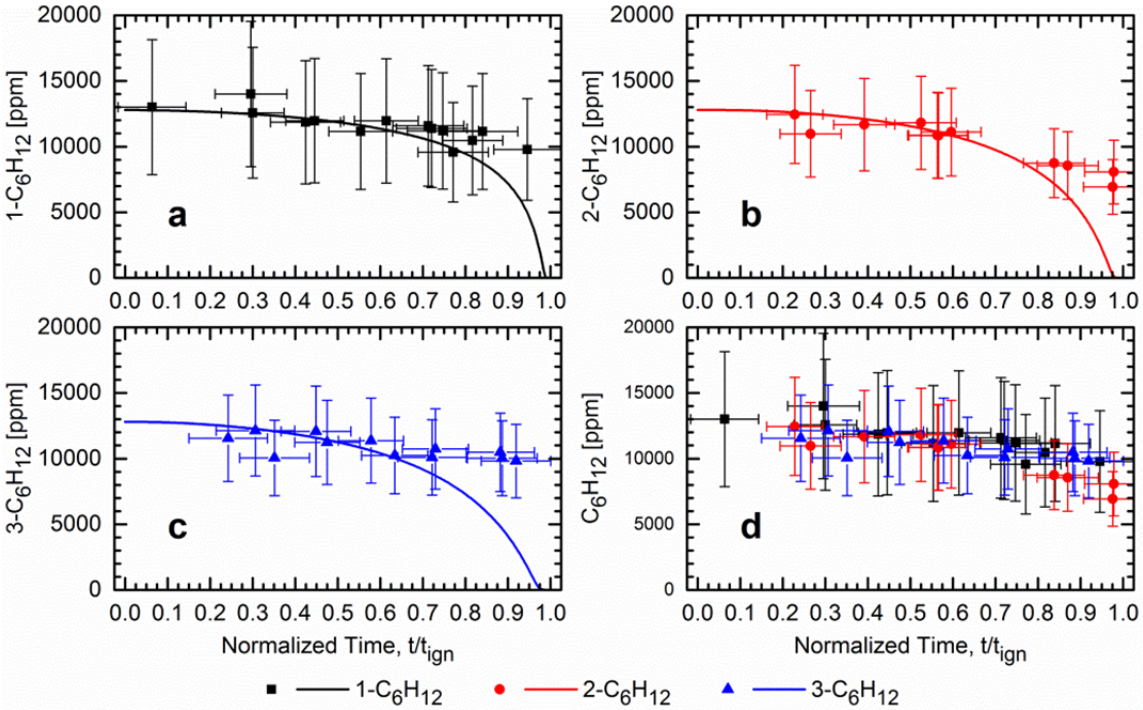

Fig 4. From Wagnon et al. [4], measured (symbols) and predicted (lines) time histories of a) 1-hexene, b) trans-2-hexene, c) trans-3-hexene, and d) all three hexene isomers. Simulations used the LLNL Mehl et al. [7] mechanism at the average compositions and conditions of the experiments (P = 11 atm, T = 900 K).

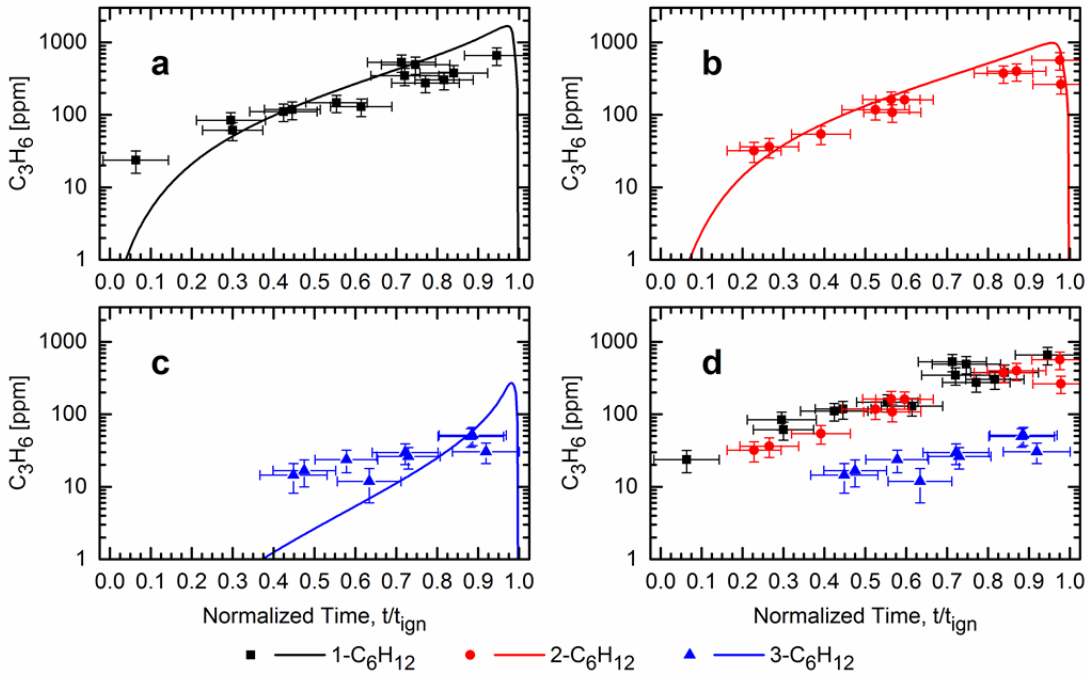

Fig. 5. From Wagnon et al. [4], measured (symbols) and predicted (lines) concentrations of propene during autoignition of a) 1-hexene, b) trans-2-hexene, c) trans-3-hexene, and d) all three hexene isomers. Simulations used the LLNL Mehl *et al.* [28] mechanism at the average compositions and conditions of the experiments (P = 11 atm, T = 900 K).

The experimental data for propene shown in **Fig. 5** indicate a longer alkyl chain promotes significantly increased propene production (a factor of ~5 increase in propene comparing trans-3-hexene with 1-hexene at t/τ_{ign} ~0.93), and this trend was well predicted by the mechanism simulations. For 1-hexene and trans-2-hexene, the experimental data and the simulations for propanal presented in **Fig. 6** are in excellent agreement, within a factor of two. Unlike propene, the experimental measurements indicate propanal production decreases for the longer alkyl chain isomers and exhibits less sensitivity to the double bond position (a factor of ~2 decrease in propanal comparing trans-3-hexene with 1-hexene at t/τign ~0.93). However, the simulations over-predict the experimental measurements for propanal during 3-hexene ignition by more than an order of magnitude.

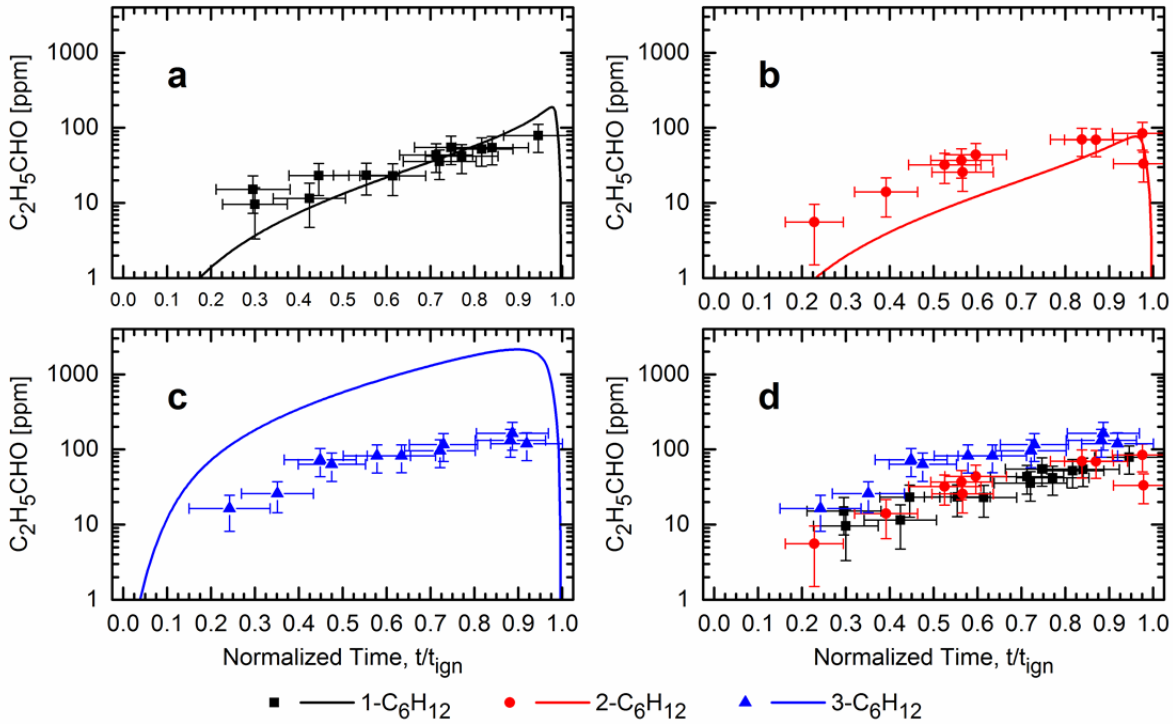

Fig. 6. From Wagnon et al. [4], measured (symbols) and predicted (lines) concentrations of propanal during autoignition of a) 1-hexene, b) trans-2-hexene, c) trans-3-hexene, and d) all three hexene isomers. Simulations used the LLNL Mehl et al. [28] mechanism at the average compositions and conditions of the experiments (P = 11 atm, T = 900 K).

The trends for the intermediate species measurements indicate the small alkene and small alkane chemistry is generally well represented in the LLNL reaction mechanism for 1-hexene and 2-hexene; however, some reaction pathways for 3-hexene differ significantly with the experimental measurements in additional to propanal including (although not shown here)

ethanal (acetaldehyde) and 1.3-butadiene. As described in Vanhove et al. [6] and Mehl et al. [14], alkene chemistry undergoes a transition from low temperatures where allyl radical reactions dominate to higher temperatures (>900 K) where β-decomposition of alkenyl radicals dominate. The over-prediction of the LLNL reaction mechanism for propanal indicates the OH addition to the double bond of 3-hexene may be too fast, and would be a good candidate reaction for further experimental and computational studies.

The results of the hexene isomer study emphasize the value of bulk reactivity data (e.g., ignition delay time) and higher fidelity data (e.g., species measurements) as important methods to identify similarities and differences in reactivity and reaction pathways, which are particularly vital towards developing reaction rate rules for classes of fuel compounds. In particular, the results of the current work are the first species measurements in the high/transition temperature regime for this important alkene. Furthermore, comparisons of the major intermediate species concentrations in **Figs. 5** and **6** of the hexene isomers show the onset of reaction for 3-hexene is somewhat different from that of the other isomers. This feature has recently been shown to be an indicator of fuel octane sensitivity [8], an important property that is highly desirable to inhibit engine knock in next-generation internal combustion engines that operate at turbocharged, high pressure conditions. Importantly, this feature of combustion chemistry is prominent over the temperature and pressure range best addressed by RCF experiments

Results - Ethanol Ignition Chemistry

Ethanol remains the most important alternative, biomass-derived fuel for the transportation sector, and the study of ethanol combustion chemistry is of high interest from scientific, industrial and environmental perspectives. In spite of the well-known relevance of ethanol, there are still limited experimental studies on ethanol auto-ignition behavior at conditions expected in combustion applications and there are even fewer studies where intermediate species have been quantified. To date, there are two major groups of experimental conditions for ethanol ignition reported in the literature. Much has been learned from shock tube studies at pressures from 1 to 10 atm for T > 1100 K [9,10,11,12], and for higher pressures, shock tube studies [13,14,15] and RCFs [13,16] have provided vital insights. Ethanol speciation data are available in the literature from low-pressure flames and flow and jet-stirred reactors, mainly at high temperatures [17,18,19,20,21,22,23,24,25,26,27,28]; however, no species measurements were previously

available at intermediate pressures and low temperatures most important in practical engines until our UM RCF speciation study of ethanol ignition.

For the ethanol studies, stoichiometric (ϕ = 1.0) mixtures were investigated using the UM RCF at pressures of 3, 6 and 10 atm and temperatures from 880-1150 K. A summary of the measured ignition delay times are presented in **Figs. 7** and **8** and compared with previous studies of ethanol ignition in **Fig. 8**. The UM RCF results provide new ignition data at conditions where no previous studies have been reported, specifically for temperatures below 1200 K and pressures ≤10 atm, and the data are in good agreement with expected trends for pressure and temperature. **Figs. 7** and **8** illustrate the strength of RCF studies to study these intermediate to low temperature combustion chemistry regimes.

The experimental results for ethanol were compared with model predictions using the detailed reaction chemistry of Burke et al. [35], which is a updated and modified version of the

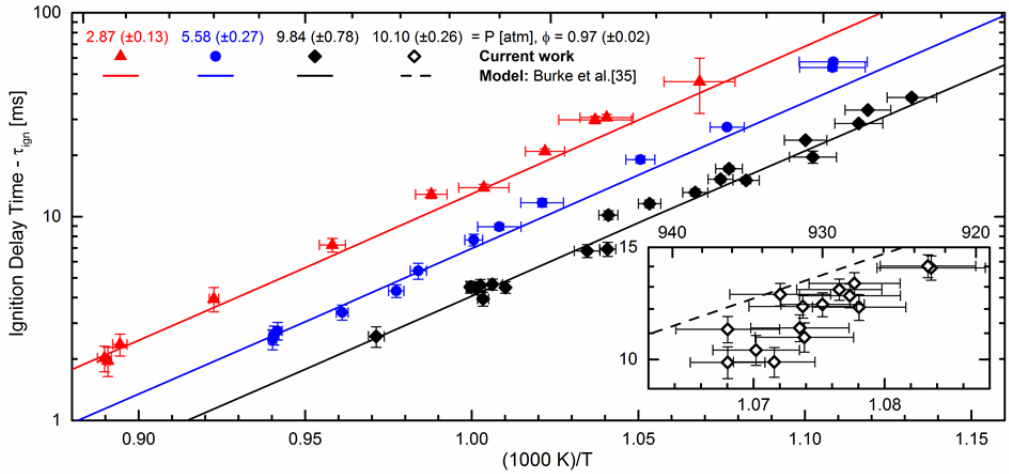

Fig 7. Experimental and modeling results for ethanol ignition delay time from Barraza-Botet et al. [29] for near stoichiometric conditions (ϕ = 0.97) and average dilution levels of inert:O_2 ratios of 8.2 (main figure) and 7.5 for speciation (inset) experiments. Model predictions (solid lines) are based on the reaction mechanism by Burke et al. [35].

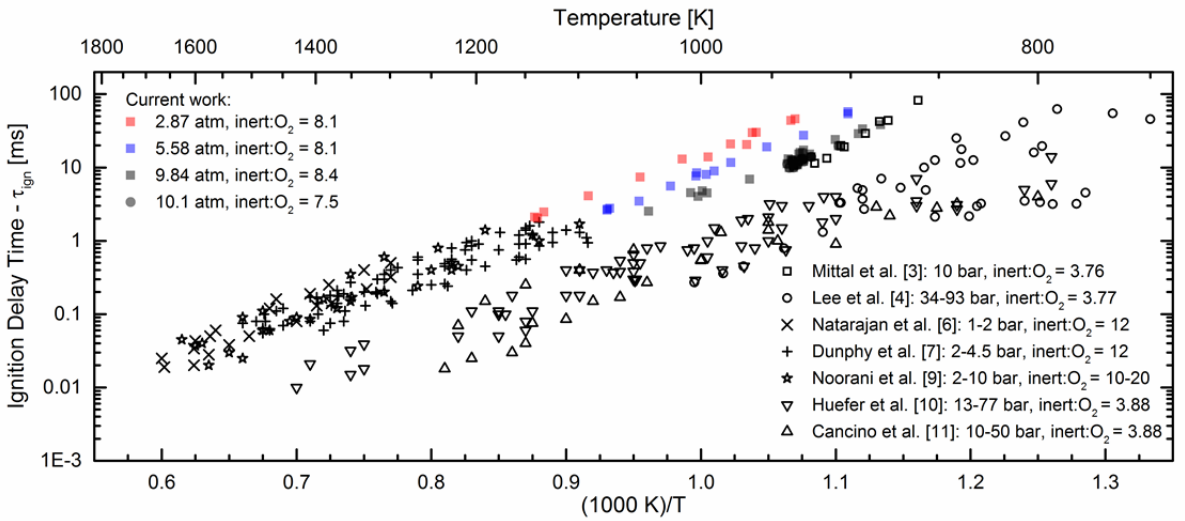

Fig. 8. Summary of results of ignition delay time from Barraza-Botet et al. [29] for stoichiometric mixtures of ethanol studied using the UM RCF (current work) and available in the literature. All data are presented as reported in the literature. No scaling was used to create this figure.

AramcoMech elementary reaction mechanism for combustion of C_1-C_3 hydrocarbon and oxygenated species. As seen in **Fig. 7**, the predictions using the mechanism by Burke et al. [35] are in excellent agreement with the UM RCF data, generally falling within the experimental uncertainty for all pressures and temperatures. Additional comparisons of experimentally observed and predicted trends for ignition delay time as a function of dilution, pressure and temperature are provided in Barraza-Botet et al. [29].

As with our hexene isomer study, fast gas sampling and gas chromatography were used to quantitatively measure ethanol and 11 stable intermediate species formed during the ignition delay period. The time histories of two of the key intermediate species are presented in **Fig. 9**. Ethanal and ethene are products of the two main reaction pathways expected for ethanol oxidation at the conditions studied. Both species were measured at peak levels of over 0.1% (mole basis). The model predictions using the reaction mechanism of Burke et al. [35] are also included in **Fig. 9**. The level of agreement between the experimental data and the model predictions was excellent for these species and other species not shown here, particularly at times close to ignition. The experimental and modeling results show ~72% of the ethanol reacted to produce ethanal as an early intermediate of the reaction sequence initiated by H abstraction by different radicals (predominantly OH and HO_2) from the more reactive α-carbon site on ethanol. Most of the ethanal was consumed in a series of steps to produce methanal (formaldehyde, CH_2O – not detectable with the current experimental set-up) before oxidizing to CO. Carbonyls

(aldehydes) are well-known concerns for ethanol use in the transportation sector from the pollution control perspective.

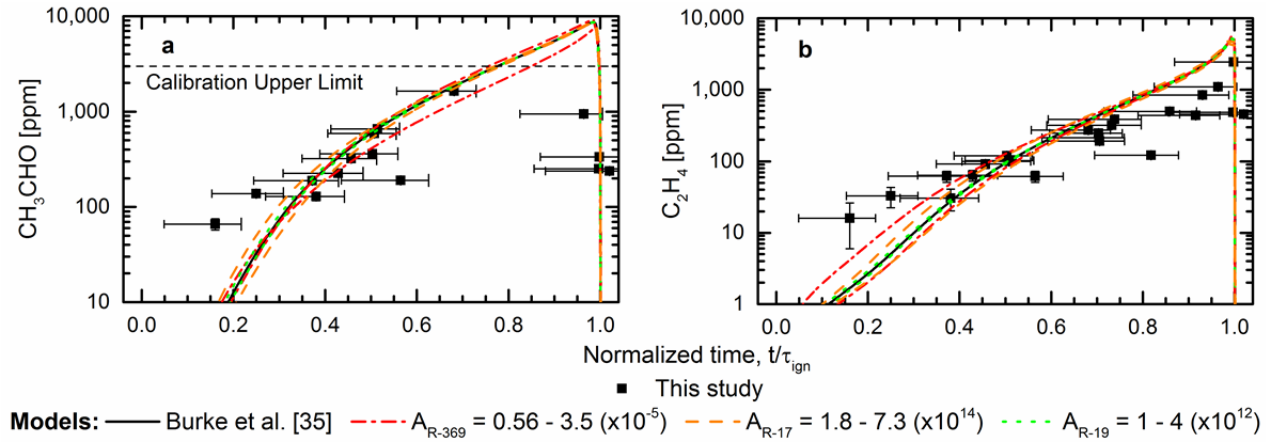

Fig. 9. From Barraza-Botet et al. [29], measured and predicted (using the reaction mechanism by Burke et al. [35]) time histories of stable intermediate species produced during ethanol autoignition: a) ethanal and b) ethene. Average conditions for the sampling experiments were used for the model predictions which were P = 10.1 atm, T = 930 K, ϕ = 0.99, C_2H_5OH = 3.75%, O_2 = 11.33%, and inert:O_2 = 7.5. The effects of modifying the pre-exponential factors within the respective uncertainty limits of reactions R-17 $2HO_2 \leftrightarrow H_2O_2 + O_2$, R-19 H_2O_2 (+ M) $\leftrightarrow$ 2OH (+M), and R-369 $C_2H_5OH + HO_2 \leftrightarrow sC_2H_4OH + H_2O_2$ are included.

The simulation results were used to identify the significant reaction pathways involving the species measured, and ethanol + HO_2 (reaction R-369) was identified as the most important reaction at the experimental conditions for both the UM RCF ignition delay time and intermediate species measurements. However, while ignition delay time showed high sensitivity to changes in the rate coefficient of the ethanol + HO_2 reaction, the speciation data did not, as seen in **Fig. 9**. The lack of sensitivity of the species time histories to the reactions controlling the ignition delay time presents an opportunity to further evaluate our understanding of reaction pathways and reaction mechanisms. New methods of analysis provide the opportunity for intermediate species measurements to be used to validate and verify reaction mechanisms beyond typical comparisons, such as demonstrated in the next section C.3 on the ignition chemistry of n-butanol.

Results - n-Butanol Ignition Chemistry

Speciation and ignition studies of n-butanol were conducted previously by Karwat et al. [2] using the UM RCF. Butanol is important as a potential major biomass-derived transportation fuel with octane sensitivity for ground transportation applications, and butanol is attractive to the air

transportation sector due to the reduced miscibility in water and higher heat of combustion compared with ethanol. As with the ethanol study described above in section B.2., the ignition delay times were well predicted using the elementary chemical kinetic mechanism developed by Black et al. [30]; however, some of the species measurements disagreed significantly with the model predictions, including the small alkenes (e.g., ethene and propene) and n-butyraldehyde. Since our first study of n-butanol, significant theoretical and experimental efforts focused on determining the elementary rate coefficients of primary n-butanol reaction pathways in combustion environments, including H atom abstraction reactions from n-butanol by key radicals such as HO_2 and OH, as well as the decomposition of the radicals formed by these H atom abstractions. In the follow-on study by Karwat et al. [31], we teamed with DOE BES researchers Drs. Stephen Klippenstein and Michael Davis to assess the impact of revisions of the rate coefficients to the n-butanol measurements we made previously, as well as for predicting data newly available in the literature. A subset of the UM RCF species measurements are presented here for the point of this discussion. Please see Karwat et al. [31] for details. Briefly, **Fig. 10** presents comparisons of the experimental data with systematic revisions to the reaction mechanism of Black et al. [30]. In **Fig. 10**, predictions using the unmodified reaction mechanism of Black et al. [30] are presented as the solid black lines. The effects of using the reaction rates for n-butanol + OH recommended by Zhou et al. [32] with the Black et al. mechanism are represented as the black dotted lines. Model predictions based on revising the Black et al. mechanism with new results from *ab initio* transition-state-theory-based master equation analysis for the hydroxybutyl and butoxy decomposition reactions by Zhang et al. [33] are presented as the purple dash-dot lines. The blue short-dot lines include both the revisions based on the work by Zhang et al. [33] and the results from Seal et al. [34] (who used multistructural variational transition state theory calculations for all H-atom abstractions by OH radicals from n-butanol) and the results from Alecu et al. [35] (who used multi-structural transition-state-theory to determine rate predictions for the H-atom abstraction by HO_2 from the 1-carbon site of n-butanol). The effects of new rate coefficient recommendations for the $HO_2 + HO_2 \rightarrow H_2O_2 + O_2$ reaction by Zhou *et al*. [24] were also explored, but found to have negligible impact on the model predictions relative to the other revisions to the Black et al. mechanism.

The revisions to the reaction mechanism had little impact on the predicted ignition delay times (17.9 ms for the first revision and 19.4 ms for the second revision, compared with the

original Black *et al*. mechanism prediction of τ_{ign} = 18.6 ms). Yet there were significant improvements in the species time-history predictions (shown by the purple dash-dot lines in **Fig. 10**) for two of the species when the rate coefficient data by Zhang et al. [33] were incorporated. The changes in the product channel for the C_4H_8OH-4 radical decomposition reaction decreased ethene production, improving the agreement with the experimental observations. The *n*-butyraldehyde predictions improved to within a factor of four at the highest measured concentrations. The updated simulation results showed practically no change in the methane, acetaldehyde, propene, 1-butene, and CO predictions, or *n*-butanol consumption. Further improvement in the model predictions for *n*-butyraldehyde (within a factor of two to three of the experimental results) were achieved with the inclusion of the new rate coefficients for H-atom abstraction from butanol by OH (the blue short dot lines), with slight improvement in the propene predictions, slight worsening of the ethene predictions and practically no change in the 1-butene predictions.

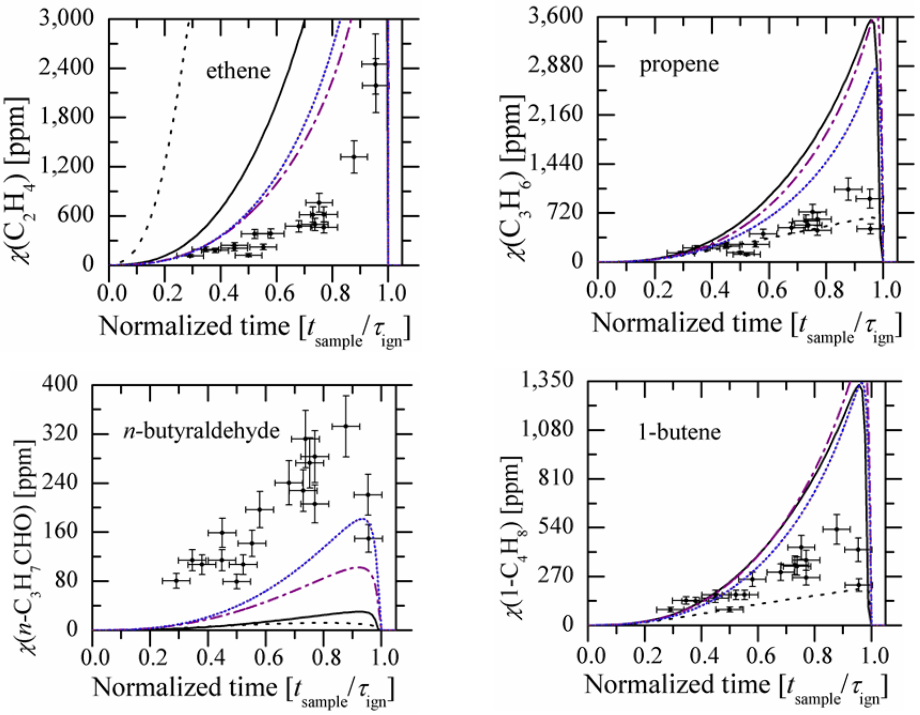

Fig 10. Comparison of experimental data and model predictions for stable intermediate species observed during *n*-butanol ignition from Karwat et al. [31]. The symbols represent the experimental measurements made by Karwat et al. [2]. Model predictions using the unmodified Black et al. [30] mechanism (solid black line) and revisions to the Black et al. mechanism are shown as lines. Please see the text for descriptions of the mechanism revisions.

The revised predictions for the intermediate species time histories significantly improved agreement with the measurements, but some discrepancies persist. If the *n*-butanol study only considered ignition delay time data, the understanding of *n*-butanol combustion chemistry would appear accurate and complete. The UM RCF intermediate species measurements were critical to identifying areas of the fuel oxidation chemistry which remain uncertain and which should be the focus of continued experimental and theoretical efforts.

Similar to the impact of the *ab initio* studies of the n-butanol combustion reactions, we expect *ab initio* studies of the rate coefficient of the ethanol + HO_2 reaction will reduce empiricism and improve the predictive accuracy of low temperature ethanol combustion. In this way, UM RCF ignition studies guide and inform complementary DOE BES research.

Conclusions

In the UM RCF ignition study of the three linear isomers of hexene, we measured the reactivity of the isomers and validated the reaction rate rules used to create reaction mechanisms of these unsaturated hydrocarbons. We found the predictive understanding was unequal for the different isomers based on the location of the double bond, with the 1- and 2-trans hexenes well represented by current reaction theory, and the 3-trans hexene less well understood. This is particularly relevant as alkenes are critical to soot formation mechanisms and as components of conventional and unconventional fossil fuels. In our ethanol study, we found excellent predictive agreement between experimental data and model predictions for ignition delay time and for most intermediate species. However, the model predictions are based on semi-empirical reaction rate theory for the most important reaction of $C_2H_5OH + HO_2$. The experimental results provide a basis for improving and validating *ab initio* reaction rates for $C_2H_5OH + HO_2$. We also revisited n-butanol ignition to understand the impact of new *ab initio* calculations of key elementary reactions on the measurements of intermediate species we made previously. The results highlight how global reactivity of n-butanol is very well understood, and advances in *ab initio* rate coefficient calculations are reducing empiricism and improving predictive accuracy of key intermediate reaction pathways. Overall, the results of this DOE project demonstrate how a combination of global and detailed reaction parameters like ignition delay time and corresponding species time histories identify divergence in the reaction chemistry and focus research efforts on which key reactions need further investigation.

Acknowledgements

The University of Michigan acknowledge the generous financial support of U.S. Department of Energy Basic Energy Sciences program via award number DE-SC00002645.

References

1. Donovan, M. T., He, X., Zigler, B. T., Palmer, T. R., Wooldridge, M. S., Atreya, A. (2004) "Demonstration of a Free-Piston Rapid Compression Facility for the Study of High Temperature Combustion Phenomena" *Combust. Flame* **137** 351-365.
2 Karwat, D. M. A., Wagnon, S., Teini, P. D., Wooldridge, M. S. (2011) "On the Chemical Kinetics of n-Butanol: Ignition and Speciation Studies," *J. Phys. Chem. A* **115** 4909-4921.
3. He, X., Donovan, M. T., Zigler, B. T., Palmer, T. R., Walton, S. M., Wooldridge, M. S., Atreya, A. (2005) "An Experimental and Modeling Study of Iso-octane Ignition Delay Times under Homogenous Charge Compression Ignition Conditions," *Combust. Flame* **142** 266-275.
4. Wagnon, S. W., Barraza-Botet, C. L., Wooldridge, M. S., (2015) "The Effects of Bond Location on the Ignition and Reaction Pathways of trans-Hexene Isomers," *J. Phys. Chem. A* **119** 7695-7703.
5. Mehl, M., Pitz, W. J., Westbrook, C. K., Yasunaga, K., Conroy, C., Curran, H. J., (2011) "Autoignition Behavior of Unsaturated Hydrocarbons in the Low and High Temperature Regions," *Proc. Combust. Inst.* **33** 201-208.
6. Vanhove, G., Ribaucour, M., Minetti, R., (2004) "On the Influence of the Position of the Double Bond on the Low-Temperature Chemistry of Hexenes," *Proc. Combust. Inst.* **30** 1065-1072.
7. Mehl, M., Pitz, W. J., Westbrook, C. K., Curran, H. J., (2011) "Kinetic Modeling of Gasoline Surrogate Components and Mixtures under Engine Conditions," *Proc. Combust. Inst.* **33** 193-200.
8. Westbrook, C. K., Mehl, M., Pitz, W. J., Sjoberg, M., (2016) "Chemical Kinetics of Octane Sensitivity in a Spark-Ignition Engine", *Combust. Flame*, http://dx.doi.org/10.1016/j.combustionflame.2016.05.22.
9. Natarajan, K, Bhaskaran, K. A. (1981) "An Experimental and Analytical Investigation of High Temperature Ignition of Ethanol," *Proc. 13th Int. Symp. Shock Tubes and Shock Waves* 834–842.
10. Dunphy, M. P., Simmie, J. M., (1991) "High-Temperature Oxidation of Ethanol: Part 1.-Ignition Delays in Shock Waves," *J. Chem. Soc. Faraday Trans.* **87** 1691–1696.
11. Curran, H. J., Dunphy, M. P., Simmie, J. M., Westbrook, C. K., Pitz, W. J., (1992) "Shock Tube Ignition of Ethanol, Isobutene and MTBE: Experiment and Modeling," *Proc. Combust. Inst.* **24** 769–776.
12. Noorani, K. E., Akih-Kumgeh, B., Bergthorson, J. M., (2010) "Comparative High Temperature Shock Tube Ignition of C1−C4 Primary Alcohols," *Energy & Fuels* **24** 5834–5843.
13. Lee, C., Vranckx, S., (2012) "On the Chemical Kinetics of Ethanol Oxidation: Shock Tube, Rapid Compression Machine and Detailed Modeling Study," *Z. Phys. Chem.* **226** 1–27.
14. Heufer, K. A., Olivier, H., (2010) "Determination of Ignition Delay Times of Different Hydrocarbons in a New High Pressure Shock Tube," *Shock Waves* **20** 307–16.
15. Cancino, L. R., Fikri, M., Oliveira, A. A. M., Schulz, C., (2010) "Measurement and Chemical Kinetics Modeling of Shock-Induced Ignition of Ethanol−Air Mixtures," *Energy & Fuels* **24** 2830–2840.
16. Mittal, G., Burke, S. M., Davies, V. A., Parajuli, B., Metcalfe, W. K., Curran, H. J. (2014) "Autoignition of Ethanol in a Rapid Compression Machine," *Combust. Flame.* **161** 1164-1171.

17. Norton, T., Dryer, F., (1992) “An Experimental and Modeling Study of Ethanol Oxidation Kinetics in an Atmospheric Pressure Flow Reactor,” *Int. J. Chem. Kinet.* **24** 319–344.
18. Alzueta, M. U., Hernandez, J. M., (2002) “Ethanol Oxidation and Its Interaction with Nitric Oxide,” *Energy & Fuels* **16** 166–171.
19. Li, J., Kazakov, A., Dryer, F. L., (2004) “Experimental and Numerical Studies of Ethanol Decomposition Reactions,” *J. Phys. Chem. A* **108** 7671–7680.
20. Kasper, T., Oswald, P., Kamphus, M., Kohsehoinghaus, K., (2007) “Ethanol Flame Structure Investigated by Molecular Beam Mass Spectrometry,” *Combust. Flame* **150** 220–231.
21. Leplat, N., Seydi, A., Vandooren, J., (2008) “An Experimental Study of the Structure of a Stoichiometric Ethanol/Oxygen/Argon Flame,” *Combust. Sci. Technol.* **180** 519–532.
22. Haas, F. M., Chaos, M., Dryer, F. L., (2009) “Low and Intermediate Temperature Oxidation of Ethanol and ethanol–PRF Blends: An Experimental and Modeling Study,” *Combust. Flame* **156** 2346–2350.
23. Dagaut, P., Togbe, C., (2009) “Experimental and Modeling Study of the Kinetics of Oxidation of Butanol "n-Heptane Mixtures in a Jet-Stirred Reactor,” *Energy & Fuels* **23** 3527–3535.
24. Leplat, N., Dagaut, P., Togbé, C., Vandooren, J., (2011) “Numerical and Experimental Study of Ethanol Combustion and Oxidation in Laminar Premixed Flames and in Jet-Stirred Reactor,” *Combust. Flame* **158** 705–725.
25. Xu, H., Yao, C., Yuan, T., Zhang, K., Guo, H., (2011) “Measurements and Modeling Study of Intermediates in Ethanol and Dimethy Ether Low-Pressure Premixed Flames Using Synchrotron Photoionization,” *Combust. Flame* **158** 1673–1681.
26. Tran, L. S., Glaude, P., Battin-Leclerc, F., (2013) “An Experimental Study of the Structure of Laminar Premixed Flames of Ethanol/Methane/Oxygen/Argon,” *Combust. Explos. Shock Waves* **49** 11–18.
27. Tran, L., Glaude, P., Fournet, R., Battin-Leclerc, F., (2013) “Experimental and Modeling Study of Premixed Laminar Flames of Ethanol and Methane,” *Energy & Fuels* **27** 2226–2245.
28. Herrmann, F., Jochim, B., Oßwald, P., Cai, L., Pitsch, H., Kohse-Höinghaus, K., (2014) “Experimental and Numerical Low-Temperature Oxidation Study of Ethanol and Dimethyl Ether,” *Combust. Flame* **161** 384–397.
29. Barraza-Botet, C. L., Wagnon, S. W., Wooldridge, M. S., (2016) “On the Ignition Chemistry of Ethanol: An Experimental Study,” *J. Phys. Chem. A* **120** 7408-7418.
30. Black, G., Curran, H. J., Pichon, S., Simmie, J. M., Zhukov, V. (2010), “Bio-butanol: Combustion Properties and Detailed Chemical Kinetic Model,” *Combust. Flame* **157** 363-373.
31. Karwat, D. M. A., Wooldridge, M. S., Klippenstein, S. J., Davis, M. J., (2015) “Effects of New Ab Initio Rate Coefficients on Predictions of Species Formed During n-Butanol Ignition,” *J. Phys. Chem. A* **119** 543-551.
32. Zhou, C.-W., Simmie, J. M., Curran, H. J. (2011) “Rate Constants for Hydrogen-Abstraction by OH from n-Butanol,” *Combust. Flame* **44** 155-164.
33. Zhang, P., Klippenstein, S. J., Law, C. K., (2013) “Ab Initio Kinetics for the Decomposition of Hydroxybutyl and Butoxy Radicals of n-Butanol,” *J. Phys. Chem. A* **117** 1890–1906.

34. Seal, P., Oyedepo, G., Truhlar, D. G., (2013) “Kinetics of the Hydrogen Atom Abstraction Reactions from 1-Butanol by Hydroxyl Radical: Theory Matches Experiment and More,” *J. Phys. Chem. A* **117** 275–282.
35. Alecu, I. M., Zheng, J., Papajak, E., Yu, T., Truhlar, D. G., (2012) “Biofuel Combustion. Energetics and Kinetics of Hydrogen Abstraction from Carbon-1 in n-Butanol by the Hydroperoxyl Radical Calculated by Coupled Cluster and Density Functional Theories and Multistructural Variational Transition-State Theory with Multidimensional Tunneling. *J. Phys. Chem. A* **116** 12206–12213.

THE JOURNAL OF PHYSICAL CHEMISTRY A

ARTICLE

pubs.acs.org/JPCA

On the Chemical Kinetics of *n*-Butanol: Ignition and Speciation Studies

Darshan M.A. Karwat,[*,†] Scott W. Wagnon,[‡] Paul D. Teini,[‡] and Margaret S. Wooldridge[†,‡]

[†]Department of Aerospace Engineering and [‡]Department of Mechanical Engineering, University of Michigan, Ann Arbor, Michigan 48109, United States

Supporting Information

ABSTRACT: Direct measurements of intermediates of ignition are challenging experimental objectives, yet such measurements are critical for understanding fuel decomposition and oxidation pathways. This work presents experimental results, obtained using the University of Michigan Rapid Compression Facility, of ignition delay times and intermediates formed during the ignition of *n*-butanol. Ignition delay times for stoichiometric *n*-butanol/O_2 mixtures with an inert/O_2 ratio of 5.64 were measured over a temperature range of 920−1040 K and a pressure range of 2.86−3.35 atm and were compared to those predicted by the recent reaction mechanism developed by Black et al. (*Combust. Flame* **2010**, *157*, 363−373). There is excellent agreement between the experimental results and model predictions for ignition delay time, within 20% over the entire temperature range tested. Further, high-speed gas sampling and gas chromatography techniques were used to acquire and analyze gas samples of intermediate species during the ignition delay of stoichiometric *n*-butanol/O_2 (χ(*n*-but) = 0.025, $\chi(O_2)$ = 0.147, $\chi(N_2)$ = 0.541, χ(Ar) = 0.288) mixtures at P = 3.25 atm and T = 975 K. Quantitative measurements of mole fraction time histories of methane, carbon monoxide, ethene, propene, acetaldehyde, *n*-butyraldehyde, 1-butene and *n*-butanol were compared with model predictions using the Black et al. mechanism. In general, the predicted trends for species concentrations are consistent with measurements. Sensitivity analyses and rate of production analyses were used to identify reactions important for predicting ignition delay time and the intermediate species time histories. Modifications to the mechanism by Black et al. were explored based on recent contributions to the literature on the rate constant for the key reaction, *n*-butanol+OH. The results improve the model agreement with some species; however, the comparison also indicates some reaction pathways, particularly those important to ethene formation and removal, are not well captured.

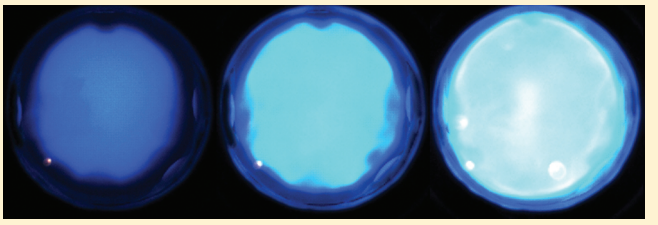

1. INTRODUCTION

Bioethanol is at present the most widely produced biofuel and is used both as an additive to petrol/gasoline and as a fuel in its own right in specially modified vehicles. There are significant concerns, ethical and environmental, about ethanol production from food stocks. Interest in butanol has therefore increased due to the variety of potential feed stock sources. Butanol has a higher lower heating value than ethanol and reduced miscibility in water as compared to ethanol.[2] Consequently, butanol is more attractive for application to aviation, transport, and storage as compared to ethanol, although toxic pollutants such as aldehydes and ketones, which are harmful to health, are formed as combustion byproducts from both ethanol and butanol.[3]

There has been much recent work studying the combustion chemistry of butanol (all four isomers), including studies of flame characteristics and propagation,[4−7] ignition,[1,8−11] decomposition,[12] pyrolysis,[13,14] and elementary reaction rates.[15,16] Most work has been performed in the high-temperature regime (T > 900 K); however, an early pyrolysis study investigated *n*-butanol pyrolysis at low temperatures (T < 800 K).[14] Recent decomposition studies have further investigated the effects of adding *n*-butanol to well-studied *n*-alkanes.[17,18]

McEnally and Pfefferle[4] compared the kinetics of the four isomers of butanol in co-flowing methane/air flames. The authors state that although oxygenates are regarded as clean-burning fuels, the alkenes formed from the butanols can participate in hydrocarbon growth processes that lead to aromatics and soot, and during their experiments they observed the butanol-doped flames to be much more luminous than the undoped methane flame. Further, the branched isomers of butanol produced more soot precursors and benzene than did the linear isomers. They concluded that the branched nature of the fuels plays a more important role in soot formation than the presence or absence of oxygen bound in the fuel.

Several reaction mechanisms have also been developed in conjunction with these experimental studies. To date, ignition studies of butanol isomers have been studied predominantly in high- and low-pressure shock tubes. Heufer et al.[9] measured ignition delay times in the range of 10−42 atm and 770−1250 K using stoichiometric fuel/oxidizer/diluent mixtures. Moss et al.[8] conducted an experimental and kinetic modeling study of the

Received: January 27, 2011
Revised: March 18, 2011
Published: April 22, 2011

oxidation of the four isomers of butanol for ϕ = 0.25, 0.5, and 1, at temperatures between 1196 and 1823 K and pressures near 1 atm, with varying dilution levels. The chemical kinetic mechanism developed did not include low-temperature alkylperoxy chemical pathways. They found that *n*-butanol is the most reactive isomer, followed by *iso*-butanol, 2-butanol, and finally *tert*-butanol. Black et al.[1] conducted a similar study, in which *n*-butanol ignition experiments were performed at ϕ = 0.5, 1, and 2, with pressures between 1 and 8 atm, over a range of temperatures from 1100 to 1800 K. Most of the data were obtained at a dilution level of ~95% (argon), with one series at a dilution of 77%. The authors also developed a chemical kinetic mechanism for *n*-butanol, based on *n*-butane chemistry[19] for a wide temperature (740−1660 K) and pressure range (1−34 atm). Included were simple β-scission reactions, as well as complex scission, in particular the four-centered elimination of water to form 1-butene:

$$CH_3CH_2CH_2CH_2OH + M \rightarrow CH_3CH_2CH{=}CH_2 + H_2O + M$$

Reaction path analysis carried out for ϕ = 1, T = 1450 K, showed H-atom abstraction to be the principal route of consumption of *n*-butanol, in accordance with previous modeling results.[8,20] Abstraction from the α position dominates, followed by the β, γ, and δ positions, while abstraction from the hydroxyl group is of lesser importance. At high temperatures, sensitivity analysis for ϕ = 2 showed that small radical reactions (such as $H + O_2$) have the greatest influence on ignition delay time. The most sensitive fuel reaction is scission of the $C_\alpha - C_\beta$ bond, which increases the overall reactivity of the system. While these works have led to major developments in the detailed reaction mechanisms for *n*-butanol combustion, the effects of lower temperatures on *n*-butanol reactivity are much less well-known.

Understanding *n*-butanol combustion chemistry is vital to the successful development of renewable fuel strategies. Experiments which provide quantitative data on the reactivity and key reaction pathways of *n*-butanol are important for understanding the fundamental chemistry of this oxygenated fuel. Measurements of intermediate species concentrations during the ignition delay time provide experimental evidence of reaction pathways of fuel consumption and pollutant formation. However, quantifying these intermediates is difficult, due to the sampling and analytical methods required. To our knowledge, only two speciation studies of *n*-butanol oxidation and ignition exist in the literature. Sarathy et al.[12] studied *n*-butanol decomposition and combustion through experimental studies in a jet-stirred reactor at a mean residence time of 0.07 s, a constant pressure of 1 atm, and over a temperature range of 800−1300 K. Their studies included measurements of the parent fuel, methane, ethane, ethene, acetylene, propene, formaldehyde, acetaldehyde, butyraldehyde, 1-butene, carbon dioxide, and carbon monoxide as a function of different reactor temperatures. They found, at T = 1160 K and ϕ = 1, the leading consumption pathways of *n*-butanol to be complex fission resulting in the formation of 1-butene and H_2O (25%) and H-atom abstraction (60%), with H atoms (29%) and OH (57%) radicals being the main contributors to H-atom abstraction.

Osswald et al.[6] studied fuel-rich (ϕ = 1.7), low-pressure flames of the four isomers of butanol using molecular beam mass spectrometry. The authors were able to identify 57 chemical species, including radical and isomeric species, at various heights above their porous plug burners using a combination of electron ionization and photoionization mass spectrometry. The authors were able to characterize pollutant emissions and soot precursors from the flames of the four isomers, with fuel structure significantly influencing the concentrations of these products; high concentrations of formaldehyde and acetaldehyde were detected in *n*-butanol flames, and while *tert*-butanol flames produced low concentrations of oxygenated intermediates, they did produce higher concentrations of propargyl and benzene, both of which are soot precursors.

The objective of the current study is to provide new insights into the low-temperature combustion chemistry of *n*-butanol through ignition and speciation studies. The experimental measurements of *n*-butanol ignition delay times and intermediate species measurements are targeted to provide new data and metrics that extend our quantitative understanding of *n*-butanol combustion chemistry at conditions relevant to modern jet and internal combustion engines.

2. EXPERIMENTAL SETUP

2.1. University of Michigan Rapid Compression Facility. The University of Michigan Rapid Compression Facility (UM RCF) is a unique and powerful apparatus for fundamental studies of fuel chemistry over a broad range of thermodynamic conditions. Numerous studies of combustion chemistry have been completed using the UM RCF, including ignition studies of reference hydrocarbon fuel compounds such as *iso*-octane,[21,22] simulated syngas mixtures of hydrogen and carbon monoxide,[23] and oxygenated hydrocarbons.[24] Differential laser absorption has been applied to UM RCF studies of *iso*-octane/air mixtures to provide time-resolved measurements of the hydroxyl (OH) radical.[25] More recent work has focused on quantitative measurements of intermediate species by gas chromatography using rapid gas sampling during UM RCF experiments of *iso*-octane/air[26] and methyl butanoate/air[27] mixtures.

The UM RCF uses a free-piston/cylinder compression process to create a chemical reactor for combustion chemistry studies. The key characteristics of the combustion kinetics are interrogated using the optical and physical access provided by the test section of the facility. The UM RCF consists of five major components as shown in Figure 1—the driver section, the driven section, the test section (or test manifold), the sabot (a free piston with a tapered nose cone that forms an interference fit with the test section), and the hydraulic globe valve system. At the start of an experiment, the sabot is located at the upstream end of the driven section. The driven section (2.74 m long, 101.2 mm inner diameter) is evacuated and then filled with a pre-prepared fuel/oxidizer/diluent mixture. The driver section (with an inner diameter of 154 mm) is charged with high-pressure gas. The driver and driven sections are separated by the fast-acting globe valve. When the valve is opened (with a typical cycle time of 100 ms), the sabot is launched down the length of the driven section compressing the test gas mixture. At the end of compression (EOC), the nose cone of the sabot seals the fuel/oxidizer/diluent mixture in the test section at specifically targeted temperatures and pressures, with the majority of the rise in temperature and pressure occurring during the last 10 ms of the stroke. Targeted temperatures and pressures are achieved by varying the compression ratio of the test section, as well as the composition of inert gases in the test mixture. At a given pressure and temperature after EOC, the fuel/oxidizer/diluent mixture in

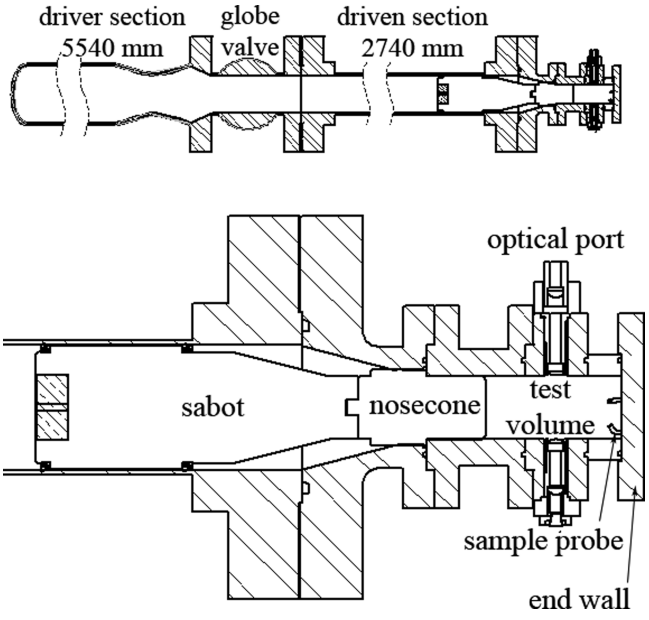

Figure 1. Top panel is a schematic of the major components of the UM RCF. The lower panel presents a detailed view of the test section showing the configuration of equipment used during high-speed gas sampling experiments. Only the probes of the gas-sampling system are shown in the schematic.

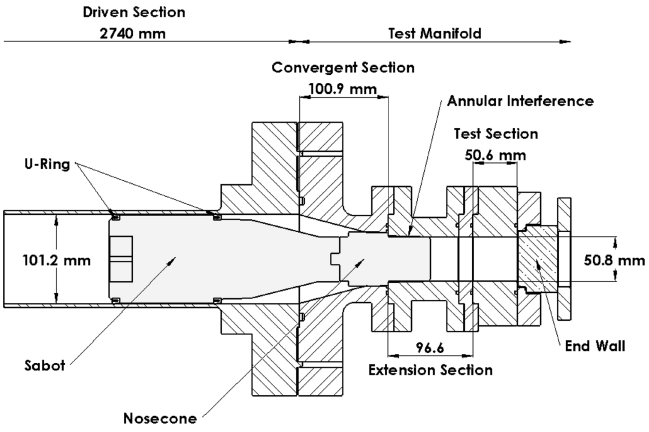

Figure 2. Schematic of the test section of the UM RCF configured for end-view imaging, including key dimensions.

the test section autoignites after a period of time that is designated the ignition delay time (τ_{ign}).

The UM RCF is designed to create uniform conditions at EOC to isolate reaction chemistry during the experiments and to minimize other interfering effects. Two important features include the geometry of the convergent section and the mixing manifold. The convergent section, the test section, and the nose cone of the sabot are designed to trap the cold boundary layer outside the test section. Figure 2 shows a schematic of these RCF components with key dimensions. The unique shape of the sabot and the geometry of the convergent section cause the core region of the test gases to be compressed into the test section, trapping the cold boundary layer gases in the shoulder region created by the body of the sabot and the convergent section. The compression of the core gases is therefore well-described as an isentropic process, and characterization studies show less than 5% difference in measured and predicted isentropic conditions in the core region of the test section.[28] The characterization studies further show that the isentropic core region extends across 70% of the diameter of the test section and that the bulk of the pressure rise (~80%) and temperature rise (~50%) occurs during the last 10 ms of the compression process, where the total stroke lasts approximately 145 ms. An additional important outcome of trapping the cold boundary layers outside the test section is that heat losses from the gases in the core region are minimized, which maximizes the amount of time the test gases are at uniform state conditions. Consequently, conditions can be maintained for long test times on the order of 50 ms, with pressure >75% of EOC pressure and temperature >80% of EOC temperature, depending on the test gas mixtures.

For this study, mixtures were prepared external to the UM RCF to ensure good reactant mixing and uniform composition for each experiment. Stoichiometric *n*-butanol/O_2 (*n*-butanol—Sigma-Aldrich, purum, >99% GC grade; O_2—Cryogenic Gases, Purity Plus 4.3, 99.993%, <40 ppm Ar, <3 ppm moisture, <10 ppm N_2, <0.5 ppm hydrocarbons) mixtures, with an inert/O_2 ratio of 5.64, were prepared manometrically using a mixing manifold and mixing tank that are connected to the UM RCF. Mixture compositions were determined using partial pressures measured with a capacitance diaphragm gauge (Varian Cerami-Cel VCMT12TFA, with an accuracy of ±0.01 Torr). All mixtures were allowed to mix diffusively for over 12 h. The partial pressure of *n*-butanol used in the mixtures was maintained at less than half the saturation vapor pressure of *n*-butanol at room temperature (8.81×10^{-3} atm or 6.69 Torr at 25 °C) to avoid concerns of fuel condensation. The concentration of inert gases in the mixture—Ar (Cryogenic Gases, Purity Plus 5.0, 99.999%, <2 ppm O_2, <2 ppm moisture, <0.5 ppm hydrocarbons) and N_2 (Cryogenic Gases, Purity Plus 5.0, 99.999%, <2 ppm O_2, <3 ppm moisture, <0.5 ppm hydrocarbons)—was varied to control the ratio of specific heats of the reactant mixture and thereby the EOC state conditions. Total mixture pressures in the mixing tank were 0.11−0.13 atm, and each mixture was typically used for two ignition experiments with initial fill pressures (P_0) in the RCF of $P_0 = 3.2 \times 10^{-2}$−3.7×10^{-2} atm.

The test section is instrumented with several diagnostics to interrogate the test gas mixture during ignition studies. The pressure in the test section is monitored using a piezoelectric transducer (Kistler 6041AX4) and charge amplifier (Kistler 5010B) with a combined accuracy of 0.01 atm and 0.015 ms. All electronic signals are acquired using a data acquisition system (National Instruments (NI) cDAQ 9172 chassis coupled with NI 9215 cards) recording at 100 kHz. High-speed imaging of the combustion phenomena in the test section can be obtained either by viewing along the axis of the test section (end-view) using a transparent end wall or orthogonal to the axis of the test section (side-view) using a transparent cylindrical section. For this study, a high-speed CMOS camera (Vision Research, Phantom v7.1, SR-CMOS 48-bit color array, maximum resolution of 800 × 600 pixels, capable of 160 kHz at reduced spatial resolution, 22 μm pixels with 0.34 μm spacing) was used to record end-view images during ignition. Side-view imaging was not used. The chemiluminescence from the test volume was captured with a fast 50 mm lens (f/0.95, Navitar) and c-mount extension tube. For these experiments, a setting of 26 000 frames per second (fps) with an image exposure time of 38 μs and a spatial resolution of 256 × 256 pixels was used. The imaging data provide qualitative and quantitative indications of the ignition homogeneity. The camera

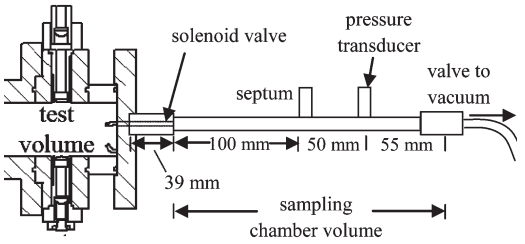

Figure 3. Schematic of the rapid gas-sampling system used in the current work.

array records color signals using red (~95% transmission above 615 nm), blue (~86% peak transmission at 460 nm), and green (~82% peak transmission at 530 nm) spectral filters. No additional spectral filtering was used.

2.2. High-Speed Gas Sampling and Gas Chromatography. For the high-speed gas sampling experiments, the transparent end wall was replaced with an end wall equipped with a gas sampling system. For the sampling experiments, a small portion of the test gas mixture is removed from the test section through the end wall (as shown in Figure 3) at targeted time intervals during the ignition delay period. The gas samples are then analyzed to identify and quantify the species present. By conducting a series of RCF ignition experiments at the same targeted EOC conditions, the overall species time histories for the intermediates are compiled.

Previous studies to investigate the intermediates formed during *iso*-octane and methyl butanoate ignition delay times have been conducted using rapid gas sampling from UM RCF experiments.[23,26] For this work, the same sampling approach was used, but a new four-valve gas-sampling system was created to improve the time response (via custom-modified valves) and decrease the level of dilution of the sample gases (via decreased dead volume in the sampling system and with the potential to acquire larger gas samples in the same sampling time). These modifications reduce the uncertainty in the species measurements. The new gas-sampling system also allows gas sampling at higher EOC pressures (up to approximately 10 atm).

The major components of the sampling system are the sample chambers (4.5 ± 0.5 mL), piezoresistive pressure transducers (Kistler 4045A2) and amplifiers (Kistler 4618A0), septa (VICI Valco, low-bleed), four fast-acting sampling valves (modified Festo MHE3 valves with a stock response time of 3 ms, 3 mm orifice), and four vacuum isolation valves (Swagelok). A schematic of the sampling system is shown in Figure 3. Up to four samples can be obtained per experiment through independent control of each sampling valve, triggered using two pulse generators (Stanford Research Systems model DG535 Digital Delay/Pulse Generators). The four samples are acquired through probes located on a square spacing (26 × 26 mm) on the end wall, 19 mm (radially) from the center of the test section (recall the test section i.d. is 50.8 mm). For the high-speed sampling data presented in this paper, two gas samples were acquired in each experiment by triggering two of the fast-acting valves located at the northeast and southwest positions, 180° from each other. Each sampling tube connected to the fast-acting valve extends approximately 10 mm from the end wall into the test section, well beyond the cold thermal boundary layer of the test section end wall. Experiments were performed to ensure the sampling end wall has no effect on the ignition kinetics of *n*-butanol. Specifically, τ_{ign} were measured with the sampling end wall in place without triggering the sampling valves. The measured values for τ_{ign} were identical to the measurements made with the imaging end wall. In addition, by acquiring small samples (as opposed to quenching the entire test volume), the ignition characteristics of each experiment remain unaffected. As will be shown below, τ_{ign} values determined from the gas-sampling experiments were in excellent agreement with experiments where gas sampling was not used.

A primary source of uncertainty in the gas-sampling measurements is the dilution of the gas samples with unreacted gases present in dead volume of the gas-sampling system. Specifically, the cold unreacted gases (essentially unreacted test gas mixture) initially present in the sampling probes are also acquired in the sampling chamber when the sampling valves are opened. The unreacted test gases dilute the concentration of the gases taken from the hot core region of the test section, and the reactant mixture can cause interference in the chromatograms. To quantify these effects, pyrolysis experiments were performed using EOC conditions that would consume all of the fuel in the reactive core before the gas samples were acquired. Any measured fuel would then be from the dead volume, and quantifying the fuel yields an accurate estimate of the dilution of the gases sampled from the core of the test section. For this work, pyrolysis experiments using *n*-butanol were used and compared to results obtained from previous characterization work for pyrolysis of C_2 hydrocarbons on the UM RCF.[29] Model predictions show that less than 0.3% of *n*-butanol would remain in the core region of the test section at 11.2 ms after the end of compression for EOC conditions of T = 1400 K and P = 3.25 atm. The *n*-butanol and C_2 pyrolysis experiments show that the dilution ranges between 5 and 16%, depending on the temperature conditions in the test section. The data for this study were analyzed using 16% dilution by the unreacted test gas mixture.

Another source of uncertainty in the gas-sampling measurements is due to nonuniformities potentially present in the test section or variability in the different gas-sampling systems. The high-speed imaging provides data on the quality of the spatial uniformity of the ignition characteristics. However, end-view imaging cannot be conducted simultaneously with gas-sampling through the end wall. Consequently, experiments were performed in which the two sampling valves were triggered at the same time such that the two gas samples had the same time history but were obtained from two different locations in the test section. The samples yielded nearly identical concentrations (less than 4% difference) for the species measured.

The temporal resolution of the gas-sampling measurements is limited by the fast-acting valves. Triggering circuits are used to open and close the gas-sampling valves at specified times during the ignition delay time. During the initial part of the triggering signal, the valves stay closed due to inertial effects. At the end of the triggering signal, the sampling valves are fully open and do not shut until the spring inside the valve body is extended. This results in a valve opening time of approximately 1.5 ms centered on the end of the valve-sampling signal. During the sampling event, the gases are quickly quenched (<0.3 ms) as they expand into the vacuum of the sample chamber ($P_{\text{test section}}/P_{\text{sample chamber}} \sim 11$, $V_{\text{test section}}/V_{\text{sample chamber}} \sim 39$). The gas-sampling results therefore represent the average value of the species during the sampling time. Once the samples are acquired, the gases are drawn into a syringe (Hamilton Gastight #1010, 10 mL) through the syringe port on the sampling chamber for delivery to the gas chromatograph.

The gas chromatograph (GC) was calibrated for quantitative measurements of the species of interest, namely, *n*-butanol

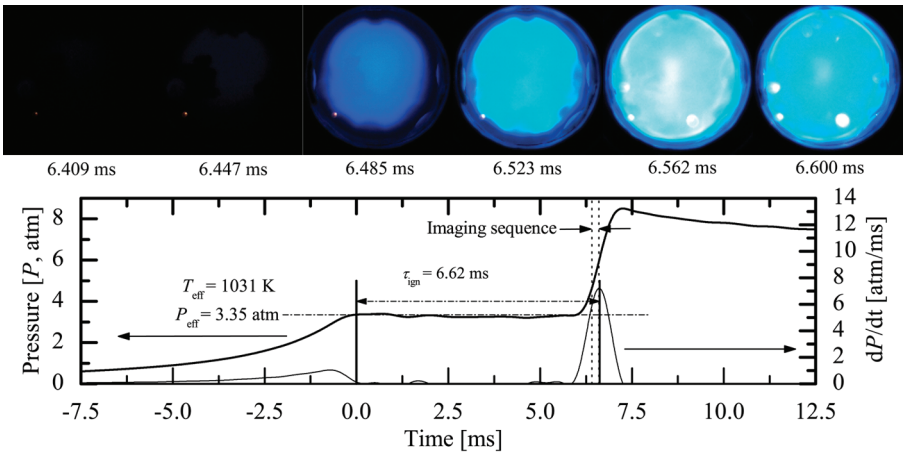

Figure 4. Results for a typical *n*-butanol ignition experiment with P_{eff} = 3.35 atm, T_{eff} = 1031 K, ϕ = 1, inert/O_2 = 5.64, and τ_{ign} = 6.6 ms. The lower panel shows the pressure (P) and the rate of pressure rise (dP/dt) in the test section. End of compression is set as time t = 0 ms. The upper panel shows the corresponding still images (end view), acquired at 26 000 fps, of the chemiluminescence during ignition (no color adjustment).

(*n*-C_4H_9OH), methane (CH_4), carbon monoxide (CO), ethene (C_2H_4), propene (C_3H_6), acetaldehyde (CH_3CHO), 1-butene (1-C_4H_8), and *n*-butyraldehyde (*n*-C_3H_7CHO). The GC system (PerkinElmer Autosystem) was equipped with a flame ionization detector (FID, air/hydrogen flame) and a thermal conductivity detector (TCD). A Restek RTX-1 capillary column was used to measure both pure hydrocarbons as well as oxygenated hydrocarbons (using the FID detector), and a Restek ShinCarbon ST packed column was used to measure CO (using the TCD detector). The columns were maintained in the GC oven at 50 °C with ultra high purity helium (Cryogenic Gases, Purity Plus, 99.999%) as the carrier gas. The helium, air, and hydrogen were further purified before use in the GC using adsorbents to remove water, hydrocarbons, and oxygen. The FID detector was maintained at 300 °C, with an attenuation of 1 and a range of 1. The TCD detector was maintained at 50 °C with an attenuation of 1 and a current of +160 mA. Split injection was used to introduce the analytes into the columns, with less than 0.5 mL of sample introduced into the septum and the sample loop being 5 μL. High-purity reference chemicals were characterized for the GC temperature programs used in the study, and the chromatograms were used to establish the calibrations for absolute concentration. Calibration gases were used for CH_4 (Cryogenic Gases, chemically pure, 99%), CO (Matheson, ultrahigh purity, 99.9%), C_2H_4 (Matheson, chemically pure, 99.5%), C_3H_6 (Cryogenic Gases, polymer grade, 99.5%), and 1-C_4H_8 (Cryogenic Gases, 99%). CH_3CHO was calibrated using the vapor of liquid CH_3CHO (Fluka, puriss. p.a., anhydrous, >99.5% GC grade, ≤0.5% free acid CH_3COOH), and *n*-C_3H_7CHO was calibrated using the vapor of liquid *n*-C_3H_7CHO (Fluka, puriss., ≥99% GC grade, ≤1% butyric acid, <0.1% BHT as a stabilizer, <1% H_2O as a stabilizer). Calibration mixtures were made in a mixing tank with the upper limit of concentrations calibrated for being greater than the maximum concentrations predicted by the Black et al.[1] mechanism for the ignition delay of a mixture with χ(*n*-but) = 0.025, $\chi(O_2)$ = 0.147, $\chi(N_2)$ = 0.541, and χ(Ar) = 0.288 at P = 3.25 atm and T = 975 K. Calibration curves were linear in all cases. Measurements of *n*-butanol were of interest for this work, and *n*-butanol was well isolated in the chromatograms. However, calibration experiments showed the *n*-butanol (Sigma-Aldrich, purum, >99% GC grade, <0.1% H_2O) features were a nonlinear function of the GC-FID detector, and the *n*-butanol saturated the FID detector for mole fractions of 0.5% and higher. Consequently, potential *n*-butanol measurements were limited to levels below 0.5% for this study. Signals from the GC detectors were recorded using a high-resolution data acquisition system (NI PXI 4472) with a sampling rate of 8 Hz. A temperature-controlled 10-port valve was used to direct the samples into the GC.

3. EXPERIMENTAL RESULTS AND DISCUSSION

3.1. Ignition Experiments. Figure 4 presents typical results from a UM RCF *n*-butanol ignition experiment. The time histories of the pressure (P) and rate of pressure rise (dP/dt) in the test section are shown in the lower panel. High-frequency (>2.5 kHz) disturbances generated by the impact of the sabot near the EOC are filtered from the pressure time histories using a fast Fourier transform. The pressure data show the compression process is smooth with no indications of disturbances or abrupt fluctuations. The pressure reaches the first maximum due to compression by the sabot, and the EOC is set to time t = 0, after which the volume in the test section is constant. After a period of time where the pressure remains nearly constant, the pressure increases rapidly to a second maximum due to ignition of the fuel/oxidizer/diluent mixture.

The upper panel of Figure 4 shows stills from the imaging sequence of the chemiluminescence emitted during ignition. The chemiluminescence is only observed during the high rates of pressure rise that occur during ignition. The emission is attributed to CH and C_2 radicals due to the strong spectroscopic features of these species in the blue (CH: 431.2 nm; C_2: 473.7 nm, 516.5 nm, 563.5 nm) and because CH and C_2 are generated through the decomposition of intermediate hydrocarbons present in the fuel/oxidizer/diluent mixture. Note the intense blue emission occurs throughout the test section with uniform intensity, indicating good homogeneity of the reactant mixture and of thermal conditions in the test section.

For each experiment, the effective test conditions are determined using the same methods as in previous UM RCF experiments[21] and are based on the pressure time history from each experiment. The effective pressure (P_{eff}) is defined by Equation 1 as the time-integrated average pressure from the maximum pressure (P_{max}) at EOC to the maximum of rate of

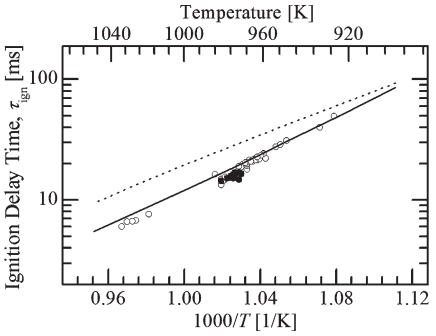

Figure 5. Comparison of experimental results for *n*-butanol ignition delay time measured in the current work with model predictions (P = 3.25 atm) based on the reaction mechanisms developed by Black et al.[1] (solid line) and Veloo et al.[5] (dotted line). All results presented are for ϕ = 1, inert/O_2 = 5.64. ○, Current work, P = 2.9−3.4 atm; ●, Current work, gas-sampling experiments, P = 3.22−3.34 atm.

pressure rise (dP/dt_{max}).

$$P_{eff} = \frac{1}{t_{dP}/dt_{max} - t_{Pmax}} \int_{t_{Pmax}}^{t_{dP/dt_{max}}} P \cdot dt \qquad (1)$$

The effective temperature for each experiment is determined using P_{eff} and numerical integration of the isentropic relation (eq 2)

$$\int_{T_0}^{T_{eff}} \frac{\gamma}{\gamma - 1} d \ln T = \ln\left(\frac{P_{eff}}{P_0}\right) \qquad (2)$$

where P_0 is the initial charge pressure, T_0 is the initial temperature, and γ is the temperature-dependent ratio of the specific heats of the unreacted test gas mixture (determined using the NASA thermodynamic database[30]). The ignition delay time, τ_{ign}, for each experiment is defined as the time between EOC (t = 0 ms, defined by the first maximum in P) and dP/dt_{max}.

n-Butanol ignition experiments were performed in a narrow pressure range (2.9−3.4 atm) between temperatures of 920 and 1040 K. The equivalence ratio (ϕ, defined as the ratio of $(fuel/O_2)_{actual}/(fuel/O_2)_{stoichiometric}$) was ϕ = 1, and the dilution (with nitrogen and argon being the sole diluents for all experiments) was inert/O_2 = 5.64 for all experiments. The *n*-butanol concentration for the experiments was 2.4−2.5%. Table S1 found in the Supporting Information accompanying this paper is a summary of the experimental conditions and results for τ_{ign}, and Figure 5 shows τ_{ign} as a function of temperature for *n*-butanol on an Arrhenius diagram. The open symbols are the results of experiments where the transparent end wall was used. The filled symbols are the results of gas-sampling experiments. The ignition data for both sets of experiments follow typical Arrhenius behavior (with no negative temperature coefficient region expected or observed) and are in excellent quantitative agreement with each other. Hence, as noted earlier, the effects of sampling on the ignition behavior of the test gas mixtures are negligible.

The uncertainty in the measured τ_{ign} is primarily due to the uncertainty in the effective temperature, which is calculated using the measured pressure and Equation 2. The accuracy of the pressure transducer is ±0.5%. This translates to approximately ±0.2% variation in T_{eff}. The random error in the measured τ_{ign} is estimated using the standard deviation of the data for the temperature range 972−978 K which is 1.3 ms or ±8%. A conservative estimate for the overall uncertainty for τ_{ign} for the entire temperature range is ±15%, which is the maximum scatter in the data at any of the temperatures investigated.

The experimental results for τ_{ign} are also compared in Figure 5 to model predictions from two recently published *n*-butanol reaction mechanisms. Veloo et al.[5] developed a mechanism specifically for atmospheric pressure flames, with 266 species and 1639 reactions. Black et al.[1] developed a mechanism based on C_4 chemistry[19] with an *n*-butanol submechanism, for a wide temperature (740−1660 K) and pressure range (1−34 atm). In total, their mechanism consists of 234 species and 1399 reactions. The two reaction mechanisms were used to predict τ_{ign} using the CHEMKIN suite of programs and assuming a zero dimensional, spatially homogeneous, adiabatic constant volume system. For the simulations, τ_{ign} was defined as the time from the start of the simulation to the maximum rate of pressure rise. The input conditions for the model simulations were mixture compositions and the effective temperatures and pressures are listed in Table S1 (Supporting Information). As seen in Figure 5, *n*-butanol ignition delay is quite linear on an Arrhenius scale with no negative temperature coefficient region expected or observed. In addition, there is excellent agreement between the results based on the reaction mechanism developed by Black et al.[1] and the experimental data. Specifically, the reaction mechanism by Black et al.[1] predicts τ_{ign} to within 20% for temperatures higher than approximately 960 K and to within 10% for temperatures below 960 K. The model results using the reaction mechanism by Veloo et al.[5] are also in good agreement with the experimental data, well within a factor of 2 for most temperatures.

A concern for experiments conducted in rapid compression facilities is the possible reaction of the fuel/oxidizer/diluent mixture during compression, which impacts the assumptions used to define the effective temperature and pressure of the experiments and therefore the input conditions to the CHEMKIN simulations. Experimentally, such concerns can be investigated by performing non-igniting experiments, where the O_2 is replaced by N_2 in the original fuel/oxidizer/diluent mixture. Such experiments were conducted as part of this study and are presented and discussed with the gas sampling data below. Briefly, the experimental data show negligible deviation in the pressure time history for the non-igniting and the igniting experiments (<1% difference in the effective pressures or pressure time histories to the time of ignition). To further investigate these concerns, the compression process was simulated. Specifically, CHEMKIN simulations were performed representing the compression stroke of the UM RCF for the targeted EOC conditions of T = 975 K and P = 3.25 atm using the Black et al.[1] reaction mechanism, with initial mole fractions of χ(*n*-but) = 0.025, $\chi(O_2)$ = 0.147, $\chi(N_2)$ = 0.541, and χ(Ar) = 0.288. The results of the simulation for τ_{ign} are within 10% of the results where the compression process was not simulated. In addition, the results show that less than 120 ppm of the *n*-butanol of the test mixture is consumed by EOC, and both the pressure and temperature are within 0.1% of the nonreacting EOC values (see Supporting Information for Figure S1 depicting this simulation). Similarly for target EOC conditions of T = 1025 K and P = 3.25 atm with initial mole fractions of χ(*n*-but) = 0.025, $\chi(O_2)$ = 0.147, $\chi(N_2)$ = 0.429, and χ(Ar) = 0.399, τ_{ign} is faster by less than 10% when the compression stroke is included in the simulation, with less than 1300 ppm of the *n*-butanol in the test mixture consumed by EOC. As with the lower temperature simulation, both the pressure and temperature are within 0.1% of the nonreacting EOC values (see Supporting Information for

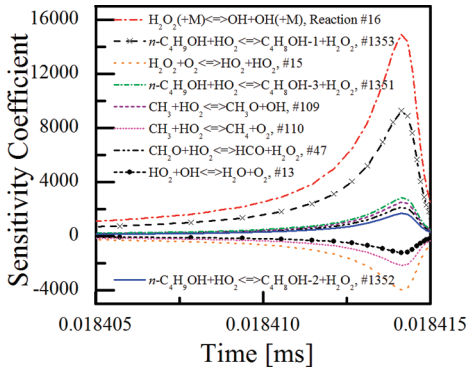

Figure 6. Results for OH sensitivity analysis using the mechanism of Black et al.[1] for the target gas-sampling conditions of $\phi = 1.0$, $T = 975$ K, $P = 3.25$ atm, and inert/$O_2 = 5.64$.

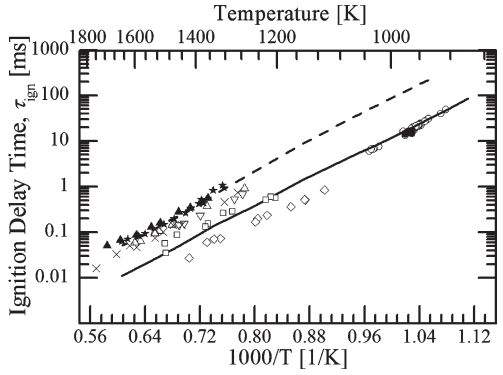

Figure 7. Comparison of the *n*-butanol ignition delay times measured in the current work with the experimental results for shock tube studies of *n*-butanol ignition by Moss et al.[8] and Black et al.,[1] where $\phi = 1$ for all data. ○, Current work, $P = 2.9-3.4$ atm, inert/$O_2 = 5.64$; ■, current work, gas-sampling experiments, $P = 3.22-3.34$ atm, inert/$O_2 = 5.64$; △, Moss et al.,[8] $P = 1$ atm, inert/$O_2 = 15.5$; ▲, Moss et al.,[8] $P = 1.3$ atm, inert/$O_2 = 32$; ▽, Moss et al.,[8] $P = 4$ atm, inert/$O_2 = 65.7$; ★, Black et al.,[1] $P = 1$ atm, inert/$O_2 = 21$; ×, Black et al.,[1] $P = 2.5-3.1$ atm, inert/$O_2 = 26.6$; □, Noorani et al.,[11] $P = 1.8-2.5$ atm, inert/$O_2 = 10$; ◇, Noorani et al.,[11] $P = 1.8-2.5$ atm, inert/$O_2 = 10$. Model predictions based on the Black et al.[1] mechanism are presented for conditions of $P = 1$ atm, inert/$O_2 = 21$ (dashed line), and $P = 3.25$ atm, inert/$O_2 = 5.64$ (solid line).

Figure S2 depicting this simulation). The results confirm that reaction during compression is of little concern for the ignition delay time experiments or the gas-sampling experiments.

Sensitivity analysis was used to identify the reactions having a significant effect on *n*-butanol ignition delay time. The analysis was performed using the initial conditions of $T = 975$ K, $P = 3.25$ atm, χ(*n*-but) = 0.025, $\chi(O_2) = 0.147$, $\chi(N_2) = 0.541$, and $\chi(Ar) = 0.288$ ($\phi = 1.0$, inert/O_2 dilution = 5.64) using the Black et al.[1] mechanism. The OH radical concentration was used as a surrogate for ignition delay time, and the results of the OH sensitivity analysis are presented in Figure 6. The most important reaction is the chain-initiating decomposition of H_2O_2 into two OH radicals. The *n*-butanol + HO_2 reaction also plays a large role at these conditions as a source of H_2O_2. These results differ from those of Black et al.,[1] who also performed sensitivity analysis for *n*-butanol ignition and found the chain branching H + O_2 reaction to be the most important. The results highlight the change in the reaction kinetics from the lower temperatures

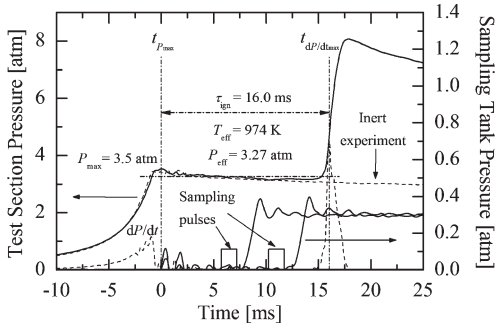

Figure 8. Results for a typical *n*-butanol ignition experiment with gas sampling during the ignition delay period. The pressure and pressure derivative time histories in the test section and in the two sampling chambers are presented. The triggering signals for the rapid gas sampling valves are also provided. The pressure time history for a non-igniting (i.e., inert) experiment is included for comparison.

considered here (975 K), where competition between H_2O_2 and HO_2 chemistry dominates the ignition chemistry, to the higher temperatures considered by Black et al.[1] (1450 K), where H, OH, and O are the radical chain carriers.

Figure 7 presents the experimental data from the current work and the previous shock tube studies by Black et al.,[1] Moss et al.,[8] and Noorani et al.[11] The shock tube data were obtained at higher temperatures and dilution levels than the current study and span pressures from 1 to 4 atm. Zero dimensional, spatially homogeneous, adiabatic, constant volume model predictions based on the reaction mechanism by Black et al.[1] are also shown in the figure. Model predictions for the shock tube data (with χ(*n*-but) = 0.008, $\chi(O_2) = 0.045$, $\chi(Ar) = 0.948$, $P = 1$ atm) span the dilution (composition and levels) and pressures of the experimental shock tube data for the extended temperature range $T = 950-1650$ K. Model predictions for the UM RCF data (with χ(*n*-but) = 0.025, $\chi(O_2) = 0.147$, $\chi(N_2) = 0.541$, and $\chi(Ar) = 0.288$, $P = 3.25$ atm) are presented for the extended temperature range $T = 900-1650$ K. The model predictions are in excellent agreement with both data sets, and they reproduce the shift to faster ignition that occurs with higher concentrations of fuel in the reacting mixtures and with slightly higher pressures.

3.2. High-Speed Gas Sampling Experiments. The ignition delay time study provided the basis to identify thermodynamic conditions where high-speed gas sampling could be applied with good accuracy and repeatability. On the basis of these results, EOC temperatures of $T_{eff} = 975$ K were targeted for the gas-sampling experiments. Specifically, UM RCF experiments with $T_{eff} = 975$ K yielded ignition delay times between 14 and 17 ms, allowing a sampling time resolution of approximately 10:1. Results from a typical sampling experiment are presented in Figure 8, where $P_{eff} = 3.27$ atm, $T_{eff} = 974$ K, and $\tau_{ign} = 16.0$ ms. Figure 8 includes the time histories of the pressure and pressure derivative in the test section, the two triggering signals of the gas-sampling system, and the pressures in the two sampling chambers. As seen in the figure, the pressure in the test section is unaffected by the sampling process, and the features are similar to the data of Figure 4, which shows ignition without gas sampling. The time histories of the two gas samples show the rapid increase in pressure that occurs after the triggering signals and confirm the sampling times as <2 ms. Figure 8 also includes for comparison the pressure time history for a non-igniting experiment (labeled "Inert experiment") with the same thermal characteristics as an

dx.doi.org/10.1021/jp200905n |J. Phys. Chem. A 2011, 115, 4909–4921

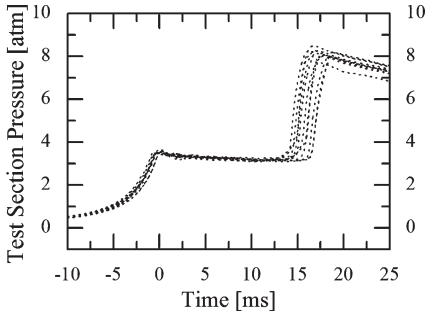

Figure 9. Comparison of the pressure time histories for the high-speed gas-sampling experiments of *n*-butanol ignition. Note the nearly identical compression processes for all experiments.

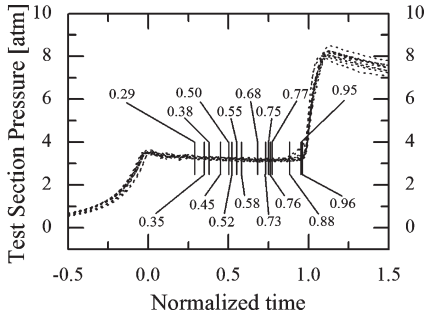

Figure 10. Comparison of the pressure time histories of the sampling experiments on a time scale normalized to τ_{ign} for each experiment. The normalized time for each gas-sample measurement is labeled in the figure.

igniting *n*-butanol/oxidizer/diluent mixture (where the O_2 in the mixture has been replaced with N_2). The non-igniting pressure time history is virtually indistinguishable from the igniting pressure time history (where P_{eff} and T_{eff} differ by less 1% and 0.5%, respectively). The comparison demonstrates that neither the ignition chemistry nor the gas sampling affects the heat transfer physics of the experiments.

A total of 11 gas-sampling experiments were performed. A summary of the experimental conditions, the measured τ_{ign}, and the sample times are provided in Table S2, found in the Supporting Information. A summary of the pressure time histories of the gas-sampling experiments is presented in Figure 9. All of the sampling experiments show nearly identical, smooth compression processes. The slight decrease in pressure after EOC (due to heat losses to the test manifold walls, prior to the sampling events) is also extremely consistent between experiments. The averages and standard deviations for the EOC conditions and measured τ_{ign} are provided in Table S2 (Supporting Information). The standard deviations of the EOC pressures, P_{eff}, and τ_{ign} for the sample experiments are 0.06 atm, 0.04 atm, and 0.84 ms, respectively.

While the data of Figure 9 and Table S2 (Supporting Information) demonstrate the excellent level of repeatability of the sampling experiments, there are slight differences in the EOC conditions and ignition delay times. To compensate for these slight differences in the experimental pressure time histories, the sampling data are reported using a time domain that is normalized by the actual τ_{ign} for each experiment. EOC is defined as $t/\tau_{ign} = 0$, and $t/\tau_{ign} = 1$ is the time of ignition. Figure 10 presents the pressure time histories of Figure 9 after normalizing by the

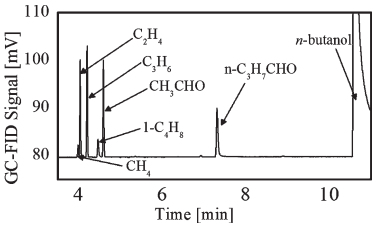

Figure 11. Typical GC-FID chromatogram results of a gas sample acquired at $t = 7.2$ ms, $t/\tau_{ign} = 0.45$, for experimental conditions of $P_{eff} = 3.27$ atm, $T_{eff} = 974$ K, and $\tau_{ign} = 16.0$ ms.

τ_{ign} for each experiment. The normalized times when each gas sample was taken during the ignition delay period are labeled in the figure. Note that due to the low levels of intermediate species at early times the sampling data were preferentially acquired closer to the time of ignition.

Figure 11 shows a typical GC-FID chromatogram from an *n*-butanol ignition experiment for conditions of $P_{eff} = 3.27$ atm, $T_{eff} = 974$ K, $\tau_{ign} = 16.0$ ms, and a sampling time of 7.2 ms. Peaks from CH_4, C_2H_4, C_3H_6, CH_3CHO, 1-C_4H_8, *n*-C_3H_7CHO, and *n*-butanol are identified in the figure. CO measurements were made using chromatograms from the GC-TCD detector and are not shown here. All major features on the chromatograms were identified. Using the calibration data for each species and the measured dilution levels of the gas samples, the chromatograms were converted into discrete measurements for each sampling time. Figure 12 presents the results for the eight intermediate species as a function of the normalized ignition delay time for the nominal experimental conditions of $P_{eff,average} = 3.29$ atm and $T_{eff,average} = 975$ K. In Figure 12, the error bars are the uncertainty in the experimental data. As described above, the uncertainty in the sampling times is ± 0.75 ms, or approximately ± 0.05 when normalized by the average ignition delay time. The uncertainty in the measured mole fractions was $\pm 16\%$ as determined by the uncertainty in the species calibration and dilution percentage, as discussed earlier. The calibration and dilution were considered independent sources of uncertainty, and the overall uncertainty for each species was determined using the square root of the sum of the squares for each source of uncertainty. Note that only two measurements were above the detectable limit for CO, and none of the *n*-butanol measurements were both below the limit that saturated the GC detector and above the detectable limit for *n*-butanol, given the uncertainty due to dilution.

Results for the model predictions using the reaction mechanism by Black et al.[1] for the initial condition of $P = 3.25$ atm, $T = 975$ K, inert/$O_2 = 5.64$, and *n*-butanol = 2.45% are presented as the solid lines in Figure 12. The predicted ignition delay time is $\tau_{ign} = 18.6$ ms, which is within 18% of the average of the experimental data ($\tau_{ign,average} = 15.7$ ms). The model predictions show good qualitative agreement with the experimental data for all species. The quantitative agreement is very good (within a factor of 2 for the duration of the ignition delay period) for CH_4. However, the model significantly overpredicts C_2H_4 (by a factor of 4−8 over the entire ignition delay period) and C_3H_6 (by a factor of 2−3 over the ignition delay period). 1-C_4H_8 shows good quantitative agreement, with differences less than a factor of 2 over most of the ignition delay period. CO was measured at detectable levels in the GC-TCD chromatograms only closer to ignition, as predicted by the model. Note that the model

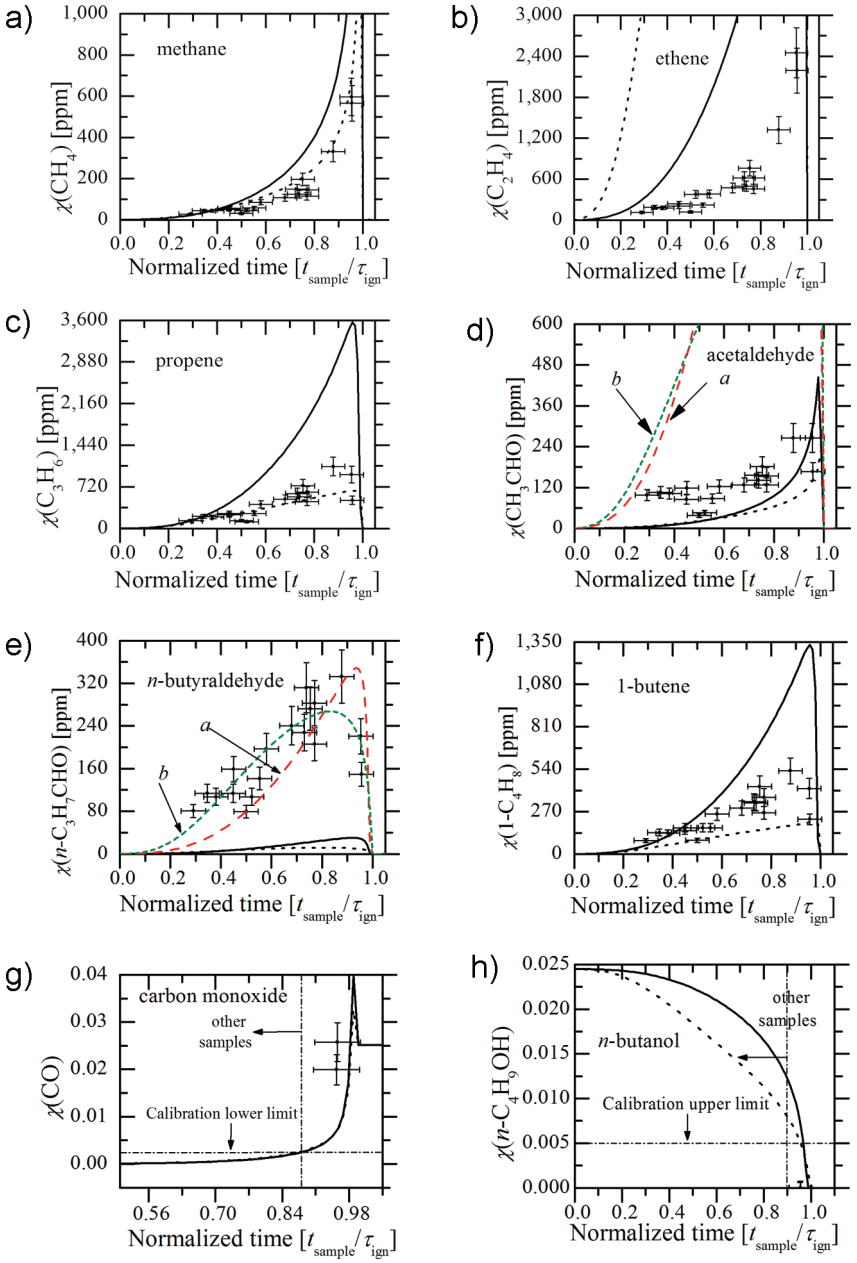

Figure 12. Comparison between measured intermediate species and model predictions using the reaction mechanism of Black et al.[1] and the initial conditions of P = 3.25 atm, T = 975 K, inert/O_2 = 5.64, and n-butanol = 2.45% ($\tau_{ign,predicted}$ = 18.6 ms). The unmodified mechanism predictions are shown with solid lines, and the modified mechanism predictions are shown with dotted black lines. The average experimental conditions are P_{eff} = 3.29 atm, T_{eff} = 975 K, inert/O_2 = 5.63, and n-butanol = 2.44% ($\tau_{ign,average}$ = 15.7 ms). The error bars represent the experimental uncertainties. The time domain has been normalized from t/τ_{ign} = 0 (end of compression) to the time of ignition, t/τ_{ign} = 1.

predictions show a narrow peak for CO, where it is formed rapidly and consumed rapidly very close to ignition. The model predictions for CO are within the experimental uncertainties when the temporal resolution of the experimental data is considered. Similarly, the model predictions for n-butanol are consistent with expectations based on the limiting factors for the measurements. Specifically, for times less than $t/\tau_{ign} \sim 0.95$ the experimental data for n-butanol are limited by the 0.5% threshold for the GC-FID detector. Quantitative measurements of CO_2 can be made using the GC configuration used in the current work. However, no CO_2 peaks were observed at any sampling conditions. The absence of CO_2 is consistent with the predictions which indicate CO_2 levels will not exceed the minimum detectable limit of 0.25% until times after $t/\tau_{ign} >$ 0.98. The aldehydes calibrated for and measured, CH_3CHO and n-C_3H_7CHO, warrant a more detailed discussion, particularly with reference to enol-keto isomerization (tautomerization) as described by Black et al.[1] and Harper et al.[31] This discussion is presented later.

The experimental data capture a reasonable fraction of the carbon in the system. By comparison with the model predictions for the concentrations of carbon-containing species, the GC measurements account for 54−75% of the carbon *not* present in n-butanol at early sampling times ($t/\tau_{ign} < 0.4$) and 15−48% of

dx.doi.org/10.1021/jp200905n |J. Phys. Chem. A 2011, 115, 4909–4921

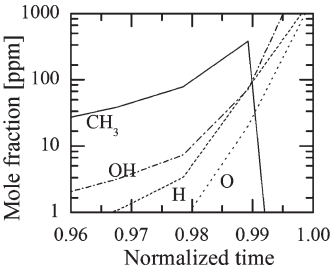

Figure 13. Species time histories of radicals predicted using the reaction mechanism of Black et al.[1] for initial conditions of P = 3.25 atm, T = 975 K, inert/O_2 = 5.64, and *n*-butanol = 2.45%.

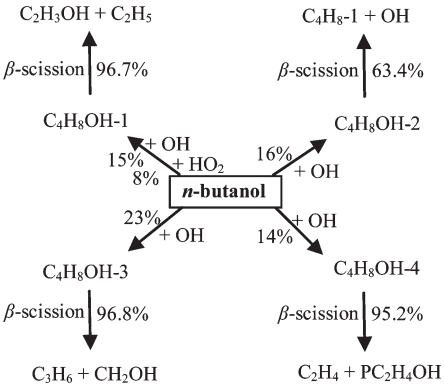

Figure 14. Reaction path diagram of the primary decomposition reactions for *n*-butanol for t/τ_{ign} = 0.75 and the initial conditions of P = 3.25 atm, T = 975 K, inert/O_2 = 5.64, and *n*-butanol = 2.45%.

this carbon at sampling times closer to ignition (t/τ_{ign} > 0.7). When CO was measurable (t/τ_{ign} > 0.9), the GC measurements capture 31−35% of the *total* carbon present in the system.

During gas sampling, radicals present in the test section are quenched and can be a source of interference with the gas-sampling measurements. For example, radicals such as O, H, OH, and CH_3 can recombine to form water vapor and small hydrocarbons. Radical recombination has potential to affect the GC results by systematically biasing the data by introducing unexpected stable species into the samples or by increasing the concentration of species beyond the levels present before quenching. However, radical recombination is not expected to be a source of error in the current work due to the low levels of radicals present prior to ignition. For example, the predicted time histories for OH, O, H, and CH_3 based on the Black et al.[1] mechanism and the initial conditions P = 3.25 atm, T = 975 K, inert/O_2 = 5.64, and *n*-butanol = 2.45% are shown in Figure 13. Negligible levels of these radicals (<30 ppm) are predicted for nearly the entire ignition delay time period, i.e., t/τ_{ign} < 0.96.

Rate of production analysis was used to identify the reaction pathways important for the species measured. The analysis was conducted at 75% of τ_{ign} using the Black et al.[1] mechanism (at the same conditions described above). Figures 14−20 show the primary reaction pathways for the major species (*n*-butanol and CO) and the intermediates. The percentages listed in the figures quantify the specific reaction pathway relative to the overall consumption of the individual species. The results for *n*-butanol (Figure 14) show that H-atom abstraction via OH followed by β-scission to form alkyl radicals and alkenes is the key decomposition pathway for *n*-butanol at these conditions. Figure 15

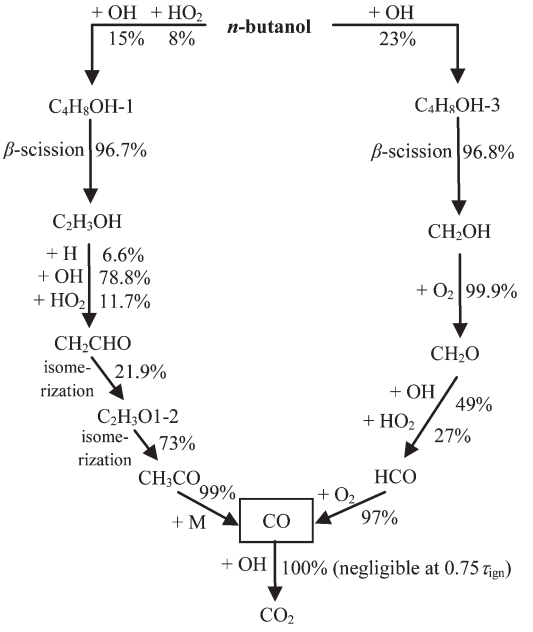

Figure 15. Reaction path diagram of the primary formation pathways for carbon monoxide. Same model conditions as Figure 14.

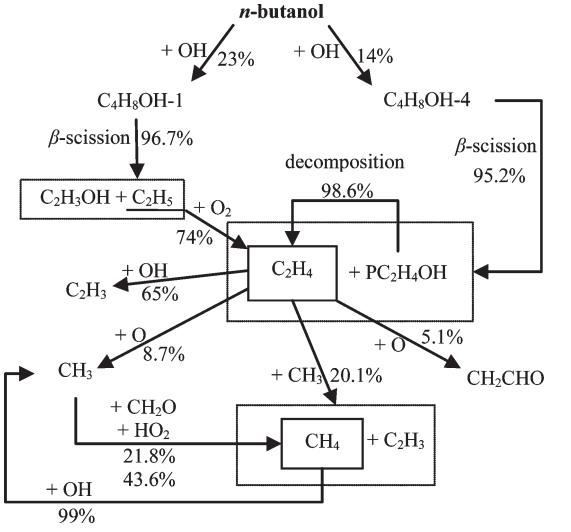

Figure 16. Reaction path diagram of the primary formation and removal pathways for ethene and methane. Same model conditions as Figure 14.

shows that CO is ultimately formed via pressure-dependent decomposition of CH_3CO, as well as via HCO reacting with O_2. Figure 16 shows that CH_4 is formed by addition of H-atoms to CH_3 radicals, while C_2H_4 is formed primarily through the decomposition of PC_2H_4OH and C_2H_5 reacting with O_2. Recall, the model predictions for C_2H_4 were significantly higher than the levels measured experimentally. As seen in Figure 16, increasing the removal of C_2H_4 with radical species like O and CH_3 would increase the CH_4 levels, both directly and indirectly, where predicted CH_4 levels were already in good agreement with the experimental data. A lower decomposition rate for PC_2H_4OH appears more appropriate.

Figure 17 shows that C_3H_6 is predominantly formed via β-scission of C_4H_8OH-3, which itself is formed through H-atom

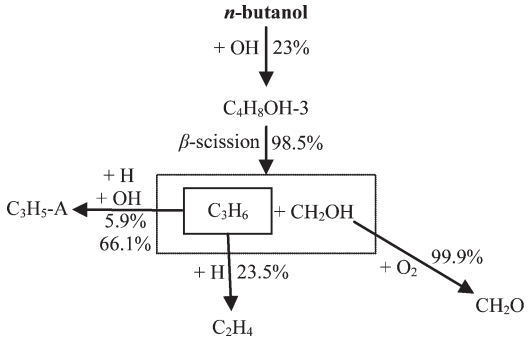

Figure 17. Reaction path diagram of the primary formation and removal pathways for propene. Same model conditions as Figure 14.

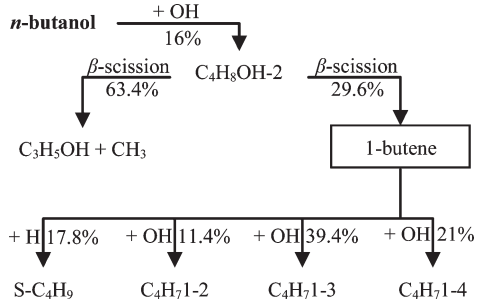

Figure 18. Reaction path diagram of the primary formation and removal pathways for 1-butene. Same model conditions as Figure 14.

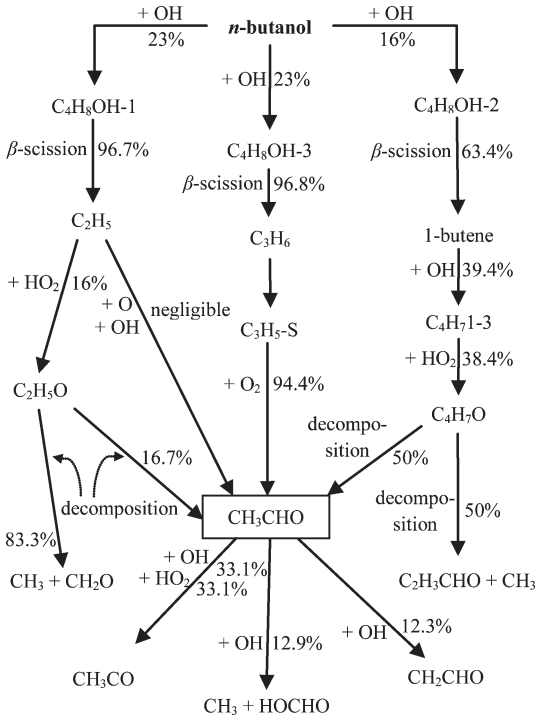

Figure 19. Reaction path diagram of the primary formation and removal pathways for acetaldehyde. Same model conditions as Figure 14.

abstraction from *n*-butanol. C_3H_6 is predominantly consumed by reactions with H-atoms. Because the model overpredicts C_3H_6, the rate of production analysis indicates that the branching

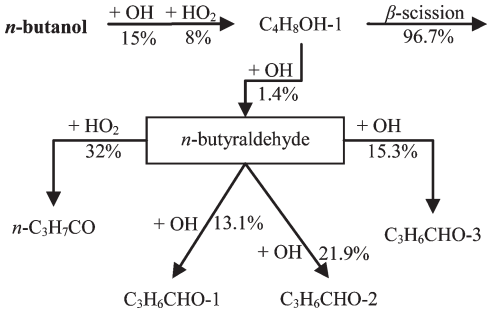

Figure 20. Reaction path diagram of the primary formation and removal pathways for *n*-butyraldehyde. Same model conditions as Figure 14.

fraction for the C_4H_8OH-3 channel of *n*-butanol decomposition may be slightly too high for the conditions studied here. 1-C_4H_8 (Figure 18) is primarily formed via β-scission of C_4H_8OH-2, which itself is formed via H-atom abstraction from *n*-butanol. 1-C_4H_8 is consumed by radical abstraction of H-atoms.

Black et al.[1] and Harper et al.[31] provide detailed descriptions of the tautomerizing of enols to ketones which is relevant to this study. In particular, tautomerization can affect the aldehyde measurements. Black et al.[1] note that the conversion from enol to ketone cannot be easily catalyzed in the gas phase. It is therefore possible that the enol is the preferred low-energy state, as the barrier height for isomerization is approximately 243 kJ/mol.[1] Furthermore, Black et al.[1] point out that these isomers cannot be distinguished by gas chromatographic techniques. Therefore, chromatograms depicting concentrations of aldehydes are likely also influenced by the presence of enols. Figure 19 shows that CH_3CHO is formed via multiple simultaneous pathways resulting from the breakdown of radicals formed via H-atom abstraction from *n*-butanol. Rate of production analysis for CH_3CHO shows that at the conditions studied tautomerization of ethenol is not an important pathway for CH_3CHO production. Furthermore, as seen in Figure 12, CH_3CHO shows good agreement, qualitatively and quantitatively, over the entire ignition delay period. However, non-negligible amounts (~100 ppm) were observed early in the experiments ($t/\tau_{ign} < 0.6$), which was not predicted by the model. Plotted in Figure 12 as the red/long dashed line, marked *a*, is also the sum of the isomers of C_2H_4O, namely, CH_3CHO and ethenol. Ethenol is predicted to be present in high concentrations (>3000 ppm) from the β-scission of C_4H_8OH-1, for $t/\tau_{ign} > 0.9$. The Black et al.[1] mechanism also predicts non-negligible amounts of ethenol for $t/\tau_{ign} < 0.4$. It was observed that even though ethenol may coelute with CH_3CHO, high concentrations of C_2H_4O isomers were not detected in the gas chromatograms. While the C_4H_8OH-3 channel for *n*-butanol decomposition is a source of CH_3CHO, decreasing the branching fraction of the C_4H_8OH-3 channel, as suggested earlier, should not significantly impact the CH_3CHO time history as the C_4H_8OH-3 channel is small relative to the other sources of CH_3CHO.

n-C_3H_7CHO shows the largest discrepancies (Figure 12) between the model predictions and measurements, where the model under-predicts *n*-C_3H_7CHO by an order of magnitude (by a factor of 10−20 for the duration of the ignition delay period). Figure 20 shows that *n*-C_3H_7CHO is formed solely via H-atom abstraction of one of the decomposition products of *n*-butanol (C_4H_8OH-1) and is consumed by H-atom abstraction.

dx.doi.org/10.1021/jp200905n |J. Phys. Chem. A 2011, 115, 4909–4921

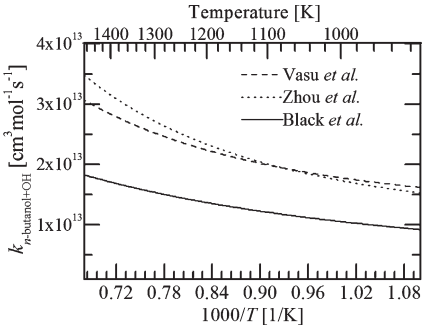

Figure 21. Rate constants for the overall *n*-butanol + OH reaction from Vasu et al.,[15] Zhou et al.,[16] and Black et al.[1]

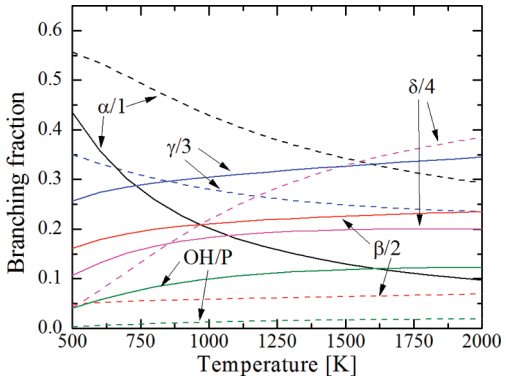

Figure 22. Branching fractions for the five H-atom abstraction channels by OH from the α, β, γ, and δ carbon sites and from the alcohol group of *n*-butanol. The legend includes the site of the H-atom abstraction and the designation of the corresponding C_4H_8OH isomer produced. The solid lines are the values used in the Black et al.[1] mechanism, and the dashed lines are the values recommended by Zhou et al.[16] based on their G3 calculations.

Tautomerization reactions for the conversion of *n*-C_3H_7CHO to butenols are not included in the Black et al.[1] mechanism. However, just like the case with the C_2H_4O isomers, the C_4H_8O isomers, namely, *n*-C_3H_7CHO, 1-buten-1-ol, 2-buten-1-ol, and 3-buten-1-ol, may coelute and be measured simultaneously with *n*-C_3H_7CHO. When the sum of the concentrations of all the C_4H_8O isomers is plotted in Figure 12 (red/long dashed line, marked *a*), the measured and predicted trends are in very good agreement (generally within the uncertainty limits of the measured data).

The rate coefficient for the reaction of *n*-butanol with OH has been the subject of recent experimental and theoretical studies.[15,16] Vasu et al.[15] measured the rate constant of the overall reaction of *n*-butanol + OH → products in a shock tube study at pressures of 2.25 atm for temperatures between 973 and 1428 K. They developed an expression for the overall rate coefficient of this reaction, of $k_{n\text{-butanol+OH}} = 4.118 \times 10^3 T^{2.944} \exp(1852/T)$ [cm^3 mol^{-1} s^{-1}]. The shock tube data are in good agreement with recent theoretical calculations performed by Zhou et al.,[16] who used both CCSD(T)/cc-pVQZ//MP2/6-311g(d,p) and G3 methods to determine overall rate constant expressions for *n*-butanol + OH. Specifically, Zhou et al.[16] determined an overall rate coefficient of $k_{n\text{-butanol+OH}} = 40.3T^{3.57} \exp(2128/T)$ [cm^3 mol^{-1} s^{-1}] based on the G3 method. As seen in Figure 21, these overall rate constants of Vasu et al.[15] and Zhou et al.[16] are a factor of 2 higher than the rate constant used in the Black et al.[1] mechanism for the range of temperatures considered in the current work. For Figure 21, the data for the Black et al.[1] mechanism are the sum of the rate constants for H-atom abstraction by OH from the α, β, γ, and δ carbon sites and from the alcohol group of *n*-butanol.

Zhou et al.[16] also determined temperature-dependent rate coefficients for the five product channels of the *n*-butanol + OH reaction. As seen in Figure 22, the branching fractions recommended by Zhou et al.[16] (specifically focusing on the G3 calculations) differ from those adopted in the mechanism by Black et al.[1] In particular, the α channel (producing the C_4H_8OH-1 isomer) is much higher, and the β (producing the C_4H_8OH-2 isomer) and alcohol (producing the PC_4H_8OH isomer) channels are much lower. In addition, the δ (producing the C_4H_8OH-4 isomer) channel has much stronger temperature dependence.

To quantify the effects of changing the overall rate coefficient and the branching fractions for the *n*-butanol + OH reaction, the recommendations from Zhou et al.[16] (based on their G3 calculations) were substituted into the reaction mechanism by Black et al.[1] As expected based on the sensitivity analysis presented earlier, the modified reaction mechanism had a minor effect on the ignition delay time at $P = 3.25$ atm, $T = 975$ K, inert/O_2 = 5.64, and *n*-butanol = 2.45%. Specifically, τ_{ign} increased from 18.6 to 21.8 ms. However, the modified reaction mechanism resulted in much higher endothermicity during the ignition delay period compared to the unmodified mechanism, with the temperature decreasing by 15 K (to 960 K) before ignition. The unmodified Black et al.[1] mechanism predicts weak endothermicity, with a decrease of only 0.5 K before ignition. There are also several significant changes in the intermediate species, and the model predictions from the modified reaction mechanism are presented as the dashed lines in Figure 12. Although there is an improvement in the prediction of CH_4, C_2H_4 is significantly overproduced, with peak concentrations almost a factor of 3 higher than the unmodified Black et al.[1] mechanism. The modified mechanism dramatically improves the quantitative agreement between the model predictions for C_3H_6 and 1-C_4H_8 and the experimental data. *n*-C_3H_7CHO concentrations are further underpredicted compared to the unmodified Black et al.[1] mechanism; however, the sum of the concentrations of the C_4H_8O isomers predicted by the modified mechanism reproduces extremely well the measured values for *n*-C_3H_7CHO concentrations, as is seen in Figure 12 with the green/short dashed line, marked *b*. The modified mechanism predicts the non-negligble amounts of these isomers for $t/\tau_{ign} < 0.4$. It is noted in Figure 12 with the green/short dashed line, marked *b*, that for CH_3CHO peak concentrations (off of scale) of the sum of the C_2H_4O isomers are around 1200 ppm, as compared to 3400 ppm for the unmodified mechanism.

The modified mechanism also changes the trend in *n*-butanol removal, where *n*-butanol is consumed almost linearly over the ignition delay time, rather than almost exponentially, as with the unmodified Black et al. mechanism. These changes are consistent with expectations based on the changes in the branching fractions and the reaction path analysis presented earlier. For example, decreasing the β/C_4H_8OH-2 and γ/C_4H_8OH-3 channels directly decreases the production of 1-C_4H_8 and C_3H_6, respectively, while increasing the δ/C_4H_8OH-4 channel increases a reaction path to form C_2H_4. Overall, the performance of the reaction mechanism improved with the revisions to the *n*-butanol + OH reactions, with the key exceptions of *n*-C_3H_7CHO and

C_2H_4, which were not captured well quantitatively with either the modified or unmodified reaction mechanism.

4. CONCLUSIONS

The current work presents new experimental data on the ignition characteristics of *n*-butanol and species time histories of important intermediates formed during an ignition delay time of *n*-butanol. The experimental data are the first of their kind at the moderate temperatures (920−1040 K) and pressures (∼3 atm) studied, and the data verify some expected trends, specifically Arrhenius behavior with no negative temperature dependence. Similar to hydrocarbons at comparable conditions, HO_2 and H_2O_2 kinetics dominate the reactivity of the *n*-butanol/air mixtures, and the data are in excellent agreement with model predictions based on recently developed reaction mechanisms for *n*-butanol. Further, the reaction mechanism by Black et al.[1] yields excellent quantitative agreement with experimental ignition data from the current work and previous shock tube studies over a broad range of temperatures (900−1800 K). Many of the reaction pathways important to predicting the intermediates are well represented in the chemical kinetic mechanism of Black et al.[1] A key exception identified in this study is C_2H_4. The speciation data from the current study show high levels (100s of ppm and higher) of aldehydes (and related isomers), and alkenes are produced as intermediate species during *n*-butanol ignition. C_2H_4 and *n*-C_3H_7CHO are expected to play a role in pollutant emissions, namely, soot and aldehydes; an understanding of their formation is essential for the successful implementation of *n*-butanol in the fuel infrastructure. Recent studies, like the important works by Vasu et al.[15] and Zhou et al.[16] on the overall reaction rate and specific branching channels of the *n*-butanol + OH reaction, have improved the understanding of the reaction pathways important to *n*-butanol combustion. However, more experimental and theoretical work is needed to improve the fidelity of our predictive understanding of *n*-butanol combustion chemistry.

■ ASSOCIATED CONTENT

Supporting Information. Figures representing the volume profile simulations of the UM RCF and tables of the experimental data are provided and can also be e-mailed upon request (contact Darshan M.A. Karwat at dippind@umich.edu). This material is available free of charge via the Internet at http://pubs.acs.org.

■ AUTHOR INFORMATION

Corresponding Author

*Fax: 734-647-3170. Phone: 734-763-7470. E-mail: dippind@umich.edu.

■ ACKNOWLEDGMENT

The authors would like to thank the U.S. Department of Energy Basic Energy Sciences, the U.S. Department of Energy via the University of Michigan Consortium on Efficient and Clean High-Pressure, Lean Burn (HPLB) Engines, the Michigan Memorial Phoenix Energy Institute, and the Graham Environmental Sustainability Institute for their financial support.

■ REFERENCES

(1) Black, G.; Curran, H. J.; Pichon, S.; Simmie, J. M.; Zhukov, V. *Combust. Flame* **2010**, *157*, 363–373.
(2) Gu, X.; Huang, Z.; Li, Q.; Tang, C. *Energy Fuels* **2009**, *23*, 4900–4907.
(3) Jacobson, M. Z. *Environ. Sci. Technol.* **2007**, *41*, 4150–4157.
(4) McEnally, C. S.; Pfefferle, L. D. *Proc. Combust. Inst.* **2005**, *30*, 1363–1370.
(5) Veloo, P. S.; Wang, Y. L.; Egolfopoulos, F. N.; Westbrook, C. K. *Combust. Flame* **2010**, *157*, 1989–2004.
(6) Osswald, P.; Güldenberg, H.; Kohse-Höinghaus, K.; Yang, B.; Yuan, T.; Qi, F. *Combust. Flame* **2011**, *158*, 2–15.
(7) Grana, R.; Frassoldati, A.; Faravelli, T.; Niemann, U.; Ranzi, E.; Seiser, R.; Cattolica, R.; Seshadri, K. *Combust. Flame* **2010**, *157*, 2137–2154.
(8) Moss, J. T.; Berkowitz, A. M.; Oehlschlaeger, M. A.; Biet, J.; Warth, V.; Glaude, P.; Battin-Leclerc, F. *J. Phys. Chem. A* **2008**, *112*, 10843–10855.
(9) Liu, W.; Kelley, A. P.; Law, C. K. *Proc. Combust. Inst.* **2011**, *33*, 995–1002.
(10) Heufer, K. A.; Fernandes, R. X.; Olivier, H.; Beeckmann, J.; Roehls, O.; Peters, N. *Proc. Combust. Inst.* **2011**, *33*, 359–366.
(11) Noorani, K. E.; Akih-Kumgeh, B.; Bergthorson, J. *Energy Fuels* **2010**, *24*, 5834–5843.
(12) Sarathy, S. M.; Thomson, M. J.; Togbe, C.; Dagaut, P.; Halter, F.; Mounaim-Rousselle, C. *Combust. Flame* **2009**, *156*, 852–864.
(13) Harper, M. R.; Van Geem, K. M.; Pyl, S. P.; Marin, G. B.; Green, W. H. *Combust. Flame* **2011**, *158*, 16–41.
(14) Barnard, J. A. *Trans. Faraday Soc.* **1957**, *53*, 1423–1430.
(15) Vasu, S. S.; Davidson, D. F.; Hanson, R. K.; Golden, D. M. *Chem. Phys. Lett.* **2010**, *497*, 26–29.
(16) Zhou, C.-W.; Simmie, J. M.; Curran, H. J. *Combust. Flame* **2011**in press.
(17) Dagaut, P.; Togbé, C. *Fuel* **2008**, *87*, 3313–3321.
(18) Dagaut, P.; Togbe, C. *Energy Fuels* **2009**, *23*, 3527–3535.
(19) Bourque, G.; Healy, D.; Curran, H.; Zinner, C.; Kalitan, D.; de Vries, J.; Aul, C.; Petersen, E. *ASME Conf. Proc.* **2008**, *2008*, 1051–1066.
(20) Dagaut, P.; Sarathy, S. M.; Thomson, M. J. *Proc. Combust. Inst.* **2009**, *32*, 229–234.
(21) He, X.; Donovan, M. T.; Zigler, B. T.; Palmer, T. R.; Walton, S. M.; Wooldridge, M. S.; Atreya, A. *Combust. Flame* **2005**, *142*, 266–275.
(22) Walton, S. M.; He, X.; Zigler, B. T.; Wooldridge, M. S.; Atreya, A. *Combust. Flame* **2007**, *150*, 246–262.
(23) Walton, S. M.; He, X.; Zigler, B. T.; Wooldridge, M. S. *Proc. Combust. Inst.* **2007**, *31*, 3147–3154.
(24) Walton, S. M.; Wooldridge, M. S.; Westbrook, C. K. *Proc. Combust. Inst.* **2009**, *32*, 255–262.
(25) He, X.; Zigler, B. T.; Walton, S. M.; Wooldridge, M. S.; Atreya, A. *Combust. Flame* **2006**, *145*, 552–570.
(26) He, X.; Walton, S. M.; Zigler, B. T.; Wooldridge, M. S.; Atreya, A. *Int. J. Chem. Kinet.* **2007**, *39*, 498–517.
(27) Walton, S. M.; Karwat, D. M.; Teini, P. D.; Gorny, A.; Wooldridge, M. S. *Fuel* **2011**in press.
(28) Donovan, M. T.; He, X.; Zigler, B. T.; Palmer, T. R.; Wooldridge, M. S.; Atreya, A. *Combust. Flame* **2004**, *137*, 351–365.
(29) Teini, P. D. *Ph.D. Thesis*, Univ. Mich. 2011
(30) McBride, B. J.; Gordon, S.; Reno, M. A. *NASA Technical Memorandum 4513*, 1993.
(31) Harper, M. R.; Van Geem, K. M.; Pyl, S. P.; Marin, G. B.; Green, W. H. *Combust. Flame* **2011**, *158*, 16–41.

THE JOURNAL OF PHYSICAL CHEMISTRY A

Article

pubs.acs.org/JPCA

On the Combustion Chemistry of *n*-Heptane and *n*-Butanol Blends

Darshan M. A. Karwat,*[,†] Scott W. Wagnon,[‡] Margaret S. Wooldridge,[†,‡] and Charles K. Westbrook[§]

[†]Deparment of Aerospace Engineering, University of Michigan, Ann Arbor, Michigan 48109, United States

[‡]Department of Mechanical Engineering, University of Michigan, Ann Arbor, Michigan 48109, United States

[§]Lawrence Livermore National Laboratory, Livermore, California 94550, United States

Supporting Information

ABSTRACT: High-speed gas sampling experiments to measure the intermediate products formed during fuel decomposition remain challenging yet important experimental objectives. This article presents new speciation data on two important fuel reference compounds, *n*-heptane and *n*-butanol, at practical thermodynamic conditions of 700 K and 9 atm, for stoichiometric fuel-to-oxygen ratios and a dilution of 5.64 (molar ratio of inert gases to O_2), and at two blend ratios, 80%−20% and 50%−50% by mole of *n*-heptane and *n*-butanol, respectively. When compared against 100% *n*-heptane ignition results, the experimental data show that *n*-butanol slows the reactivity of *n*-heptane. In addition, speciation results of *n*-butanol concentrations show that *n*-heptane causes *n*-butanol to react at temperatures where *n*-butanol in isolation would not be considered reactive. The chemical kinetic mechanism developed for this work accurately predicts the trends observed for species such as carbon monoxide, methane, propane, 1-butene, and others. However, the mechanism predicts a higher amount of *n*-heptane consumed at the first stage of ignition compared to the experimental data. Consequently, many of the species concentration predictions show a sharp rise at the first stage of ignition, a trend that is not observed experimentally. An important discovery is that the presence of *n*-butanol reduces the measured concentrations of the large linear alkenes, including heptenes, hexenes, and pentenes, showing that the addition of *n*-butanol affects the fundamental chemical pathways of *n*-heptane during ignition.

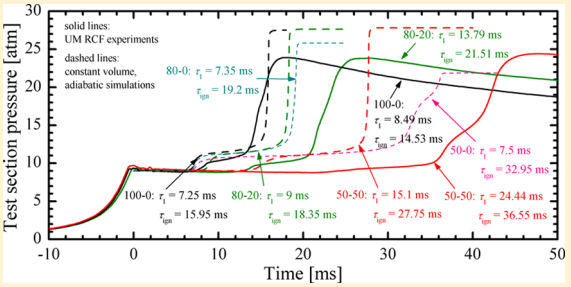

1. INTRODUCTION

There is significant interest in biofuels for the transportation sector, and the first point of entry is to blend biofuels with traditional petroleum-based fuels. Biofuels can be single component fuels (such as ethanol or butanol) or multicomponent fuels (such as biodiesels derived from rapeseed or soy methyl esters). There is an immediate need to understand how biofuels change the chemistry of conventional fuels in terms of global reactivity, as well as the effects of biofuels on air pollutant, particulate, and greenhouse gas emissions. Significant effort has been made to understand the combustion chemistry of large *n*-alkanes, which comprise a significant fraction of complex fuel mixtures such as kerosene, gasoline, and diesel. *n*-Heptane (*n*-C_7H_{16}) has received particular attention because it is a primary reference fuel along with *iso*-octane (*i*-C_8H_{18}). *n*-C_7H_{16} has a high vapor pressure, allowing gas-phase studies of its chemistry, and it also exhibits chemical kinetic features such as negative temperature coefficient (NTC) behavior that distinguishes large-chain *n*-alkanes from many other hydrocarbons.

The global reactivity of *n*-C_7H_{16} has been extensively studied in shock tubes,[1−7] jet-stirred reactors,[8] rapid compression machines,[9−13] and premixed laminar flames.[14−18] However, there have been only a few studies in which the intermediate and final products of *n*-C_7H_{16} oxidation have been measured. Specifically, gas sampling techniques have been used in jet-stirred reactors[8] and rapid compression machines,[12,19] individual species concentrations have been measured optically using laser diagnostics in shock tubes,[7] and one set of measurements has been performed in a premixed laminar flame.[14] These studies have provided important insights into reaction pathways and fuel consumption rates; however, as has been noted by Karwat et al.,[19] there are significant differences between model predictions and experimental measurements of key intermediate species formed during the ignition delay time of *n*-C_7H_{16}. Several chemical kinetic mechanisms have been developed to describe *n*-C_7H_{16} chemistry at both low and high temperatures. The most recently published mechanism,[20] based on the work of Curran et al.,[21] was used in the Karwat et al.[19] study. Other such mechanisms include a recently updated mechanism from Côme et al.[22] and a mechanism developed by researchers at Politechnico di Milano.[23]

Like *n*-C_7H_{16}, the biofuel *n*-butanol (*n*-C_4H_9OH) has garnered much interest in the recent combustion chemistry literature. Its low vapor pressure, reduced miscibility in water, and high energy density[24] lend *n*-C_4H_9OH considerable advantages over ethanol in applications such as aviation fuel, and studies have investigated flame characteristics and

Received: September 20, 2012
Revised: December 3, 2012

   dx.doi.org/10.1021/jp309358h | *J. Phys. Chem. A* XXXX, XXX, XXX−XXX

propagation,[25−28] ignition,[29−34] decomposition,[35] pyrolysis,[36,37] and elementary reaction rates.[38,39] Speciation of *n*-C_4H_9OH has been explored as well in jet-stirred reactors,[35,40] laminar flame configurations,[27,41] and rapid compression facilities.[34] When compared to a recently published chemical kinetic mechanism,[33] a speciation study in a rapid compression facility by Karwat et al.[34] showed excellent reproducibility of global ignition delay times, but with important differences between ethene and aldehyde measurements and predictions. A more comprehensive mechanism for *n*-C_4H_9OH has since been developed by Sarathy et al.[42]

While it is apparent that speciation studies are capable of providing insights into the chemical kinetic effects of blending oxygenated biofuels with conventional hydrocarbon fuels, only two studies, both in a jet stirred reactor,[43,44] have examined the chemical kinetic effects of adding *n*-C_4H_9OH to a large *n*-alkane. Dagaut and Togbé[44] studied the oxidation kinetics of *n*-C_7H_{16}/*n*-C_4H_9OH blends at two blend ratios (80%−20% and 50%−50% by volume) at a residence time of 0.7 s, over a wide temperature range (500−1100 K) and constant pressure (10 atm), in highly diluted mixtures with initial fuel concentrations of 750 ppm at two fuel-to-O_2 equivalence ratios (0.5 and 1). They observed that fuel consumption decreased as temperature was increased between 620 and 770 K, signifying the presence of an NTC region of *n*-C_7H_{16} oxidation, and that *n*-C_4H_9OH was consumed at temperatures much lower than it would be consumed without the presence of *n*-C_7H_{16}. The *n*-C_7H_{16} oxidation at low temperatures thus induced *n*-C_4H_9OH to react. Furthermore, the rates of consumption of each of the components reflected the blend ratio; when *n*-C_7H_{16} was present in concentrations four times higher than *n*-C_4H_9OH, the rate of *n*-C_7H_{16} consumption was four times higher than that of *n*-C_4H_9OH, whereas in equimolar mixtures of *n*-C_7H_{16} and *n*-C_4H_9OH, the two components were consumed at the same rate. Dagaut and Togbé[44] produced two chemical kinetic mechanisms for the study, one detailed and one reduced, and found that the reduced mechanism, which omitted reactions that left ignition predictions unaffected, predicted fast formation of CO, CO_2, and H_2O above 800 K.

In the study by Saisirirat et al.,[43] similar measurements to the Dagaut and Togbé[44] study were made (along with measurements of *n*-C_7H_{16}/*n*-C_4H_9OH blends in a homogeneous charge compression ignition engine) but at an equivalence ratio of 0.3 and a 50%−50% blend of *n*-C_7H_{16} and *n*-C_4H_9OH. The authors' analyses, using a chemical kinetic mechanism generated by merging separate mechanisms for *n*-C_4H_9OH and *n*-C_7H_{16},[44,45] showed the presence of *n*-C_4H_9OH tempered the NTC behavior of *n*-C_7H_{16} because the overall rate of production of OH radicals that consumed fuel molecules decreased due to the presence of *n*-C_4H_9OH, and because the overall production of OH radicals itself decreased with the presence of *n*-C_4H_9OH.

The work presented in this article uses the unique features of the University of Michigan Rapid Compression Facility as a chemical reactor and builds on previous speciation work to present the first measurements of species time-histories of *n*-C_7H_{16}/*n*-C_4H_9OH blends under autoignition conditions. The goal of the work is to provide insights into changes in reaction pathways and product formation in the combustion of conventional, petroleum-based fuels when blended with oxygenated alternative fuels, using *n*-C_7H_{16} as an example of a conventional hydrocarbon fuel and *n*-C_4H_9OH as an example of a single-component biofuel.

2. EXPERIMENTAL SETUP

2.1. University of Michigan Rapid Compression Facility. The University of Michigan Rapid Compression Facility (UM RCF), as a unique and powerful chemical reactor, has allowed fuel chemistry studies over a broad range of thermodynamic conditions. Ignition studies of reference hydrocarbon compounds such as *i*-C_8H_{18},[46,47] simulated syngas mixtures of hydrogen and carbon monoxide,[48] and oxygenated hydrocarbons[49] have been performed previously using the UM RCF, and the facility has also been used to study soot formation and morphology.[50,51] The UM RCF has also been used to obtain time-resolved measurements of hydroxyl radical formation during the ignition of *i*-C_8H_{18}/air mixtures,[52] as well as quantitative measurements of the intermediate species formed during the combustion of *i*-C_8H_{18},[53] methyl butanoate,[54] *n*-C_4H_9OH,[34] and *n*-C_7H_{16},[19] using rapid gas sampling and gas chromatography.

As described in detail previously,[34] the UM RCF uses a free-piston/cylinder compression process to create the thermodynamic conditions necessary for combustion chemical kinetic studies, the features of which are interrogated using optical, pressure, and sampling measurements. The five major components of the UM RCF, seen in Figure 1, are the driver section, the driven section, the test section (or test manifold), the sabot (a free piston with a tapered nosecone), and the fast-

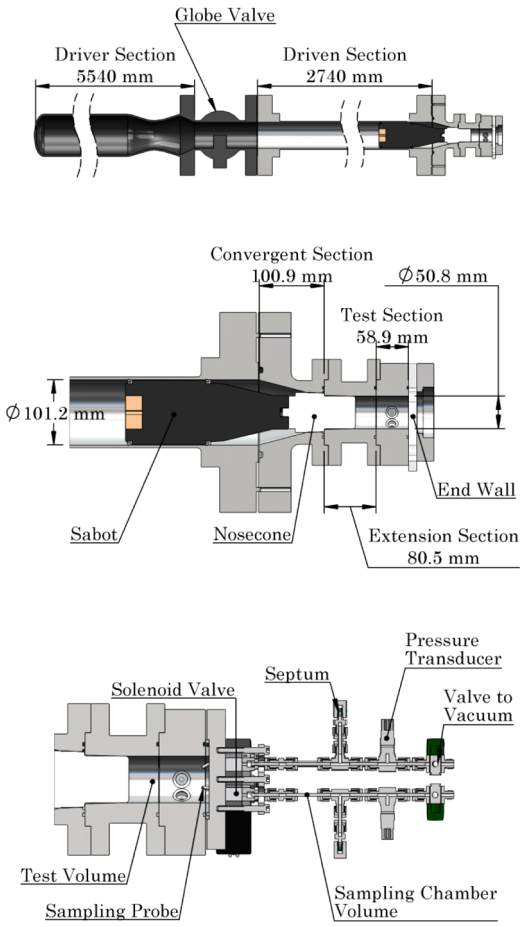

Figure 1. Schematic representations of the UM RCF (top panel) with key dimensions, the configuration of the UM RCF test section for end-view imaging (middle panel), and the configuration for high-speed gas sampling (bottom panel).

dx.doi.org/10.1021/jp309358h | J. Phys. Chem. A XXXX, XXX, XXX−XXX

acting hydraulic globe valve system. For each experiment, preprepared fuel/oxidizer/diluent mixtures are filled into the evacuated driven section and compressed with the sabot using high pressure gas released by the globe valve from the driver section. At the end of compression (EOC), the nosecone of the sabot seals the fuel/oxidizer/diluent mixture in the test section through an interference fit at specifically targeted temperatures and pressures achieved by varying the compression ratio and the composition of the inert gases in the test gas mixture. The majority of the pressure and temperature increases due to compression occur in the last 10 ms of the 145 ms compression stroke. After EOC, the fuel/oxidizer/diluent mixture in the test section autoignites after a period of time that is designated the ignition delay time (τ_{ign}). Details on the uniformity of the temperature and pressure conditions created in the test section can be found in Karwat et al.[34]

This study builds upon two previous studies, the first being a study of the combustion chemistry of n-C_4H_9OH,[34] and the second being a similar study of n-C_7H_{16}.[19] The two studies serve as references to understand how the combustion chemistry of n-C_7H_{16} and n-C_4H_9OH blended together are similar or contrasting to their respective chemistries in isolation. For this study, stoichiometric n-C_7H_{16}/n-C_4H_9OH/O_2 mixtures, with an inert/O_2 ratio of 5.64 (molar basis), were studied at two molar blend ratios: 80% n-C_7H_{16} with 20% n-C_4H_9OH (80−20) and 50% n-C_7H_{16} with 50% n-C_4H_9OH (50−50). Mixtures were prepared manometrically using high-purity compounds (n-C_7H_{16}, Sigma-Aldrich, puriss. p.a., ≥99.5%, GC grade; n-C_4H_9OH, Sigma-Aldrich, purum, >99% GC grade; O_2, Cryogenic Gases, Purity Plus 4.3, 99.993%, <40 ppm Ar, <3 ppm moisture, <10 ppm N_2, <0.5 ppm hydrocarbons; inert diluents, CO_2, Cryogenic Gases, Laser grade, 99.995%, <1 ppm of O_2, moisture and hydrocarbons, <0.2 ppm CO; and N_2, Cryogenic Gases, Purity Plus 5.0, 99.999%, <2 ppm O_2, <3 ppm moisture, <0.5 ppm hydrocarbons) in a magnetically stirred mixing tank external to the UM RCF. Mixture compositions were determined using partial pressures measured with a capacitance diaphragm gauge (Varian CeramiCel VCMT12TFA). The partial pressures of n-C_7H_{16} and n-C_4H_9OH were maintained well below their respective saturation vapor pressures at room temperature (5.9×10^{-2} atm or 45 Torr at 25 °C for n-C_7H_{16} and 8.81×10^{-3} atm or 6.69 Torr at 25 °C for n-C_4H_9OH) in order to avoid fuel condensation. Total mixture pressures in the mixing tank were approximately 0.8 atm, with initial fill pressures (P_0) in the RCF being approximately 1.3×10^{-1} atm. The pressure in the test section was monitored using a piezoelectric transducer (Kistler 6041AX4) and charge amplifier (Kistler 5010B), and all electronic data were acquired at 100 kHz using a National Instruments (NI) cDAQ 9172 chassis coupled with NI 9215 cards. For ignition experiments, a transparent end wall (shown in the middle panel of Figure 1) allowed a high-speed camera with a widescreen CMOS array (Vision Research Phantom v711), a fast 50 mm lens (f/0.95, Navitar), and a c-mount extension tube to record ignition events in the test section by viewing along the axis of the test section. The imaging data, acquired at 30 000 frames per second (fps) at a spatial resolution of 256 × 256 pixels, provide qualitative and quantitative indications of the ignition homogeneity.

2.2. High-Speed Gas Sampling and Gas Chromatography. For gas sampling experiments, an end wall with a high-speed gas sampling system replaces the transparent end wall (configuration shown in the bottom panel of Figure 1). The gas sampling system removes a very small portion of the test gas mixture at targeted times during the ignition delay period. The intermediate species present in the sample are identified and quantified using gas chromatographic techniques. Overall species time-histories for the intermediates are compiled by taking samples at different times from a series of experiments conducted at the same targeted EOC conditions. Several previous studies, including those with fuels such as i-C_8H_{18},[53] methyl butanoate,[54] n-C_4H_9OH,[34] and n-C_7H_{16}[19] have proved the validity of this experimental technique.

The sampling system used for these experiments consisted of sample chambers equipped with piezoresistive pressure transducers (Kistler 4045A2), charge amplifiers (Kistler 4618A0), low-bleed septa (VICI Valco), fast-acting sampling valves (modified Festo MHE3 valves), and vacuum isolation valves (Swagelok). Up to four samples can be obtained per experiment, through probes located on a square spacing (26 × 26 mm) on the end wall and 19 mm (radially) from the center of the test section, by independently controlling each valve using two digital delay/pulse generators (Stanford Research Systems Model DG535). For the sampling data presented here, one gas sample was collected from each experiment by triggering the fast-acting valve located at the northeast position of the sampling end wall. The samples were taken from the core of the test section (beyond the cold thermal boundary layer). Furthermore, the sampling process had no effect on the ignition events in the test section, as τ_{ign} values determined from the gas-sampling experiments were in excellent agreement with experiments where gas sampling was not used. The reactive gases, when sampled, are quenched as they expand into the vacuum of the sample chamber ($P_{test\ section}/P_{sample\ chamber} \approx 11$; $V_{test\ section}/V_{sample\ chamber} \approx 39$). The samples are then drawn into a syringe (Hamilton Gastight #1010) through the syringe port on the sampling chamber and then introduced into the gas chromatographs for analysis. Further details on the gas sampling system can be found in Karwat et al.[34]

The main contributors to the uncertainty of the gas sampling measurements include the dilution of the sample by unreacted gases trapped in the dead volume of the sampling system of the sampling probe (±16%, as determined previously[34]) and the gas chromatography calibration uncertainties for each species. The uncertainty in the sampling time is ±0.75 ms centered on the falling edge of the sampling pulse sent to the fast-acting valves. This uncertainty is determined from the pressure time histories of the sample volume and the falling edge of the trigger signal. The gas sampling results therefore represent the average value of the intermediate species present in the test section during the sampling time.

For the current experimental setup, end-view imaging cannot be conducted simultaneously with gas sampling through the end wall. An experiment to ensure no spatial bias to the gas sampling was performed by rotating the high-speed gas sampling system by 180° to acquire a sample from the southwest corner of the test section at almost the same time during the ignition delay period as a sample acquired from the northeast corner. The sample yielded species concentrations that were within measurement uncertainties (different for each species, as seen later) with the overall species time-histories.

Intermediate species formed during the ignition delay time were quantified using three gas chromatographs (GCs) equipped with four different columns, with each column connected to a separate detector. A temperature-controlled 10-

dx.doi.org/10.1021/jp309358h | J. Phys. Chem. A XXXX, XXX, XXX−XXX

port gas sampling valve injected the samples into the columns in the GCs. Ultra-high purity helium (Cryogenic Gases, Purity Plus, 99.999%) was used as the carrier gas for all of the GCs. *n*-Heptane (*n*-C_7H_{16}), methanol (CH_3OH), acetaldehyde (CH_3CHO), and propionaldehyde (C_2H_5CHO) were detected with a Perkin-Elmer Autosystem GC with a Varian CP-PoraBOND Q (25 m × 0.53 mm × 0.7 μm) column connected to a flame ionization detector (FID). The temperature program for this GC was 30 °C for 4.5 min → 45 °C/minute → 110 °C for 9 min → 45 °C/minute → 150 °C for 20 min. Methane (CH_4), ethane (C_2H_6), ethene (C_2H_4), propane (C_3H_8), propene (C_3H_6), 1-butene (1-C_4H_8), 1-pentene (1-C_5H_{10}), 1-hexene (1-C_6H_{12}), 1,3-butadiene (1,3-C_4H_6), and 3-heptene (3-C_7H_{14}) were detected with a Perkin-Elmer Autosystem GC with a Varian CP-Al_2O_3/Na_2SO_4 (25 m × 0.53 mm × 0.7 μm) column connected to an FID. The temperature program for this GC was 30 °C for 4 min → 25 °C/minute → 150 °C for 7 min → 45 °C/minute → 200 °C for 2 min. The third GC, a Perkin-Elmer Clarus 500, used an Agilent DB-Wax (30 m × 0.25 mm × 0.25 μm) column connected to an FID to detect 2-heptene (2-C_7H_{14}) and *n*-butyraldehyde (*n*-C_3H_7CHO), and a Restek ShinCarbon ST packed (2 m × 1 mm, silica steel) column connected to a thermal conductivity detector (TCD) to detect carbon monoxide (CO). The temperature program for this GC was 25 °C for 5 min → 45 °C/minute → 200 °C for 5 min. The FIDs used a hydrogen/air flame, were maintained at 300 °C, and were set with a range and attenuation of 1. The TCD was maintained at 100 °C with an attenuation of 1 and current of ±160 mA. Further purification of the helium, air, and hydrogen was applied using adsorbents to remove water, hydrocarbons, and oxygen before use in the GCs. High-purity reference chemicals (either gaseous or vapors of liquid) were used to develop the GC temperature programs used in the study, and the chromatograms were used to establish the calibrations for absolute concentration. (See Table S1, Supporting Information, for a detailed list of calibration chemicals used.) Calibration mixtures were made in the magnetically stirred mixing tank with the upper limit of concentrations calibrated for greater than the maximum concentrations predicted by the Curran et al.[21] mechanism for the ignition delay of a mixture with reactant mole fractions of χ(*n*-C_7H_{16}) = 0.0135, $\chi(O_2)$ = 0.1486, $\chi(N_2)$ = 0.2179, and $\chi(CO_2)$ = 0.62 at P = 9 atm and T = 700 K. Calibration curves were linear in all cases, except for *n*-C_4H_9OH, which showed nonlinearities and saturation at high concentrations. Only measurements later during the ignition delay time were considered for *n*-C_4H_9OH, to remain in the linear portion of the calibration curve. A data acquisition system (NI PXI 4472) recorded voltage signals from the GC detectors with a sampling rate of 8 Hz.

3. MODEL DESCRIPTION

Kinetic modeling calculations were carried out using CHEMKIN Release 10101 (x64).[55] The detailed chemical kinetic mechanism for *n*-C_7H_{16} was taken from an updated version of the mechanism described in Mehl et al.,[20] which was based on the original mechanism of Curran et al.[21] The *n*-C_4H_9OH portion of the kinetic mechanism was taken from the recent work of Sarathy et al.[42] The core mechanism for hydrocarbons from C_1 to C_4 species was taken from a recently refined mechanism from Metcalfe et al.[56] The resulting full mechanism was previously used to carry out modeling analysis of *n*-C_7H_{16} autoignition.[19]

The kinetic mechanism includes the extensive submechanism that leads to the NTC behavior that is seen for *n*-C_7H_{16} at temperatures from about 650 to 850 K. This reaction pathway is initiated by the addition of molecular oxygen O_2 to heptyl radicals that are produced from the *n*-C_7H_{16} fuel by H atom abstraction reactions:

$$n\text{-}C_7H_{16} + OH \leftrightarrow C_7H_{15} + H_2O \quad \text{(R1)}$$

$$C_7H_{15} + O_2 \leftrightarrow C_7H_{15}O_2 \quad \text{(R2)}$$

followed by isomerization of the $C_7H_{15}O_2$ species via internal H atom abstraction from within the $C_7H_{15}O_2$ species and additional reactions at low temperatures.[21] This sequence of reactions ultimately produces two or more OH radicals, as well as other radical species, along with a modest amount of heat. The reaction sequence ceases when gas temperature reaches a level where the dissociation of the heptylperoxy radicals, the reverse of reaction R2, becomes faster than the same reaction in the addition direction. The reaction sequence produces the first stage ignition that will be seen below in Figures 2 through 5.

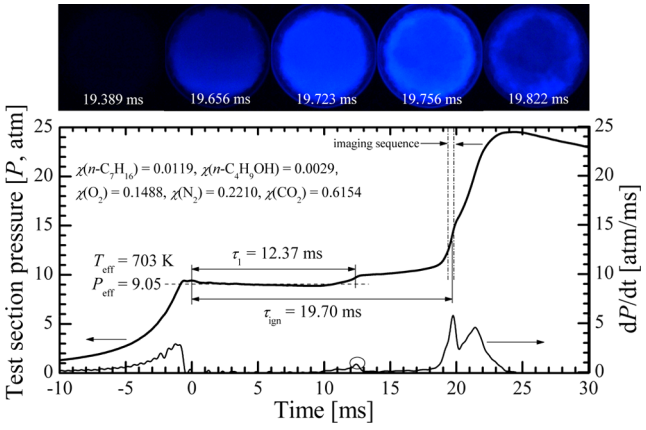

Figure 2. Results from a typical UM RCF 80−20 ignition experiment. The lower panel shows the pressure time-history in the test section, the rate of pressure rise used to define τ_{ign}, and the effective pressure and temperature conditions. The upper panel shows still images taken at 30 000 fps via end-view imaging. Note the homogeneity of the ignition event. The color of the images has been adjusted for clarity.

In contrast, although low temperature radical isomerization reaction pathways are included in the *n*-C_4H_9OH oxidation mechanism,[42] *n*-C_4H_9OH exhibits little or no NTC behavior[34,42] under the present conditions. As a result, in the kinetic model calculations described below, OH radicals are consumed by H atom abstraction reactions with *n*-C_4H_9OH

$$n\text{-}C_4H_9OH + OH \leftrightarrow C_4H_8OH + H_2O \quad \text{(R3)}$$

where C_4H_8OH refers to any of the five radicals that can be produced by H atom abstraction from *n*-C_4H_9OH. Molecular O_2 can add to all of these radicals via reactions analogous to reaction R2 above, but because of the highly strained transition state rings involved, little isomerization occurs, and there is only a minor amount of low-temperature reaction or heat release from *n*-C_4H_9OH reactions via the reaction pathways that are so productive in the oxidation of *n*-C_7H_{16}. The small amounts of low-temperature reactivity are insufficient to replace the OH radicals that are consumed in reaction R3, so the net effect of the addition of *n*-C_4H_9OH to *n*-C_7H_{16} is to reduce the levels of

dx.doi.org/10.1021/jp309358h | J. Phys. Chem. A XXXX, XXX, XXX−XXX

OH and therefore reduce the levels of consumption of n-C_7H_{16} compared to the reactivity of n-C_7H_{16} alone, as observed below.

Somewhat in contrast with the effects of n-C_4H_9OH inhibiting ignition of n-C_7H_{16} in the NTC region, the presence of n-C_7H_{16} clearly sensitizes the ignition of n-C_4H_9OH in the NTC region. At temperatures from about 650 to 850 K, n-C_4H_9OH as the sole fuel is distinctly unreactive under most conditions,[42] but when some n-C_7H_{16} is added to the n-C_4H_9OH fuel at these low temperatures, the high reactivity of n-C_7H_{16} contributes a sufficiently large amount of OH and other radical species that makes n-C_4H_9OH oxidation proceed at a rate similar to that of the n-C_7H_{16}, also observed in the present study.

The interactions between n-C_7H_{16} and n-C_4H_9OH are very similar to those between the gasoline primary reference fuels n-C_7H_{16} and i-C_8H_{18}.[57] In the low temperature regime, i-C_8H_{18} reduces the reactivity of n-C_7H_{16} and delays its ignition, while the addition of n-C_7H_{16} increases the low temperature reactivity of iso-C_8H_{18} at temperatures where i-C_8H_{18} is not ordinarily reactive at all. The high octane fuels (i-C_8H_{18} RON = 100; n-C_4H_9OH RON = 96) produce very little low temperature reactivity and do not return new OH to the radical pool, but both react easily with OH and other radicals produced by the other low octane fuel n-C_7H_{16} (n-C_7H_{16} RON = 0). This type of fuel interaction is common, where two or more fuels with quite different individual reactivities interact via the radical pool that is produced almost entirely by one of the components, and all of the fuel components are observed to be consumed effectively simultaneously.

Kinetic interactions between the fuel components, where heptyl radicals abstract H atoms from n-C_4H_9OH and radicals from n-C_4H_9OH abstract H atoms from n-C_7H_{16}, were examined and found to have little effect on the mechanism and were not retained in the combined model. The same conclusion was reached for fuel/radical interactions between n-C_7H_{16} and i-C_8H_{18} in previous kinetic modeling studies of these gasoline PRF fuels,[57] which were also found to be negligible.

In the course of the present project, portions of the kinetic mechanism for n-C_7H_{16} were found to be insufficient to describe the present experimental results. The n-C_7H_{16} mechanism had been developed primarily[21] on the basis of integrated system experiments such as ignition delay times in shock tubes and rapid compression machines and laminar flame speed measurements, with very few species-specific measurements to provide especially demanding validation tests. The new speciation measurements provided by the present experiments (and similar experiments using only n-C_7H_{16}[19]) provide new and more challenging sets of validation data, and further refinements for the n-C_7H_{16} mechanism will be needed in response to these new experiments.

4. RESULTS AND DISCUSSION

4.1. Ignition Experiments and Modeling. Ignition experiments were conducted to understand the dependence of ignition delay time (τ_{ign}) on blend ratio at a fixed temperature (700 K) and pressure (9 atm). A study of n-C_7H_{16} chemical kinetics[19] provided baseline τ_{ign} data against which the influence of the presence of n-C_4H_9OH was compared. It was expected that increasing the amount of n-C_4H_9OH would increase the ignition delay time, given the much greater low-temperature reactivity of n-C_7H_{16}.[19,34] Since in the baseline study[19] the chemical kinetics of n-C_7H_{16} were studied at a temperature of 700 K and a pressure of 9 atm, yielding a τ_{ign} on the order of 15 ms, the presence of n-C_4H_9OH would allow for several discrete sampling events (each lasting 1.5 ms, as described earlier) during the ignition delay period.

For each experiment, the effective test conditions are determined based on the pressure time-history from each experiment. Examples are provided in Figures 2 and 3. Since

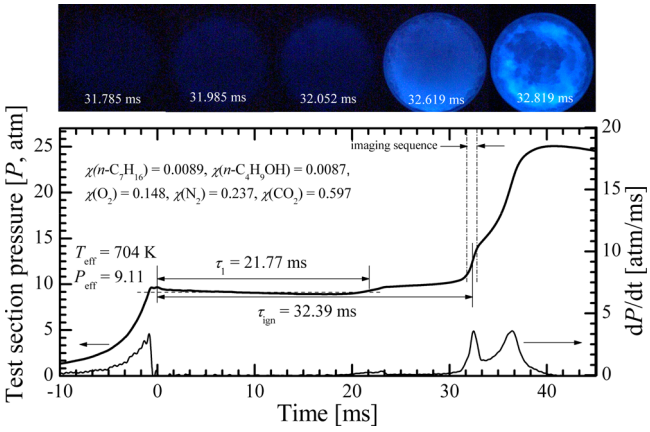

Figure 3. Results from a typical UM RCF 50−50 ignition experiment. The lower panel depicts the pressure time-history in the test section and the rate of pressure rise. The upper panel shows still images taken at 30 000 fps via end-view imaging. The color of the images has been adjusted for clarity.

the 80−20 and 50−50 blends studied, like the previous experiments with pure n-C_7H_{16},[19] exhibited two-stage ignition for all experiments, eq 1 was used to determine the effective pressure (P_{eff}), which is the time-integrated average pressure from the maximum pressure (P_{max}) at EOC to the maximum of the rate of pressure rise at the 1st stage of ignition ($dP/dt_{max,\ first\ stage}$)

$$P_{eff} = \frac{1}{t_{dP/dt_{max}} - t_{P_{max}}} \times \int_{t_{P_{max}}}^{t_{dP/dt_{max},1st\ stage}} P\,dt \quad (1)$$

The effective temperature (T_{eff}) for each experiment was determined using P_{eff} and numerical integration of the isentropic relationship (eq 2)

$$\int_{T_0}^{T_{eff}} \frac{\gamma}{\gamma - 1} d\ln T = \ln\left(\frac{P_{eff}}{P_0}\right) \quad (2)$$

where P_0 is the initial charge pressure, T_0 is the initial temperature, and γ is the temperature-dependent ratio of the specific heats of the unreacted test gas mixture (determined using the NASA thermodynamic database[58]). The ignition delay time (τ_{ign}) for each experiment was defined as the time between EOC (t = 0 ms, defined by the first maximum in P) and the maximum rate of pressure rise corresponding to autoignition ($dP/dt_{max,\ second\ stage}$). The time for the first stage of ignition (τ_1) was defined as the time between EOC (t = 0 ms, defined by the first maximum in P) and the pressure rise corresponding to the first stage of ignition. All mixtures had an equivalence ratio (ϕ) of 1, and a dilution (with N_2 and CO_2 being the sole diluents for all experiments) of inert/O_2 = 5.62−5.64. Table S2 found in the Supporting Information accompanying this article is a summary of the experimental conditions and results for all of the UM RCF data presented.

dx.doi.org/10.1021/jp309358h | J. Phys. Chem. A XXXX, XXX, XXX−XXX

Figure 2 presents typical results from a UM RCF ignition experiment for the 80−20 blend for which imaging data were acquired. The lower panel depicts the time-histories of the pressure and rate of pressure rise in the test section. A fast Fourier transform has been applied to filter high frequency disturbances greater than 2.5 kHz generated by the impact of the sabot near EOC. The motion of the sabot compresses the test gas mixture into the test section to the first maximum. The EOC time is set to time $t = 0$, after which the volume in the test section is constant. The first stage of ignition occurs at τ_1 = 12.37 ms, corresponding to a local maximum in dP/dt (circled in the lower panel of Figure 2). The pressure time-history from EOC to τ_1 defines P_{eff} and T_{eff} as 9.05 atm and 703 K, respectively. After another time interval, the pressure rises abruptly again to its maximum value. The second pressure rise corresponds to autoignition of the test mixture at 19.70 ms.

The upper panel of Figure 2 shows stills from the image sequence corresponding to the pressure data of the lower panel. Intense chemiluminescence occurs only during the second stage of ignition. The chemiluminescence is attributed to CH and C_2 radicals, which have strong spectroscopic features in the blue part of the visible spectrum (CH, 431.2 nm; C_2, 473.7, 516.5, and 563.5 nm) and are generated only through the decomposition of intermediate hydrocarbons present in the test mixture. Note the uniformity of the blue emission throughout the test section, attesting to the homogeneity of the reactant mixture and the state conditions in the test section. Such uniformity gives confidence in localized sampling.

Figure 3 shows similar imaging and pressure data for a 50−50 blend. The general features of the pressure time-history are the same as observed for the 80−20 blend. However, both τ_1 and τ_{ign} increase to 21. 77 and 32.39 ms, respectively, compared to 12.37 and 19.70 ms for the 80−20 blend.

As is seen in Figures 2 and 3, the addition of n-C_4H_9OH slows the ignition process. A clearer representation of the influence of n-C_4H_9OH can be seen in Figure 4, which compares the pressure time-histories obtained experimentally for the blends with the baseline (100−0) case. Also shown in Figure 4 are zero-dimensional, constant volume, adiabatic CHEMKIN simulations, using the blend reaction mechanism described earlier, of the ignition delay times for the 80−20 and 50−50 experiments. The initial pressure and temperature conditions used in the simulations corresponded to the effective pressure and temperature conditions obtained experimentally. As described previously,[19,34] the effective pressure and temperature definitions adequately account for the heat transfer physics occurring in the test section of the UM RCF during the time interval leading to the first stage ignition. As the amount of n-C_4H_9OH increases in the blend, the differences between the model predictions and the experimental results increase. While experiments show that τ_1 and τ_{ign} increase by a factor of approximately three from the 100−0 to the 50−50 case, the model predicts an increase by a smaller factor of approximately two (see also Table 1). Also, it is observed experimentally that the rise in pressure during the first stage of ignition decreases with increasing concentrations of n-C_4H_9OH. This is not the case with the model predictions, for even though the heat release of the first stage of ignition occurs over a slightly longer period of time with increasing concentrations of n-C_4H_9OH, the computed pressure reached at the end of the first stage of ignition is nearly the same for the 100−0, 80−20, and 50−50 conditions, and the calculated pressure increase is consistently greater than the pressure rise measured experimentally.

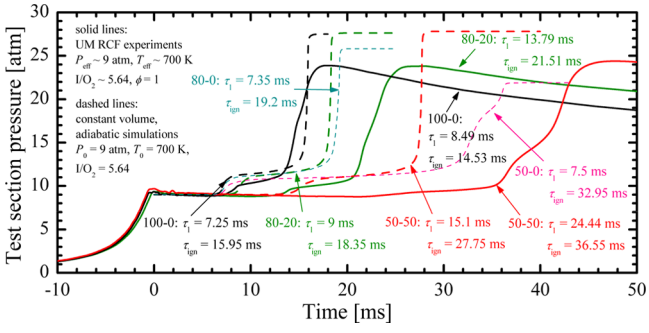

Figure 4. Comparison of experimental (solid lines) and modeling (dashed lines) pressure time-histories for the 100−0, 80−20, and 50−50 blend cases. While the model and the experimental data agree adequately for the 100−0 case, differences increase with increasing concentrations of n-C_4H_9OH in the mixture. Shown also are time-histories for simulations in which n-C_4H_9OH was removed from the 80−20 and 50−50 mixtures, thus simulating lean 80−0 (dark cyan) and 50−0 (pink) n-C_7H_{16} mixtures.

In order to understand why ignition slows as the blend ratio increases and to compare important features of the pressure time-histories, the ignition times were normalized, and the results are presented in Figure 5. Specifically, the period of time between EOC and the first stage of ignition of each experiment was normalized by τ_1 (resulting in a normalized time domain of 0 to 1), and the period of time between the first stage of ignition and autoiginition ($\tau_{ign} - \tau_1$) was normalized by $\tau_{ign} - \tau_1$ and added to the first normalized time domain, so the ignition delay between the first and second stages of ignition takes place over a normalized time interval from 1 to 2.

The experimental data show that as the amount of n-C_4H_9OH in the blend increases, the first stage of ignition becomes less pronounced, indicating the amount of heat released and the pressure rise during the first stage ignition become smaller. The model simulations, also shown in Figure 5, differ from the experimental data in several ways. The predicted pressure rise in the first stage of ignition is larger than observed experimentally. The predicted rate of pressure rise at the second stage of ignition is much larger than observed experimentally. The predicted changes in the relative time between the first and second stages of ignition are unchanged for the blends, whereas the experimental data exhibit an increase in the relative time between the first and second stages of ignition with increasing amount of n-C_4H_9OH.

The effects described above can be interpreted based on an understanding of n-C_7H_{16} ignition chemistry.[19] The main stage of autoignition occurs at approximately 900−1000 K with the decomposition of H_2O_2,[59] which accumulates during chemical reactions at low temperatures. When the reactive mixture reaches this temperature, H_2O_2 decomposition releases a large quantity of highly reactive OH radicals, and ignition occurs. Different fuels or fuel mixtures reach this H_2O_2 decomposition temperature and ignite at different times, depending on the amount of heat release and temperature increase they experience during the first stage, low temperature ignition.[21] Fuels that exhibit larger amounts of low temperature heat release, such as n-C_7H_{16}, release more heat and increase the mixture temperature more than fuels like n-C_4H_9OH and i-C_8H_{18} that produce very little low temperature heat release, and replacement of n-C_7H_{16} with n-C_4H_9OH reduces the overall amount of low temperature heat release, with the amount of

dx.doi.org/10.1021/jp309358h | J. Phys. Chem. A XXXX, XXX, XXX−XXX

Table 1. Comparison of Experimental and Predicted Ignition Results Based on the Current Mechanism for First Stage Ignition and Autoignition Features

	experiment		current model		Saisirirat[43] model	
blend	τ_1 (ms)	τ_{ign} (ms)	τ_1 (ms)	τ_{ign} (ms)	τ_1 (ms)	τ_{ign} (ms)
100−0	7.94	14.09	7.25	15.95	9.55	14.85
80−20	13.45	20.86	9.00	18.35	9.90	16.30
50−50	23.16	35.16	15.10	27.75	12.25	22.40
20−80			37.50	67.25	25.50	64.05
0−100				268		>400
% increase 80−20/100−0	69	48	24	15	4	10
% increase 50−50/100−0	190	150	110	74	28	51
% increase 20−80/100−0			420	320	170	330
% increase 0−100/100−0				1600		>2600

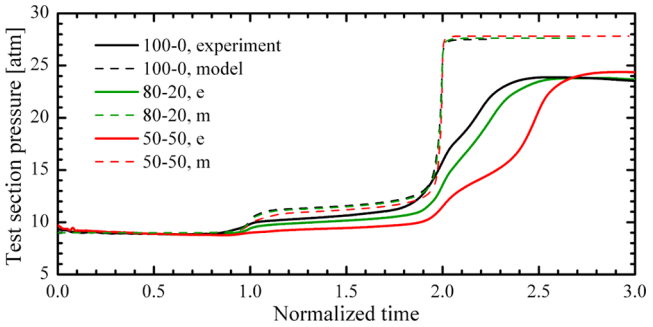

Figure 5. Comparison of experimental and modeling pressure time-histories for the 100−0, 80−20, and 50−50 blend cases using a normalized time domain, where 0 corresponds to EOC, 1 corresponds to the first stage of ignition, and 2 corresponds to overall ignition.

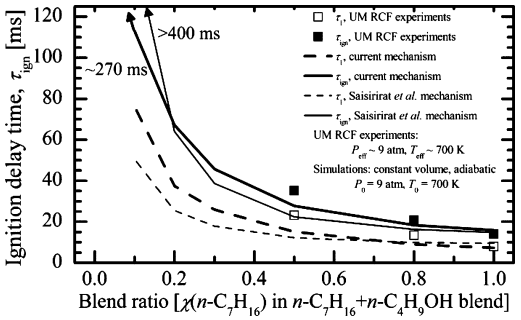

Figure 6. Ignition delay times as a function of blend ratio and a comparison of the current model and a model developed by Saisirirat et al.[43]

heat release being approximately proportional to the ratio of n-C_7H_{16} to n-C_4H_9OH. The decreasing amount of heat release with increasing blend fraction of n-C_4H_9OH reduces the temperature of the reactive mixture at the end of the first stage of ignition and therefore lengthens the time for the reactive mixture to reach H_2O_2 decomposition temperatures, thus lengthening τ_{ign}. The other dominant products of the low temperature, first stage of ignition are highly reactive OH radicals that then react with all of the fuel components. Fuels that are highly reactive at low temperatures, such as n-C_7H_{16}, produce large amounts of OH, while fuels that have little low temperature reactivity produce little OH under the same conditions. The presence of n-C_4H_9OH in the fuel blend therefore reduces the levels of OH in the reactive mixture because there is less n-C_7H_{16} in the reactive mixture, while the n-C_4H_9OH removes OH from the reactive mixture without producing new OH radicals.

Recent work by Saisirirat et al.[43] reflects similar trends. In that work, the authors studied n-C_7H_{16}/n-C_4H_9OH blends in a homogeneous charge compression ignition engine and found that the presence of n-C_4H_9OH both reduced the amount of low temperature, cool flame behavior and retarded autoignition and phasing. They concluded that, since the fuel mixtures were oxidized primarily by OH radicals formed from decomposition of alkylperoxy and ketoperoxy radicals, the presence of n-C_4H_9OH, which decreased the rate of production of OH radicals, slowed overall reactivity.

We thus observe computationally from Table 1 and Figure 6 a nonlinear increase in τ_1 and τ_{ign} as the amount of n-C_4H_9OH increases in the blend ratio, seen especially when the amount of n-C_4H_9OH in the mixture is greater than 50%. While the model adequately captures the increase in τ_1 and τ_{ign} as a function of blend ratio, the model predicts slightly smaller increases than observed experimentally. Shown also in Figure 6 with the thinner lines are modeling results using the Saisirirat et al.[43] mechanism, which predicts faster τ_1 and τ_{ign} compared to the current mechanism as long as n-C_7H_{16} is present in the mixture. The Saisirirat et al.[43] mechanism is explored in greater detail below.

It is clear that n-C_7H_{16} reacts much more quickly than n-C_4H_9OH; at a temperature of 700 K and a pressure of 9 atm, n-C_7H_{16} reacts almost an order of magnitude faster than n-C_4H_9OH. However, when n-C_4H_9OH is blended with n-C_7H_{16}, the low-temperature reactivity of n-C_7H_{16} forms a radical pool that stimulates n-C_4H_9OH to react at temperatures where it normally would not react. These results are similar to the results observed in the JSR study by Dagaut and Togbé,[44] who measured the consumption of n-C_4H_9OH in the presence of n-C_7H_{16} at NTC conditions, again, conditions where n-C_4H_9OH would not normally react. Furthermore, the amount of n-C_4H_9OH consumed was proportional to the amount of it present in the blend. For example, in an 80−20 molar blend, when the concentration of n-C_7H_{16} was four times higher than that of n-C_4H_9OH, four times more n-C_7H_{16} was consumed than n-C_4H_9OH.

The influence of n-C_4H_9OH on the chemical kinetics of blends is complicated and nuanced. In order to show the influence of the presence of n-C_4H_9OH, simulations were performed in which the n-C_4H_9OH was removed from the blends, thus leaving lean reactive mixtures of only n-C_7H_{16}. The simulation results are shown in Figure 4 as the 80−0 (ϕ = 0.88, dark cyan dashed line) and 50−0 (ϕ = 0.64, pink dashed line) mixtures. The τ_1 values for these mixtures are approximately the same, while the τ_{ign} values increase with decreasing

dx.doi.org/10.1021/jp309358h | J. Phys. Chem. A XXXX, XXX, XXX−XXX

concentrations of n-C_7H_{16}. Interestingly, when compared to the respective 80−20 and 50−50 blends, the model predicts that n-C_4H_9OH not only *lengthens* τ_1 but it also *shortens* τ_{ign} compared to the respective 80−0 and 50−0 cases when n-C_4H_9OH is not present in the mixture; this can be attributed to the fact that the 80−0 and 50−0 mixtures are fuel lean.

As noted earlier, such changes in ignition behavior can arise due to the less reactive component of the fuel consuming radicals that would otherwise act on the more reactive fuel and its fuel fragments. Mehl et al.[20] and Vanhove et al.[60] in their studies of binary blends of n-C_7H_{16} and toluene have discussed at length the radical scavenging properties of a compound like toluene that reacts on much longer time scales than n-C_7H_{16}. Like n-C_4H_9OH, toluene is a single stage fuel, and easily abstractable H-atoms on the methyl group of toluene act as a radical scavenger, suppressing the reactivity of the system. Just as has been observed experimentally in this work, when n-C_7H_{16} was mixed with toluene to create a 50−50 blend, Mehl et al.[20] observed that the two-stage behavior was maintained, with the first stage and second stages of ignition being lengthened, and a lower amount of heat released during the first stage of ignition. From their chemical kinetic mechanism, they observed that lower concentrations of H_2O_2 were produced by the first stage of ignition. The reduced amount of heat released by the 50−50 blend fuel served to lengthen the time delay until the second stage ignition, just as noted above for the n-C_7H_{16}/n-C_4H_9OH fuel blends. Vanhove et al.[60] make similar conclusions, but note that the effect of the presence of a slowly reacting compound like toluene is more significant on other slowly reacting compounds, such as *iso*-C_8H_{18}, given that toluene actually increases the activation energy of *iso*-octane ignition. In the case of toluene being blended with n-C_7H_{16}, the mixture reactivity is still driven by n-C_7H_{16}.

An early study of a similar nonlinear interaction of ignition of mixtures of two such different fuels was reported by Westbrook for shock tube ignition of mixtures of methane and ethane.[61] Ethane is the highly reactive fuel, while methane is much less reactive. At a postshock temperature of 1500 K, stoichiometric ethane/O_2/Ar mixtures were predicted to ignite at 16 μs, and stoichiometric methane/O_2/Ar mixtures were calculated to ignite at 270 μs. Stoichiometric mixtures of 95% methane + 5% ethane with O_2 and Ar ignited at 155 μs; the replacement of only 5% of the methane by ethane reduced the ignition delay by nearly 50% of the difference in the individual ignition delay times. From the opposite direction, the addition of methane to ethane, starting at 100% ethane, increased the ignition delay time very slowly until the mixtures were about 60% methane, and further replacement of ethane by methane rapidly increased the computed ignition delay time, producing an ignition delay curve very similar to that in Figure 6 for mixtures of n-C_7H_{16} and n-C_4H_9OH. Conversely, the addition of the more reactive component, n-C_7H_{16} in the present case, rapidly lowers the ignition delay time for a small amount of n-C_7H_{16} additive, just as was reported for the addition of small amounts of ethane to methane.[61] This sensitization of the less reactive mixture by small amounts of the more reactive component is quite familiar in combustion kinetics.

4.2. High-Speed Gas Sampling Experiments. While the ignition studies provide an understanding of the global kinetics of ignition of n-C_7H_{16} and n-C_4H_9OH blends, speciation measurements provide a more detailed understanding of the dominant chemical pathways in the reacting test gas mixture. Sampling experiments were performed to identify intermediates formed during the ignition delay time. Figure 7 presents results from a typical sampling experiment for an 80−20 blend in

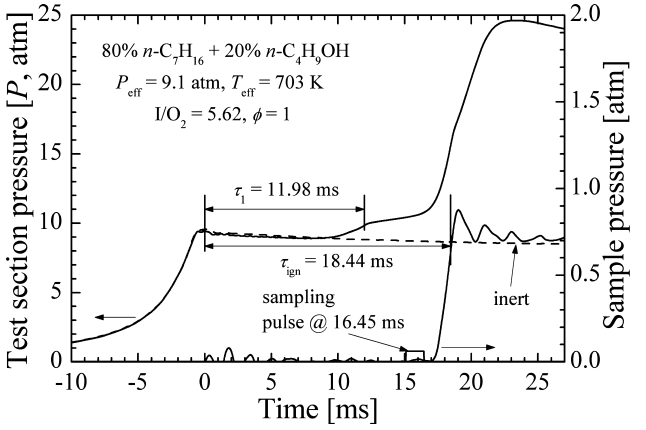

Figure 7. Typical results for the pressure time-histories in the test section and the sampling volume for an 80−20 sampling experiment (solid lines). The pressure time-history from a nonigniting (labeled inert) experiment is presented as the dashed line. The agreement until the first stage of ignition between the nonigniting pressure trace and the igniting pressure trace indicates that the heat transfer physics of the sampling experiments are unaffected by the sampling event.

which P_{eff} = 9.1 atm, T_{eff} = 703 K, τ_1 = 11.98 ms, and τ_{ign} = 18.44 ms. Shown are the pressure and pressure derivative time-histories in the test section, the sampling pulse used to trigger the high-speed gas sampling system, and the pressure in the sampling chamber. Since only a very small amount of sample is removed from the reacting mixture in the test section, the pressure in the test section remains unaffected by the sampling process. All the general features seen in Figure 2, which depicts an ignition experiment without sampling, are identical to those seen in Figure 7. As indicated by the pressure rise in the sampling volume, the sample is collected within 2 ms after the falling edge of the trigger signal.

Also shown in Figure 7 is the time-history of a nonigniting experiment, in which the O_2 of an igniting mixture is replaced by N_2. The almost identical thermal characteristics of O_2 and N_2 permit direct comparison of the pressure time-histories. As seen in Figure 7, the bulk of the compression process in the UM RCF occurs during the last ten ms before EOC. There is always concern about possible reaction of the test gas mixture during compression, which affects the assumptions used to define the effective thermodynamic conditions (eqs 1 and 2) of the experiment. The nonigniting experiment, however, shows a nearly identical compression process to the igniting experiment and is almost indistinguishable from the igniting experiment (P_{eff} and T_{eff} differ by less 0.3% and 0.1%, respectively) until the first stage of ignition. As will be seen later, even though intermediate species are observed between EOC and the first stage of ignition, signaling the decomposition of small amounts of n-C_7H_{16}, the extent of reaction is small, and the use of effective pressure and temperature definitions remains valid. Furthermore, the heat transfer physics of the experiments remain unaffected by the sampling events. Similar results are observed for the sampling experiments of 50−50 blends. Details on all of the gas sampling experiments, including mixture compositions, can be found in Table S2, Supporting Information.

dx.doi.org/10.1021/jp309358h | J. Phys. Chem. A XXXX, XXX, XXX−XXX

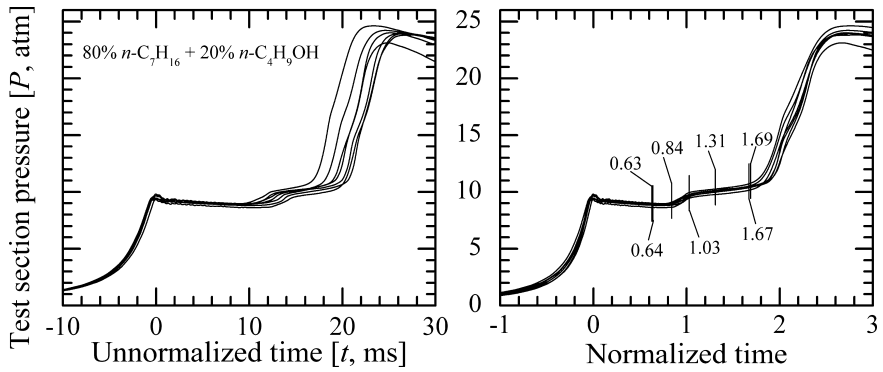

Figure 8. Left panel depicts the unnormalized experimental pressure time-histories of the sampling experiments for the 80−20 blend. Note the level of repeatability of the compression process, as well as of the first and second stages of ignition and heat release. Right panel presents the normalized data where 0 represents EOC, 1 represents the first stage of ignition, and 2 represents the second stage of ignition. Shown also are the normalized times when samples were taken from the test section.

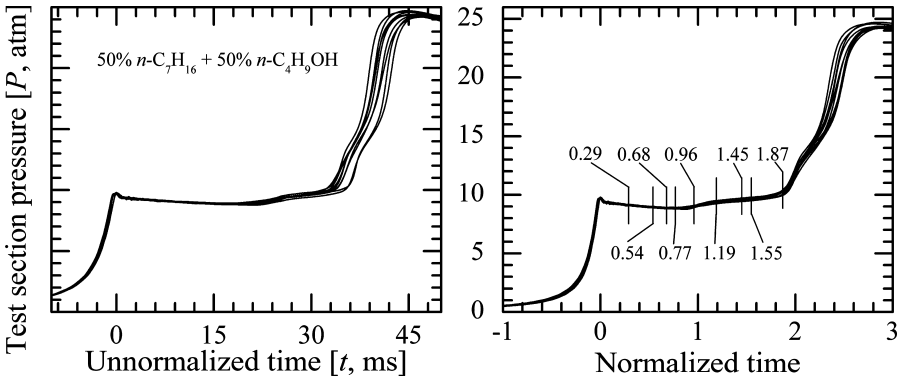

Figure 9. Left panel depicts the unnormalized experimental pressure time-histories of the sampling experiments for the 50−50 blend. Right panel presents the normalized data where 0 represents EOC, 1 represents the first stage of ignition, and 2 represents the second stage of ignition. Shown also are the normalized times when samples were taken from the test section.

The left panels of Figures 8 and 9 show the pressure time-histories for the sampling experiments for the 80−20 and 50−50 blends, respectively. All of the experiments showed nearly identical compression processes and very similar pressure time-histories after EOC. The experiments showed excellent repeatability; for the 80−20 blend, the average P_{eff}, T_{eff}, τ_1, and τ_{ign} were 8.98 atm, 700 K, 13.45 ms, and 20.86 ms, respectively, with the corresponding standard deviations of 0.19 atm, 3.2 K, 1.51 ms, and 1.62 ms, respectively. For the 50−50 blend, the average P_{eff}, T_{eff}, τ_1, and τ_{ign} were 9.06 atm, 701 K, 23.16 ms, and 35.16 ms, respectively, with the corresponding standard deviations being 0.06 atm, 1.3 K, 1.11 ms, and 0.98 ms, respectively. The slight differences that exist between experiments are attributed to the small variations in effective temperatures and pressures, and in mixture preparation. The temporal error bars on the speciation results represent only the uncertainty introduced by the sampling valve system and not by the statistical variation in ignition delay, which would increase the error bars in the time domain by about 5%. To compensate for the differences that remain in the sampling data, the pressure time-histories are plotted using a time domain normalized by the first stage of ignition and the second stage of ignition, as described earlier. These results can be seen in the right panels of Figures 8 and 9 for the 80−20 and 50−50 blends, respectively. The normalized pressure time-histories are virtually identical.

Figure 10 provides an example of the chromatograms obtained from the sampling experiment depicted in Figure 7

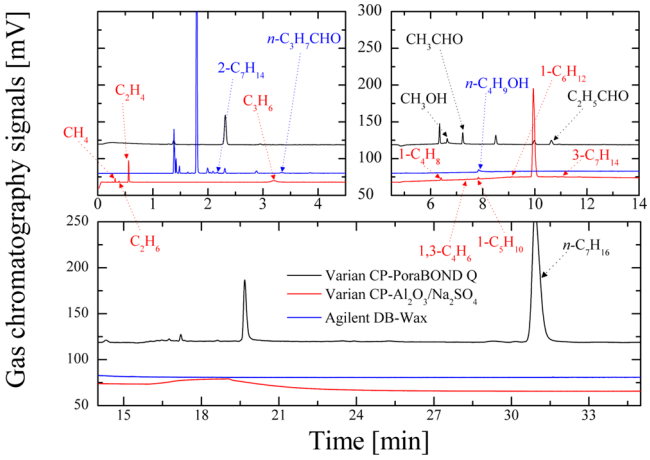

Figure 10. Typical gas chromatograms obtained from the three gas chromatographs. The data are for the experiment depicted in Figure 7, which was an 80−20 blend experiment with a normalized sampling time of 1.69.

and the species identified from the GC data. Although several peaks remained unidentified, for the 80−20 blend, the carbon balance for the species measured was 82 ± 14% for sampling at early times during the ignition delay period and 60 ± 10% for sampling closer to autoignition. The carbon balances were 72 ± 15% and 60 ± 10%, respectively, for the 50−50 blend. Using the calibrations for each species, the peaks were converted into

dx.doi.org/10.1021/jp309358h | J. Phys. Chem. A XXXX, XXX, XXX−XXX

discrete measurements of intermediate species for each normalized sampling time. It is worth noting that the total amounts of carbon and oxygen in the system change very little as a function of blend ratio: for the 100−0 case, χ(C) = 0.09401 and χ(O) = 0.2980; for the 80−20 case, χ(C) = 0.09455 and χ(O) = 0.3003; for the 50−50 case, χ(C) = 0.09526 and χ(O) = 0.3054.

Radicals such as O, H, OH, and CH_3 can recombine when gases from the test section are sampled and quenched, potentially forming water vapor and small hydrocarbons that can interfere with species measurements by changing concentrations. However, predicted radical concentrations, presented in Figure 11, are very low (<40 ppm) until very close to autoignition. Radicals are thus not expected to be a source of error in the species concentration measurements presented in this work.

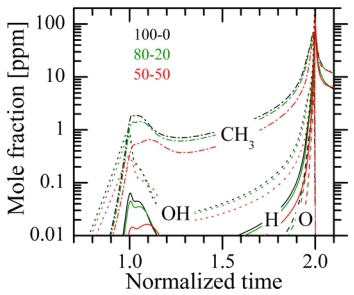

Figure 11. Small radical concentration predictions using the current mechanism at T_0 = 700 K, P_0 = 9 atm, ϕ = 1, at a dilution of ~5.64.

Figures 12−28 present the species time-histories for the 80−20 (green squares) and 50−50 (red triangles) blends, with

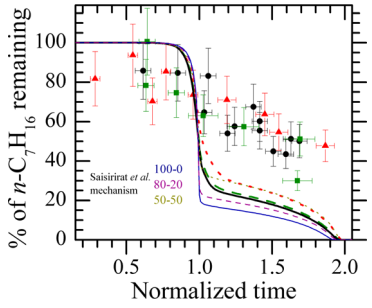

Figure 12. Experimental n-C_7H_{16} concentration time-histories for stoichiometric 100−0 (black circles), 80−20 (green squares), and 50−50 (red triangles) blends obtained from the UM RCF at nominal conditions of 700 K and 9 atm. Also shown with lines are zero-dimensional, constant volume, adiabatic mechanism predictions using the current mechanism (100−0, thick solid black; 80−20, thick dashed green; 50−50, thick red dotted) and the Saisirirat et al.[43] mechanism (100−0, thin solid blue; 80−20, thin dashed purple; 50−50, thin dotted gold).

results for 100−0 (black circles) from Karwat et al.[19] serving as a comparative baseline. The average experimental conditions for the 100−0 results are P_{eff} = 9.02 atm, T_{eff} = 701 K, χ(n-C_7H_{16}) = 0.0134, $\chi(O_2)$ = 0.1490, $\chi(N_2)$ = 0.2336, and $\chi(CO_2)$ = 0.6040, resulting in τ_1 = 7.94 ms and τ_{ign} = 14.09 ms with standard deviations of 0.52 and 0.63 ms, respectively, for the first and overall stages of ignition. The nominal conditions and ignition data for the 80−20 sampling experiments were reported above and were for an average mixture composition of χ(n-C_7H_{16}) = 0.0118, χ(n-C_4H_9OH) = 0.0029, $\chi(O_2)$ = 0.1487, $\chi(N_2)$ = 0.2417, and $\chi(CO_2)$ = 0.5949. The nominal conditions and ignition data for the 50−50 sampling experiments were also reported above and were for an average mixture composition of χ(n-C_7H_{16}) = 0.0087, χ(n-C_4H_9OH) = 0.0087, $\chi(O_2)$ = 0.1484, $\chi(N_2)$ = 0.2580, and $\chi(CO_2)$ = 0.5762. The species concentrations are plotted as a function of normalized time in which 0 represents EOC, 1 represents the first stage of ignition, and 2 represents overall ignition. Measured concentrations for all species except n-C_7H_{16} and n-C_4H_9OH are plotted in two ways, each providing different information on the chemical kinetics of the mixtures. On the left-hand side, the data are plotted as absolute units of mole fraction, and on the right-hand side, the data are normalized by the initial amount of n-C_7H_{16} in the mixtures. Plotted with solid black lines, dashed green lines, and dotted red lines are the corresponding zero-dimensional, constant volume, adiabatic, mechanism predictions for the average experimental conditions of the 100−0, 80−20, and 50−50 cases, respectively. The ignition results for these simulations are also included in Table 1.

The mechanism predictions agree well with the experimental data for some species and not for others. For all intermediate species, the model predicts an abrupt production at the first stage of ignition. While concentrations were measured to be nonzero near the time of the first stage of ignition for many species, the abruptness of the rise in concentrations was not observed experimentally. This is due at least in part to the finite amount of time required for the gas sampling valves to open and shut.

Figure 12 shows the data for n-C_7H_{16} as a function of time. Within experimental uncertainties, each of the blend mixtures results in 30−40% of the initial n-C_7H_{16} consumed during the first stage of ignition, which is approximately a factor of 2 less than the amount predicted computationally. (Model predictions using the Saisirirat et al.[43] mechanism, plotted in Figure 12, also show significant consumption at the first stage of ignition. These results will be discussed below.) The experimental and modeling results are self-consistent in that heat released during the first stage of ignition is attributed to n-C_7H_{16} consumption (caused mainly due to n-C_7H_{16} + OH to form n-C_7H_{15} and water). Consequently, since the experiments indicate lower n-C_7H_{16} consumption during the first stage of ignition, there is lower heat release during the first stage of ignition, and hence, the time from first stage to autoignition increases. The converse is true of the model predictions, where more n-C_7H_{16} is consumed during the first stage, yielding higher heat release and less time from first stage to autoignition. Many of the differences between the computationally predicted and experimentally measured intermediate species are due in part to the differences in consumption of n-C_7H_{16} at the first stage of ignition.

Since n-C_4H_9OH reacts only because of the presence of n-C_7H_{16} at a temperature of 700 K and a pressure of 9 atm, it follows that the amount of n-C_4H_9OH consumed is at some level proportional to the concentration of n-C_7H_{16} consumed. Figure 13 shows these trends for n-C_4H_9OH, computationally. The experimental and modeling results are in fairly good agreement, particularly at later times.

Also shown in Table 1 and Figures 6, 12, and 13 are predictions using the Saisirirat et al.[43] mechanism. As observed in Table 1 and Figure 6, while the Saisirirat et al.[43] mechanism predicts slower first stages of ignition for the 100−0 and 80−20

dx.doi.org/10.1021/jp309358h | J. Phys. Chem. A XXXX, XXX, XXX−XXX

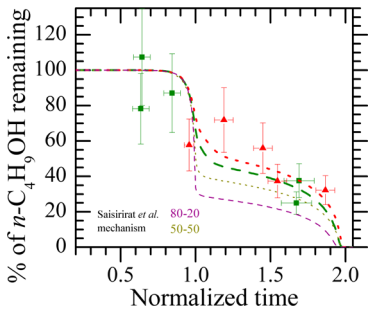

Figure 13. Experimental n-C_4H_9OH concentration time-histories for stoichiometric 80−20 and 50−50 blends obtained from the UM RCF. Also shown are mechanism predictions using the current mechanism and the Saisirirat et al.[43] mechanism. Experimental and simulation conditions and symbol and line details are the same as those in Figure 12.

blends, the autoignition predictions are in very good agreement (within 10−20%) with each other for cases in which n-C_7H_{16} is present in the mixture. However, key differences are observed in Figures 12 and 13, which predict greater consumption of both n-C_7H_{16} and n-C_4H_9OH at the first stage of ignition.

Figures 14−16 show measurements and predictions for CH_4, C_2H_6, and C_2H_4, respectively. The left-hand side (LHS) of

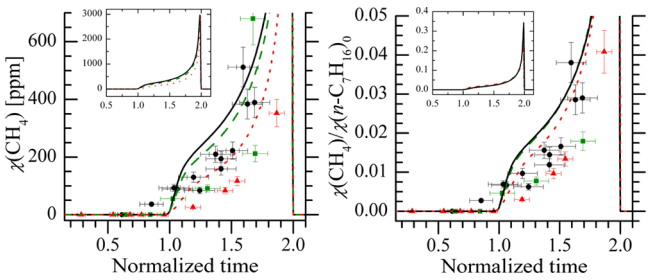

Figure 14. Experimental CH_4 time-histories for stoichiometric 100−0, 80−20, and 50−50 blends. Also shown are predictions using the current mechanism. Experimental and simulation conditions and symbol and line details are the same as those in Figure 12.

Figure 14 compares the experimental and modeling data for the blends on an absolute basis. The current mechanism predicts slightly higher values for CH_4 compared to the experimental data. When the data are normalized by the initial amount of n-C_7H_{16} present, as seen on the right-hand side (RHS) of Figure 14, it is evident that the model predictions are a function of the amount of n-C_7H_{16} in the system. Figure 15 shows that model

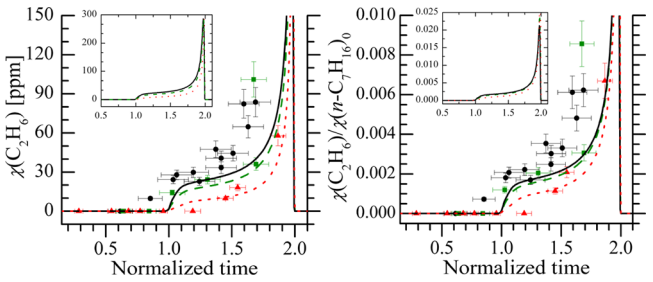

Figure 15. Experimental C_2H_6 time-histories for stoichiometric 100−0, 80−20, and 50−50 blends. Also shown are predictions using the current mechanism. Experimental and simulation conditions and symbol and line details are the same as those in Figure 12.

predictions for C_2H_6 agree well with experimental results (within less than a factor of 2) and that the rate of production of C_2H_6 slows as the amount of n-C_4H_9OH increases. C_2H_4 concentrations are predicted within a factor of 2 to 3 of the experimental results, as seen on the LHS of Figure 16.

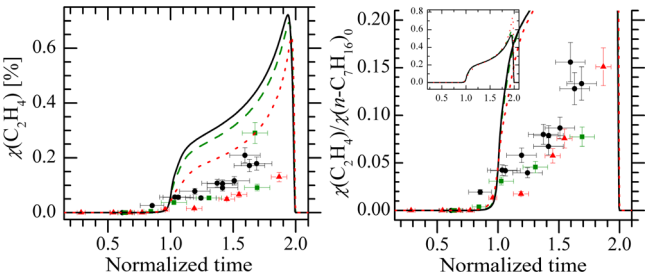

Figure 16. Experimental C_2H_4 time-histories for stoichiometric 100−0, 80−20, and 50−50 blends. Also shown are predictions using the current mechanism. Experimental and simulation conditions and symbol and line details are the same as those in Figure 12.

C_3H_8 predictions shown in Figure 17 are generally in very good agreement with the experimental measurements. While

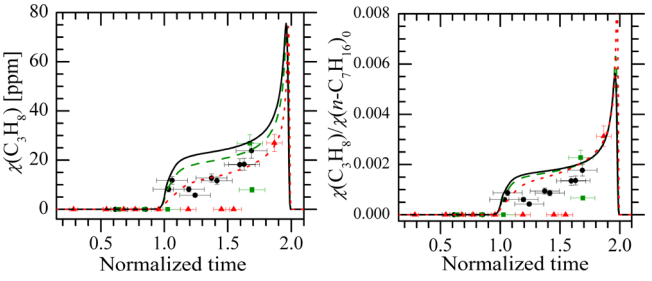

Figure 17. Experimental C_3H_8 time-histories for stoichiometric 100−0, 80−20, and 50−50 blends. Also shown are predictions using the current mechanism. Experimental and simulation conditions and symbol and line details are the same as those in Figure 12.

the model does predict slower formation of C_3H_8 with increasing n-C_4H_9OH, C_3H_8 was not observed in the experiments until much later for the 80−20 and 50−50 cases. The LHS of Figure 18 shows that while n-C_4H_9OH decreases the amount of C_3H_6 predicted on an absolute basis, C_3H_6 concentrations are predicted to increase on a per n-C_7H_{16} basis.

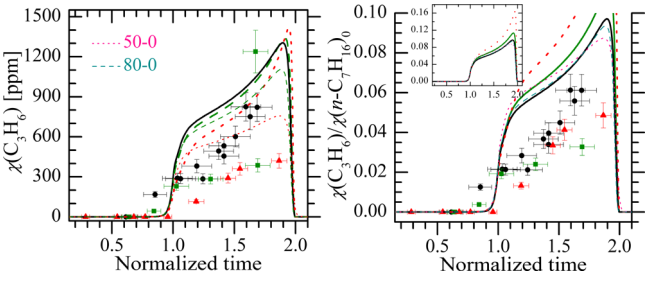

Figure 18. Experimental C_3H_6 time-histories for stoichiometric 100−0, 80−20, and 50−50 blends. Also shown are predictions using the current mechanism, as well as mechanism predictions where the n-C_4H_9OH has been removed from the initial reactant mixture (i.e., 80−20 → 80−0 [thin dashed dark cyan lines] and 50−50 → 50−0 [thin dotted pink lines]). Experimental and simulation conditions and other symbol and line details are the same as those in Figure 12.

dx.doi.org/10.1021/jp309358h | J. Phys. Chem. A XXXX, XXX, XXX−XXX

It is observed experimentally that C_3H_6 concentrations do indeed decrease with the addition of n-C_4H_9OH on an absolute basis, although the normalized experimental data do not show an increase in C_3H_6 relative to the initial amount of n-C_7H_{16}. The influence of n-C_4H_9OH on C_3H_6 is clearer when comparing the 80−20 to the 80−0 predictions and the 50−50 to the 50−0 predictions, also presented in Figure 18. It is seen on the LHS of Figure 18 that n-C_4H_9OH not only slows the formation of C_3H_6 but also slows its consumption, thereby causing an accumulation of C_3H_6. At the same time, the model predicts that C_3H_6 production is enhanced relative to the amount of n-C_7H_{16} in the system.

Figure 19, which shows 1-C_4H_8 measurements and predictions, shows similar trends to C_3H_6. Although there are

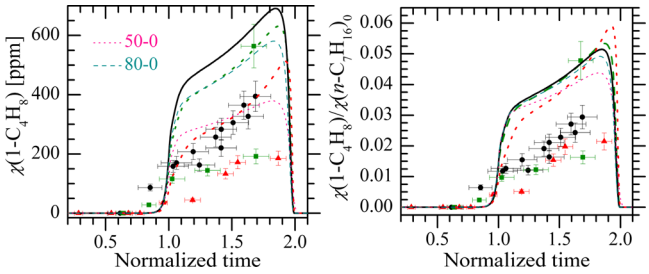

Figure 19. Experimental 1-C_4H_8 time-histories for stoichiometric 100−0, 80−20, and 50−50 blends. Also shown are predictions using the current mechanism, as well as mechanism predictions where the n-C_4H_9OH has been removed from the initial reactant mixture (i.e., 80−20 → 80−0 [thin dashed dark cyan lines] and 50−50 → 50−0 [thin dotted pink lines]). Experimental and simulation conditions and other symbol and line details are the same as those in Figure 12.

larger differences between the experimental and modeling results, the data show that production of 1-C_4H_8 on an absolute basis decreases with the addition of n-C_4H_9OH. While it is evident that n-C_7H_{16} is the source of 1-C_4H_8 as seen in Figure 19 on the RHS, the 1-C_4H_8 data do not show an enhancement with the addition of n-C_4H_9OH like C_3H_6 does. (The 0−100 simulation, the ignition results of which are shown in Table 1, shows a maximum concentration of less than 200 ppm of 1-C_4H_8 *right before ignition*, indicating that n-C_4H_9OH contributes very little to 1-C_4H_8 production during the ignition delay period.) The 1,3-C_4H_6 data, seen in Figure 20, are in good agreement with model predictions, and both experimental and modeling results show that the presence of n-C_4H_9OH suppresses 1,3-C_4H_6 formation.

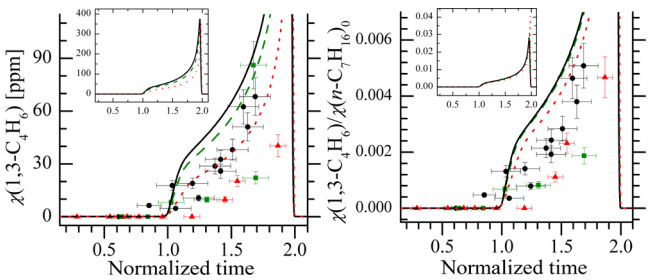

Figure 20. Experimental 1,3-C_4H_6 time-histories for stoichiometric 100−0, 80−20, and 50−50 blends. Also shown are predictions using the current mechanism. Experimental and simulation conditions and symbol and line details are the same as those in Figure 12.

Experimental and computational results for CH_3CHO are presented in Figure 21. As seen on the LHS, while the model

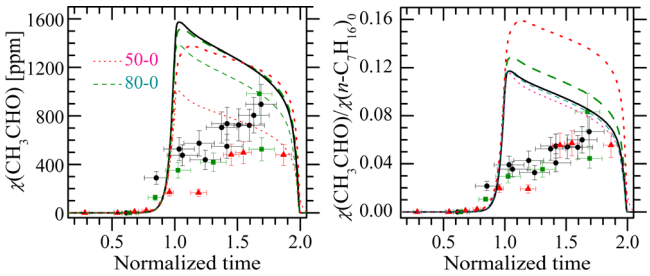

Figure 21. Experimental CH_3CHO time-histories for stoichiometric 100−0, 80−20, and 50−50 blends. Also shown are predictions using the current mechanism, as well as mechanism predictions where the n-C_4H_9OH has been removed from the initial reactant mixture (i.e., 80−20 → 80−0 [thin dashed dark cyan lines] and 50−50 → 50−0 [thin dotted pink lines]). Experimental and simulation conditions and other symbol and line details are the same as those in Figure 12.

predicts very little change in the concentration between the 100−0, 80−20, and 50−50 cases, experimental results point to a decrease in concentrations with increasing blend ratio. By comparison with the 50−0 and 80−0 simulations, the mechanism indicates the decrease in production of CH_3CHO due to decreasing amounts of n-C_7H_{16} offset by increasing CH_3CHO production through n-C_4H_9OH oxidation. The modeling results on the RHS of Figure 21 indicate an enhancement effect for increasing n-C_4H_9OH in the reaction mixture. However, the experimental data indicate that the total amount of carbon in the system dictates the concentration of CH_3CHO and that n-C_4H_9OH does not enhance CH_3CHO production.

It is evident from the experimental results presented in Figure 22 that there is early formation of CH_3OH, prior to the

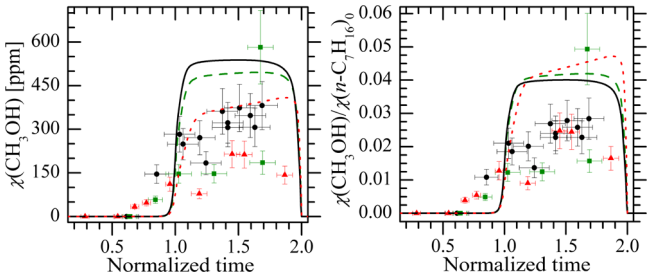

Figure 22. Experimental CH_3OH time-histories for stoichiometric 100−0, 80−20, and 50−50 blends. Also shown are predictions using the current mechanism. Experimental and simulation conditions and symbol and line details are the same as those in Figure 12.

first stage of ignition. The model predicts a decrease in CH_3OH, also seen experimentally, as the n-C_4H_9OH blend ratio increases. Both the experimental data and the model results in the RHS of Figure 22 show that CH_3OH is formed primarily from n-C_7H_{16}.

Although the formation of n-C_3H_7CHO is one of the key decomposition pathways of n-C_4H_9OH,[34] the kinetic model shows that most of its production in these experiments at 700 K comes from the low temperature oxidation of the n-C_7H_{16} via reactions of three different heptyl ketohydroperoxide species and a heptyl-hydroperoxide species. As is seen in Figure 23, n-C_3H_7CHO is formed earlier during the ignition delay period

dx.doi.org/10.1021/jp309358h | J. Phys. Chem. A XXXX, XXX, XXX−XXX

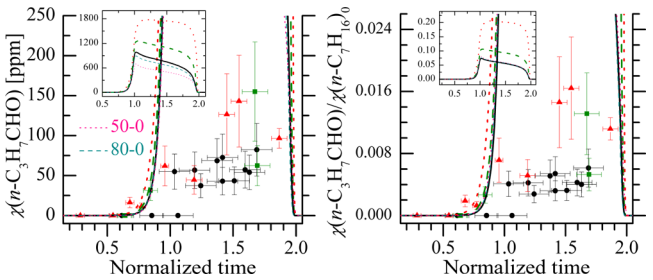

Figure 23. Experimental n-C_3H_7CHO time-histories for stoichiometric 100−0, 80−20, and 50−50 blends. Also shown are predictions using the current mechanism, as well as mechanism predictions where the n-C_4H_9OH has been removed from the initial reactant mixture (i.e., 80−20 → 80−0 [thin dashed dark cyan lines] and 50−50 → 50−0 [thin dotted pink lines]). Experimental and simulation conditions and other symbol and line details are the same as those in Figure 12.

when n-C_4H_9OH is present in the reacting mixture. It is clear, experimentally as well as computationally, that the presence of n-C_4H_9OH increases n-C_3H_7CHO formation, as the 50−0 and 80−0 simulations show that n-C_3H_7CHO concentrations decrease compared to the 50−50 and 80−20 simulations. However, the model overpredicts n-C_3H_7CHO concentrations by an order of magnitude compared to the experimental data and indicates much larger increases in n-C_3H_7CHO with n-C_4H_9OH addition to the mixtures. Relative confidence in the reaction pathways for n-C_4H_9OH[42] and uncertainties in the low temperature n-C_7H_{16} reaction pathways and rates indicate that the current model seriously overpredicts production of n-C_3H_7CHO and that further analysis is needed.

Experimental results presented in Figure 24 show that CO is produced at a slower rate when n-C_4H_9OH is present in the

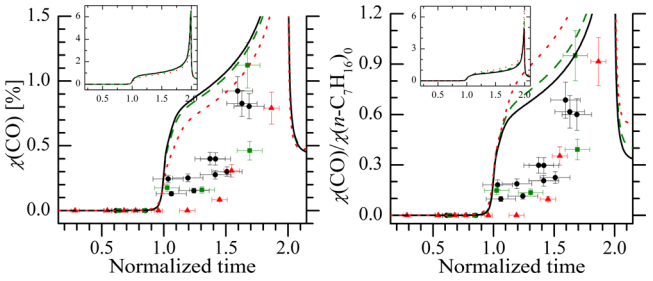

Figure 24. Experimental CO time-histories for stoichiometric 100−0, 80−20, and 50−50 blends. Also shown are predictions using the current mechanism. Experimental and simulation conditions and symbol and line details are the same as those in Figure 12.

mixture. The model predicts a higher rate of production than observed experimentally; however, there is good agreement between the experimental and modeling data at later times during ignition. For CO and other species that are strongly correlated with the initial n-C_7H_{16} present in the mixture, the higher values observed from the model predictions compared to the experimental data are likely a direct result of the higher consumption rate predicted by the model for n-C_7H_{16}. As with n-C_7H_{16} consumption, the model predicts only slight differences in CO as a function of n-C_4H_9OH.

Speciation results of smaller hydrocarbons do not provide a full understanding of how kinetics are changed with fuel blends. Indeed, the size of chemical kinetic mechanisms and the multiple and interrelated production and consumption channels of small hydrocarbons such as CH_4 and C_2H_4 (regardless of parent fuel) make it difficult to understand how mechanisms might be revised to more accurately represent experimental data. However, some intermediate species are only produced by one component of the fuel blend. These species, discussed below, shed light on how branching fractions from the parent fuel change, how global activation energies change, and how particular chemical pathways are enhanced or suppressed.

Figures 25 and 26 show experimental measurements and computational predictions of the two smallest alkenes larger

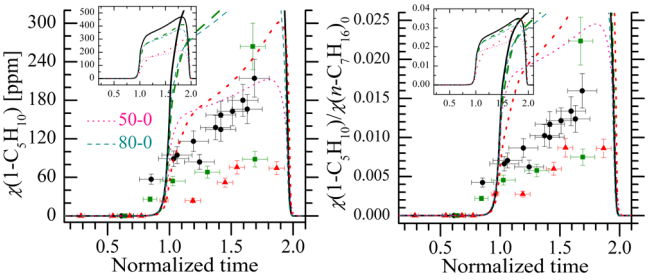

Figure 25. Experimental 1-C_5H_{10} time-histories for stoichiometric 100−0, 80−20, and 50−50 blends. Also shown are predictions using the current mechanism, as well as mechanism predictions where the n-C_4H_9OH has been removed from the initial reactant mixture (i.e., 80−20 → 80−0 [thin dashed dark cyan lines] and 50−50 → 50−0 [thin dotted pink lines]). Experimental and simulation conditions, and other symbol and line details are the same as those in Figure 12.

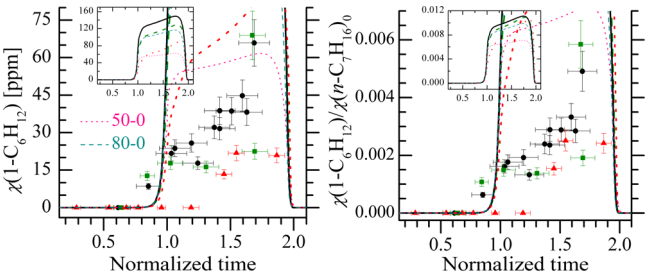

Figure 26. Experimental 1-C_6H_{12} time-histories for stoichiometric 100−0, 80−20, and 50−50 blends. Also shown are predictions using the current mechanism, as well as mechanism predictions where the n-C_4H_9OH has been removed from the initial reactant mixture (i.e., 80−20 → 80−0 [thin dashed dark cyan lines] and 50−50 → 50−0 [thin dotted pink lines]). Experimental and simulation conditions, and other symbol and line details are the same as those in Figure 12.

than are expected to be produced through n-C_4H_9OH oxidation. In Figure 25, 1-C_5H_{10} concentrations decrease when less n-C_7H_6 is present in the fuel mixture, as expected. The model predicts higher 1-C_5H_{10} concentrations than the experimental data by a factor of 2 to three for all cases. As seen in the computational results on the LHS of Figure 25, comparison between the 50−0 and 50−20 simulations and the 80−0 and 80−20 simulations indicates that 1-C_5H_{10} is slightly affected by the n-C_4H_9OH, even though n-C_4H_9OH is not a direct source of 1-C_5H_{10}. The RHS of Figure 25 interestingly highlights that, even though n-C_4H_9OH does not produce 1-C_5H_{10}, it reduces the amount of 1-C_5H_{10} produced from the n-C_7H_{16}. Similar conclusions can be made regarding 1-C_6H_{12}, where the experimental and modeling results are presented in Figure 26.

Figures 27 and 28 present results for two heptene isomers. Since the n-C_7H_{16} consumption rates were much higher than

dx.doi.org/10.1021/jp309358h | J. Phys. Chem. A XXXX, XXX, XXX−XXX

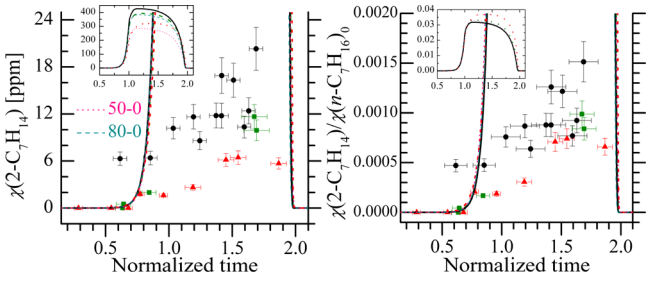

Figure 27. Experimental 2-C_7H_{14} time-histories for stoichiometric 100−0, 80−20, and 50−50 blends. Also shown are predictions using the current mechanism, as well as mechanism predictions where the *n*-C_4H_9OH has been removed from the initial reactant mixture (i.e., 80−20 → 80−0 [thin dashed dark cyan lines] and 50−50 → 50−0 [thin dotted pink lines]). Experimental and simulation conditions and other symbol and line details are the same as those in Figure 12.

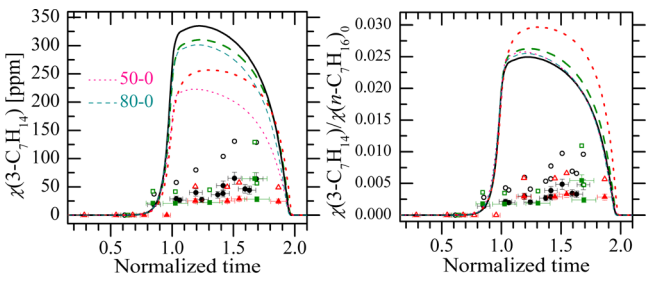

Figure 28. Experimental 3-C_7H_{14} time-histories for stoichiometric 100−0, 80−20, and 50−50 blends. Also shown are predictions using the current mechanism, as well as mechanism predictions where the *n*-C_4H_9OH has been removed from the initial reactant mixture (i.e., 80−20 → 80−0 [thin dashed dark cyan lines] and 50−50 → 50−0 [thin dotted pink lines]). Experimental and simulation conditions and other symbol and line details are the same as those in Figure 12.

observed experimentally, it is not surprising that the modeling results for 2-C_7H_{14} and 3-C_7H_{14} are much higher (20 times higher for 2-C_7H_{14} and a factor of 3 higher for 3-C_7H_{14}) than the experimental data. The experimental data indicate that 2-C_7H_{14} is suppressed by the presence of *n*-C_4H_9OH. Computationally, however, the opposite trends are predicted. Comparison of the 50−0 and 80−0 simulations with their 50−50 and 80−20 counterparts in Figure 27 shows that *n*-C_4H_9OH actually increases the predicted concentrations of 2-C_7H_{14} from *n*-C_7H_{16}. The model thus predicts a change in the branching fractions of *n*-C_7H_{16} decomposition with the addition of *n*-C_4H_9OH.

The experimental data for 3-C_7H_{14} were convolved with additional uncertainties compared to 2-C_7H_{14}. The 3-C_7H_{14} calibration standard was an uncertain mixture of *cis*-3-C_7H_{14} and *trans*-3-C_7H_{14}, and the measured areas of these two isomers were approximately equal in the chromatograms. Consequently, 3-C_7H_{14} was quantified to within a factor of 2. The upper limit of the measurements is thus represented by the open symbols in Figure 28. Predictions for 3-C_7H_{14} are of the same order of magnitude as the 2-C_7H_{14} predictions.

The differences between the experimental results and the computed results for the heptene isomers were sufficiently large that they motivate revisiting and revising the low temperature oxidation of *n*-C_7H_{16}. Specifically, reaction flux analysis showed that two reaction pathways were responsible for production of the C_7H_{14} isomers. These reaction pathways consist of the direct reaction of heptyl radicals with molecular oxygen and the alkylperoxy radical isomerization of heptylperoxy radicals to the $C_7H_{14}OOH$ radical, with the OOH and the radical site adjacent to each other in the $C_7H_{14}OOH$. These reactions are written as

$$C_7H_{15} + O_2 = C_7H_{14} + HO_2 \quad \text{(R4)}$$

$$C_7H_{15}O_2 \rightarrow C_7H_{14}OOH \rightarrow C_7H_{14} + HO_2 \quad \text{(R5)}$$

and our ongoing study[19] focuses on the contributions of these reactions to ignition at low temperature conditions

It is important to note that most large *n*-alkane chemical kinetic mechanisms follow similar general rate rules for fuel consumption and that the present experimental results point out the degree to which corrections to the mechanisms are necessary. The kinetics of the low temperature reactions of large olefin species, heptenes in the present case, have received very little attention in experimental and computational work, and it appears likely that greater reactivity of these olefins would correct the present differences between computed and experimental results. The low temperature chemistry of *n*-C_7H_{16} is the subject of current work, and the results will be reported in a forthcoming paper.[19]

5. CONCLUSIONS

The results of this study inform an important part of our understanding on how biofuel blends affect combustion chemistry and how to develop and validate reaction mechanisms for biofuel blends. New ignition and speciation data have been presented on blends of two important reference fuel compounds, *n*-heptane and *n*-butanol, at practical thermodynamic conditions of 700 K and 9 atm and at two blend ratios. When compared with 100% *n*-heptane ignition results, the experimental data show that *n*-butanol slows the reactivity of *n*-heptane, and several characteristics of the first stage ignition and autoignition time-histories are affected. While there is good agreement between the experimental data and model predictions for some key features of the blend ignition data, the results also highlight the need for a more detailed understanding of some of the *n*-heptane reaction pathways, and new kinetic modeling work on this subject will be reported in the near future.

The speciation data revealed information not identifiable from the ignition data alone, and comparison of the speciation data on absolute and relative scales (i.e., relative to the initial amount of *n*-heptane in the mixtures) provided further insights. The *n*-heptane caused *n*-butanol to react at temperatures where *n*-butanol is not normally reactive. Several smaller hydrocarbons—including species such as methane, ethane, ethane, propane, propene, methanol, and acetaldehyde—which are formed through congruous chemical pathways of the two fuels were not significantly affected by the composition of the fuel blend. The concentrations of smaller species were well correlated with the initial amount of *n*-heptane in the reactant mixture, indicating *n*-butanol suppressed their formation only insomuch as the *n*-butanol displaced *n*-heptane in the fuel blend. However, the speciation data of several larger hydrocarbons indicate significant synergy between the chemistry of the two fuel components. Specifically, the presence of *n*-butanol changed the measured concentrations of the large linear alkenes 1-pentene, 1-hexene, and 2-heptene. This discovery indicates that the presence of *n*-butanol changed the fundamental chemical pathways of *n*-heptane during ignition. More broadly, the suppression of large unsaturated hydrocarbon intermediate formation points toward the soot suppression tendencies of *n*-

dx.doi.org/10.1021/jp309358h | J. Phys. Chem. A XXXX, XXX, XXX−XXX

butanol, where soot has significant global warming potential. From an engine design standpoint, the measurably slower reactivity of blends as compared to pure large *n*-alkanes, which tend to drive the reactivity of complex fuel mixtures such as kerosene, directs changes in practical engine design; for example, jet engines used in aviation might require longer combustor lengths or increased pressure ratios. The conclusions of this study thus critically inform the broader discussions of alternative fuels, including engine design and climate change policy.

■ ASSOCIATED CONTENT

Ⓢ Supporting Information

Tables of experimental data. This material is available free of charge via the Internet at http://pubs.acs.org.

■ AUTHOR INFORMATION

Corresponding Author

*Tel: 734-763-7470. Fax: 734-647-3170. E-mail: dippind@umich.edu.

Notes

The authors declare no competing financial interest.

■ ACKNOWLEDGMENTS

We would like to thank the U.S. Department of Energy Basic Energy Sciences, the U.S. Department of Energy via the University of Michigan Consortium on Efficient and Clean High-Pressure, Lean Burn (HPLB) Engines, the Michigan Memorial Phoenix Energy Institute, and the Graham Environmental Sustainability Institute for their financial support. This work was also supported by the U.S. Department of Energy, Office of Vehicle Technologies, and was performed under the auspices of the U.S. Department of Energy by Lawrence Livermore National Laboratory under contract No. DE-AC52-07NA27344. We would like to thank Dr. William Pitz and Dr. Marco Mehl for their very helpful discussions and insights into the chemical mechanism. We also thank Dr. Henry Curran, Dr. Darren Healy, Dr. John Griffiths, Dr. Guillaume Vanhove, and Dr. Rodolfo Minetti for sharing their experimental data. We would also like to thank the anonymous reviewers for providing helpful comments and suggestions.

■ REFERENCES

(1) Ciezki, H. K.; Adomeit, G. *Combust. Flame* **1993**, *93*, 421−433.
(2) Shen, H.-P. S.; Steinberg, J.; Vanderover, J.; Oehlschlaeger, M. A. *Energy Fuels* **2009**, *23*, 2482−2489.
(3) Herzler, J.; Jerig, L.; Roth, P. *Proc. Combust. Inst.* **2005**, *30*, 1147−1153.
(4) Smith, J. M.; Simmie, J. M.; Curran, H. J. *Int. J. Chem. Kinet.* **2005**, *37*, 728−736.
(5) Davidson, D. F.; Oehlschlaeger, M. A.; Hanson, R. K. *Proc. Combust. Inst.* **2007**, *31*, 321−328.
(6) Akih-Kumgeh, B.; Bergthorson, J. M. *Energy Fuels* **2010**, *24*, 2439−2448.
(7) Davidson, D. F.; Hong, Z.; Pilla, G. L.; Farooq, A.; Cook, R. D.; Hanson, R. K. *Combust. Flame* **2010**, *157*, 1899−1905.
(8) Dagaut, P.; Reuillon, M.; Cathonnet, M. *Combust. Flame* **1995**, *101*, 132−140.
(9) Silke, E. J.; Curran, H. J.; Simmie, J. M. *Proc. Combust. Inst.* **2005**, *30*, 2639−2647.
(10) Tanaka, S.; Ayala, F.; Keck, J. C.; Heywood, J. B. *Combust. Flame* **2003**, *132*, 219−239.
(11) Griffiths, J. F.; Halford-Maw, P. A.; Mohamed, C. *Combust. Flame* **1997**, *111*, 327−337.
(12) Minetti, R.; Carlier, M.; Ribaucour, M.; Therssen, E.; Sochet, L. R. *Combust. Flame* **1995**, *102*, 298−309.
(13) Cox, A.; Griffiths, J. F.; Mohamed, C.; Curran, H. J.; Pit, W. J.; Westbrook, C. K. *Symp. Int. Combust. Proc.* **1996**, *26*, 2685−2692.
(14) Ingemarsson, Å.; Pedersen, J.; Olsson, J. *J. Phys. Chem. A* **1999**, *103*, 8222−8230.
(15) Bakali, A. E.; Delfau, J. L.; Vovelle, C. *Combust. Sci. Technol.* **1998**, *140*, 69−91.
(16) Doute, C.; Delfau, J. L.; Akrich, R.; Vovelle, C. *Combust. Sci. Technol.* **1997**, *124*, 249−276.
(17) D'Anna, A.; Alfe, A.; Apicella, B.; Tregrossi, A.; Ciajolo, A. *Energy Fuels* **2007**, *21*, 2655−2662.
(18) Ji, C.; Dames, E.; Wang, Y. L.; Wang, H.; Egolfopoulos, F. N. *Combust. Flame* **2010**, *157*, 277−287.
(19) Karwat, D. M. A.; Wagnon, S. W.; Wooldridge, M. S.; Westbrook, C. K. Manuscript in preparation.
(20) Mehl, M.; Pitz, W. J.; Westbrook, C. K.; Curran, H. J. *Proc. Combust. Inst.* **2011**, *33*, 193−200.
(21) Curran, H. J.; Gaffuri, P.; Pitz, W. J.; Westbrook, C. K. *Combust. Flame* **1998**, *114*, 149−177.
(22) Côme, G. M.; Warth, V.; Glaude, P. A.; Fournet, R.; Scacchi, G.; Battin-Leclerc, F. *Symp. Int. Combust. Proc.* **1996**, 755−762.
(23) CRECK Modeling Complete Mechanism (Low and High Temperature), version 1201. http://creckmodeling.chem.polimi.it/kinetic.html.
(24) Gu, X.; Huang, Z.; Li, Q.; Tang, C. *Energy Fuels* **2009**, *23*, 4900−4907.
(25) McEnally, C. S.; Pfefferle, L. D. *Proc. Combust. Inst.* **2005**, *30*, 1363−1370.
(26) Veloo, P. S.; Wang, Y. L.; Egolfopoulos, F. N.; Westbrook, C. K. *Combust. Flame* **2010**, *157*, 1989−2004.
(27) Oßwald, P.; Güdenberg, H.; Kohse-Höinghaus, K.; Yang, B.; Yuan, T.; Qi, F. *Combust. Flame* **2011**, *158*, 2−15.
(28) Grana, R.; Frassoldati, A.; Faravelli, T.; Niemann, U.; Ranzi, E.; Seiser, R.; Cattolica, R.; Seshadri, K. *Combust. Flame* **2010**, *157*, 2137−2154.
(29) Moss, J. T.; Berkowitz, A. M.; Oehlschlaeger, M. A.; Biet, J.; Warth, V.; Glaude, P.-A.; Battin-Leclerc, F. *J. Phys. Chem. A* **2008**, *112*, 10843−10855.
(30) Liu, W.; Kelley, A. P.; Law, C. K. *Proc. Combust. Inst.* **2011**, *33*, 995−1002.
(31) Heufer, K. A.; Fernandes, R. X.; Olivier, H.; Beeckmann, J.; Roehls, O.; Peters, N. *Proc. Combust. Inst.* **2011**, *33*, 359−366.
(32) Noorani, K. E.; Akih-Kumgeh, B.; Bergthorson, J. M. *Energy Fuels* **2010**, *24*, 5834−5843.
(33) Black, G.; Curran, H. J.; Pichon, S.; Simmie, J. M.; Zhukov, V. *Combust. Flame* **2010**, *157*, 363−373.
(34) Karwat, D. M. A.; Wagnon, S. W.; Teini, P. D.; Wooldridge, M. S. *J. Phys. Chem. A* **2011**, *115*, 4909−21.
(35) Dagaut, P.; Sarathy, S. M.; Thomson, M. J. *Proc. Combust. Inst.* **2009**, *32*, 229−237.
(36) Harper, M. R.; Van Geem, K. M.; Pyl, S. P.; Marin, G. B.; Green, W. H. *Combust. Flame* **2011**, *158*, 16−41.
(37) Barnard, J. A. *Trans. Faraday Soc.* **1957**, *53*, 1423−1430.
(38) Vasu, S. S.; Davidson, D. F.; Hanson, R. K.; Golden, D. M. *Chem. Phys. Lett.* **2010**, *497*, 26−29.
(39) Zhou, C.-W.; Simmie, J. M.; Curran, H. J. *Combust. Flame* **2011**, *158*, 726−731.
(40) Sarathy, S. M.; Thomson, M. J.; Togbé, C.; Dagaut, P.; Halter, F.; Mounaim-Rousselle, C. *Combust. Flame* **2009**, *156*, 852−864.
(41) Yang, B.; Oßwald, P.; Li, Y.; Wang, J.; Wei, L.; Tian, Z.; Qi, F.; Kohse-Höinghaus, K. *Combust. Flame* **2007**, *148*, 198−209.
(42) Sarathy, S. M.; Vranckx, S.; Yasunaga, K.; Mehl, M.; Oßwald, P.; Metcalfe, W. K.; Westbrook, C. K.; Pitz, W. J.; Kohse-Höinghaus, K.; Fernandes, R. X.; et al. *Combust. Flame* **2012**, *159*, 2028−2055.
(43) Saisirirat, P.; Togbé, C.; Chanchaona, S.; Foucher, F.; Mounaim-Rousselle, C.; Dagaut, P. *Proc. Combust. Inst.* **2011**, *33*, 3007−3014.
(44) Dagaut, P.; Togbé, C. *Energy Fuels* **2009**, *23*, 3527−3535.
(45) Dagaut, P.; Togbé, C. *Fuel* **2010**, *89*, 280−286.

(46) He, X.; Donovan, M. T.; Zigler, B. T.; Palmer, T. R.; Walton, S. M.; Wooldridge, M. S.; Atreya, A. *Combust. Flame* **2005**, *142*, 266−275.
(47) Walton, S. M.; He, X.; Zigler, B. T.; Wooldridge, M. S.; Atreya, A. *Combust. Flame* **2007**, *150*, 246−262.
(48) Walton, S. M.; He, X.; Zigler, B. T.; Wooldridge, M. S. *Proc. Combust. Inst.* **2007**, *31*, 3147−3154.
(49) Walton, S. M.; Wooldridge, M. S.; Westbrook, C. K. *Proc. Combust. Inst.* **2009**, *32*, 255−262.
(50) Teini, P. D.; Karwat, D. M. A.; Atreya, A. *Combust. Flame* **2011**, *158*, 2045−2055.
(51) Teini, P. D.; Karwat, D. M. A.; Atreya, A. *Combust. Flame* **2012**, *159*, 1090−1099.
(52) He, X.; Zigler, B. T.; Walton, S. M.; Wooldridge, M. S.; Atreya, A. *Combust. Flame* **2006**, *145*, 552−570.
(53) He, X.; Walton, S. M.; Zigler, B. T.; Wooldridge, M. S.; Atreya, A. *Int. J. Chem. Kinet.* **2007**, *39*, 498−517.
(54) Walton, S. M.; Karwat, D. M.; Teini, P. D.; Gorny, A.; Wooldridge, M. S. *Fuel* **2011**, *90*, 1796−1804.
(55) *CHEMKIN*, release 10101 (x64); Reaction Design: San Diego, CA , 2010.
(56) Metcalfe, W. K.; Burke, S. M.; Aul, C. J.; Petersen, E. L.; Curran, H. J. *Proc. Eur. Combust. Meet.* **2011**.
(57) Westbrook, C. K.; Pitz, W. J.; Mehl, M.; Curran, H. J. *Proc. Combust. Inst.* **2011**, *33*, 185−192.
(58) McBride, B. J.; Gordon, S.; Reno, M. A. *Coefficients for Calculating Thermodynamic and Transport Properties of Individual Species*; NASA Technical Memorandum 4513, 1993.
(59) Westbrook, C. K. *Proc. Combust. Inst.* **2000**, *28*, 1563−1577.
(60) Vanhove, G.; Petit, G.; Minetti, R. *Combust. Flame* **2006**, *145*, 521−532.
(61) Westbrook, C. K. *Combust. Sci. Technol.* **1979**, *20*, 5−17.

Combustion and Flame 160 (2013) 2693–2706

Contents lists available at ScienceDirect

Combustion and Flame

journal homepage: www.elsevier.com/locate/combustflame

Low-temperature speciation and chemical kinetic studies of *n*-heptane

Darshan M.A. Karwat [a,*], Scott W. Wagnon [a], Margaret S. Wooldridge [b,a], Charles K. Westbrook [c]

[a] Department of Mechanical Engineering, University of Michigan, Ann Arbor, MI 48109, USA
[b] Department of Aerospace Engineering, University of Michigan, Ann Arbor, MI 48109, USA
[c] Lawrence Livermore National Laboratory, Livermore, CA 94550, USA

ARTICLE INFO

Article history:
Received 6 March 2013
Received in revised form 30 June 2013
Accepted 30 June 2013
Available online 7 August 2013

Keywords:
n-Heptane
Ignition delay
Chemical kinetics
Speciation
Rapid compression facility

ABSTRACT

Although there have been many ignition studies of *n*-heptane—a primary reference fuel—few studies have provided detailed insights into the low-temperature chemistry of *n*-heptane through direct measurements of intermediate species formed during ignition. Such measurements provide understanding of reaction pathways that form toxic air pollutants and greenhouse gas emissions while also providing key metrics essential to the development of chemical kinetic mechanisms. This paper presents new ignition and speciation data taken at high pressure (9 atm), low temperatures (660–710 K), and a dilution of inert gases-to-molecular oxygen of 5.64 (mole basis). The detailed time-histories of 17 species, including large alkenes, aldehydes, carbon monoxide, and *n*-heptane were quantified using gas chromatography. A detailed chemical kinetic mechanism developed previously for oxidation of *n*-heptane reproduced experimentally observed ignition delay times reasonably well, but predicted levels of some important intermediate chemical species that were significantly different from measured values. Results from recent theoretical studies of low temperature hydrocarbon oxidation reaction rates were used to upgrade the chemical kinetic mechanism for *n*-heptane, leading to much better agreement between experimental and computed intermediate species concentrations. The implications of these results to many other hydrocarbon fuel oxidation mechanisms in the literature are discussed.

1. Introduction

n-Heptane (*n*-C_7H_{16}) is an important reference compound used to study the chemical kinetics of large *n*-alkanes, which are significant fractions of complex commercial fuels such as gasoline, kerosene, and diesel fuel. The size and structure of *n*-C_7H_{16} lead to chemical kinetic features that distinguish long-chain *n*-alkanes such as *n*-C_7H_{16} from other hydrocarbons, and in particular the strong negative-temperature coefficient (NTC) behavior of long-chain *n*-alkanes. As a component of primary reference fuels, *n*-C_7H_{16} has been studied extensively in shock tubes [1–7], jet-stirred reactors [8,9], rapid compression machines (RCMs) [10–14], premixed laminar flames [15–19], and flow reactors [20]. There have been a smaller number of studies [8,9,13,15,17,20] in which the products of *n*-C_7H_{16} oxidation—intermediate and final—have been measured experimentally. The level of detail observed and measured in experimental studies of *n*-C_7H_{16} combustion and the kinetic complexity in the chemical kinetic reaction mechanisms used to interpret those experiments have grown steadily over the past 20 years. More detailed experiments have motivated better kinetic models and vice versa; recent advances in theoretical chemistry capabilities, such as the *ab initio* studies described later, have also been important.

Nearly 20 years ago, Dagaut et al. [8] studied the oxidation of diluted stoichiometric *n*-C_7H_{16} mixtures in a jet-stirred reactor at residence times between 0.1 and 2 s, between pressures of 1–40 atm, temperatures of 550–1150 K, and an inert/O_2 ratio between 90 and 180 (mole basis). Using gas chromatography and mass spectrometry, the authors were able to measure 44 different chemical species. They noted that increasing the pressure from 10 to 40 atm increased CO and CO_2 formation, while cyclic ethers such as cis-2-methyl-5-ethyltetrahydrofuran became more prevalent at higher temperatures as the pressure increased. The shift in cyclic ether production was attributed to QOOH formation, which increases with increasing pressure.

Herbinet et al. [9] very recently studied *n*-C_7H_{16} oxidation in a jet-stirred reactor, focusing on reactions in the low-temperature regime from 500 to 1100 K and measuring concentrations of species important in that temperature range, including cyclic ethers, alkenes, species with two carbonyl groups and ketohydroperoxides. They used a kinetic model to interpret their measurements, with generally good comparisons between computed and experimental results.

* Corresponding author. Address: Department of Mechanical Engineering, University of Michigan, 2350 Hayward St., Ann Arbor, MI 48109-2125, USA. Fax: +1 734 647 3170.
E-mail address: dippind@umich.edu (D.M.A. Karwat).

0010-2180/$ - see front matter © 2013 The Combustion Institute. Published by Elsevier Inc. All rights reserved.
http://dx.doi.org/10.1016/j.combustflame.2013.06.029

While they did not measure product compositions, one intention of the Cox et al. [14] study was to explore the extent of reaction of n-C_7H_{16} during compression in an RCM. The authors used gas chromatography to measure the amount of n-C_7H_{16} that reacted during the 22 ms stroke of their RCM as a function of temperature. They supplemented these data with chemiluminescence measurements of the first stage of ignition and found significant amounts of fuel consumption during the compression stroke when the targeted top-dead center (TDC) temperature exceeded 800 K.

In another study carried out nearly 20 years ago, Minetti et al. [13] sampled stoichiometric n-C_7H_{16} mixtures with a dilution of inert gases-to-O_2 of 3.76 at a temperature of 667 K and a pressure of 3.4 bar, i.e., $\chi(n\text{-}C_7H_{16}) = 0.0187$, $\chi(O_2) = 0.2061$, $\chi(N_2) = 0.7$, and $\chi(CO_2) = 0.0752$. Using gas chromatography/mass spectrometry, they identified 36 distinct compounds formed during an ignition delay time of 41 ms, with the first stage of ignition occurring 30 ms after top dead center in their RCM. They compared their experimental data with model predictions based on an early chemical mechanism by Warnatz [21]. The model adequately reproduced ignition delay times, but did not perform well at predicting the time-histories of many of the intermediate species. The mechanism predicted significant consumption of n-C_7H_{16} at the first stage of ignition (80%), while experimental measurements were closer to 20%. Minetti et al. [13] concluded that a great deal more mechanism development was needed before reliable species predictions would be possible.

Finally, Ingemarsson et al. [15], Doute et al. [17] and Held et al. [20] measured intermediate species levels in laminar flames and turbulent flow reactors, but these studies concerned high and intermediate temperature oxidation conditions where low temperature reaction pathways could be ignored.

There have been numerous chemical kinetic mechanisms developed to describe chemical kinetics of n-C_7H_{16} oxidation, a few of which are described below. Some early chemistry models were developed [22,23] to address temperatures above the NTC regime, and descriptions of low-temperature chemistry were added later. The mechanism developed by Curran et al. [24] included 25 reaction classes involving n-C_7H_{16} as fuel and its immediate reaction products, as well as an extensive low-temperature kinetic submechanism. Côme et al. [22] used a computer package to generate detailed and semi-detailed high- and low-temperature chemical kinetic mechanisms for n-C_7H_{16}. More recent kinetic mechanisms, including n-C_7H_{16} oxidation at high and low temperatures, have been developed [25,26] with considerable attention to alkylperoxy radical isomerization reactions that led to the recent study of Herbinet et al. [9]. A mechanism developed at Politechnico di Milano [27] includes low-temperature chemistry, building on a previous mechanism [23], and contains more than 13,000 reactions and 400 chemical species to describe the kinetics of alkanes with up to sixteen carbon atoms. In order to study gasoline surrogate mixtures, Mehl et al. [28] updated the Curran et al. [24] mechanism by incorporating improved kinetic rates for linear alkenes.

Minetti et al. [13] remains the only study to date with extensive sampling of the intermediates of n-C_7H_{16} consumption in an RCM. Given the importance of n-C_7H_{16} as a reference compound for the combustion chemistry of long-chain n-alkanes, the present work builds on these previous experimental and kinetic modeling studies by presenting new measurements and analysis of intermediate species formed during the ignition delay of n-C_7H_{16} at high pressure and low temperatures. In the present study, an upgraded chemical kinetic model based on past work but incorporating the results of recent theoretical *ab initio* studies is used to simulate the new experimental data and test the predictive capabilities of the model.

Given the increasing interest in utilizing low-temperature heat release of fuels and bio-based fuels in advanced engine strategies such as homogeneous charge compression ignition, this project provides a new set of baseline experiments and kinetic modeling results for n-C_7H_{16} that can be used to study combustion of mixtures of n-C_7H_{16} and selected alcohol fuel species. The idea is to develop some kinetic understanding of fuel behavior in internal combustion engines when a biofuel (e.g., n-butanol) is blended with conventional petrochemical fuels such as gasoline, diesel fuel or jet fuel, for which n-C_7H_{16} can be used as a surrogate component [29].

2. Experimental setup

2.1. The University of Michigan Rapid Compression Facility

As a unique and powerful apparatus for studying fuel chemistry over a broad range of thermodynamic conditions, the University of Michigan Rapid Compression Facility (UM RCF) has been used to study ignition of reference hydrocarbon fuel compounds such as *iso*-octane [30,31], simulated syngas mixtures of hydrogen and carbon monoxide [32], and oxygenated hydrocarbons [33], as well as soot formation and morphology [34,35]. The UM RCF has been applied to obtain time-resolved measurements of hydroxyl radical formation during *iso*-octane/air ignition [36], and quantitative measurements of the intermediate species of *iso*-octane [37], methyl butanoate [38], and *n*-butanol [39] oxidation using gas chromatography and rapid gas sampling.

The UM RCF is a chemical reactor that uses a free-piston/cylinder compression process to create the thermodynamic conditions necessary for combustion chemical kinetic studies, the features of which are interrogated using the optical and physical access provided by the test section of the facility. The five major components of the UM RCF, seen in the top panel of Fig. 1, are the driver section (with an inner diameter of 154 mm), the driven section (2.74 m long, 101.2 mm inner diameter), the test section (or test manifold), the sabot (a free piston with a tapered nosecone) and the fast-acting hydraulic globe valve (with a typical cycle time of 100 ms) system. Experiments begin with delivering a pre-prepared fuel/oxidizer/diluent mixture into the evacuated driven section, with the sabot located at the upstream end of the driven section. High-pressure gas in the driver section is released by the globe valve and launches the sabot down the length of the driven section, compressing the test gas mixture. At the end of compression (EOC), the nose cone of the sabot seals the fuel/oxidizer/diluent mixture in the test section, through an interference fit, at specifically targeted EOC temperatures and pressures. The thermodynamic conditions are achieved by varying the compression ratio of the test section, as well as the composition of gases in the test mixture. The majority of the temperature rise (~50%) and pressure rise (~80%) occur during the last 10 ms of the 145 ms compression stroke. After EOC, the fuel/oxidizer/diluent mixture in the test section autoignites after a period of time that is designated the ignition delay time (τ_{ign}), which is a function primarily of the test gas mixture composition, temperature and pressure.

The UM RCF is designed to create nominally uniform conditions at EOC to isolate reaction chemistry during the experiments and to minimize interfering effects. Two important features of the UM RCF—the geometry of the convergent section and the sabot—are critical to isolating reaction chemistry from the effects of fluid mechanics and heat transfer. Specifically, the unique shapes of the sabot and the convergent section allow the nearly isentropic compression of the gases in the center or core region of the driven section into the test section, while the cold boundary layer that is shed during the compression process is sealed from the core gases,

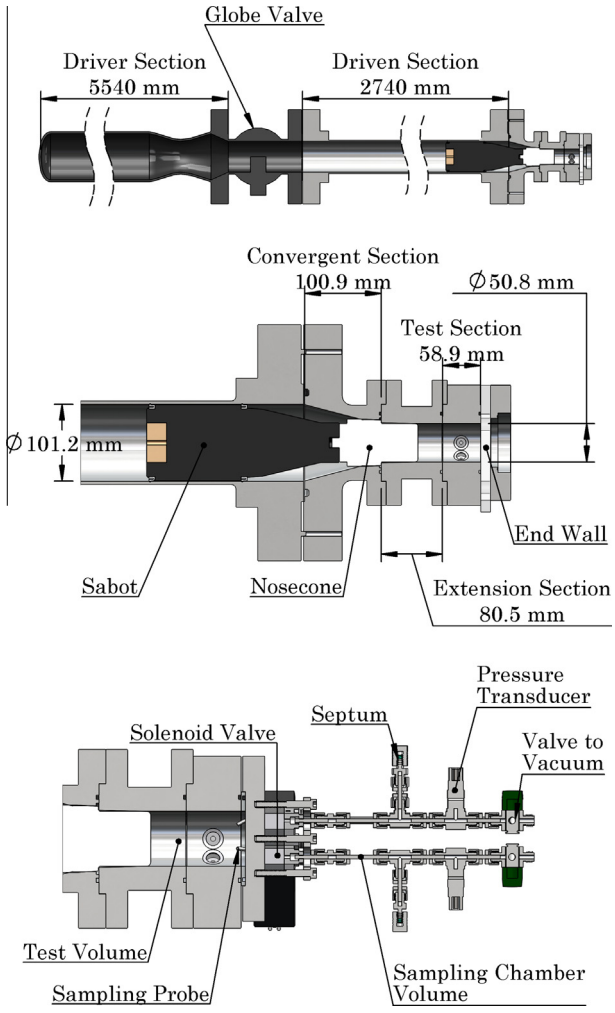

Fig. 1. Shown are a representation of the UM RCF with key dimensions (top panel), the configuration of the RCF test section for end-view imaging (middle panel), and the configuration of the RCF test section for high-speed gas sampling (bottom panel).

remaining trapped outside the test section in the space between the sabot and the convergent section. Heat losses from the gases in the core region are thus minimized, maximizing the amount of time the test gases are at uniform state conditions. Characterization studies of the UM RCF show the difference in measured and predicted isentropic conditions in the core region of the test section are less than 5% and the isentropic core region extends across 70% of the diameter of the test section [40]. These characteristics allow long test times (on the order of 50 ms, depending on test gas mixtures) during which pressure and temperature conditions remain at >75% and >80% of their EOC values, respectively [40].

For this study, stoichiometric n-C_7H_{16}/O_2 mixtures, with an inert/O_2 diluent ratio of 5.64 (mole basis), were prepared manometrically in a magnetically-stirred mixing tank external to the UM RCF using a mixing manifold (n-C_7H_{16}—Sigma–Aldrich, puriss. p.a., ⩾99.5%, GC grade; O_2—Cryogenic Cryogenic Gases, Purity Plus 4.3, 99.993%, <40 ppm Ar, <3 ppm moisture, <10 ppm N_2, <0.5 ppm hydrocarbons; inert diluents: CO_2—Cryogenic Gases, Laser Grade, 99.995%, <1 ppm of O_2, moisture and hydrocarbons, <0.2 ppm CO; and N_2—Cryogenic Gases, Purity Plus 5.0, 99.999%, <2 ppm O_2, <3 ppm moisture, <0.5 ppm hydrocarbons). Mixture compositions were determined using partial pressures measured with a capacitance diaphragm gauge (Varian CeramiCel VCMT12TFA, with an accuracy of ±0.01 torr). The partial pressure of n-C_7H_{16} was maintained well below its saturation vapor pressure at room temperature (0.059 atm or 45 torr at 25 °C) in order to avoid concerns of fuel condensation. Total mixture pressures in the mixing tank were 0.5–0.8 atm, with initial fill pressures (P_0) in the RCF of approximately 0.13 atm.

The pressure in the test section is monitored using a piezoelectric transducer (Kistler 6041AX4) and charge amplifier (Kistler 5010B) with a combined accuracy of 0.01 atm and 0.015 ms. All electronic signals were recorded at 100 kHz (National Instruments cDAQ 9172 chassis coupled with National Instruments 9215 cards). For ignition experiments, a transparent end wall (configuration seen in the middle panel of Fig. 1) coupled with a high-speed camera with a widescreen CMOS array (Vision Research Phantom v711, maximum resolution of 1280 × 800 pixels, capable of 1.4 million frames per second at reduced resolution, 20 μm pixels with 0.34 μm spacing) and a fast 50 mm lens (f/0.95, Navitar) and c-mount extension tube recorded the ignition events in the test section by viewing along the axis of the test section. Imaging data provide qualitative and quantitative indications of the ignition homogeneity. Imaging data were acquired at 30,000 frames per second (fps) at a spatial resolution of 256 × 256 pixels, with an image exposure time of 34 μs.

2.2. High-speed gas sampling and gas chromatography

For gas sampling, the transparent end wall is replaced with an endwall equipped with a high-speed gas sampling system (shown in the bottom panel of Fig. 1). The gas sampling system removes a very small portion (quantified below) of the test gas mixture at targeted times during the ignition delay period. The samples are then analyzed using gas chromatographic techniques to identify and quantify the intermediate species present in sample. A series of samples acquired from experiments conducted at the same targeted EOC conditions allows a compilation of overall species time-histories for the intermediates identified. Several previous studies, including fuels such as *iso*-octane [37], methyl butanoate [38], and *n*-butanol [39] have demonstrated the validity of this experimental technique.

The sampling system used for these experiments consisted of sample chambers (∼4.5 ± 0.5 mL) equipped with piezoresistive pressure transducers (Kistler 4045A2), charge amplifiers (Kistler 4618A0), low-bleed septa (VICI Valco), fast-acting sampling valves (modified Festo MHE3 valves with a stock response time of 3 ms, 3 mm orifice), and vacuum isolation valves (Swagelok). Independent control of each sampling valve using two digital delay/pulse generators (Stanford Research Systems Model DG535) allows the collection of up to four samples per experiment. The four samples are acquired through probes located on a square spacing (26 × 26 mm) on the end wall, 19 mm (radially) from the center of the test section. (Recall the test section inner diameter is 50.8 mm.) For the sampling data presented here, one gas sample was collected in each experiment by triggering the fast-acting valve located at the northeast position of the sampling end wall. Significant care was taken to ensure that the samples were taken from the volume of the test section well beyond the cold thermal boundary layer of the test section end wall; specifically, the sampling tips extend 1.2 cm into the core volume of the test section, whereas the boundary layer thickness is approximately 0.3 cm (see Fig. 2 described below). During the sampling event, the reacting gases removed from the test section gases are quenched in less than 0.3 ms as they expand into the vacuum of the sample chamber ($P_{\text{test section}}/P_{\text{sample chamber}} \sim 11$, $V_{\text{test section}}/V_{\text{sample chamber}} \sim 39$). Once the samples are acquired, the gases are drawn into a syringe (Hamilton Gastight #1010, 10 mL) through the syringe port on the sampling chamber for delivery to the gas chromatographs. As will

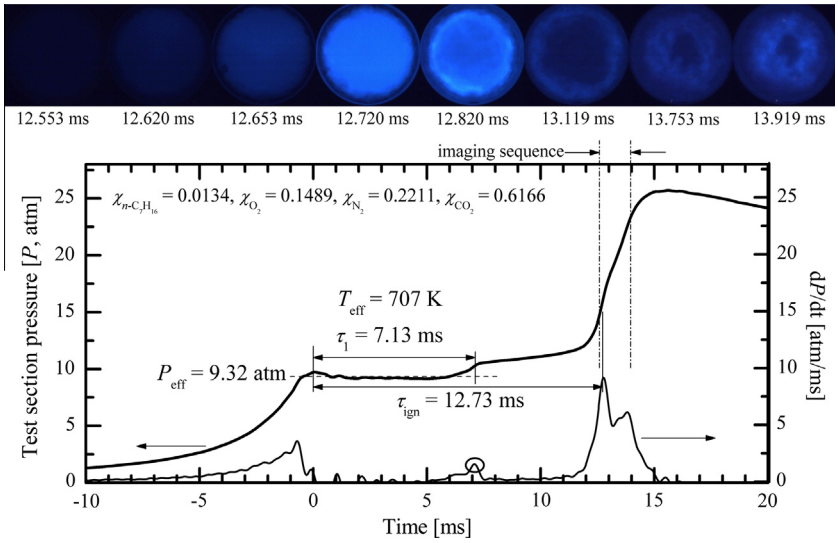

Fig. 2. Results from a typical UM RCF n-C_7H_{16} ignition experiment. The lower panel depicts the pressure time-history in the test section, along with the rate of pressure rise, which allows definition of τ_{ign} and the effective pressure and temperature conditions. The upper panel shows still images taken at 30,000 fps via end-view imaging. Note the homogeneity of the ignition event. The color of the images has been adjusted for clarity. (For interpretation of the references to color in this figure legend, the reader is referred to the web version of this article.)

be shown later, the sampling of very small volumes of test gases leaves the reactive mixture in the test section unaffected. The τ_{ign} values determined from the gas-sampling experiments were in excellent agreement with experiments where gas sampling was not used. Further details on the gas sampling system can be found in Karwat et al. [39].

The dilution of the sample by unreacted gases trapped in the "dead" volume of the sampling system of the sampling probe (±16%, as determined previously [39]), along with the gas chromatography calibration uncertainties for each species, are the chief contributors to the uncertainty of the gas sampling measurements. For the data presented in this paper, the temporal uncertainties resulting from the triggering of the fast-acting sampling valves were the same as described previously [39]—the uncertainty in the sampling time is ±0.75 ms centered on the falling edge of the sampling pulse sent to the fast-acting valves. The gas-sampling results therefore represent the average values of the species during the sampling time.

Three gas chromatographs (GCs) equipped with four different columns, with each connected to a separate detector (either a flame ionization detector, FID, or a thermal conductivity detector, TCD), were calibrated for quantitative measurements of species of interest. A temperature-controlled 10-port gas sampling valve injected the samples into the columns in the GCs. Ultra high purity helium (Cryogenic Gases, Purity Plus, 99.999%) was the carrier gas for all of the GCs. Each of the FIDs used a hydrogen/air flame, were maintained at 300 °C, and were set with a range and attenuation of 1. The TCD was maintained at 100 °C with an attenuation of 1 and current of ±160 mA. The helium, air, and hydrogen were further purified before use in the GCs using adsorbents to remove water, hydrocarbons, and oxygen. High-purity reference chemicals, either gaseous or vapors of liquid, were used to develop the GC temperature programs applied in the study and to calibrate the targeted intermediate species. (Details on purity levels of reference chemicals are provided in Table S1.) Calibration mixtures were made in the magnetically-stirred mixing tank. Upper limits to the calibrations for all species except n-C_7H_{16} were established using the maximum concentrations predicted by the reaction mechanism discussed below during the ignition delay period of a mixture with $\chi(n\text{-}C_7H_{16}) = 0.0135$, $\chi(O_2) = 0.1486$, $\chi(N_2) = 0.2179$, and $\chi(CO_2) = 0.62$ at $P = 9$ atm and $T = 700$ K, and the maximum amount of carbon in the system. Calibration curves were linear in all cases. Voltage signals from the GC detectors were recorded using a data acquisition system with a sampling rate of 8 Hz (NI

Table 1
Experimental details of the gas chromatography systems used in the current work.

GC	System	Column(s)	Detector(s)	Temperature profile	Species detected
1	Perkin Elmer Autosystem	Varian CP-PoraBOND Q 25 m × 0.53 mm × 0.7 μm	Flame ionization detector (FID)	30 °C (4.5 min) → 45 °C/min → 110 °C (9 min) → 45 °C/min → 150 °C (20 min)	n-C_7H_{16}, methanol (CH_3OH), acetaldehyde (CH_3CHO), propionaldehyde (C_2H_5CHO)
2	Perkin Elmer Autosystem	Varian CP-Al_2O_3/Na_2SO_4 25 m × 0.53 mm × 0.7 μm	FID	30 °C for 4 min → 25 °C/min → 150 °C for 7 min → 45 °C/min → 200 °C for 2 min	Methane (CH_4), ethane (C_2H_6), ethene (C_2H_4), ethyne (C_2H_2), propane (C_3H_8), propene (C_3H_6), 1-butene (1-C_4H_8), 1-pentene (1-C_5H_{10}), 1-hexene (1-C_6H_{12}), 1,3-butadiene (1,3-C_4H_6), 3-heptene (3-C_7H_{14})
3	Perkin Elmer Clarus 500	Agilent DB-Wax 30 m × 0.25 mm × 0.25 μm	FID	25 °C for 5 min → 45 °C/min → 200 °C for 5 min	2-Heptene (2-C_7H_{14}), n-butyraldehyde (n-C_3H_7CHO)
		Restek ShinCarbon ST packed 2 m × 1 mm	Thermal conductivity detector (TCD)	25 °C for 5 min → 45 °C/min → 200 °C for 5 min	Carbon monoxide (CO)

PXI 4472). Table 1 provides details about the temperature profiles and columns used in the GCs and the species detected.

3. Experimental results and discussion

3.1. Ignition experiments

Experiments with end-view imaging were performed not only to measure the ignition delay time (τ_{ign}) as a function of temperature, but also to identify the appropriate temperature and pressure conditions at which to conduct sampling experiments. Given that each sampling event lasts approximately 1.5 ms, we targeted a τ_{ign} of approximately 15 ms for the sampling experiments. This time would comfortably allow for at least 10 discrete sampling events during the ignition delay period. The dilution in these experiments (inert/O_2 = 5.64 rather than the more commonly used ratio of 3.76 in normal air) was selected to extend the ignition delay period to 15 ms, as discussed further below. For each experiment, the effective test conditions corresponding to a τ_{ign} value are determined based on the pressure time-history, an example of which is seen in Fig. 2. n-C_7H_{16} exhibited two-stage ignition for all of the experimental data presented here. Therefore, a modified method compared to previous studies [38,39] was used to describe the experimental conditions. Eq. (1) was used to determine the effective pressure (P_{eff}), which is the time-integrated average pressure from the maximum pressure (P_{max}) at the EOC to the maximum rate of pressure rise at the *1st stage of ignition* ($dP/dt_{max,\ 1st\ stage}$),

$$P_{eff} = \frac{1}{t_{dP/dt_{max}} - t_{P_{max}}} \int_{t_{P_{max}}}^{t_{dP/dt_{max,1st\ stage}}} P \cdot dt \tag{1}$$

The effective temperature (T_{eff}) for each experiment was determined using P_{eff} and numerical integration of the isentropic relation (Eq. (2)),

$$\int_{T_0}^{T_{eff}} \frac{\gamma}{\gamma - 1} d\ln T = \ln\left(\frac{P_{eff}}{P_0}\right) \tag{2}$$

where P_0 is the initial charge pressure, T_0 is the initial temperature, and γ is the temperature-dependent ratio of the specific heats of the unreacted test gas mixture (determined using the NASA thermodynamic data base [41]). τ_{ign} for each experiment was defined as the time between EOC (t = 0 ms, defined by the first maximum in P) and the maximum rate of pressure rise corresponding to autoignition ($dP/dt_{max,\ 2nd\ stage}$). Ignition experiments were performed in the narrow temperature range of 660–707 K at an effective pressure between 8.92 and 9.53 atm. The lowest EOC temperature was dictated by the compression ratio of the UM RCF in the configuration used, with CO_2 as the sole diluent. The highest EOC temperature was chosen to avoid significant reaction and heat release during compression, thereby avoiding complications in defining the experimental state conditions and the interpretation of the resulting τ_{ign} and gas sampling results. All mixtures used an equivalence ratio of 1 (based on the molar ratio of fuel to O_2) and a dilution of inert/O_2 = 5.62–5.64, with N_2 and CO_2 as the diluents. The n-C_7H_{16} concentration for the experiments was 1.34–1.35%. Table S2 of the Supplemental Information provides a summary of the experimental conditions and results for τ_{ign} for all of the UM RCF data presented.

Figure 2 presents typical results from a UM RCF n-C_7H_{16} ignition experiment in which imaging data were acquired. The lower panel depicts the time-histories of the pressure (P) and rate of pressure rise (dP/dt) in the test section. A fast Fourier transform has been applied to filter high-frequency disturbances greater than 2.5 kHz generated by the impact of the sabot near EOC. A smooth compression process due to the motion of the sabot brings the pressure to the first maximum, and the EOC is set as time t = 0, after which the volume in the test section is constant. The first stage of ignition (τ_1) occurs at 7.13 ms, corresponding to a local maximum in dP/dt (circled at the bottom in Fig. 2), and P_{eff} and T_{eff} are 9.32 atm and 707 K, respectively. After the first stage of ignition, the pressure

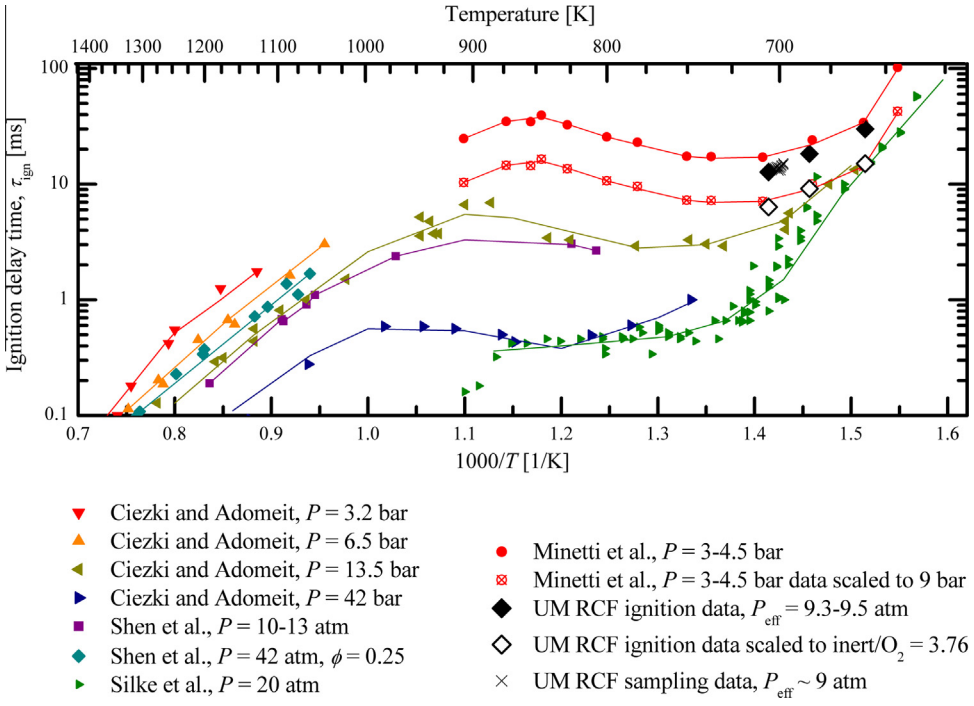

Fig. 3. Ignition characteristics of n-C_7H_{16} over a wide range of temperatures (650–1400 K) and pressures (3–42 atm), including results of the current work. All data with ϕ = 1 unless otherwise noted. UM RCF data with inert/O_2 ~5.64, and all other data with inert/O_2 ~3.76. Shock tube ignition delay data are represented at T_5 corresponding to P_5 in shock tubes, the Minetti et al. [13] RCM ignition data are represented at T_{EOC}, and the data of the current work are represented at T_{eff} corresponding to P_{eff}. Error bars representing the standard deviation of τ_{ign} (0.63 ms) for the UM RCF data are not visible at the resolution used in the plot. Lines represent curve fits to experimental data.

rises again slowly for a while, then more abruptly, to the maximum value corresponding to the autoignition of the test mixture—τ_{ign} = 12.73 ms.

The upper panel of Fig. 2 shows stills from the image sequence of the chemiluminescence that occurs during ignition. This emission is attributed [42] to CH^* ($C_2 + OH \rightarrow CO + CH^*$) and C_2^* ($C + CH \rightarrow C_2^* + H$) radicals, which have strong spectroscopic features in the blue part of the visible spectrum (CH^*: 431.2 nm; C_2^*: 473.7 nm, 516.5 nm, 563.5 nm). The intense blue emission occurs simultaneously throughout the test section with uniform intensity, attesting to the high degree of homogeneity of the reactant mixture and the state conditions in the test section. Such uniformity gives confidence in the application of localized sampling.

Figure 3 presents results of UM RCF ignition and sampling experiments, along with n-C_7H_{16} ignition data from other studies, including RCM studies of Minetti et al. [13] and Silke et al. [10], and shock tube studies of Shen et al. [2] and Ciezki and Adomeit [1]. Data for this plot have been selected to illustrate the influences of pressure, equivalence ratio, and dilution on τ_{ign} and to show that the present RCF experimental results are consistent with previous ignition delay experiments using n-C_7H_{16} as the fuel. As shown in Fig. 3, n-C_7H_{16} ignition exhibits significant NTC behavior between 720 K and 950 K, and the NTC region shifts to higher temperatures as pressure increases. Reasons for this shift are well known; NTC behavior is governed by the ratio of RO_2 to R, and since at higher pressures the concentrations of O_2 are higher, the equilibrium is shifted towards RO_2 formation, consequently moving the NTC region to higher temperatures [43]. The magnitude of the NTC behavior also decreases with increasing pressure, illustrated in Fig. 3 by the Ciezki and Adomeit results at 42 and 13.5 bar pressure [1]. The decrease in NTC behavior with increasing pressure, discussed by Ciezki and Adomeit [1] and by Westbrook et al. [57], can be best attributed to the quadratic increase with pressure of the bimolecular reaction rates, which release most of the energy in the autoignition. This is in contrast to the equilibrium of the $R + O_2 = RO_2$ and $QOOH + O_2 = O_2QOOH$ reactions, reactions that control the NTC behavior and are equilibrated in most of the NTC region, which shift only linearly with increasing pressure.

Also seen in Fig. 3 are data from the ignition delay experiments of Shen et al. [2], which show that at temperatures between approximately 1050 and 1250 K, fuel–lean mixtures take longer to ignite than the stoichiometric mixtures. The authors reported similar behavior for n-decane, n-dodecane and n-tetradecane in addition to n-C_7H_{16}, with lean mixtures igniting more slowly than stoichiometric mixtures, an effect consistent for many hydrocarbon fuels at lower temperatures [1,30,44–46]. The results of Minetti et al. [13] are shown as two curves, the upper one in Fig. 3 showing the results of the experiments actually carried out at pressures from 3 to 4.5 bar, and the lower curve showing the same results scaled to a pressure of 9 bar (using a scaling proportional to P^{-1} following Davidson et al. [58]) in order to compare them with the present experiments, which were conducted at an effective pressure close to 9 bar.

The values measured for τ_{ign} in the current study are shown as the three filled black diamonds in Fig. 3. The rather limited temperature range of these experiments is evident from the figure, but the trend seen in the slope of the three experimental points clearly matches the slope of the Minetti et al. [13] and Ciezki and Adomeit [1] results over the same temperature range. However, the present experimental ignition delay times, measured at an effective pressure of approximately 9 bar, are somewhat longer than the shock tube values of Ciezki and Adomeit [1] at the comparable pressure of 13.5 bar and similarly longer than the RCM results of Minetti et al. [13] when scaled to 9 bar. The differences are attributed to the higher dilution used in the present work. As noted above, the UM RCF data were obtained using an inert/O_2 molar dilution of ~5.64, while the other studies summarized in Fig. 3, as well as the experiments of Griffiths et al. [12], were obtained using an inert/O_2 molar dilution of 3.76, i.e. the N_2/O_2 ratio in normal air. We used the current kinetic mechanism to compare computed ignition delay times for the same reactive mixtures with dilutions of 3.76 and 5.64, indicating a difference of approximately a factor of 0.5, concluding that the higher diluent levels in our experiments produced ignition delay times twice as long as would be observed if the amount of diluent was 3.76, the value of the other experimental studies reported in Fig. 3. Scaling the three UM RCF experimental points in Fig. 3 by this ratio resulted in the open diamond symbols shown in Fig. 3, which are in excellent agreement with the other experiments at comparable conditions.

3.2. High-speed gas sampling experiments

While ignition studies provide a good test of the global kinetics of n-C_7H_{16} ignition, speciation measurements require a more detailed understanding of the important chemical pathways in the reacting test gas mixture and place stricter constraints on the chemical kinetic reaction mechanism used to simulate the experiments. Intermediate species formed during the ignition delay time were measured through gas sampling experiments. Figure 4 shows results from a typical sampling experiment, in which P_{eff} = 9.01 atm, T_{eff} = 700 K, τ_1 = 8.49 ms and τ_{ign} = 14.53 ms, showing the pressure time-history in the test section, the electronic pulse used to trigger the high-speed gas sampling system, and the pressure in the sampling chamber. Since only a very small amount of sample is removed from the reacting mixture in the test section, the pressure in the test section remains unaffected by the sampling process. The pressure features seen in Fig. 4 are thus very similar to those seen in Fig. 2, where no sampling was employed.

Also shown as the dashed curve in Fig. 4 is the time-history of a non-igniting experiment, in which the O_2 of an igniting experiment was replaced with N_2. Given the almost identical thermal characteristics of O_2 and N_2, the mixture compressed in a non-igniting experiment provides a baseline for comparison, including an understanding of the effects of heat transfer during the experiments. As seen in Fig. 4, the pressure time-history of the non-igniting experiment is almost indistinguishable from the igniting experiment (P_{eff} and T_{eff} differ by less 0.1% and 0.3%, respectively) until the first stage of ignition, demonstrating that the heat transfer physics of the experiments remain unaffected by the sampling events. Moreover, because the non-igniting experiment shows a nearly identical compression process to the igniting experiment,

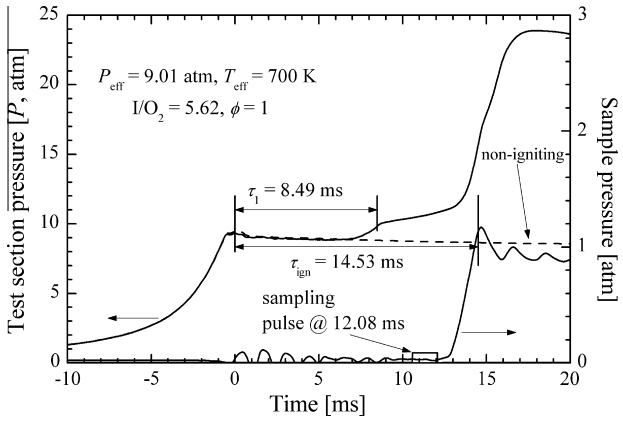

Fig. 4. Typical pressure time-histories from the test section and sampling volume of a gas-sampling experiment. The electronic signal used to trigger the gas sampling event is included for reference. Also included in the figure is the pressure time-history of a non-igniting experiment. See text for details.

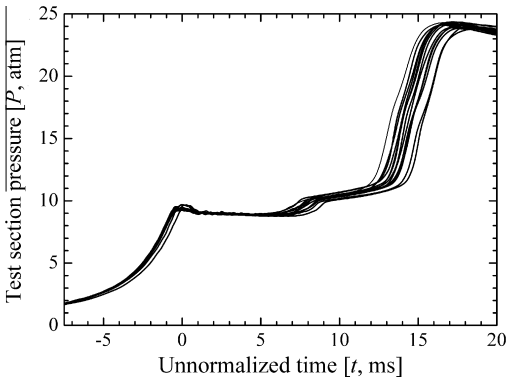

Fig. 5. The experimental pressure time-histories of the thirteen gas-sampling experiments. Although unnormalized, note the level of repeatability of the compression process, as well as the first and second stages of ignition and heat release.

the data support that reaction during compression is not a concern in these experiments.

A summary of the gas-sampling experiments, including mixture compositions, can be found in Table S2 in the Supporting Information. Figure 5 shows the pressure time-histories for the thirteen experiments, all of which show nearly identical, smooth compression processes, and very similar pressure time-histories after EOC. The average P_{eff}, T_{eff}, τ_1, and τ_{ign} for all of the gas-sampling experiments were 9.02 atm, 701 K, 7.94 ms, and 14.09 ms, respectively, with corresponding standard deviations (representing the uncertainty of the data) of 0.07 atm, 1.5 K, 0.52 ms, and 0.63 ms, respectively, which demonstrate the excellent repeatability of the experiments. Furthermore, since gas-sampling and end-view imaging cannot be conducted simultaneously, an experiment to confirm spatial homogeneity of the reacting mixture in the test section was performed by rotating the gas sampling system by 180° and acquiring a sample from the southwest corner of the test section at almost the same time during the ignition delay period as a sample acquired in another experiment from the northeast corner. The data from the rotated gas sampling system were within measurement uncertainties of the baseline (i.e. unrotated) species concentrations.

For comparison with kinetic mechanism predictions, the pressure time-histories and sampling times were converted to normalized times. The period of time between EOC and first stage of ignition of each experiment was normalized by τ_1 (resulting in a normalized time domain of 0 to 1), and the period of time between

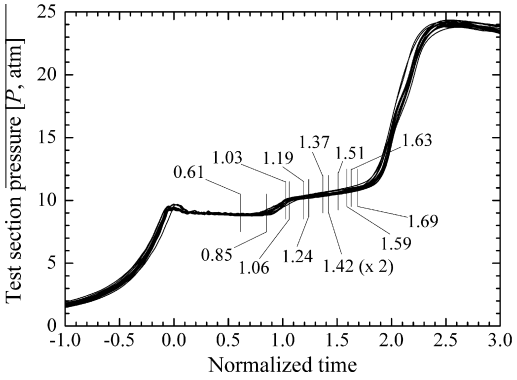

Fig. 6. The normalized experimental pressure time-histories of the thirteen gas-sampling experiments. 0 represents EOC, 1 represents the first stage of ignition, and 2 represents the second stage of ignition. Shown also are the normalized sampling times of each experiment.

the first stage of ignition and autoiginition ($\tau_{ign} - \tau_1$) was normalized by $\tau_{ign} - \tau_1$ and added to the first normalized time domain. The result, seen in Fig. 6, is an overall normalized time domain in which 0 to 1 represents the first stage of ignition, and 1 to 2 represents the second stage of ignition.

Figure 7 presents typical chromatograms obtained from the GCs during a sampling experiment, specifically, the experiment depicted in Fig. 4. All identified species except CO are shown in Fig. 7. C_2H_2 was not observed in any experiment, and some peaks remained unidentified. The carbon balance was 90 ± 12% for sampling at early times during the ignition delay period and 65 ± 9% for sampling closer to autoignition. The peaks identified in the chromatograms were converted into discrete measurements of intermediate species for each normalized sampling time using the calibrations for each species.

Several peaks corresponding to large hydrocarbons and oxygenated compounds remained unidentified in our GC-FID analyses. In particular, we were unable to identify from the GC-FID analysis any large, C_7 oxygenated species such as furans, cyclic ethers, or ketohydroperoxides (chemical standards were difficult to find for many of these species). The Minetti et al. study [13] detailed results of classes of compounds such as furans and oxirane, as well as large ketones. The kinetic model, described below, showed appreciable levels of these species during the later stages of the ignition delay period. For example, just before the onset of the first stage ignition, when the computed n-C_7H_{16} mole fraction had decreased from its initial value of 0.0135 to 0.0059, the model showed a sum of the C_7 cyclic ether mole fractions of about 0.002 and a total of about 0.0005 of C_7 ketohydroperoxides, equal to about 32% of the n-C_7H_{16} consumed at this point. Based on these results, it is likely that much of the carbon missing from the experimental carbon balance is in the form of these large C_7 oxygenated species, whose concentrations increase steadily during the ignition delay period.

Figure 8 presents as symbols (black circles) the UM RCF species measurements during the ignition delay time of n-C_7H_{16} for the average experimental conditions of P_{eff} = 9.02 atm, T_{eff} = 701 K, $\chi(n\text{-}C_7H_{16})$ = 0.0134, $\chi(O_2)$ = 0.149, $\chi(N_2)$ = 0.2336, and $\chi(CO_2)$ = 0.6040, where the average ignition features occur at τ_1 = 7.94 ms and τ_{ign} = 14.09 ms. The ±0.75 ms uncertainty in the sampling times, when normalized by the average τ_{ign}, corresponds to approximately ±0.053. The uncertainty in the species calibrations (varying for each species) and the uncertainty due to pressure measurements in the sampling volume (±10%) were considered as independent sources of uncertainty on the species concentrations, and were therefore combined by using the square root of the sum of the squares. The quenching and recombination of small radicals can also be considered a source of error or uncertainty in the experimental measurements. Small radicals such as O, H, OH, HO_2, and CH_3 can recombine to form water vapor and small hydrocarbons, which may interfere with measurements of stable species. However, predicted small radical mole fractions, seen in Fig. 9, are very low (~40–100 ppm) relative to most of the measured intermediate species before autoignition. Radical recombination during the quenching process of sampling is thus not expected to be a source of error in the species measurements presented in this work.

Seen also in Fig. 8 (open red squares) are measurements of the species time-histories reported by Minetti et al. [13] in their ignition and speciation study. Their experiments were conducted with stoichiometric mixtures of n-C_7H_{16} and O_2 with an EOC pressure and temperature of 3.4 bar and 667 K, resulting in an average τ_{ign} of 41 ms, with τ_1 around 30 ms. The sampling experiments by Minetti et al. [13] were at a similar temperature to the present UM RCF experiments, but at a lower pressure. At 3.76, the dilution in their experiments was lower than the 5.64 dilution in the present study. Also, in contrast to the high-speed sampling used in the

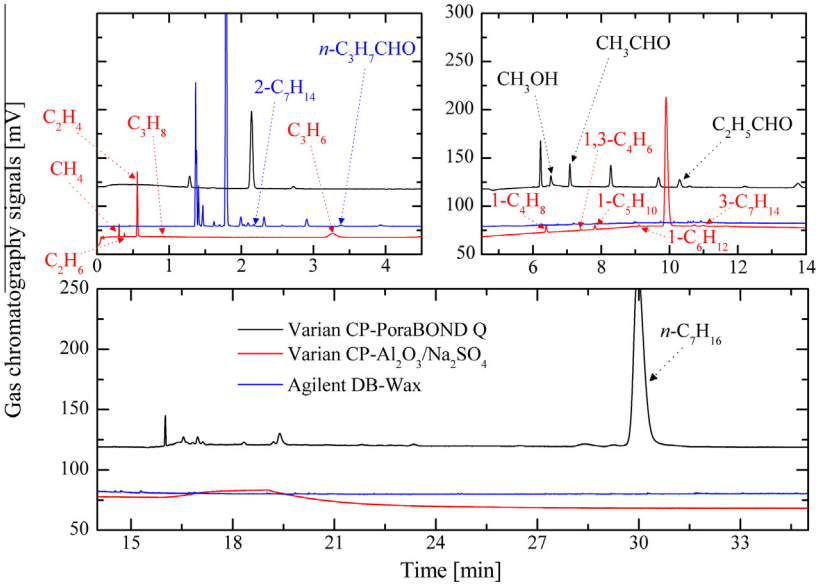

Fig. 7. An example of typical gas chromatograms of a gas sample from an n-C_7H_{16} sampling experiment. The data are from the experimental results presented in Fig. 4, in which sampling was performed at 12.08 ms after EOC.

present study, Minetti et al. [13] quenched the entire contents of the combustion chamber in their experiments by bursting a diaphragm, thereby combining their measured species with the contents of a cold boundary layer. Nevertheless, the species results from the present study are broadly consistent with those of Minetti et al. [13].

4. Kinetic modeling

Chemical kinetic modeling is frequently used to interpret RCM experimental results, usually considering zero-dimensional constant volume, adiabatic model predictions using a detailed reaction mechanism for the fuel studied. For very reactive fuels, chemical reactions and heat release during the compression stroke can be included in the modeling calculations, and heat losses to combustion chamber walls can also be included, often by making small adiabatic expansions of the combustion volume after the end of the compression stroke to simulate the cooling of the reacting gases. In the present simulations, reactions during the compression stroke and simulated heat losses were examined, and neither process was found to have significant impacts on computed results. For example, taking the experimental pressure time-history as an indicator of heat loss, the pressure decreases less than 3% between EOC and the first stage of ignition, corresponding to a temperature decrease of less than 1%. This low heat loss is primarily due to the very high volume-to-surface area ratio of the test section. As a consequence, all simulations used a constant volume, adiabatic approach, and for comparison with the species measurements, all the simulations used a reactant mixture of $\chi(n\text{-}C_7H_{16}) = 0.0134$, $\chi(O_2) = 0.149$, $\chi(N_2) = 0.2334$, and $\chi(CO_2) = 0.6042$, and initial conditions of $P_0 = 9$ atm and $T_0 = 700$ K.

The kinetic modeling calculations were carried out using the CHEMKIN Release 10101 (x64) [47]. The core $H_2/O_2/C_1$–C_4 species mechanism was taken from a recently refined mechanism of Metcalfe et al. [48]. The kinetic reaction mechanism for n-C_7H_{16} first selected for this study was developed by Mehl et al. [28], which was based on an earlier mechanism of Curran et al. [24]. Both mechanisms are constructed using 25 reaction rate rules for the distinct classes of reactions that describe the fuel oxidation. This approach, combining a core small molecule kinetic mechanism with additional submechanisms for the larger fuels of interest in a specific study, is commonly employed by a majority of kinetic model builders. The result in the present case was tested by simulations of most of the validation targets used to first develop the earlier version of the reaction mechanism [24,28], and the present mechanism reproduced all of those tests in satisfactory fashion. Three examples of such reaction classes include the abstraction of H atoms from the fuel by small radical species such as OH or H,

$$n\text{-}C_7H_{16} + X = C_7H_{15} + XH \qquad \text{(C-2)}$$

where X represents the radical; the addition of molecular oxygen to an alkyl radical, a heptyl radical in the present case, to produce an alkylperoxy radical RO_2,

$$C_7H_{15} + O_2 = C_7H_{15}O_2 \qquad \text{(C-10)}$$

and isomerization reactions of RO_2 to produce a hydroperoxy alkyl species QOOH,

$$C_7H_{15}O_2 = C_7H_{14}OOH \qquad \text{(C-12)}$$

These reactions are labeled according to the reaction classes defined by Curran et al. [24]. The complete kinetic mechanism contains approximately 1800 chemical species and 7250 elementary chemical reactions, and is included in the supplemental information.

Since most of the reactions in such a large kinetic mechanism have never been studied individually, their rates are usually estimated on the basis of other reactions that are somehow similar to the one being examined. For example, for reactions in class (C-10) above (there are 4 unique primary and secondary heptyl radicals in the present mechanism for n-C_7H_{16}), the rates are assumed to be equal to the rates of addition of O_2 to primary and secondary sites in n-butane or propane, reactions whose rates have been studied. However, for some reaction classes, there were no reliable reaction rates for any similar fuels at the time the original kinetic mechanisms were developed. One such class involves RO_2 isomerization reactions of class (C-12) above. Models for this class in the n-C_7H_{16} mechanism of Curran et al. [24] were taken from alkyl radical isomerizations with the same size transition state rings by which the reaction proceeded and the same type of C–H bond being broken (i.e., primary, secondary or tertiary), but did not account for the –O–O– structure that is part of the transition

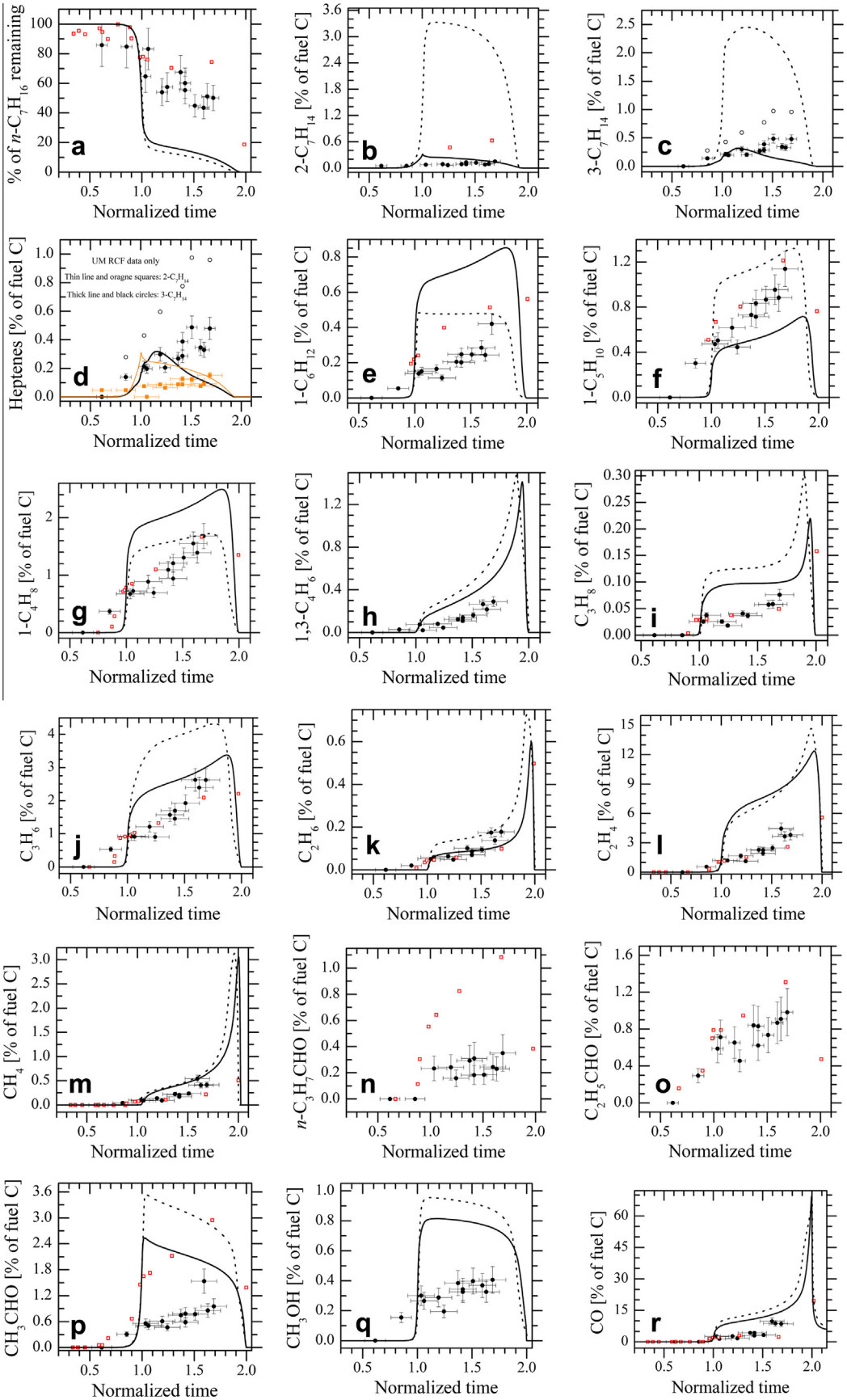

Fig. 8. (a–r) Species concentration time-histories from the UM RCF sampling experiments (solid black circles), from the Minetti et al. [13] study (open red squares), and from the model predictions for the UM RCF data based on the Mehl et al. [28] mechanism (dashed line), and the current, modified reaction mechanism (solid line). (Note the unique symbols for figure (d).) The model predictions are shown for constant volume, adiabatic conditions with P_0 = 9 atm, T_0 = 700 K, $\chi(n\text{-}C_7H_{16})$ = 0.0134, $\chi(O_2)$ = 0.149, $\chi(N_2)$ = 0.2336, and $\chi(CO_2)$ = 0.6040. All data are presented as normalized to the % of fuel carbon in the initial reactant mixture. (For interpretation of the references to color in this figure legend, the reader is referred to the web version of this article.)

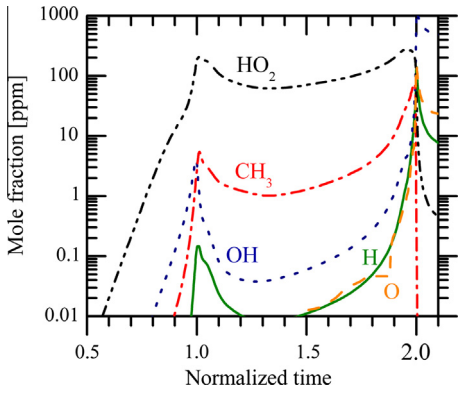

Fig. 9. Predictions (constant volume, adiabatic simulations with $P_0 = 9$ atm, $T_0 = 700$ K, $\chi(n\text{-}C_7H_{16}) = 0.0134$, $\chi(O_2) = 0.149$, $\chi(N_2) = 0.2336$, and $\chi(CO_2) = 0.6040$) using the current mechanism of radical concentrations at the first and second stages of ignition.

state ring in reaction class (C-12), which should be expected to influence the amount of ring strain energy in the transition state. This logic had been proposed by Pollard [49], based in turn on analysis from Fish [50] and was necessary because no rate data were available for any of the RO_2 isomerizations. The same type of approximation strategy was necessary for other reaction classes involving large hydrocarbon radicals that contained O atoms, including cyclic ether production from the hydroperoxy alkyl radical QOOH, class (C-19); QOOH decomposition to produce an alkene and HO_2, class (C-20); QOOH β-decomposition to produce an alkene and a carbonyl species as well as an OH radical, class (C-21); addition of molecular oxygen to the QOOH species, class (C-22); and isomerization of the O_2QOOH radical to produce a stable ketohydroperoxide species and OH, class (C-23). The common feature of these reaction classes is that they are all part of the RO_2 isomerization sequence of reactions where low temperature (650–850 K) NTC behavior occurs.

Kinetic reaction mechanisms built according to past reaction rate rules, with many of their reaction rates estimated because of the absence of supporting experimental or theoretical values, have been quite successful in reproducing integrated experimental quantities such as ignition delay times and laminar burning velocities. However, in most such experiments, few if any intermediate species concentrations are reported that can provide much more challenging tests of the predictive capabilities of reaction mechanisms, especially in the low temperature regime where so many of the reaction rates are poorly known. As noted above, the intermediate species measurements of Dagaut et al. [8] and Minetti et al. [13] from their jet-stirred reactor and RCM experiments, respectively, were used by Curran et al. [24] to build the original n-C_7H_{16} kinetic mechanism, but those were the only previously existing such measurements that were suitable for mechanism validation. The recent jet-stirred reactor experiments of Herbinet et al. [9], together with the current RCF data, provide much-needed additional validation data for n-C_7H_{16} chemical kinetic models, as these experimental data focus especially on intermediate chemical species concentration measurements in the low-temperature regime.

In this study, the mechanism developed by Mehl et al. [28] was used for initial calculations. Figure 10 presents the comparison of the initial model results and experimental results for pressure time history. The preliminary calculations produced two-stage ignition for the current experimental conditions, with first-stage and second-stage ignition delay times that were somewhat shorter than but within a factor of two of the experimental results, as shown in Fig. 10. Specifically, for the initial calculations at 700 K, the predicted τ_1 was 5.5 ms and τ_{ign} was 8.5 ms, compared with the experimental values of about 8.5 ms and 14.5 ms, respectively.

Results for the initial model predictions for the intermediate species are compared with the experimental measurements in Fig. 8 as the dashed lines. The initial calculations showed that approximately 80% of the n-C_7H_{16} fuel was consumed in the first ignition stage, more than the approximately 40–60% consumption observed in the experiments, as seen in Fig. 8a. More dramatically, the computed results showed that the intermediate concentrations of the heptene intermediates produced from n-C_7H_{16} during the time interval between the first and second ignition stages were higher than the experimentally measured levels by a factor of 5 to 25, as seen in Fig. 8b and c. The 3-C_7H_{14} calibration standard was an uncertain mixture of *cis*-3-C_7H_{14} and *trans*-3-C_7H_{14} and the measured areas of these two isomers were approximately equal in the chromatograms. Due to the uncertainty in the calibration standard, the 3-C_7H_{14} was quantified within a factor of two. In Fig. 8c and d, the solid black circles represent measurements of a single 3-C_7H_{14} isomer, and the open circles represent the upper bound/cumulative measurement of the 3-C_7H_{14} isomers.

The initial mechanism predicted many species quite accurately. For example, as seen in Fig. 8, CH_4 and C_2H_6 were well reproduced, as were CO and some small alkenes such as C_3H_6 and 1-C_4H_8. Other key species such 1-C_5H_{10}, 1-C_6H_{12} and C_2H_4, together with smaller oxygenates such as CH_3CHO and CH_3OH, were captured within factors of about two by the initial mechanism. However, the large errors in the computed amounts of the heptene isomers, together with the considerable differences between modeled and experimental rates

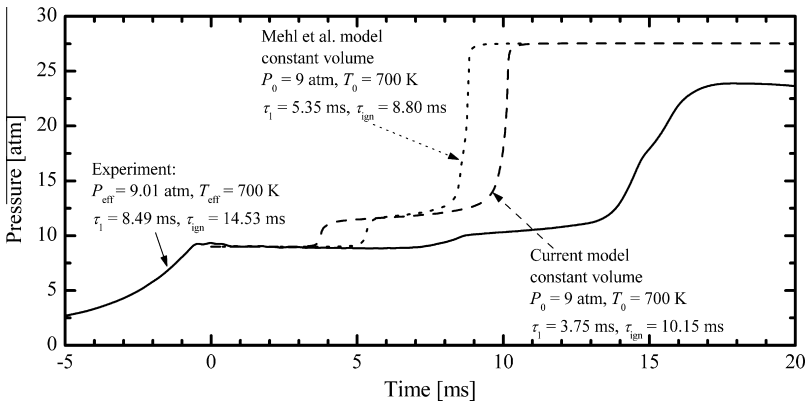

Fig. 10. A comparison of experimental and computational pressure time-histories. The models include predictions (constant volume, adiabatic simulations with $P_0 = 9$ atm, $T_0 = 700$ K, $\chi(n\text{-}C_7H_{16}) = 0.0134$, $\chi(O_2) = 0.149$, $\chi(N_2) = 0.2336$, and $\chi(CO_2) = 0.6040$) based on the current reaction mechanism and the Mehl et al. [28] mechanism.

of n-C_7H_{16} consumption in the first stage ignition, indicated that improvements in the kinetic modeling of the low temperature portion of the reaction mechanism were needed.

Two recent publications by Villano et al. [43,51] provided a basis for making significant improvements to the n-C_7H_{16} kinetic mechanism. In the papers by Villano et al., the reaction rates for the most important reaction classes that control ignition at low temperature conditions were calculated with electronic structure calculations performed at the CBS-QB3 level of theory combined with canonical transition state theory calculations. The first of these papers [43] reported rates of addition of O_2 to large alkyl radicals to produce RO_2 (class (C-10) above); the dissociation of the RO_2 back to alkyl radicals and O_2 (the reverse reactions for class (C-10)); the isomerization of RO_2 to produce hydroxyalkyl radicals QOOH (class (C-12) above); and the concerted elimination reactions of RO_2 to produce alkenes and HO_2 radicals, seen below:

$$C_7H_{15}O_2 = C_7H_{14} + HO_2 \quad \text{(C-12b)}$$

The second paper [51] extended the same approach to include the reverse reaction rates for hydroperoxyalkyl radicals QOOH back to RO_2 (the reverse direction for class (C-12) above); the cyclization of the QOOH species to produce a cyclic ether and OH

$$C_7H_{14}OOH = OH + \text{cyclic ether} \quad \text{(C-19)}$$

and β-scission reactions of QOOH to produce stable species and a radical:

$$C_7H_{14}OOH = HO_2 + \text{alkene} \quad \text{(C-20)}$$

$$C_7H_{14}OOH = OH + \text{alkene} + \text{carbonyl} \quad \text{(C-21)}$$

All of these reaction rates were modified in the n-C_7H_{16} kinetic mechanism, replacing the rates that had been estimated based on the discussions of Pollard [49].

In most kinetic reaction mechanisms and in the present work, the reaction rates in the mechanism are given in one direction and the rates of the reverse reactions are determined from the forward rates and detailed balance from the relevant thermochemistry. The reverse rates for some multistep reactions that are not genuine elementary reactions, such as Reaction (C-21) above, are usually set to zero, since the net reverse reaction cannot occur. The theory work of Villano et al. calculated the rates of elementary reactions in the absence of their corresponding reverse reactions, and some of their theoretical computations addressed both forward and reverse rates of truly elementary reactions. In particular, their work provides elementary rates of both Reaction (C-12) and its reverse. We chose to specify the forward and reverse reaction rates as determined by Villano et al.; in principle, this may not satisfy detailed balance and may not provide the correct equilibrium constants for these reactions. However, we felt that the precision of the forward and reverse reaction rate determinations was likely to be as accurate or better than our knowledge of the thermochemistry of the species involved. Further analysis of these theoretically determined reaction rates may lead to future improvements in the thermochemistry of the RO_2 and QOOH species.

However, several important reaction pathways in the low temperature submechanism were not evaluated by Villano et al., including reaction classes (C-22) and (C-23); the addition of molecular O_2 to the hydroperoxy alkyl radicals QOOH; and the isomerization reactions of the resulting O_2QOOH species to produce a relatively stable ketohydroperoxide species.

$$QOOH + O_2 = O_2QOOH \quad \text{(C-22)}$$

$$O_2QOOH = \text{ketohydroperoxide} + OH \quad \text{(C-23)}$$

These last two reaction classes are especially important since chain branching at low temperatures cannot occur without the second addition of O_2 to QOOH and the subsequent isomerization and decomposition reactions that produce multiple small radical species [24,52,53].

Fortunately, the work of Villano et al. [43,51] enables us to estimate the rates of reactions in classes (C-22) and (C-23) with much greater confidence than based on Pollard's estimates, as follows:

1. Since Villano et al. recommended rates of O_2 addition to primary, secondary and tertiary sites in alkyl radicals, we assumed that addition rates of O_2 to primary, secondary and tertiary sites in QOOH radicals would be approximately the same at each type of site as those for alkyl radicals.
2. Villano et al. calculated rates of RO_2 isomerization reactions by specifying the number of C, O, and H atoms in the transition state ring by which the isomerization took place and the type of C–H bond being broken. We therefore assumed that the same transition state rings would have the same energy barriers for O_2QOOH species isomerization. That is, we have assumed that the transition state ring strain energy for each isomerization reaction should depend only on the size of the transition state ring and the atoms arranged in that transition state ring, i.e., this energy would be the same in an RO_2 reactant as in a O_2-QOOH reactant, with the only differences being the bond energy of the C–H bond that is broken.
3. Curran et al. [24] assumed that the C–H bonds for the C atom holding the OOH moiety in the initial RO_2 species have a bond energy 3 kcal/mol lower than the original value. Following this, in the revised mechanism, we assumed that the O_2QOOH radical isomerization reactions have the same rates as their logically similar RO_2 isomerizations, but with an activation energy 3 kcal/mol lower. The Nancy kinetic modeling group [25,26] uses the same logic but reduce this activation energy by only 2 kcal/mol. As further theoretical studies of reaction classes (C-22) and (C-23) become available, we will use them to replace the current rate expressions, but the present approximations are likely to be considerably better than past values, since they contain much more of the fundamental chemistry features of these reactions.

Uncertainties in the rates of the RO_2 isomerization reactions have been a concern for many years, and the inadequacy of the Pollard/Fish approach used previously was noted by Villano et al. [43]. Earlier studies by Baldwin et al. [54], Hughes et al. [55], and Robertson et al. [56] on the energy barriers for the multiple RO_2 isomerization pathways led to improved rates employed by Buda et al. [25] and discussed by Battin-Leclerc [26]. However, until experimentally measured chemical species concentrations specific to the low temperature reaction pathways were available in addition to the macroscopic data such as ignition delay times, the details of the low temperature reaction pathways and rates had little impact on kinetic models. The most important quantity that is required of low temperature kinetic models has been the ratio of chain branching to chain propagation within the NTC regime, since this parameter controls the rate of heat release in the NTC region and therefore the extent to which ignition advances as a result of low temperature chemistry [26,57]. This ratio can be provided accurately by rather crude kinetic mechanisms, explaining why global, lumped, or significantly reduced kinetic mechanisms can accurately reproduce complex ignition delay behavior for many hydrocarbon fuels, even with substantial contributions from low temperature reaction pathways. The present measurement of heptene isomers; however, could not be accurately simulated without more accurate low temperature kinetic rate parameters.

With the modified low temperature kinetic parameters, new computational results were generated for the pressure time histories and intermediate species. Figures 8 and 10 present the results

of the modified rate parameters. The computed results for n-C_7H_{16} ignition showed significantly better results for the heptene isomers, as well as improved agreement for many other species with the experimental results. The computed ignition delay times with the improved low temperature kinetics were still faster than the experimental values. Specifically, the first stage ignition was about 4 ms and the second stage ignition was at about 10 ms, compared with the experimental values of 8.5 ms and 14.5 ms. The greatly improved predictions for 2-C_7H_{14} and 3-C_7H_{14} and smaller changes in other species predictions indicate that the new mechanism is significantly improved.

Of the 17 species measured experimentally, all of the concentrations computed from the kinetic model are in reasonable agreement with the measurements except the fuel and two aldehydes—propionaldehyde (C_2H_5CHO) and n-butyraldehyde (n-C_3H_7CHO). C_2H_5CHO and n-C_3H_7CHO are assumed to be produced in the new mechanism by a number of low temperature reactions that are quite speculative. Little attention has been given to C_2H_5CHO and n-C_3H_7CHO formation or consumption reactions and much more work would be needed to be more confident in their kinetics. We have therefore not included their computational predictions in the Fig. 8. The differences between the measured and computed consumption of n-C_7H_{16} are more troublesome, especially since the amounts of n-C_7H_{16} in both the present experiments and the experiments of Minetti et al. [13] disagree with the high extents of consumption predicted by the kinetic mechanism. Further analysis of these results will be needed to resolve this discrepancy, but it is interesting to note that even with this difference in fuel consumption, the model is able to predict the concentrations of so many intermediate species as seen in the rest of these species profiles.

5. Discussion

Using the present, upgraded kinetic reaction mechanism, n-C_7H_{16} autoignition was simulated for the same constant volume condition using the pressure and mixture composition described earlier, but over a wider temperature range from 600 K to 800 K. The results were used to calculate the difference in values of τ_{ign} and τ_1 as a function of initial temperature, as well as the percentage of the n-C_7H_{16} fuel consumed during the first stage of ignition. The results are plotted in Fig. 11. It is clear from this figure that the nature of the ignition changes profoundly as the initial temperature increases from 600 K to 800 K. For temperatures below 650 K, the ignition delay decreases at an increasing rate as the temperature increases, with the duration of the first stage of ignition forming a large portion of the overall ignition delay. As the temperature nears 700 K, where the present experiments were carried out, the total ignition delay time reaches a local minimum and the interval between τ_1 and τ_{ign} increases. At 700 K, Fig. 11a shows an interval of about 6–7 ms between τ_1 and τ_{ign} events, essentially the same as the interval measured in the present experiments and in the final model simulations (see Fig. 10). This indicates that the major difference between the model predictions and the experiments is the time of the first stage of the ignition. Also, according to the model, the amount of fuel consumed at the first stage decreases as the initial temperature increases and as the duration of the second stage increases. Yet, the good agreement between the model and experimental concentrations of the species in Fig. 8 indicates that the detailed chemistry of the ignition is otherwise well reproduced by the kinetic model.

Two factors make kinetic simulations of n-C_7H_{16} autoignition particularly challenging at temperatures near 700 K, in particular the complex transition taking place in the important reaction pathways from fuel consumption by H atom abstraction reactions with RO_2 and HO_2 radicals below 700 K to abstraction reactions with OH and H radicals at higher temperatures. Also at approximately 700 K, the amount of fuel consumed at the first stage starts to decrease significantly with increasing temperature, as seen in Fig. 11b. This complex temperature range will need further attention to clarify the details of the reaction rates and pathways, and our results indicate that many of the kinetic processes are quite sensitive to this relatively narrow temperature range.

The difficulty of predicting n-C_7H_{16} consumption at 700 K has been seen frequently in kinetic modeling studies. In their experimental and kinetic modeling study of fuel consumption at 750 K during the compression stroke in a rapid compression machine, Cox et al. [14] calculated approximately 40% n-C_7H_{16} fuel conversion in the first stage ignition while their experiments showed 10–20% conversion. In RCM experiments at 667 K, Minetti et al. [13] measured 20–30% n-C_7H_{16} consumption in the first stage ignition and calculated 80% fuel consumption, as noted earlier. In a very recent jet-stirred reactor study that is similar in some regards to the present study, combining excellent experimental analysis over a wide range of reactor temperatures (500–1100 K) with detailed chemical kinetic modeling, Herbinet et al. [9] provided very good agreement between measured and computed species levels over the entire range of temperatures for nearly all of the 47 different species measured. Herbinet et al. [9] note in particular for n-C_7H_{16} that their model "reproduces well the reactivity over the whole range of temperatures." However, a close examination of the plotted results (Fig. 2 of [9]) shows that there is a difference between the computed and measured mole fractions of n-C_7H_{16} of a factor of two at a reactor temperature of 700 K (computed mole fraction $\sim 2 \times 10^{-3}$, experimental mole fraction $\sim 4 \times 10^{-3}$), although the model reproduces the rather complex overall shape

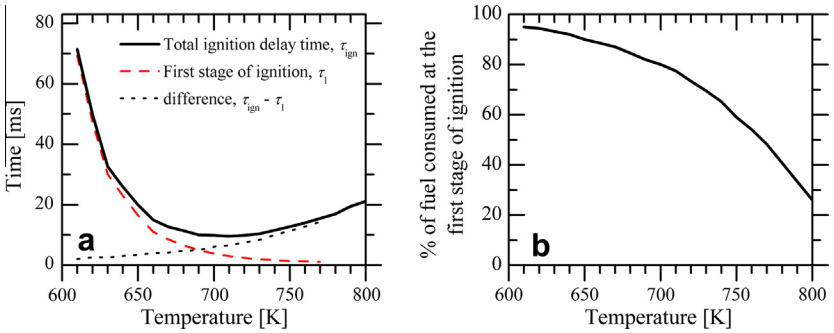

Fig. 11. The panel on the left shows the sensitivity of the new n-C_7H_{16} mechanism predictions ($P_0 = 9$ atm, $\chi(n\text{-}C_7H_{16}) = 0.0134$, $\chi(O_2) = 0.149$, $\chi(N_2) = 0.2336$, and $\chi(CO_2) = 0.6040$) of the first and second stages of ignition to temperature. The panel on the right shows that the predicted amount of fuel consumed at the first stage of ignition decreases significantly above 700 K.

of the n-C_7H_{16} mole fraction variation over the full temperature range. It is interesting to note that Herbinet et al. [9] predicted an excess consumption of n-C_7H_{16} of about the same magnitude as the present work at about 700 K, even after including a similar family of low temperature RO_2 isomerization and other reaction rates as those in our upgraded kinetic reaction mechanism, leaving a good explanation for the over-prediction of fuel consumption elusive.

The changes made to produce the new n-C_7H_{16} kinetic mechanism involved improved rates of reactions forming RO_2 and their subsequent isomerization and decomposition reactions; the subsequent addition of O_2 to the RO_2 isomerization products QOOH; and the isomerization of the O_2QOOH species to produce OH and ketohydroperoxide intermediates. The opportunity to upgrade the current mechanism with these new rate values based on theory rather than estimations offers some new interesting insights into the overall kinetic reaction mechanism. Villano et al. [43] conducted important calculations to suggest an increase in the fraction of RO_2 radicals that react via 1–5 and 1–6 isomerizations, that is, via 6-atom (·CCCOOH) and 7-atom (·CCCCOOH) transition state rings, as opposed to 1–4 or 1–7 isomerizations. They noted that recent electronic structure calculations by Davis and Francisco [53], not possible previously when the original kinetic mechanisms for fuels such as n-C_7H_{16} had been developed, showed that the incorporation of the O atoms into transition state rings has a considerable impact on the energetics for these isomerizations not seen in alkyl radical isomerization reactions. Specifically, the 1–5 and 1–6 isomerization rates are faster by factors of nearly 30 for RO_2 radicals than the previous rates based on analogous alkyl radical isomerizations, making RO_2 isomerizations the dominant reaction pathways for the low temperature kinetics. The 1–5 reaction leads primarily to QOOH products that favor O_2 addition and eventually chain *branching*, while the 1–6 reaction leads to QOOH cyclization and chain *propagation*. The dominance of these two reaction pathways simplifies the balance between branching and propagation that determines the amount of NTC behavior observed in both the experiments and the kinetic model. Such information could be valuable in developing reduced kinetic models for ignition of all types of hydrocarbon fuels.

The reduced fraction of RO_2 reaction via 1–4 isomerization in the revised mechanism leads to less heptene production, further reducing the excess heptene production observed in the simulations prior to the mechanism upgrade and seen as the dashed lines in Fig. 8b and c. The enhanced fraction of the 1–6 isomerization leads to the relatively high levels of large cyclic ethers in the intermediate species composition. In Section 3.2 above, we attributed most of the missing carbon in the experimental carbon balance to large C_7 cyclic ethers, and the relatively high rates of the 1–6 isomerizations lead preferentially to large amounts of C_7 cyclic ethers with 4 C atoms and one O atom. From the detailed output from the upgraded kinetic model, we find that most (i.e., about 75%) of the missing carbon is found in the form of $C_7H_{14}O2$–5. This is the cyclic ether produced via H atom abstraction at either the 2-site or the 3-site in n-C_7H_{16} (both of them being secondary sites with weakly bonded H atoms), followed by addition of O_2 to the radical site to produce either $C_7H_{15}O_2$-2 or $C_7H_{15}O_2$-3 and then the 1–6 isomerization reaction to produce the QOOH species C_7H_{14}OOH2-5 or C_7H_{14}OOH3-6, both of which then decompose to produce the same cyclic ether, $C_7H_{14}O2$-5. Each step of these sequences follows an energetically favored path, from the initial H atom abstraction from the fuel at secondary C–H sites to the energetically favored 1–6 isomerization reaction, and then the cyclization reaction to produce the –C–C–C–C–O– ring. We note that the cyclization reaction of the 1–6 isomerization product has a rate at 700 K that is 20 times faster than the similar cyclization reaction of the 1–5 isomerization reaction product at the same temperature. Under the present conditions, the cyclization reaction rate is faster than the addition rate of molecular oxygen to either the QOOH species C_7H_{14}OOH2-5 or C_7H_{14}OOH3-6, so the dominant reaction pathway for products of 1–6 isomerization is cyclization. Cyclization also yields a single OH product, so cyclization is effectively a chain propagation reaction pathway. In contrast, the product of 1–5 isomerization is much more likely to react via addition of molecular oxygen and subsequent chain branching, since its rate of cyclization is much smaller than the cyclization reactions of the 1–6 isomerization products. For these reasons, the 1–5 RO_2 isomerization reaction is generally regarded as a chain branching pathway while the 1–6 RO_2 isomerization reaction is generally regarded as a chain propagation reaction pathway. Since the 1–4 and 1–7 RO_2 isomerization reaction rates are significantly smaller than the 1–5 and 1–6 isomerization rates, the major factor influencing the relative amounts of chain propagation and chain branching in the present mechanism are the relative rates of the 1–5 and 1–6 isomerization rates.

A second observation provided by the new, more theory-based low temperature kinetic rates is that the production of heptenes is significantly reduced relative to the previous mechanism because the new rates of the concerted elimination reactions, reaction class (C-12b), are slower than in the previous mechanism. Reaction class (C-12b) produces a heptene species and HO_2 and is thus formally a chain propagation step, but it actually limits the overall rate of ignition more strongly than other chain propagation reactions because HO_2 is less reactive than most other radicals. In the Mehl et al. mechanism [28], the rate of reaction class (C-12b) had to be reduced in order to retard the time of ignition, but that led to extremely high computed levels of heptenes. A firm establishment of the rates of these reactions greatly reduced uncertainties in many of the other low temperature reactions and reaction pathways.

6. Conclusions

Speciation data presented in this work provide important new insights into the intermediates formed during the ignition delay of n-heptane. Computational results using an established chemical kinetic mechanism that has been widely used for many years [24,28] for the concentrations of several important intermediate species such as heptenes initially showed poor agreement with the speciation data (obtained at an effective pressure of 9 atm and an effective temperature of 700 K) from the current work. A refined chemical kinetic reaction mechanism that includes low temperature rate expressions taken from newly published theoretical studies by Villano et al. [43,51] predicts ignition delay times and intermediate species concentrations that are in much better agreement with experimental data; however, the mechanism predicts higher consumption of n-heptane at the first stage of ignition and predicts more heat release at the first stage of ignition than observed experimentally.

While previous n-heptane ignition studies have provided remarkable understanding of the effects of a broad range of temperatures and pressures on ignition delay times, few experimental studies have interrogated the reaction pathways proposed and represented in chemical kinetic mechanisms in the form of intermediate chemical species concentrations. The present study provides new measurements of intermediate species levels during n-heptane ignition in the low-temperature regime that could not be reproduced using currently available kinetic mechanisms. The discrepancies are largely due to poorly known rates of alkylperoxy radical reactions and reactions of other species produced via alkylperoxy isomerization reactions. New theory results of Villano et al. [43,51] reduced these uncertainties, and improvements in the mechanism made possible by these new studies were key to improving the agreement between computed and measured

intermediate species concentrations. Previous rates for alkylperoxy and alkylperoxy isomerization reactions had been based primarily on well-intentioned estimates, so the new rate information, based on established theoretical principles, are a significant upgrade to current kinetic models. While improvements have been made in this study for kinetics of *n*-heptane oxidation, considerable uncertainties remain. New studies of these reactions, particularly including experiments that address oxidation reactions and rates in the low temperature range are critical to making further mechanism refinements in this very important temperature regime.

Acknowledgments

The authors would like to thank the US Department of Energy Basic Energy Sciences, the US Department of Energy via the University of Michigan Consortium on Efficient and Clean High-Pressure, Lean Burn (HPLB) Engines, the Michigan Memorial Phoenix Energy Institute and the Graham Environmental Sustainability Institute for their financial support. The computational portion of this work was supported by the US Department of Energy, Office of Vehicle Technologies and the Office of Basic Energy Sciences and was performed under the auspices of the US Department of Energy by Lawrence Livermore National Laboratory under Contract DE-AC52-07NA27344. The authors would like to thank Dr. Stephanie Villano and Professor Anthony Dean of the Colorado School of Mines and Dr. William Pitz and Dr. Marco Mehl from LLNL for their insights into low-temperature chemistry. We would also like to thank Dr. Henry Curran, Dr. Darren Healy, Dr. John Griffiths, Dr. Guillaume Vanhove, and Dr. Rodolfo Minetti for sharing their experimental data.

Appendix A. Supplementary material

Supplementary data associated with this article can be found, in the online version, at http://dx.doi.org/10.1016/j.combustflame.2013.06.029.

References

[1] H.K. Ciezki, G. Adomeit, Combust. Flame 93 (1993) 421–433.
[2] H.-P.S. Shen, J. Steinberg, J. Vanderover, M.A. Oehlschlaeger, Energy Fuels 23 (2009) 2482–2489.
[3] J. Herzler, L. Jerig, P. Roth, Proc. Combust. Inst. 30 (2005) 1147–1153.
[4] J.M. Smith, J.M. Simmie, H.J. Curran, Int. J. Chem. Kinet. 37 (2005) 728–736.
[5] D.F. Davidson, M.A. Oehlschlaeger, R.K. Hanson, Proc. Combust. Inst. 31 (2007) 321–328.
[6] B. Akih-Kumgeh, J.M. Bergthorson, Energy Fuels 24 (2010) 2439–2448.
[7] D.F. Davidson, Z. Hong, G.L. Pilla, A. Farooq, R.D. Cook, R.K. Hanson, Combust. Flame 157 (2010) 1899–1905.
[8] P. Dagaut, M. Reuillon, M. Cathonnet, Combust. Flame 101 (1995) 132–140.
[9] O. Herbinet, B. Husson, Z. Serinyel, M. Cord, V. Warth, R. Fournet, P.-A. Glaude, B. Sirjean, F. Battin-Leclerc, Z. Wang, M. Xie, Z. Cheng, F. Qi, Combust. Flame 159 (2012) 3455–3472.
[10] E.J. Silke, H.J. Curran, J.M. Simmie, Proc. Combust. Inst. 30 (2005) 2639–2647.
[11] S. Tanaka, F. Ayala, J.C. Keck, J.B. Heywood, Combust. Flame 132 (2003) 219–239.
[12] J.F. Griffiths, P.A. Halford-Maw, C. Mohamed, Combust. Flame 111 (1997) 327–337.
[13] R. Minetti, M. Carlier, M. Ribaucour, E. Therssen, L.R. Sochet, Combust. Flame 102 (1995) 298–309.
[14] A. Cox, J.F. Griffiths, C. Mohamed, H.J. Curran, W.J. Pitz, C.K. Westbrook, Proc. Combust. Inst. 26 (1996) 2685–2692.
[15] Å. Ingemarsson, J. Pedersen, J. Olsson, J. Phys. Chem. A 103 (1999) 8222–8230.
[16] A.E. Bakali, J.L. Delfau, C. Vovelle, Combust. Sci. Technol. 140 (1998) 69–91.
[17] C. Doute, J.L. Delfau, R. Akrich, C. Vovelle, Combust. Sci. Technol. 124 (1997) 249–276.
[18] A. D'Anna, A. Alfe, B. Apicella, A. Tregrossi, A. Ciajolo, Energy Fuels 21 (2007) 2655–2662.
[19] C. Ji, E. Dames, Y.L. Wang, H. Wang, F.N. Egolfopoulos, Combust. Flame 157 (2010) 277–287.
[20] T.J. Held, A.J. Marchese, F.L. Dryer, Combust. Sci. Technol. 123 (1997) 107–146.
[21] J. Warnatz, Gas/Surface Interactions and Damaging Mechanisms in Knocking Combustion, CEC Contract: JOUE-0028D-MB, 1993.
[22] G.M. Côme, V. Warth, P.-A. Glaude, R. Fournet, G. Scacchi, F. Battin-Leclerc, Proc. Combust. Inst. 26 (1996) 755–762.
[23] E. Ranzi, P. Gaffuri, T. Faravelli, P. Dagaut, Combust. Flame 103 (1995) 91–106.
[24] H.J. Curran, P. Gaffuri, W.J. Pitz, C.K. Westbrook, Combust. Flame 114 (1998) 149–177.
[25] F. Buda, R. Rounaceur, V. Warth, P.A. Glaude, R. Fournier, F. Battin-Leclerc, Combust. Flame 142 (2005) 170–186.
[26] F. Battin-Leclerc, Prog. Energy Combust. Sci. 34 (2008) 440–498.
[27] CRECK Modeling Complete Mechanism (Low and High Temperature), Version 1201. <http://creckmodeling.chem.polimi.it/kinetic.html>.
[28] M. Mehl, W.J. Pitz, C.K. Westbrook, H.J. Curran, Proc. Combust. Inst. 33 (2011) 193–200.
[29] D.M.A. Karwat, S.W. Wagnon, M.S. Wooldridge, C.K. Westbrook, J. Phys. Chem. A 116 (2012) 12406–12421.
[30] X. He, M.T. Donovan, B.T. Zigler, T.R. Palmer, S.M. Walton, M.S. Wooldridge, A. Atreya, Combust. Flame 142 (2005) 266–275.
[31] S.M. Walton, X. He, B.T. Zigler, M.S. Wooldridge, A. Atreya, Combust. Flame 150 (2007) 246–262.
[32] S.M. Walton, X. He, B.T. Zigler, M.S. Wooldridge, Proc. Combust. Inst. 31 (2007) 3147–3154.
[33] S.M. Walton, M.S. Wooldridge, C.K. Westbrook, Proc. Combust. Inst. 32 (2009) 255–262.
[34] P.D. Teini, D.M.A. Karwat, A. Atreya, Combust. Flame 158 (2011) 2045–2055.
[35] P.D. Teini, D.M.A. Karwat, A. Atreya, Combust. Flame 159 (2012) 1090–1099.
[36] X. He, B.T. Zigler, S.M. Walton, M.S. Wooldridge, A. Atreya, Combust. Flame 145 (2006) 552–570.
[37] X. He, S.M. Walton, B.T. Zigler, M.S. Wooldridge, A. Atreya, Int. J. Chem. Kinet. 39 (2007) 498–517.
[38] S.M. Walton, D.M. Karwat, P.D. Teini, A. Gorny, M.S. Wooldridge, Fuel 90 (2011) 1796–1804.
[39] D.M.A. Karwat, S.W. Wagnon, P.D. Teini, M.S. Wooldridge, J. Phys. Chem. A 115 (2011) 4909–4921.
[40] M.T. Donovan, X. He, B.T. Zigler, T.R. Palmer, M.S. Wooldridge, A. Atreya, Combust. Flame 137 (2004) 351–365.
[41] B.J. McBride, S. Gordon, M.A. Reno, Thermodynamic and Transport Properties of Individual Species, vol. NASA Techn., 1993
[42] A.G. Gaydon, The Spectroscopy of Flames, Wiley, New York, 1957.
[43] S.M. Villano, L.K. Huynh, H.-H. Carstensen, A.M. Dean, J. Phys. Chem. A 115 (2011) 13425–13442.
[44] E. Ranzi, A. Frassoldati, S. Granata, R. Faravelli, Ind. Eng. Chem. Res. 44 (2005) 5170–5183.
[45] C.K. Westbrook, H.J. Curran, W.J. Pitz, J.F. Griffiths, C. Mohamed, S.K. Wo, Proc. Combust. Inst. 27 (1998) 371–378.
[46] S.M. Sarathy, C.K. Westbrook, M. Mehl, W.J. Pitz, C. Togbe, P. Dagaut, H. Wang, M.A. Oehlschlaeger, U. Niemann, K. Seshadri, P.S. Veloo, F.N. Egolfopoulos, T. Lu, Combust. Flame 158 (2011) 2338–2357.
[47] Reaction Design CHEMKIN Release 10101 (x64), 2010.
[48] W.K. Metcalfe, S.M. Burke, C.J. Aul, E.L. Petersen, H.J. Curran, Proc. Euro. Combust. Mtg., 2011.
[49] R.T. Pollard, in: C.H. Bamford, C.F.H. Tipper (Eds.), Comprehensive Chemical Kinetics: Gas Phase Combustion, vol. 17, Elsevier, New York, 1977, pp. 249–367 (Chapter 2).
[50] A. Fish, Angew. Chem., Int. Ed. 7 (1968) 45–60.
[51] S.M. Villano, L.K. Huynh, H.-H. Carstensen, A.M. Dean, J. Phys. Chem. A 116 (2012) 5068–5089.
[52] J. Zador, C.A. Taatjes, R.X. Fernandes, Prog. Energy Combust. Sci. 37 (2011) 371–421.
[53] A.C. Davis, J.S. Francisco, J. Phys. Chem. A 115 (2011) 2966–2977.
[54] R.R. Baldwin, M.W. Hisham, R.W. Walker, J. Chem. Soc., Faraday Trans. I (78) (1982) 1615–1627.
[55] K.J. Hughes, P.A. Halford-Maw, P.D. Lightfoot, T. Turanyi, M.J. Pilling, Proc. Combust. Inst. 24 (1992) 645–652.
[56] S.H. Robertson, P.W. Seakins, M.J. Pilling, in: M.J. Pilling (Ed.), Comprehensive Chemical Kinetics: Low-Temperature Combustion and Autoignition, vol. 35, Elsevier, Amsterdam, 1997.
[57] C.K. Westbrook, W.J. Pitz, O. Herbinet, H.J. Curran, E.J. Silke, Combust. Flame 156 (2009) 181–199.
[58] D.F. Davidson, D.R. Haylett, R.K. Hanson, Combust. Flame 155 (2008) 108–117.

Combustion and Flame 161 (2014) 898–907

Contents lists available at ScienceDirect

Combustion and Flame

journal homepage: www.elsevier.com/locate/combustflame

Effects of buffer gas composition on autoignition

Scott W. Wagnon [a,*], Margaret S. Wooldridge [a,b]

[a] Department of Mechanical Engineering, University of Michigan, Ann Arbor, MI 48109, USA
[b] Department of Aerospace Engineering, University of Michigan, Ann Arbor, MI 48109, USA

ARTICLE INFO

Article history:
Received 30 July 2013
Received in revised form 22 September 2013
Accepted 23 September 2013
Available online 17 October 2013

Keywords:
Dilution
Ignition
n-Heptane
iso-Octane
n-Butanol

ABSTRACT

This work quantifies the chemical kinetic and thermal effects of buffer gas composition on autoignition of three fuels at conditions relevant to engines, combustors, and experimental facilities used to study ignition kinetics. Computational simulations of autoignition of *iso*-octane, *n*-heptane, and of *n*-butanol were used to characterize the effects of buffer gas composition on ignition delay time and heat release rate. Stoichiometric mixtures, $\phi = 1.0$, and a temperature range of 600–1100 K were considered. *Iso*-octane and *n*-heptane were studied at initial pressures of 9.0 atm and 60.0 atm, and *n*-butanol was studied at initial pressures of 3.2 atm and 60.0 atm. Two dilution levels of buffer gas to O_2 of 3.76:1 (mole basis) and 5.64:1 were considered (~21% and ~15% O_2 respectively, mole basis). The fuels and simulation conditions were selected based on the relevance to engine operating conditions and previously published ignition studies. The buffer gases considered were argon, nitrogen, water, and carbon dioxide. Simulation results predicted changes of greater than a factor of 2 in ignition delay time and heat release rate as a function of buffer gas composition in the negative temperature coefficient (NTC) region for *n*-heptane and *iso*-octane. Outside the NTC region, the predicted effects of changes in buffer gas composition were small (<20%); however, experimental data for *n*-heptane indicate larger effects of buffer gas composition on ignition delay time at higher temperatures (>a factor of 2). The heat release rates were also sensitive to buffer gas composition, with carbon dioxide exhibiting relatively high levels of early and late heat release relative to the other buffer gases. Sensitivity analysis of the third-body collision efficiencies for the buffer gases showed the effects of uncertainties in the third body collision efficiencies on ignition delay time and heat release rate. The results highlight the significance of buffer gas composition on low-temperature combustion chemistry, particularly via H_2O_2 and HO_2 decomposition and recombination reactions.

1. Introduction

Dilution strategies, such as exhaust gas recirculation (EGR), are important tools to achieve high efficiency, low pollutant emissions combustion. There are multiple mechanisms by which EGR can improve combustion performance, including direct cooling or heating, dilution, and potential chemical kinetic interactions through three-body reactions and through trace reactive components in the EGR gases, to name a few. The chemical kinetic and thermal effects of EGR are important as they play significant roles on reaction rates and thereby affect autoignition times and heat release rates. Moreover, thermal, dilution, and chemical kinetic effects are often convolved. For example, thermal effects of buffer gas composition include changes in the specific heat capacity of the fuel/air mixture which affect compression heating and heat transfer losses, and thereby impact chemical reaction rates. Dilution impacts reaction rates (chemical kinetic effects) and heat transfer rates (thermal effects). Chemical kinetic effects also include the impact of third-body collision efficiencies. It is challenging to isolate the effects of EGR composition in internal combustion engine (ICE) studies due to the complexities of the combustion systems and the often limited access for engine diagnostics. Despite these challenges, there have been valuable experimental and computational ICE studies that have investigated some of the thermal and chemical kinetic effects of buffer gases on autoignition, or combustion phasing, and exhaust gas emissions [1–5].

Ladommatos et al. [1] investigated EGR effects which they categorized as thermal (due to changes in the specific heat capacity of the mixture), dilution (due to changing the oxygen concentration of the mixture), and chemical kinetic effects (associated with dissociation of CO_2) on ignition delay times and exhaust emissions using CO_2 as an EGR substitute in a single cylinder, direct injection diesel engine. The authors found that the magnitudes of the three effects on ignition delay times and exhaust emissions ranked dilution effects as most important, chemical kinetic effects second, and thermal effects as the least important at the conditions studied.

* Corresponding author. Address: University of Michigan, Department of Mechanical Engineering, 2350 Hayward Street, Ann Arbor, MI 48109-2125, USA. Fax: +1 734 647 3170.
E-mail address: swagnon@umich.edu (S.W. Wagnon).

0010-2180/$ - see front matter © 2013 The Combustion Institute. Published by Elsevier Inc. All rights reserved.
http://dx.doi.org/10.1016/j.combustflame.2013.09.022

With increased EGR (i.e., CO_2) Ladommatos et al. [1] reported decreased NO_x emissions and increased ignition delay times, unburnt hydrocarbons, and particulate emissions. A single-cylinder engine operated in homogeneous charge compression ignition (HCCI) mode was used by Sjöberg et al. [2] to study EGR effects via simulated complete stoichiometric products (i.e., N_2, CO_2, and H_2O) and real EGR on autoignition behavior of gasoline and gasoline surrogates (including *iso*-octane and primary reference fuel, PRF, blends of *iso*-octane and *n*-heptane). The authors reported enhanced EGR dilution effects (due to changing the oxygen concentration of the mixture) in fuels with two-stage heat release compared to fuels with single stage heat release, stronger acceleration of autoignition by water (considered a chemical effect, where the authors stated that early reactions were enhanced by the presence of H_2O) for two-stage fuels relative to single stage fuels, and a higher sensitivity to the specific heat capacity of the mixture for single stage fuels. In the work by Machrafi et al. [3], the authors used simulated EGR gases during HCCI operation of a single cylinder engine. They considered the chemical kinetic effects of trace reactive species found in real EGR (the authors added small quantities of CO, NO, and CH_2O to the simulated EGR mixtures), dilution effects (specifically the oxygen concentration of the mixture), and the thermal effects of the specific heat capacity of the EGR gases. Machrafi et al. [3] proposed the formation and consumption rates of OH were critical to the effects of the EGR gases on autoignition. In the work by Al-Qurashi et al. [4], the authors spent considerable effort to isolate and quantify the thermal (specific heat capacity of the mixture), dilution (oxygen concentration of the mixture), and chemical kinetic (dissociation of CO_2) effects of CO_2 on the reactivity of soot produced in co-flow flames and compared the results with soot produced in diesel engines using CO_2 with simulated and actual EGR. The authors found the thermal effects were the most important (45%) on the soot oxidation rate compared to the dilution (35%) and chemical kinetic effects (20%). Sjöberg and Dec [5] studied EGR effects on autoignition of ethanol in an HCCI operated engine and compared results to their previous study of gasoline and PRF blends [2]. The authors found that ethanol was less sensitive to EGR effects. Sjöberg and Dec attributed the difference in sensitivity to the shorter chain length of ethanol and generally lower intermediate temperature heat release rates. The authors also noted that water decreased ignition delay times for ethanol, but less than was observed for gasoline and PRF blends.

In other devices, buffer gas composition is used to control state conditions in combustion chemistry studies using shock tube (ST) and rapid compression machine (RCM) facilities. These facilities, which provide important experimental knowledge of chemical kinetics, rely on buffer gases ranging from monatomics (typically Ar and He) and diatomics (typically N_2) to polyatomics (typically CO_2) to control shock wave characteristics and thermodynamic conditions. The composition of the buffer gases affects the specific heat capacity of the test gas mixtures, the three-body collision reactions, and the heat transfer rates of the test gas mixtures. Few studies have focused on these important and interrelated mechanisms; however, some researchers have identified concerns particularly with autoignition studies. Davidson and Hanson compared predictions for autoignition times for *iso*-octane using two reaction mechanisms and conditions of $\phi = 1.0$, 2% O_2, and $P = 2$ atm [6]. They considered argon and nitrogen as buffer gases and found the change in specific heat capacity significantly affected the autoignition time (~50%) for one reaction mechanism, but not the other, at 1400 K. At NUI-Galway, Würmel et al. [7] conducted an experimental and computational study of buffer gas composition (Ar, Xe, He, N_2) effects in an RCM for 2,3-dimethylpentane ($\phi = 1.0$, 15 atm, and 650–950 K) [7], and a computational study of *iso*-octane ($\phi = 1.0$, 2.0 atm) and methane ($\phi = 0.5$, 1.8 atm) each with Ar and N_2 buffer gases at time scales relevant to shock tubes. Würmel et al. [8] also conducted a separate computational study of their RCM which focused on the effects of buffer gas composition as related to piston head design and heat transfer. Würmel et al. concluded that argon tends to increase autoignition times in their RCM [7,8] and decrease autoignition times in their ST [7], with different physical phenomena dominating the behavior over the wide time scales relevant to the RCM and ST facilities. Shen et al. [9] conducted experimental shock tube studies of *iso*-octane over a range of equivalence ratios, pressures, and temperatures with argon and nitrogen as buffer gases, and made comparisons with three chemical kinetic mechanisms. Shen et al. [9] determined that argon autoignition times were 20% shorter than autoignition times of nitrogen buffer gas experiments, primarily due to the lower specific heat capacity of argon, and that the mechanisms accurately captured the trend but generally failed to accurately predict autoignition times.

In summary, previous studies have highlighted the value of identifying conditions that are most and least sensitive to buffer gas composition and the mechanisms causing such sensitivity. Isolating, in as much as possible, the chemical kinetic and thermal effects of buffer gas composition on fuel ignition characteristics will help interpret previous results as well as guide future efforts to leverage buffer gas composition as a combustion design tool. The objective of this study was to quantify specific chemical kinetic and thermal effects of buffer gas composition using reaction mechanisms that have been well validated and are widely accepted for representing the autoignition chemistry of three important fuels. The computational simulations of autoignition of test gas mixtures were used to identify conditions where buffer gas composition has the highest impact on ignition delay times and heat release rates, and to quantify the effects of uncertainties in the species-specific collision efficiencies used in three-body reactions.

The computational methods were applied across a range of thermodynamic conditions for *iso*-octane, *n*-heptane, and *n*-butanol. The autoignition characteristics of each of the fuels have been previously studied by several research groups, providing a range of data for comparison, and the experiments provide the basis for the conditions simulated in this study. *Iso*-octane and *n*-heptane, as primary reference fuels, have been extensively studied using rapid compression machines (*i*-C_8H_{18} [10–16], *n*-C_7H_{16} [10,16–19]) and shock tubes (*i*-C_8H_{18} [9,20–24], *n*-C_7H_{16} [20,25–30]) encompassing a wide range of conditions. Studies of *n*-butanol have occurred with greater frequency over the last 5 years, and autoignition data are available from rapid compression machines [31,32] and shock tubes [33–39].

2. Computational methods

Computational simulations were carried out using the CHEMKIN suite of software (version 10113, x64) [40] and assuming a closed 0-D homogeneous batch reactor at adiabatic, constant volume conditions. Default values from CHEMKIN were used for the solver tolerances and solver time-steps. Detailed chemical kinetic mechanisms were used for each of the fuels, and extensive information on the mechanisms can be found in the literature for *iso*-octane [41], *n*-heptane [19], and *n*-butanol [34]. Brief summaries of the development and validation of each reaction mechanism used in this study are provided below. The reaction mechanisms were selected due to the maturity and extensive validation that has been previously completed on the reaction chemistry. No modifications to reaction rates were made to the mechanisms considered in this study. The mechanisms do not consider NO_x chemistry. Table 1 provides a brief summary of the characteristics of the reaction mechanisms, including the range of conditions for which the mechanisms have been developed and validated. The

Table 1
Summary of the reaction mechanisms used in this work. Detailed descriptions of the development and validation of the reaction mechanisms can be found in the references listed.

Fuel	# Species	# Reactions	Validation devices and conditions[a]	References
i-C_8H_{18}	874	3796	RCM, ST, JSR, PFR (ϕ = 0.3–1.5, P = 1–45 atm, T = 550–1700 K)	[41,42]
n-C_7H_{16}	1795	7245	RCM, ST, JSR, PFR (ϕ = 0.3–1.5, P = 1–50 atm, T = 550–1700 K)	[19,41,43,46]
n-C_4H_9OH	243	1446	ST (ϕ = 0.5–2.0, P = 1–8 atm, T = 1100–1800 K) JSR (ϕ = 0.5–2.0, P = 10 atm, T = 750–1100 K)	[34,44,45]

[a] RCM = rapid compression facility, ST = shock tube, JSR = jet stirred reactor, PFR = plug flow reactor.

chemical kinetic mechanisms used in this study are provided in the Supplemental material.

Initial conditions were selected based on relevance to internal combustion engine operating conditions and existing experimental ST and RCM data, particularly the initial pressures. The simulations were conducted at stoichiometric fuel-to-oxygen equivalence ratios (ϕ = 1.0) and over a minimum temperature range of 600–1100 K in 25 K increments for all fuels. Two dilution levels of 3.76:1 and 5.64:1 (buffer gas to O_2 ratios, mole basis) were considered in this study. The dilution levels correspond to air levels of oxygen (or ~21% O_2) and a more dilute mixture with ~15% O_2, mole basis. Argon, nitrogen, carbon dioxide, and water vapor were each evaluated as buffer gases in this study. Devices such as rapid compression machines and internal combustion engines often use mixtures of buffer gases (e.g., 50% argon/50% nitrogen, or 10% carbon dioxide/15% water/75% nitrogen). In this study, only pure buffer gases (e.g., 100% nitrogen) were considered to isolate and maximize the effects of a particular component on the autoignition behavior. Table 2 provides the initial conditions and mixture compositions studied.

2.1. n-Heptane mechanism

Simulations of *n*-heptane autoignition in this study used the reaction mechanism from the *n*-heptane ignition and speciation study of Karwat et al. [19]. Their *n*-heptane mechanism was largely based on the most recent Lawrence Livermore National Laboratory (LLNL) *n*-heptane chemical kinetic mechanism by Mehl et al. [41], which originates from the work of Curran et al. [43]. The *n*-heptane mechanism from Karwat et al. [19] can be categorized as having 25 distinct reaction classes which describe the low and high temperature chemical kinetic pathways for normal alkanes up to heptane, and a detailed small hydrocarbon (H_2 and C_1–C_4) submechanism updated from the work of Aul et al. [46]. Reaction classes are schemes that allow modelers to assign reaction rates to molecules that have not been studied either theoretically or experimentally based on similar structure. Karwat et al. [19] also modified the low-temperature chemistry (e.g., reactions involving alkylperoxy radicals, RO_2, and hydroperoxyalkyls, QOOH) based on theoretical calculations by Villano et al. [47,48] to improve agreement between model predictions and experimental measurements of heptane intermediates. Karwat et al. [19] found their mechanism produced satisfactory results for their experimental results, in addition to agreeing with the validation targets tested from the Mehl et al. [41] and Curran et al. [43] studies.

2.2. iso-Octane mechanism

Autoignition simulations of *iso*-octane in this study were conducted using the LLNL *iso*-octane chemical kinetic mechanism (Version 3) [41] available online. Version 3 is the most recent available update of the LLNL *iso*-octane mechanism by Curran et al. [42]. Two sets of reaction blocks compose the *iso*-octane mechanism, the first is a chemistry set for hydrocarbons up to C_4. The second is the main reaction set comprising the same general 25 reaction classes as the *n*-heptane mechanism with rates for branched hydrocarbons up to C_8. The most recent updates to small hydrocarbon chemistry and low-temperature chemistry pathways made to the *n*-heptane mechanism in Karwat et al. [19] are not reflected in the Mehl et al. [41] *iso*-octane mechanism used in this study. Mehl et al. [41] reported satisfactory validation of their *iso*-octane mechanism with recent shock tube, rapid compression machine, and jet stirred reactor data, in addition to the original validation data used by Curran et al. [42].

2.3. n-Butanol mechanism

For the *n*-butanol simulations, the chemical kinetic mechanism by Black et al. [34] was used. Reactions in the Black et al. [34] mechanism consist of a sub-set of reactions for hydrocarbons up to C_4 based on the work of Donato et al. [45] and a sub-set of reactions for *n*-butanol generated using EXGAS and modified to fit the validation data. The authors reported good agreement between the modeled and experimental ignition delay times for lean and stoichiometric mixtures at all pressures investigated. Black et al. [34] found their mechanism was less accurate for rich conditions and indicated that the ratio of unimolecular decomposition to hydrogen atom abstractions may be the cause. Dilution effects (buffer gas:O_2 of 3.6:1 and 26.6:1) on ignition delay times of stoichiometric mixtures at 2.6 atm were also captured well by the authors' mechanism. Experimental species measurements by Dagaut et al. [44] made in their jet-stirred reactor for stoichiometric mixtures at 10 atm were captured reasonably well by the *n*-butanol mechanism, with the largest disagreements observed for the rate

Table 2
Initial conditions for 0-D homogeneous batch reactor simulations used in CHEMKIN. Composition is provided on a mole basis.

Fuel (–)	Fuel (%)	O_2 (%)	Buffer gas (%)	Φ (–)	Buffer gas:O_2 (–)	P_o (atm)	T_o (K)
i-C_8H_{18}	1.65	20.66	77.69	1.0	3.76	9.0	600–1100[a]
i-C_8H_{18}	1.19	14.88	83.93	1.0	5.64	9.0	600–1100
i-C_8H_{18}	1.19	14.88	83.93	1.0	5.64	60.0	600–1100
n-C_7H_{16}	1.87	20.61	77.52	1.0	3.76	9.0	600–1100[a]
n-C_7H_{16}	1.34	14.90	83.76	1.0	5.62	9.0	600–1100
n-C_7H_{16}	1.34	14.90	83.76	1.0	5.62	60.0	600–1100
n-C_4H_9OH	3.38	20.30	76.32	1.0	3.76	3.2	600–1100[a]
n-C_4H_9OH	2.45	14.71	82.84	1.0	5.63	3.2	600–1100
n-C_4H_9OH	2.45	14.71	82.84	1.0	5.63	60.0	600–1100

[a] Additional high temperature simulations (600–1800 K) were carried out for comparison to experimental data at these conditions.

of *n*-butanol consumption, ethyne (C_2H_2) concentrations, and butanal (C_3H_7CHO) concentrations.

3. Results and discussion

Pressure–time histories from the CHEMKIN simulations were used to determine ignition delay times for the *n*-heptane, *iso*-octane, and *n*-butanol mixtures. When single stage ignition occurred, the overall ignition delay time was defined as the time from the start of the simulation to the time corresponding to the maximum rate of pressure rise, dP/dt_{max}, as has been used previously [10–12,19,31]. For conditions where two stage ignition occurred, the first stage of ignition was determined from the start time of the simulation to the time of the first maxima in the rate of pressure rise. The overall ignition delay time for two stage ignition was defined as the start time of the simulation to the time of the second maxima in the rate of pressure rise. The temperatures reported for the ignition delay times and pressure–time histories were the initial temperatures of the simulations. Figure 1 compares the pressure time histories and corresponding pressure derivatives for the different buffer gases for *n*-heptane at a low temperature (700 K), low pressure (9.0 atm), and dilute mixture condition (where dilution was quantified by the molar ratio of the buffer gas to the O_2 in the mixture). As expected, the final pressures after ignition vary based on the specific heat capacity of the buffer gases. Additionally, the CO_2 results show a slow rate of pressure rise compared to the other buffer gases during ignition.

Figure 2 shows results for computed first stage ignition delay times (+ symbols) and the overall ignition delay times (solid lines) in an Arrhenius diagram for the case of *n*-heptane at $\phi = 1.0$, $P = 9.0$ atm, buffer gas:$O_2 = 5.62$, over the temperature range 600–1100 K for the four buffer gases considered. While only the results for *n*-heptane are presented in Fig. 2, similar trends were observed for *iso*-octane at the same equivalence ratio, pressure, and dilution level. (Please see the Supplemental material for simulation results not shown in the text. The Arrhenius diagram for *iso*-octane at these conditions is provided as Fig. S4.) Within the negative temperature coefficient (NTC) region (~650–850 K for *n*-heptane, ~600–800 K for *iso*-octane), buffer gas composition had significant effect on the overall ignition delay time, with argon and water vapor decreasing overall ignition times up to 31% (30% for *iso*-octane) and carbon dioxide increasing times up to 49% (65% for *iso*-octane) relative to N_2. However, the first stage of ignition shows little variance (<7% for *n*-heptane, <16% for *iso*-octane) for any of the buffer gases relative to nitrogen. Outside of the NTC region for both fuels, the buffer gases had less impact on the computed ignition delay times, with water vapor showing the most significant effect in the intermediate

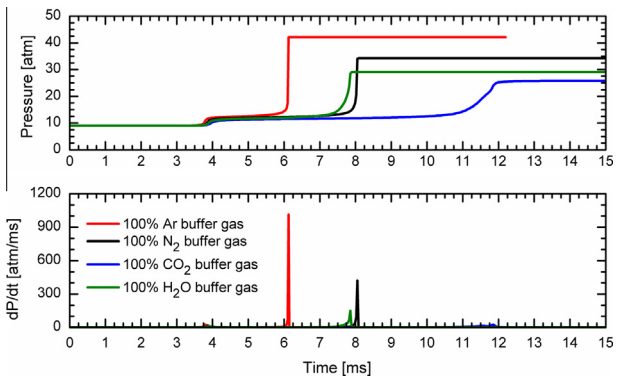

Fig. 1. Computed pressure–time histories and corresponding pressure derivatives for stoichiometric *n*-heptane mixtures. Initial conditions of 700 K, 9.0 atm, *n*-$C_7H_{16} = 1.34\%$, $O_2 = 14.90\%$, buffer gas = 83.76% (mole basis).

temperature chemistry regime, decreasing times up to 37% (34% for *iso*-octane). Rate of production analysis showed that OH and HO_2 radicals from water are not significant reaction pathways at the conditions studied for either PRF, and therefore are not the source of the decrease in ignition delay times at higher temperatures when water is considered as the buffer gas. Water, and carbon dioxide at higher temperatures ($T >$ ~850 K for *n*-heptane), decrease ignition delay times by their role in three-body reactions (e.g., H_2O_2 decomposition) and the corresponding enhanced collision efficiencies of water and carbon dioxide in such reactions. In the intermediate temperature chemistry regime for *n*-heptane ($T > 900$ K), argon and carbon dioxide did not alter ignition times more than 17% (15% for *iso*-octane), which is considered reasonably within the uncertainty of the overall reaction mechanisms.

For *n*-butanol at conditions of $\phi = 1.0$, $P = 3.2$ atm, and buffer gas:$O_2 = 5.63$, there was no NTC behavior over the range of temperatures considered, and the relative reactivity due to the buffer gases was consistent throughout the temperature range. (The Arrhenius diagram for *n*-butanol at these conditions is provided as Fig. S9.) Water vapor and carbon dioxide decreased ignition times up to 52% and 32%, respectively, compared to N_2, and argon increased ignition delay times less than 10% compared to N_2. As with the primary reference fuels, water was not a significant source of radical formation when used as the buffer gas for the conditions studied and the decrease in ignition delay times caused by CO_2 and H_2O is explained by enhanced collision efficiencies.

Figure 3 presents the pressure time histories for the buffer gases at a high pressure condition of 60 atm and 700 K. The duration of the first stage of ignition is considerably reduced for each buffer gas compared to the same temperature and lower pressure conditions of Fig. 1. The CO_2 continues to exhibit longer times for heat release relative to the other buffer gases. This high pressure condition is near the low temperature limit for the NTC behavior predicted for *n*-heptane, as seen in Fig. 4. The simulations conducted at high pressure ($\phi = 1.0$, 60.0 atm, buffer gas:$O_2 = 5.64$) show the NTC region shifted to higher temperatures compared to the low pressure simulations (to ~750–950 K for *n*-heptane, to ~700–900 K for *iso*-octane), and the general trends as a function of buffer gas composition were the same as observed at low pressure. Buffer gas effects on the first stage ignition delay times were negligible (less than 15%) for *n*-heptane and *iso*-octane. Although only two pressures were considered in this study, the results indicate the ignition delay times for the fuels scale by $\sim P^{-1}$ on the high temperature side of the NTC region.

Simulations at the lower level of dilution (3.76 molar ratio of buffer gas to O_2) and the lower pressure (9 atm) revealed similar trends to the higher dilution results as seen in Fig. 5. The NTC region was shifted slightly (<25 K) for *n*-heptane and *iso*-octane by decreasing the dilution level from 5.62:1 to 3.76:1. Outside the NTC region, the effects of dilution were approximately proportional, e.g., the 33% decrease in dilution resulted in ~35% decrease in ignition delay times outside of the NTC region for *n*-heptane/nitrogen and *iso*-octane/nitrogen mixtures. Within the NTC region, the decrease in dilution led to ~60% decrease in ignition delay times for the *n*-heptane/nitrogen and *iso*-octane/nitrogen mixtures.

As expected, decreasing the dilution de-amplified the effects of buffer gas composition to the point where changing the buffer gas composition resulted in less than 30% change in the ignition delay time throughout the range of conditions studied for *iso*-octane and *n*-heptane. Lowering the level of dilution for *n*-butanol indicated an approximately proportional impact on ignition delay time (the 33% decrease in dilution yielded a systematic decrease in ignition delay time of ~20%). Air levels of dilution were not considered for the high pressure case ($P = 60$ atm) for any fuel.

As seen in this study, conditions of lower pressure (<~10 atm) and higher levels of dilution (buffer gas:$O_2 > 3.76$) amplify the

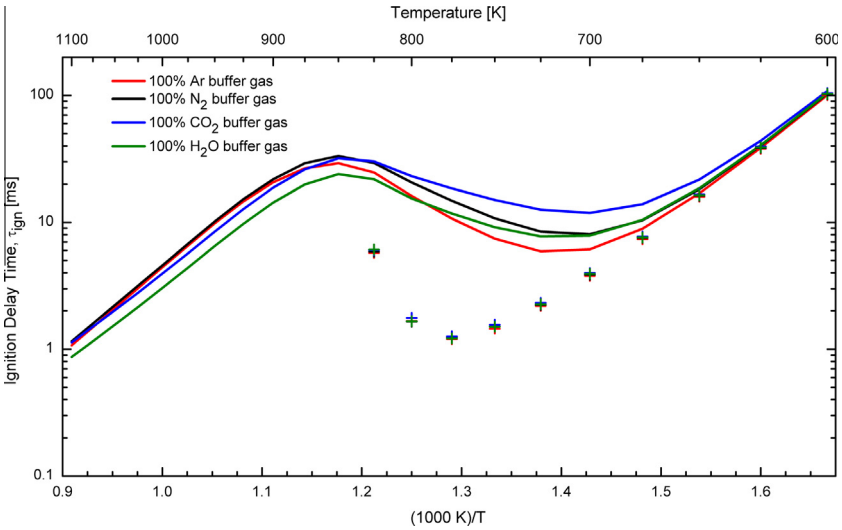

Fig. 2. Arrhenius diagram for computed ignition delay times of *n*-heptane. For conditions where two stages of ignition were observed, the + symbols indicate the computed first stage ignition delay times. Initial conditions of $P = 9.0$ atm, n-C_7H_{16} = 1.34%, O_2 = 14.90%, buffer gas = 83.76% (mole basis).

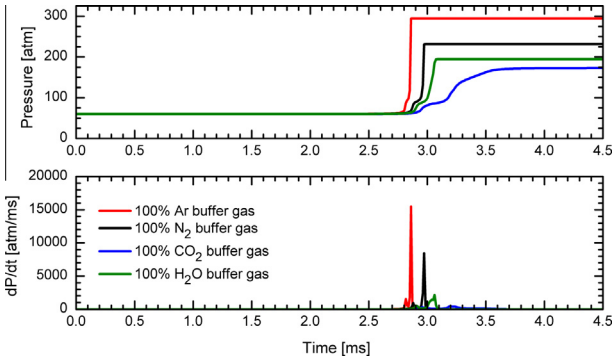

Fig. 3. Computed pressure–time histories and corresponding pressure derivatives for stoichiometric *n*-heptane mixtures. Initial conditions of 700 K, 60.0 atm, n-C_7H_{16} = 1.34%, O_2 = 14.90%, buffer gas = 83.76% (mole basis).

effects of buffer gas composition, and the NTC region is particularly sensitive to buffer gas composition. NTC behavior is generally attributed to the ratio of reactions forming alkylperoxy radicals (RO_2) to reactions forming alkyl radicals (R). The subsequent isomerization of RO_2 to hydroperoxyalkyl radicals (QOOH), and resulting pathways lead to chain-branching decomposition. Increases in pressure result in a shift in favor of RO_2 formation as shown by Villano et al. [47], shifting the NTC region to higher temperatures as pressure increases. Increasing pressure also decreases the magnitude of the NTC behavior as observed in the experimental study by Ciezki and Adomeit [25]. As dilution decreases, the O_2 concentrations increase also shifting the ratio towards RO_2 formation and moving the NTC region to higher temperatures. Comparing Figs. 2, 4 and 5, pressure exhibits greater influence than dilution on the NTC behavior for the conditions studied here.

3.1. Comparison of model trends with experimental data

Simulated autoignition times for stoichiometric *n*-butanol mixtures at air levels of dilution and initial pressures of 3.2 atm are compared with existing data from the literature in Fig. 6. The experimental data shown in the figure are from stoichiometric mixtures and initial temperatures from 678 K < T < 1711 K. The

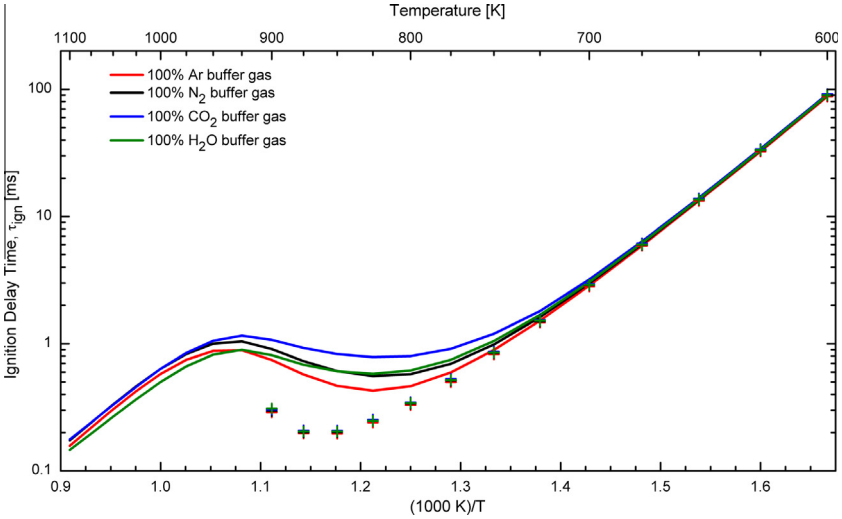

Fig. 4. Computed ignition delay times for stoichiometric *n*-heptane mixtures at high pressures. For conditions where two stages of ignition were observed, the + symbols indicate the computed first stage ignition delay times. Initial conditions of $P = 60.0$ atm, n-C_7H_{16} = 1.34%, O_2 = 14.90%, buffer gas = 83.76% (mole basis).

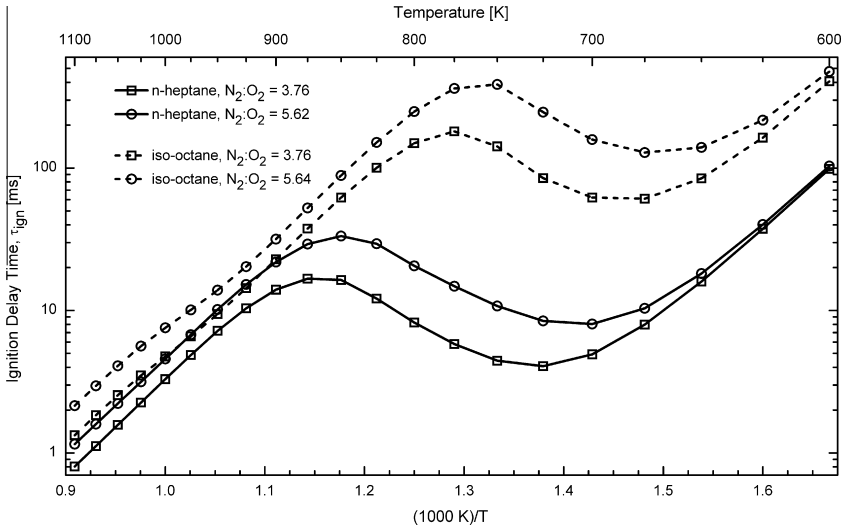

Fig. 5. Dilution level effects on ignition delay times for stoichiometric mixtures of the primary reference fuels, *iso*-octane and *n*-heptane, at low pressure (P = 9.0 atm) using N_2 as the buffer gas.

experimental data were obtained for a wide range of pressures and dilution levels, with pressures from 0.9 to 90.3 atm and buffer gas:O_2 ratios from 3.6 to 65.5. Based on the trends observed in this study and in previous work [19,49], all experimental ignition delay times presented in Fig. 6 were scaled assuming ignition delay times scale inversely with pressure (i.e., as P^{-1}) and proportionally with dilution based on the molar ratio of buffer gas:O_2. All experimental data were scaled to 3.2 atm and buffer gas:O_2 = 3.76. These scaling rules are considered reasonable for data outside the NTC region, with higher uncertainty introduced by scaling within the NTC region.

For temperatures above ~1000 K, there is fair agreement amongst the experimental data, within a factor of 3, from all facilities regardless of buffer gas composition. The degree of scatter above 1000 K cannot be attributed to buffer gas effects as the majority of data were acquired with argon. For temperatures below ~900 K, the model predictions deviate from the experimental data. For the long ignition times (>100 ms), this may be due in part because the adiabatic 0-D model is not appropriate for many RCM data. For example, low temperature ignition experiments may be complicated by heat losses as well as weak ignition phenomena, where heat losses typically increase experimental measurements of ignition delay times and weak ignition effects decrease ignition delay times [50–52]. Additionally, the reaction mechanisms used in the study have limited validation targets at low temperatures.

The trends between the simulations and experimental data for buffer gas composition are generally consistent. In the temperature range 927–1034 K, Karwat et al. [31] varied argon levels from 15% to 35% of the buffer gas (with the balance being N_2) for experiments at 3.2 atm and buffer gas:O_2 = 5.63. They observed no changes in autoignition behavior with changes to the buffer gas composition, which is consistent with the model predictions for Ar and N_2. Further, in the limited temperature window where data from different facilities and different buffer gases overlap (~950–1250 K), the results are consistent for argon and nitrogen as is predicted by the model, albeit the scatter in the experimental data is greater than the effects predicted by changing the buffer gas composition.

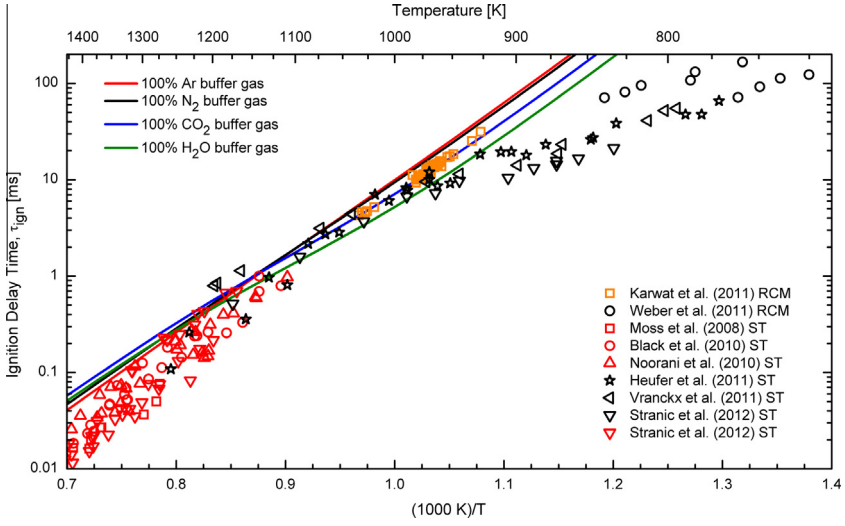

Fig. 6. Comparison of computed and experimental ignition delay times of stoichiometric mixtures of *n*-butanol at air dilution levels. Simulation results are presented as lines for initial conditions of P = 3.2 atm, *n*-C_4H_9OH = 3.38%, O_2 = 20.30%, buffer gas = 76.32% (mole basis). The symbols are the experimental results and are colored-coded based on the buffer gas composition used: red for argon, black for nitrogen, and orange for mixtures of Ar/N_2 buffer gases. All experimental data have been scaled to P = 3.2 atm and dilution of 3.76:1 (see text for details). (For interpretation of the references to color in this figure legend, the reader is referred to the web version of this article.)

Ignition delay times from the *n*-heptane simulations are compared with experimental data at air dilution levels in Fig. 7. Due to the significant NTC characteristics of *n*-heptane and the effects of pressure on NTC behavior, experiments within a narrow range of pressures (6–12 atm) were used for comparison. The dilution levels considered in the experiments were in the range of 2.48–5.62, molar ratio of buffer gas to O_2. As with the n-butanol comparison, the experimental data were scaled inversely with pressure and proportionally with dilution throughout the temperature range considered. The RCM studies used three buffer gases (Ar, N_2, and CO_2) and blends of the buffer gases to vary the end of compression temperatures over the range considered. There is little overlap in the experimental data using different buffer gases. However, at high temperatures ($T > 1000$ K), the shock tube data using N_2 are systematically slower than the shock tube data using Ar, with larger differences at higher temperatures. This trend extends to higher temperatures not shown on the figure. While the reaction mechanism predicts faster ignition for Ar mixtures compared to N_2, the model predicts only a slight (~5%) decrease in ignition delay time compared to the difference in the experimental data sets (a factor of ~2). Within the NTC region, the scatter in the RCM data is larger than the variation predicted by the model for the range of buffer gases considered, so no conclusions on the effect of buffer gas can be drawn.

Results of stoichiometric *iso*-octane simulations at air levels of dilution are compared with experimental data in Fig. 8. The experimental data span a pressure range of 6–12 atm, and have been scaled to 9 atm in the figure using $\tau \propto P^{-1}$. The experimental data span dilution levels of 2.48–5.00 and have been scaled to air levels of dilution using $\tau \propto$ (buffer gas:O_2). There is a small temperature range (~950–1000 K) where there are experimental data using N_2 (black symbols), Ar (red symbols), and N_2/Ar and N_2/CO_2 blends (orange symbols). The trends are consistent with the model predictions, with Ar yielding the fastest ignition and the blends yielding the slowest; however, the reaction mechanism predicts less sensitivity to the buffer gas than observed in the experiments.

3.2. Thermal effects of buffer gas composition

In the mechanisms considered in this study, typical third-body collision efficiencies for carbon dioxide and water vapor are ~2–4 and ~5–12 times that of nitrogen, respectively. The third-body collision efficiencies for argon are typically ~0.3–0.9 that of nitrogen. To isolate the thermal effects of buffer gas composition from the chemical kinetic effects of the collision efficiencies on ignition delay times, simulations were conducted where all the third-body collision efficiencies were set to 1, the collision efficiency of nitrogen. The simulations considered mixtures of $\phi = 1.0$ with buffer gas:O_2 = 5.64 and low pressures of 3.2 atm (*n*-butanol) and 9.0 atm (*n*-heptane and *iso*-octane). Results from the simulations are provided in the Supplemental material. The resulting first stage and overall ignition delay times correlated with expectations based on the specific heat capacity of the buffer gases (i.e., $\tau_{Ar} < \tau_{N2} < \tau_{H2O} < \tau_{CO2}$) for all three fuels, for all temperatures.

Outside of the NTC region, buffer gases without enhanced (or reduced) collision efficiencies relative to N_2 changed the ignition delay by ~±25%. Within the NTC region for *n*-heptane (Fig. S2) and *iso*-octane (Fig. S6), the changes to the collision efficiencies changed the overall ignition delay time by nearly a factor of 2, while the first stage of ignition was virtually unchanged (<7% for *n*-heptane and <16% for *iso*-octane). The large difference in the sensitivity to buffer gas composition in the NTC region is attributed to the specific heat capacities of the buffer gases when the collision efficiencies are set to 1. Carbon dioxide and water vapor with higher specific heat capacities than nitrogen exhibit smaller pressure and temperature increases during the first stage of ignition. Since mixtures with carbon dioxide and water vapor are significantly cooler after the first stage compared to nitrogen, the second stage of ignition is demonstrably longer for H_2O and CO_2 when collision efficiencies are set equal to 1. The second stage of ignition is discernibly shorter for argon when compared to nitrogen, due to a higher second stage temperature, when the efficiencies of all the buffer gases are set to 1.

When the recommended collision efficiencies are considered, as in Figs. 2 and 7 for *n*-heptane, the effects of carbon dioxide and water vapor change from increasing ignition delay times at low temperatures (<700 K for *n*-heptane) to decreasing ignition delay times (relative to nitrogen) as temperature increases. This effect is observed at both low and high pressures and for both air and dilute mixtures for *iso*-octane and *n*-heptane, and shows how the chemical kinetic and thermal effects are particularly convolved in the NTC region.

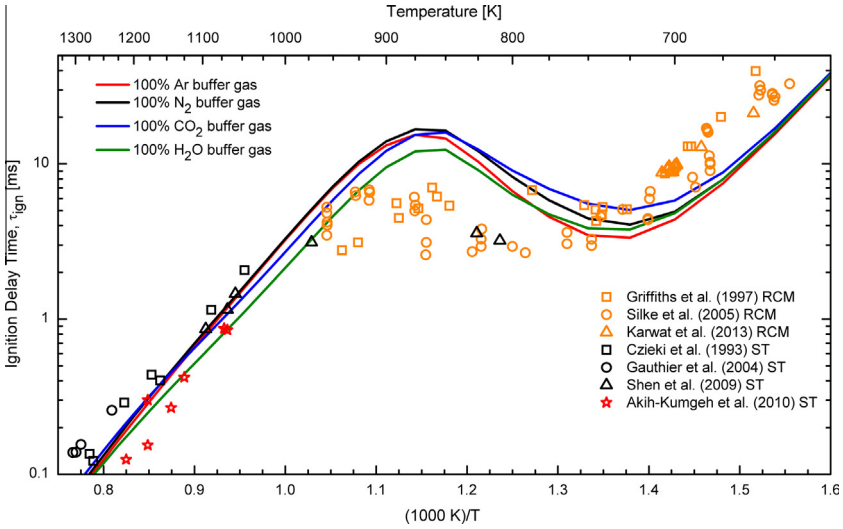

Fig. 7. Comparison of computed and experimental ignition delay times of stoichiometric mixtures of *n*-heptane at air dilution levels. Simulation results are presented as lines for initial conditions of $P = 9.0$ atm, *n*-C_7H_{16} = 1.87%, O_2 = 20.61%, buffer gas = 77.52%. Experimental results are presented as symbols and are colored-coded based on buffer gas composition: red for argon, black for nitrogen, and orange for either Ar/N_2 or CO_2/N_2 buffer gases. (For interpretation of the references to color in this figure legend, the reader is referred to the web version of this article.)

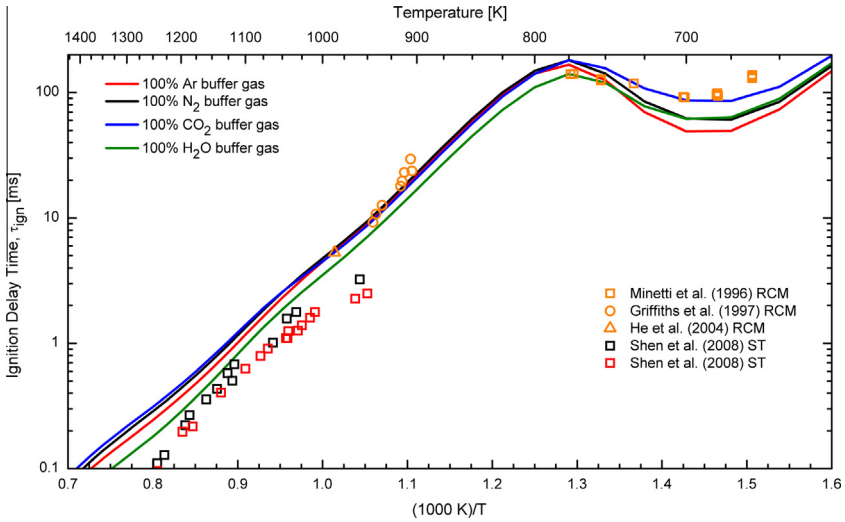

Fig. 8. Comparison of computed and experimental ignition delay times of stoichiometric mixtures of *iso*-octane at air dilution levels. Simulation results are presented as lines for initial conditions of $P = 9.0$ atm, i-$C_8H_{18} = 1.65\%$, $O_2 = 20.66\%$, buffer gas = 77.69%. Experimental results are colored based on buffer gas composition: red for argon, black for nitrogen, and orange for either Ar/N_2 or CO_2/N_2 buffer gases. (For interpretation of the references to color in this figure legend, the reader is referred to the web version of this article.)

3.3. Effects of buffer gas composition on heat release rate

As seen in Fig. 1, buffer gas composition affects heat release rates as well as ignition delay times. The maximum rate of pressure rise (MRPR) correlates with the maximum heat release rate during autoignition, and MRPR is a key metric of engine performance. A characteristic time for heat release, τ_{HR}, can be defined using the MRPR and the overall pressure rise during ignition, $P_{max} - P_o$:

$$\tau_{HR} = (P_{max} - P_o)/\text{MRPR}$$

Figure 9 shows the relationship between the simulation results for τ_{HR} and ignition delay time for n-heptane at $\phi = 1.0$ and the dilution levels and pressures considered in this work. Results showing the relationship for τ_{HR} and ignition delay times from n-butanol and *iso*-octane simulations are provided in the Supplemental material. For n-heptane at the air levels of dilution and $P = 9$ atm, the results show characteristic times for heat release correlate linearly with the autoignition times, and the composition of the buffer gas has a larger effect on heat release at faster ignition delay times. The effects of buffer gas composition on heat release are amplified at higher levels of dilution and higher pressures, with over an order of magnitude difference between the characteristic time for heat release for CO_2 and N_2 at $P = 60$ atm for the same autoignition time. The results indicate that strategies that fix engine autoignition phasing will yield different combustion rates based on the buffer gas composition, and higher engine speeds will be affected more than lower engine speeds. However, while the impact of composition is dramatic at some conditions in Fig. 9, the concentrations of CO_2 and H_2O in EGR are generally each less than 5% mole fraction, so the effects will be reduced at expected engine levels of dilution.

3.4. Sensitivity analysis

Sensitivity of the ignition delay time and heat release rate results to the third-body collision efficiencies, η, were examined for the three fuels at the stoichiometric, lower pressures of 3.2 atm (n-butanol) and 9.0 atm (n-heptane and *iso*-octane), and higher level of dilution (buffer gas:$O_2 = 5.64$) conditions. Third-body collision efficiencies were varied by a factor of 2 from their nominal values, η_o, for this local sensitivity analysis. The factor of 2 was considered a reasonable estimate of the uncertainties of the collision efficiencies. The authors of the n-heptane mechanism used a separate reaction, (R20), to represent hydrogen peroxide decomposition with water as a third-body reactant rather than include a third-body collision efficiency for water in (R18). Consequently, the sensitivity results for water were computed by varying the low-pressure A-factor of (R20) by a factor of 2. The local sensitivity coefficient was defined as the difference between the new and the baseline ignition delay times (i.e., ignition delay times with modified collision efficiencies and the nominal values respectively), normalized by the baseline ignition delay time. Two reactions were found to have significant impact on the predicted ignition delay times and heat release rates:

$$H + O_2(+M) \rightleftharpoons HO_2(+M) \quad \text{(R9)}$$

$$H_2O_2(+M) \rightleftharpoons 2OH(+M) \quad \text{(R18)}$$

All other reactions involving 3rd body collision efficiencies had negligible impact on the calculated ignition delay times.

Results of the sensitivity analysis for ignition delay time are presented in Fig. 10 for n-heptane at the conditions of $\phi = 1.0$, $P = 9.0$ atm, buffer gas:$O_2 = 5.62$. The results show a factor of 2 uncertainty in the values of the collision efficiencies can have as much as a 23% effect on ignition delay time for temperatures $\geqslant 750$ K. For all fuels, the sensitivities for all the buffer gases remained below 30% for (R18) throughout the entire temperature range at this pressure and dilution level. Sensitivity analysis of (R9) revealed that ignition delays were affected less than 10%/30%/5% for n-heptane/*iso*-octane/n-butanol respectively at this same initial condition.

Results of the sensitivity analysis for representative pressure and pressure derivative time histories are shown in Fig. 11 for $T = 700$ K for n-heptane at $\phi = 1.0$, $P = 9.0$ atm, buffer gas:$O_2 = 5.62$ and using CO_2 as the buffer gas. The first stage of ignition was unaffected by changes in the collision efficiencies for all fuels and buffer gases. Varying the collision efficiency of (R9) resulted in less than a 5% change of the ignition delay time for the n-heptane/carbon dioxide mixture. However, (R9) significantly altered the maximum rate of pressure rise in the second stage of ignition for the n-heptane/carbon dioxide mixture, by nearly a factor of two between the two limiting values of the collision efficiencies. The results

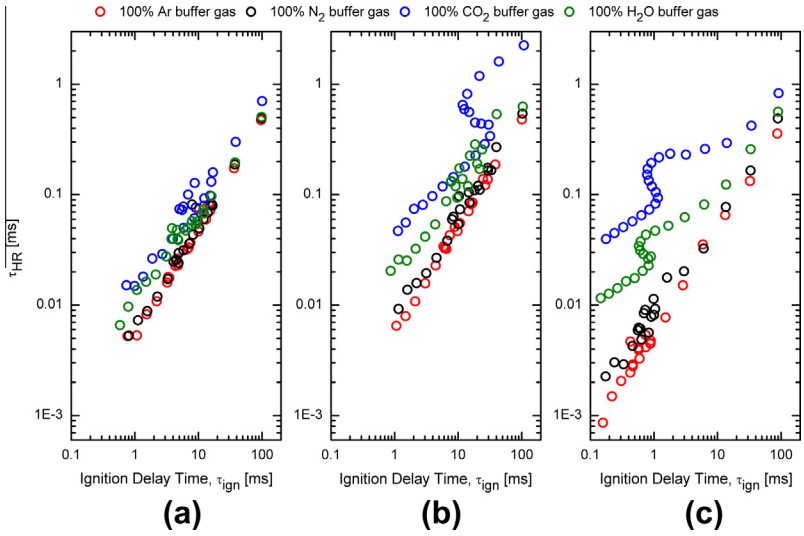

Fig. 9. Simulation results for characteristic times of heat release as a function of ignition delay time for stoichiometric *n*-heptane mixtures at initial conditions of: (a) $P = 9.0$ atm, buffer gas:$O_2 = 3.76$, (b) $P = 9.0$ atm, buffer gas:$O_2 = 5.62$, (c) $P = 60.0$ atm, buffer gas:$O_2 = 5.62$.

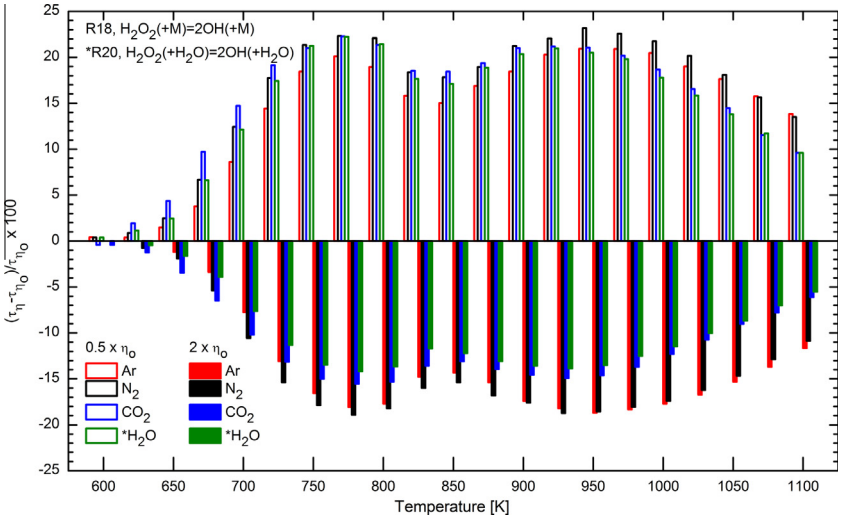

Fig. 10. Results of the sensitivity analysis of ignition delay time for *n*-heptane to changing the third body collision efficiencies of the reaction (R18) H_2O_2 (+M) = OH + OH (+M) by a factor of 2. The initial conditions of the simulations were $P = 9$ atm, *n*-$C_7H_{16} = 1.34\%$, $O_2 = 14.90\%$, buffer gas = 83.76%. *The H_2O sensitivity coefficients were determined by changing the A factor for reaction (R20) by a factor of 2. See text for details.

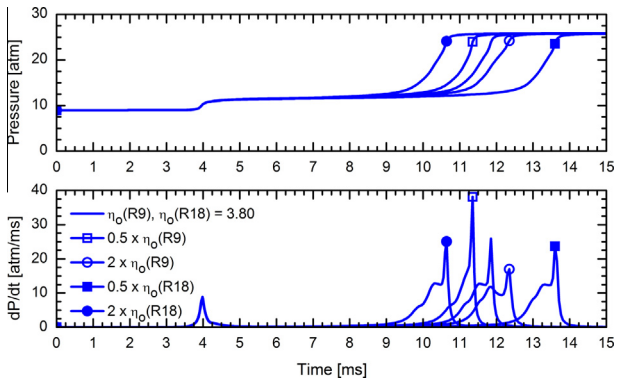

Fig. 11. Results of changing the collision efficiencies of reactions (R9) and (R18) on pressure and pressure derivative time histories of *n*-heptane at initial conditions of $T = 700$ K, $P = 9.0$ atm, *n*-$C_7H_{16} = 1.34\%$, $O_2 = 14.90\%$, $CO_2 = 83.76\%$.

for (R18) show while the ignition delay time was affected significantly, the maximum rate of pressure rise was nominally unchanged (<9%) for *n*-heptane/carbon dioxide. Water vapor showed similar effects to carbon dioxide on the pressure rise rate for *n*-heptane, while argon and nitrogen exhibited little sensitivity (<14% change). The pressure derivative time histories were less affected (<20% change) by changes in the collision efficiencies for (R9) and (R18) at 700 K for *iso*-octane or *n*-butanol for any of the buffer gases.

4. Conclusions

This study improves our understanding of the thermal and chemical kinetic effects of buffer gas composition on the important combustion characteristics of ignition and heat release rate for three reference fuels. Simulations were presented for *n*-heptane, *iso*-octane, and *n*-butanol in stoichiometric mixtures with four buffer gases (Ar, N_2, H_2O, and CO_2) for a range of pressures, dilution levels, and temperatures. Based on the conditions examined in this

study, low pressures (<10 atm), high levels of dilution (>1.5× that of air), and negative temperature coefficient conditions are most likely to result in significant thermal and chemical kinetic effects on ignition delay time and heat release rates due to the composition of buffer gases. Fuels that exhibit negative temperature coefficient behavior may show significantly more pronounced buffer gas effects during two stage ignition, with a factor of 2 or more impact on overall ignition times. Caution should be exercised when comparing and compiling data acquired in the NTC region from different experimental facilities that may have used different buffer gases. Ignition data are also subject to uncertainties in the collision efficiencies of the different buffer gases. Experimental data for *n*-heptane at high temperatures indicated a faster ignition for Ar compared to N_2 (on the order of a factor of 2); however, the model simulations predicted much smaller sensitivity to buffer gas composition for *n*-heptane. There are currently few experimental studies which target the effects of buffer gas composition on ignition; particularly studies that vary buffer gas composition using the same facility. Additional experimental and computational studies will reduce the chemical kinetic uncertainties associated with buffer gas composition, and such work has potential to significantly improve predictive understanding of the complex chemistry and thermal interactions of NTC behavior.

Acknowledgments

The authors acknowledge the generous financial support of the U.S. Department of Energy Basic Energy Sciences and the U.S. Department of Energy via the University of Michigan Consortium on Efficient and Clean High-Pressure, Lean Burn (HPLB) Engines.

Appendix A. Supplementary material

Supplementary data associated with this article can be found, in the online version, at http://dx.doi.org/10.1016/j.combustflame.2013.09.022.

References

[1] N. Ladommatos, S.M. Abdelhalim, H. Zhao, Z. Hu, Proc. Inst. Mech. Eng. 212 (1998) 25–42.
[2] M. Sjöberg, J.E. Dec, W. Hwang, SAE Technical Paper, 2007-01-0207, 2007.
[3] H. Machrafi, S. Cavadias, P. Guibert, Combust. Flame 155 (2008) 476–489.
[4] K. Al-Qurashi, A.D. Lueking, A.L. Boehman, Combust. Flame 158 (2011) 1696–1704.
[5] M. Sjöberg, J.E. Dec, Proc. Combust. Inst. 33 (2011) 3031–3038.
[6] D.F. Davidson, R.K. Hanson, Int. J. Chem. Kinet. 36 (2004) 510–523.
[7] J. Würmel, E.J. Silke, H.J. Curran, M.S. Ó Conaire, J.M. Simmie, Combust. Flame 151 (2007) 289–302.
[8] J. Würmel, J.M. Simmie, H.J. Curran, Int. J. Vehicle Des. 44 (2007) 84–106.
[9] H.S. Shen, J. Vanderover, M.A. Oehlschlaeger, Combust. Flame 155 (2008) 739–755.
[10] X. He, M.T. Donovan, B.T. Zigler, T.R. Palmer, S.M. Walton, M.S. Wooldridge, A. Atreya, Combust. Flame 142 (2005) 266–275.
[11] X. He, B.T. Zigler, S.M. Walton, M.S. Wooldridge, A. Atreya, Combust. Flame 145 (2006) 552–570.
[12] S.M. Walton, X. He, B.T. Zigler, M.S. Wooldridge, A. Atreya, Combust. Flame 150 (2007) 246–262.
[13] M.P. Halstead, L.J. Kirsch, C.P. Quinn, Combust. Flame 30 (1977) 45–60.
[14] R. Minetti, M. Carlier, M. Ribaucour, E. Therssen, L.R. Sochet, Proc. Combust. Inst. 26 (1996) 747–753.
[15] J.F. Griffiths, P.A. Halford-Maw, C. Mohamed, Combust. Flame 111 (1997) 327–337.
[16] S. Tanaka, F. Ayala, J.C. Keck, J.B. Heywood, Combust. Flame 132 (2003) 219–239.
[17] R. Minetti, M. Carlier, M. Ribaucour, E. Therssen, L.R. Sochet, Combust. Flame 102 (1995) 298–309.
[18] E.J. Silke, H.J. Curran, J.M. Simmie, Proc. Combust. Inst. 30 (2005) 2639–2647.
[19] D.M.A. Karwat, S.W. Wagnon, M.S. Wooldridge, C.K. Westbrook, Combust. Flame (2013), http://dx.doi.org/10.1016/j.combustflame.2013.06.029.
[20] D.J. Vermeer, J.W. Meyer, A.K. Oppenheim, Combust. Flame 18 (1972) 327–336.
[21] K. Fieweger, R. Blumenthal, G. Adomeit, Proc. Combust. Inst. 25 (1994) 1579–1585.
[22] D.F. Davidson, M.A. Oehlschlaeger, J.T. Herbon, R.K. Hanson, Proc. Combust. Inst. 29 (2002) 1295–1301.
[23] D.F. Davidson, B.M. Gauthier, R.K. Hanson, Proc. Combust. Inst. 30 (2005) 1175–1182.
[24] T. Malewicki, A. Comandini, K. Brezinsky, Proc. Combust. Inst. 34 (2013) 353–360.
[25] H.K. Ciezki, G. Adomeit, Combust. Flame 93 (1993) 421–433.
[26] B.M. Gauthier, D.F. Davidson, R.K. Hanson, Combust. Flame 139 (2004) 300–311.
[27] J. Herzler, L. Jerug, P. Roth, Proc. Combust. Inst. 30 (2005) 1147–1153.
[28] J.M. Smith, J.M. Simmie, H.J. Curran, Int. J. Chem. Kinet. 37 (2005) 728–736.
[29] H.S. Shen, J. Steinberg, J. Vanderover, M.A. Oehlschlaerger, Energy Fuels 23 (2009) 2482–2489.
[30] B. Akih-Kumgeh, J.M. Bergthorson, Energy Fuels 24 (2010) 2439–2448.
[31] D.M.A. Karwat, S.W. Wagnon, P.D. Teini, M.S. Wooldridge, J. Phys. Chem. A 115 (2011) 4909–4921.
[32] B.W. Weber, K. Kumar, Y. Zhang, C. Sung, Combust. Flame 158 (2011) 809–819.
[33] J.T. Moss, A.M. Berkowitz, M.A. Oehlschlaeger, J. Biet, V. Warth, P.A. Glaude, F. Battin-Leclerc, J. Phys. Chem. A 112 (2008) 10843–10855.
[34] G. Black, H.J. Curran, S. Pichon, J.M. Simmie, V. Zhukov, Combust. Flame 157 (2010) 363–373.
[35] R. Grana, A. Frassoldati, T. Faravelli, U. Niemann, E. Ranzi, R. Seiser, R. Cattolica, S. Kalyanasundaram, Combust. Flame 157 (2010) 2137–2154.
[36] K.E. Noorani, B. Akih-Kumgeh, J.M. Bergthorson, Energy Fuels 24 (2010) 5834–5843.
[37] K.A. Heufer, R.X. Fernandes, H. Olivier, J. Beeckmann, O. Röhl, N. Peters, Proc. Combust. Inst. 33 (2011) 359–366.
[38] S. Vranckx, K.A. Heufer, C. Lee, H. Olivier, L. Schill, W.A. Kopp, K. Leonhard, C.A. Taatjes, R.X. Fernandes, Combust. Flame 158 (2011) 1444–1455.
[39] I. Stranic, D.P. Chase, J.T. Harmon, S. Yang, D.F. Davidson, R.K. Hanson, Combust. Flame 159 (2012) 516–527.
[40] Reaction Design CHEMKIN Release 10113 (x64), 2012.
[41] M. Mehl, W.J. Pitz, C.K. Westbrook, H.J. Curran, Proc. Combust. Inst. 33 (2011) 193–200.
[42] H.J. Curran, P. Gaffuri, W.J. Pitz, C.K. Westbrook, Combust. Flame 129 (2002) 253–280.
[43] H.J. Curran, P. Gaffuri, W.J. Pitz, C.K. Westbrook, Combust. Flame 114 (1998) 149–177.
[44] P. Dagaut, S.M. Sarathy, M.J. Thomson, Proc. Combust. Inst. 32 (2009) 229–237.
[45] N. Donato, C. Zinner, H. Curran, G. Bourque, C. Aul, E. Petersen, J. Eng. Gas Turbines Power 132 (2010) 051502. pp. 1–9.
[46] C.J. Aul, W.K. Metcalfe, S.M. Burke, H.J. Curran, E.L. Petersen, Combust. Flame 160 (2013) 1153–1167.
[47] S.M. Villano, L.K. Huynh, H.H. Carstensen, A.M. Dean, J. Phys. Chem. A 115 (2011) 13425–13442.
[48] S.M. Villano, L.K. Huynh, H.H. Carstensen, A.M. Dean, J. Phys. Chem. A 116 (2012) 5068–5089.
[49] D.F. Davidson, D.R. Haylett, R.K. Hanson, Combust. Flame 155 (2008) 108–117.
[50] A.K. Oppenheim, Philos. Trans. R. Soc. Lond. Ser. A 315 (1985) 471–508.
[51] S.M. Walton, X. He, B.T. Zigler, M.S. Wooldridge, Proc. Combust. Inst. 31 (2007) 3147–3154.
[52] A.B. Mansfield, M.S. Wooldridge, High-pressure low-temperature ignition behavior of syngas mixtures, Combust. Flame, 2013 (submitted for publication).

energy&fuels

Article

pubs.acs.org/EF

Experimental and Modeling Study of Methyl *trans*-3-Hexenoate Autoignition

Scott W. Wagnon,*[,†] Darshan M. A. Karwat,[†,‡] Margaret S. Wooldridge,[†,‡] and Charles K. Westbrook[§]

[†]Department of Mechanical Engineering, and [‡]Department of Aerospace Engineering, University of Michigan, Ann Arbor, Michigan 48109, United States

[§]Lawrence Livermore National Laboratory, Livermore, California 94551, United States

Supporting Information

ABSTRACT: This work presents the results of an experimental and computational study of methyl *trans*-3-hexenoate autoignition. Experimental autoignition studies were conducted using the University of Michigan rapid compression facility. Pressure time histories were used to determine ignition delay times as a function of test gas composition and experimental conditions. The fuel/oxygen equivalence ratio and dilution level were ϕ = 0.3 and inert/O_2 = 3.76 (mole basis). End of compression conditions targeted an average pressure of 10.5 atm and temperatures ranging from 884 to 1085 K. A correlation in Arrhenius form was developed by regression analysis of the experimental data, where the ignition delay time is τ_{ign} (ms) = 1.4×10^{-6} exp[30 100/($\overline{R}_{(cal\ mol^{-1}\ K^{-1})}T$)] with a R^2 value of 0.99. Gas-sampling experiments were also conducted to measure stable intermediates formed during autoignition. A detailed reaction mechanism was developed and model predictions were compared to the experimental data. While ignition delay time predictions are in excellent agreement with the experimental data, the speciation results highlight uncertainties in the reaction chemistry of unsaturated esters and small hydrocarbon intermediates.

1. INTRODUCTION

With more stringent vehicle emission standards imminent and the rising demand for renewable energy, there are concerted efforts to transition to renewable fuels that can deliver higher efficiencies and lower emissions. Biodiesel fuels are promising alternatives to petroleum-derived fuels, particularly if they can be produced from feedstocks that do not compete with food crops. While much has been learned about the combustion properties of hydrocarbon fuels, much less is known on the combustion chemistry of oxygenated hydrocarbons, such as the methyl and ethyl esters that are the primary components of biodiesel fuels. The esters in biodiesel fuels are long-chain, typically C_{18}, species, and the majority, typically over 50%, are unsaturated compounds.[1−3] In addition, the unsaturated esters found in biodiesel fuels are often *cis* isomers of the compounds.[4] Few studies have examined the combustion behavior of stereoisomeric (*cis*/*trans*) olefins,[5−9] and to the authors' knowledge, no studies have investigated the effects of stereoisomerism coupled with an ester moiety. In a recent study, Hellier et al.[8] investigated octene isomers (including *cis*- and *trans*-3-octene) in a single-cylinder direct-injection diesel engine. Hellier et al.[8] concluded that *trans*-3-octene ignited slower than *cis*-3-octene at the conditions of their study because the *trans* conformation of olefins must isomerize to a *cis* configuration prior to proceeding through low-temperature pathways, in agreement with prior studies by Salooja[5] and Bounaceour et al.[7] Very recently, Fridyland et al.[9] studied four decene isomers (including *cis*- and *trans*-5-decene) at high-pressure (40−66 bar) conditions in a single-pulse shock tube over temperatures of 850−1500 K. Fridyland et al.[9] found that results for the two *cis*/*trans* isomers were indistinguishable for the conditions of their study. It is unclear based on the available literature whether proposed biodiesel surrogates should consist of *cis* or *trans* (or both) compounds to appropriately capture the combustion kinetics of real biodiesel fuels, and studies of both isomeric forms in esters should be considered relevant.

While much has been learned from these and previous hydrocarbon studies, the structural features of chain length and degree of saturation are not as well understood for esters. Early studies evaluated methyl butanoate and other C_5 esters proposed as the smallest structural unit necessary to represent the chemical kinetics important in biodiesel fuels.[10−28] These efforts produced key data on reactivity and reaction pathways; however, these works also revealed that longer chain esters are required to accurately represent biodiesel fuel combustion pathways, in particular the negative temperature coefficient behavior observed with real biodiesel fuels.[1,29]

Computational and experimental efforts have expanded to evaluate the reaction chemistry of longer chain esters, such as methyl hexanoate (a saturated C_7),[30] methyl heptanoate (a saturated C_8),[31] methyl decanoate (a saturated C_{11}),[1,32,33] methyl dec-5-enoate and methyl dec-9-enoate (two unsaturated C_{11} species),[2,34] methyl laurate (a saturated C_{13}),[33] methyl myristate (a saturated C_{15}),[33] methyl palmitate (a saturated C_{17}),[33,35] methyl oleate (an unsaturated C_{19}),[33,36,37], and methyl linoleate (a polyunsaturated C_{19}).[37] A recent kinetic model for biodiesel fuels, including both soy and rapeseed methyl ester fuels,[38] has pointed to a critical need for better understanding of the kinetics of C=C double bonds that are components of practical biodiesel fuels. Even more recently, Zhang et al.[39] studied the oxidation of methyl *trans*-3-hexenoate/nitrogen mixtures in a jet-stirred reactor at high

Received: August 12, 2014
Revised: October 7, 2014
Published: October 24, 2014

   dx.doi.org/10.1021/ef501806s | *Energy Fuels* 2014, 28, 7227−7234

pressure (P = 10 atm), for several equivalence ratios (ϕ = 0.6, 1.0, 2.0), and low temperatures (T = 560−1220 K), from which a chemical kinetic mechanism was developed and validated. Zhang et al.[39] concluded that lower temperature oxidation was slowed by the presence of the double bond and higher temperature oxidation resulted in the production of more unsaturated (both mono- and poly-) and oxygenated intermediate species relative to the saturated methyl hexanoate.

Despite this recent progress, there is a clear need for more data and understanding of the effects of ester, allylic, and vinylic structures on combustion kinetics. This work presents the results of an experimental and computational investigation of the autoignition chemistry of methyl *trans*-3-hexenoate (mh3d, $C_7H_{12}O_2$), an unsaturated C_7 ester. The results highlight progress in understanding and remaining uncertainties in unsaturated ester combustion chemistry.

2. EXPERIMENTAL SECTION

Autoignition data and intermediate species concentrations for mh3d/air mixtures were obtained using the University of Michigan rapid compression facility (UM RCF). Autoignition delay studies quantify the reactivity of reference compounds over a range of thermodynamic state conditions and mixture compositions using ignition delay times (τ_{ign}). Measurements of intermediate species identify and quantify reaction pathways important during autoignition.

2.1. Autoignition Studies. A complete description of the UM RCF, including dimensions, characterization results, and diagnostic capabilities, can be found in the studies by Donovan et al.[40,41] Five primary modules combine to form the UM RCF: the driver section, the driven section, the test section, the sabot, and the hydraulic control valve assembly. A scored polyester film and the hydraulic globe valve assembly seal the driver section from the stainless-steel driven section. The sabot abuts the polyester film and, at the start of an experiment, is seated at the upstream end of the driven section. The sabot consists of a deformable ultrahigh-molecular-weight polyethylene nosecone (outer diameter of the sealing surface = 5.28 cm) and a Delrin body (outer diameter = 10.01 cm). The test section is located at the downstream end of the driven section and is sealed using a 12.7 mm thick polycarbonate plate, which provides end-view optical access. The test section is connected to the driven section by a convergent section, which bridges the larger diameter of the driver and driven sections (inner diameter = 10.13 cm) to the smaller diameter of the test section (inner diameter = 5.08 cm).

For each experiment, a diffusion pump is used to evacuate the driven and test sections. Mixtures of fuel (methyl *trans*-3-hexenoate, Sigma-Aldrich, 98%), oxygen, and inert gases are prepared in a dedicated mixing tank, where composition is determined using partial pressures measured using a capacitance diaphragm gauge (Varian CeramiCel VCMT12TFA). Prepared mixtures are then used to fill the driven and test sections. The driver section is pressurized with air, and when the globe valve is opened, the polyester film is broken and the high-pressure air accelerates the sabot compressing the test gas mixture. At the end of the compression stroke, the nosecone of the sabot seals the test gas mixture in the test section through an interference fit between the annulus of the nosecone and the test section. Because of the unique geometry of the sabot and convergent section, bridging the driven and test sections, the colder boundary layer gases are trapped outside the test section. This approach minimizes heat losses and ensures long test times at uniform state conditions.

The pressure time history within the test section is measured using a piezoelectric transducer (Kistler 6041AX4) in series with a charge amplifier (Kistler 5010B). A high-speed color digital video camera (Vision Research Phantom, version 7.1) is used to record the chemillunimescence emitted during an experiment. The imaging data are used to characterize the spatial uniformity of ignition, which is critical for the localized gas-sampling methods applied here. Videos were taken at 26 000 frames per second (fps) with an exposure time of 38 μs with a fast 50 mm lens (f/0.95, Navitar) and a c-mount extension tube. Please refer to the study by Walton et al.[42] for further details regarding the high-speed optical imaging setup.

2.2. High-Speed Gas-Sampling Studies. Measurements of intermediate species are made using discrete sampling events applied to autoignition experiments each targeting the same end-of-compression conditions. Details on the high-speed gas-sampling system and the gas chromatography analysis are provided by Karwat et al.[43] The methods are described briefly here. For gas-sampling experiments, the transparent end wall is replaced with a stainless-steel plate equipped with two sampling systems located at opposite positions on the stainless-steel plate, i.e., 180° apart. Each sampling tube (0.20/0.32 cm, inner diameter/outer diameter) extends ∼10 mm into the volume of the test section. Each sampling system includes a fast sampling valve (a modified Festo MHE3 valve with a stock response time of 3 ms, 3 mm orifice), a sampling chamber (4.5 ± 0.5 mL), a piezoresistive pressure transducer (Kistler 4045A2) and amplifier (Kistler 4618A0), a septa port (VICI Valco, low bleed), and an isolation valve. Before each experiment, the sampling chambers are evacuated. During an experiment, samples are acquired by triggering the fast valves using a pulse generator (Stanford Research Systems DG535). Sampling times of the modified valves are ∼1.5 ms. When the timing of the trigger signals is changed, samples can be acquired at any time during the autoignition delay period. To provide good temporal resolution, end-of-compression conditions leading to an ignition delay time of ∼14.6 ms were used for this study. Further, sampling simultaneously at two locations provides a measurement of the spatial homogeneity of the test gases. The gases are quenched by expansion into the evacuated sampling chambers (ratio of the test section volume/sample volume of ∼39:1). After an experiment, a portion of each gas sample is removed via syringe (Hamilton Gastight 1010, 10 mL) through the septa port and injected into gas chromatographs (GCs) for analysis. A complete description of the GC systems and methods of calibration are provided in the Supporting Information.

3. REACTION MECHANISM DEVELOPMENT

A reaction mechanism for mh3d was developed on the basis of the mechanism by Herbinet et al.[2] for methyl dec-5-enoate. The key features of the mechanism were found to be those portions that describe the effects of the C═C double bond, which is located at the midpoint or "3" location in the chain of five carbon−carbon bonds in the fuel, which can be described as

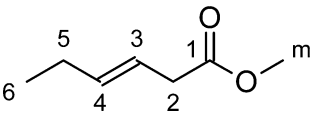

The C atoms are labeled, starting with the C atom in the C═O bond as 1. In contrast with saturated methyl esters, the vinyl C−H bonds (carbon sites 3 and 4) are very strong and those H atoms are difficult to abstract. The C−H bonds at the C atoms adjacent to the double bond (carbon sites 2 and 5) are very weak allylic bonds, and these H atoms are preferentially abstracted by reactive radical species during autoignition and oxidation of mh3d. As a result, the dominant alkyl-like radicals produced during mh3d combustion are these allylic radicals.

4. RESULTS AND DISCUSSION

4.1. Ignition Delay Time. A typical plot of the test section pressure and pressure derivative from a mh3d autoignition experiment is presented in Figure 1. The maximum pressure at the end of compression (EOC) is defined as t = 0 s and labeled P_{max}. The time from the end of compression to the maximum rate of pressure rise is defined as the ignition delay time for the experiment, i.e., the time between P_{max} and dP/dt_{max}. Figure 1

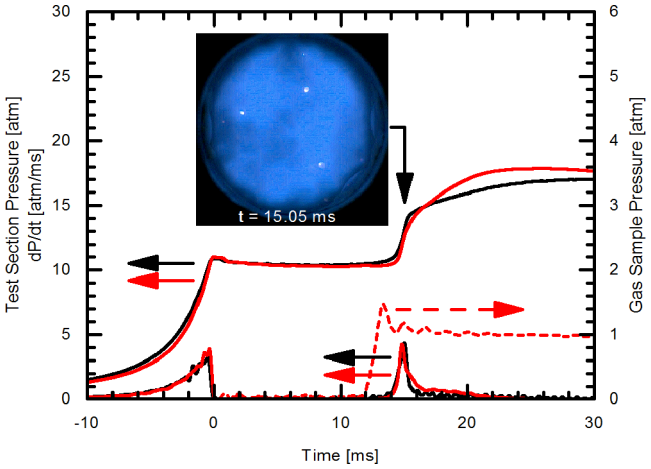

Figure 1. Typical results for test section pressure (imaging and speciation experiments), sampling chamber pressure, and pressure derivative time histories. The inset image corresponds to t = 15.05 ms. Imaging experiment (black solid lines): P_{eff} = 10.6 atm, T_{eff} = 937 K, ϕ = 0.30, inert/O_2 ratio = 3.76, χ(mh3d) = 0.69%, $\chi(O_2)$ = 20.86%, $\chi(N_2)$ = 73.74%, $\chi(CO_2)$ = 4.70%, and τ_{ign} = 15.2 ms. Speciation experiment (red solid and dashed lines): P_{eff} = 10.4 atm, T_{eff} = 938 K, ϕ = 0.28, inert/O_2 ratio = 3.77, χ(mh3d) = 0.65%, $\chi(O_2)$ = 20.84%, $\chi(N_2)$ = 76.13%, $\chi(CO_2)$ = 2.37%, τ_{ign} = 14.9 ms, and t_{sample} = 11.2 ms.

also presents typical pressure time histories of a sampling experiment and the corresponding pressure data from one of the sample chambers. During sampling experiments, individual trigger pulses are used to actuate the two sampling systems. A frame from the imaging data corresponding to the pressure time history of the non-gas-sampling ignition experiment is presented as an inset in Figure 1. The image shows that autoignition is volumetric and characterized by blue emission (attributed to C_2 and CH radicals).[44,45] The maximum intensity of the emission corresponds to the peak in the pressure derivative.

The effective pressure (P_{eff}) for each experiment is defined as the time-integrated average pressure from P_{max} to dP/dt_{max}, which captures heat losses from the test section. The effective temperature (T_{eff}) for each experiment is determined by numerically integrating the isentropic compression equation and using the known values of P_{eff}, the initial charge pressure, the initial temperature (~295 K), and the temperature-dependent ratio of the specific heats of the unreacted test gas mixture, which are determined using the NASA thermodynamic polynomial formatted fits[46] to their thermodynamic properties. A summary of all experimental conditions and results is presented in Table S1 of the Supporting Information. Equivalence ratio (ϕ) is defined as the molar ratio of the fuel/oxygen divided by the stoichiometric ratio of fuel/oxygen. Different inert gases (argon, carbon dioxide, and nitrogen) were used in the study to control (partially) the end of compression conditions via the ratio of the specific heats of the test gas mixture. Experimental conditions were held at a fixed equivalence ratio of ϕ = 0.3 and a fixed inert gas/oxygen ratio of 3.76. P_{eff} targeted 10.5 atm and the data range from 9.5 to 11.5 atm, and T_{eff} spans 884−1085 K.

Regression analysis was used to develop an expression for τ_{ign} (ms) as a function of the temperature. An Arrhenius form of the fit equation was used, and the result with R^2 = 0.99 is

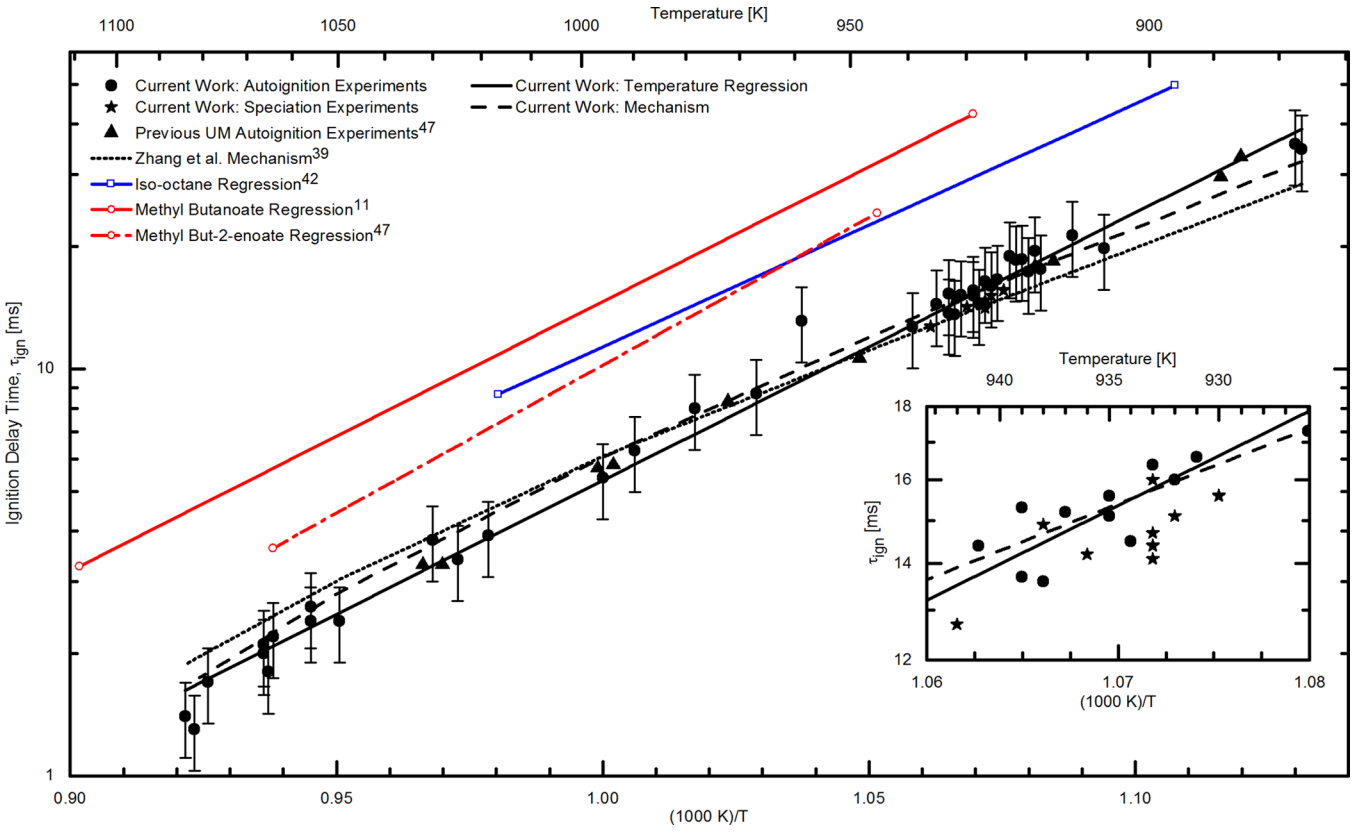

Figure 2. Results for experimentally measured methyl *trans*-3-hexenoate ignition delay time and comparison to other fuel ignition characteristics. The mh3d data were acquired at nominal conditions of P = 10.5 atm, ϕ = 0.30, and $\chi(O_2)$ = 20.90%. Please see the main text for details.

dx.doi.org/10.1021/ef501806s | *Energy Fuels* 2014, 28, 7227−7234

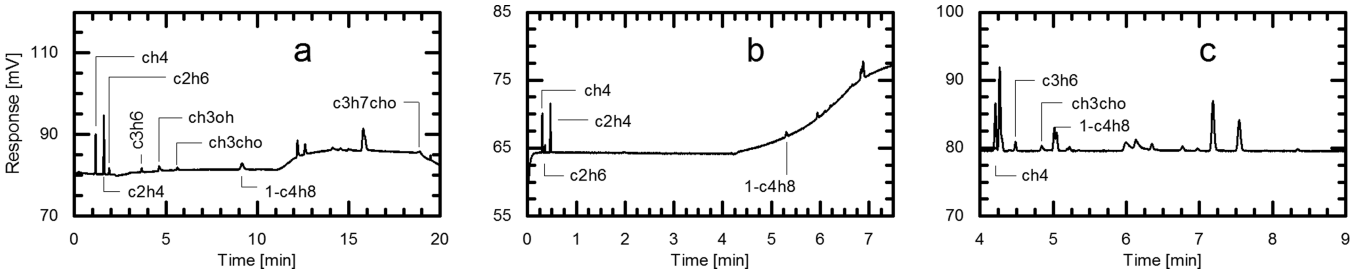

Figure 3. Typical gas chromatograms from methyl *trans*-3-hexenoate experiments: (a) GC2, oxygenates; (b) GC3, smaller hydrocarbons; and (c) GC4, larger hydrocarbons. The data are from the speciation experiment shown in Figure 1.

$$\tau_{ign} = 1.4 \times 10^{-6} \exp\left[\frac{30100}{\bar{R}_{(\text{cal K}^{-1}\,\text{mol}^{-1})}T}\right] \quad (1)$$

A summary of the autoignition data and eq 1 are presented in Figure 2. The subset of data that correspond to the speciation experiments is highlighted by the inset in Figure 2. The autoignition delay measurements are highly repeatable, as evidenced by the standard deviation of 0.9 ms or ±6% over the temperature range of 930−938 K, where most of the gas-sampling experiments were conducted. The overall uncertainty in the ignition delay time measurements is ±21%, which is based on experimental accuracy of the state conditions. The two largest contributors to the experimental uncertainty are the accuracy of the pressure transducer ($\pm 0.5\%_{FS}$) and the concentration of mh3d in the mixture. A more detailed discussion surrounding the uncertainty of the mh3d concentration is provided in section 4.2.

The experimental ignition delay time data of mh3d are compared to results of previous autoignition studies of iso-octane,[42] methyl butanoate,[11] and methyl but-2-enoate[47] in Figure 2. Regression correlations were used to normalize the previous results to the conditions considered in this study, i.e., P = 10.5 atm, ϕ = 0.3, and $\chi(O_2)$ = 20.9%. The data show a clear progression from the least reactive saturated C_5 ester methyl butanoate, to unsaturated C_5 ester, to the fastest ignition observed with unsaturated C_7. The current work supports our understanding of the effects of chain length and the double bond leading to faster ignition chemistry as observed in other studies, including recent work by Wang et al.[34] Negative temperature coefficient behavior is not observed for any of the fuels at these temperatures and pressures.

The reaction mechanism developed in this study and the mechanism by Zhang et al.[39] were used with the CHEMKIN software to model a zero-dimensional (0D), adiabatic, constant volume reactor while solving the energy equation at the average conditions of the experiments. Inert gas composition was varied during the simulations to reflect the changes made experimentally to control the end of compression temperatures. The results of the model predictions are presented in Figure 2 as the dashed line (current work) and dotted line (Zhang et al.[39]). During the process of developing the reaction mechanism (provided in the Supporting Information) in the current work, sensitivity analysis was performed to identify important reactions.

Although recent experimental and kinetic modeling studies of saturated methyl esters[31,32,48−51] have identified the reaction pathways that are important over a wide range of reaction temperatures and pressures, the present modeling study focused primarily on the main novel feature of the fuel molecule, mh3d, specifically the effects of the C═C double bond in the middle of the carbon chain in the molecule. As noted above, the primary fuel consumption reactions are the abstractions of H atoms from the "2" and "5" sites in the molecule and the subsequent reactions of the resonantly stabilized allylic radicals that these abstraction reactions produce. While production of both allylic radicals involves breaking an allylic C−H bond, the C−H bond at the "2" site is somewhat weaker because of the adjacent carbonyl group, as noted by Zhang et al.;[39] therefore, mh3d2j is produced in somewhat larger amounts than mh3d5j. At temperatures below about 850 K, the stability of these allylic radicals and the weak bonds between them and molecular oxygen retards ignition.[52,53] However, the present study was carried out at higher temperatures, where O_2 addition reactions to alkyl or alkenyl radicals are not important. Instead, the most important reactions specifically related to the presence of the C═C double bond in the present reaction mechanism are the thermal decomposition reactions of the allylic alkenyl radicals, mh3d2j and mh3d5j

$$\text{mh3d2j} = CH_3O + C_4H_7CHCO\ (C{-}C{-}C{=}C{-}C{=}C{=}O)$$

$$\text{mh3d2j} \leftrightarrow \text{mh2d4j} = CH_3 + \text{mf24d}\ (C{=}C{-}C{=}C{-}(C{=}O){-}O{-}C)$$

$$\text{mh3d5j} \leftrightarrow \text{mh4d3j} = CH_3OCO + C_5H_8\text{-}13\ (C{-}C{=}C{-}C{=}C)$$

which show how the decomposition reactions can proceed via their resonant isomers. The locations of the double bonds in the decomposition products are also noted above. The subsequent reactivity of the products of these decompositions is difficult to predict, for two major reasons, both of which are caused by the presence of multiple double bonds in these products. First, the thermochemistry of these species has not been well studied, and the equilibria and reverse reaction rates of each of the decomposition reactions can be very sensitive to the thermochemistry. This is particularly important because the reaction rates of these reactions are written in the thermoneutral addition direction, with the endothermic decomposition rates determined from the thermochemistry. Furthermore, the reaction rates and kinetic pathways of species with multiple double bonds have not received nearly as much attention and study as the reactions of saturated species or species with one double bond; therefore, the reaction rates and product distributions for many reactions of species that are intermediates of mh3d combustion, such as C_4H_7CHCO, mf24d, and C_5H_8-13 (1,3-pentadiene), are mostly estimated and subject to significant uncertainties. The reactions and rates for mh3d itself can be estimated with some confidence using existing information, as demonstrated in the present study and the earlier modeling work by Zhang et al.,[39] but the greatest uncertainties lie in the reaction rates and product distributions of the allylic radical intermediates of mh3d oxidation.

dx.doi.org/10.1021/ef501806s | Energy Fuels 2014, 28, 7227−7234

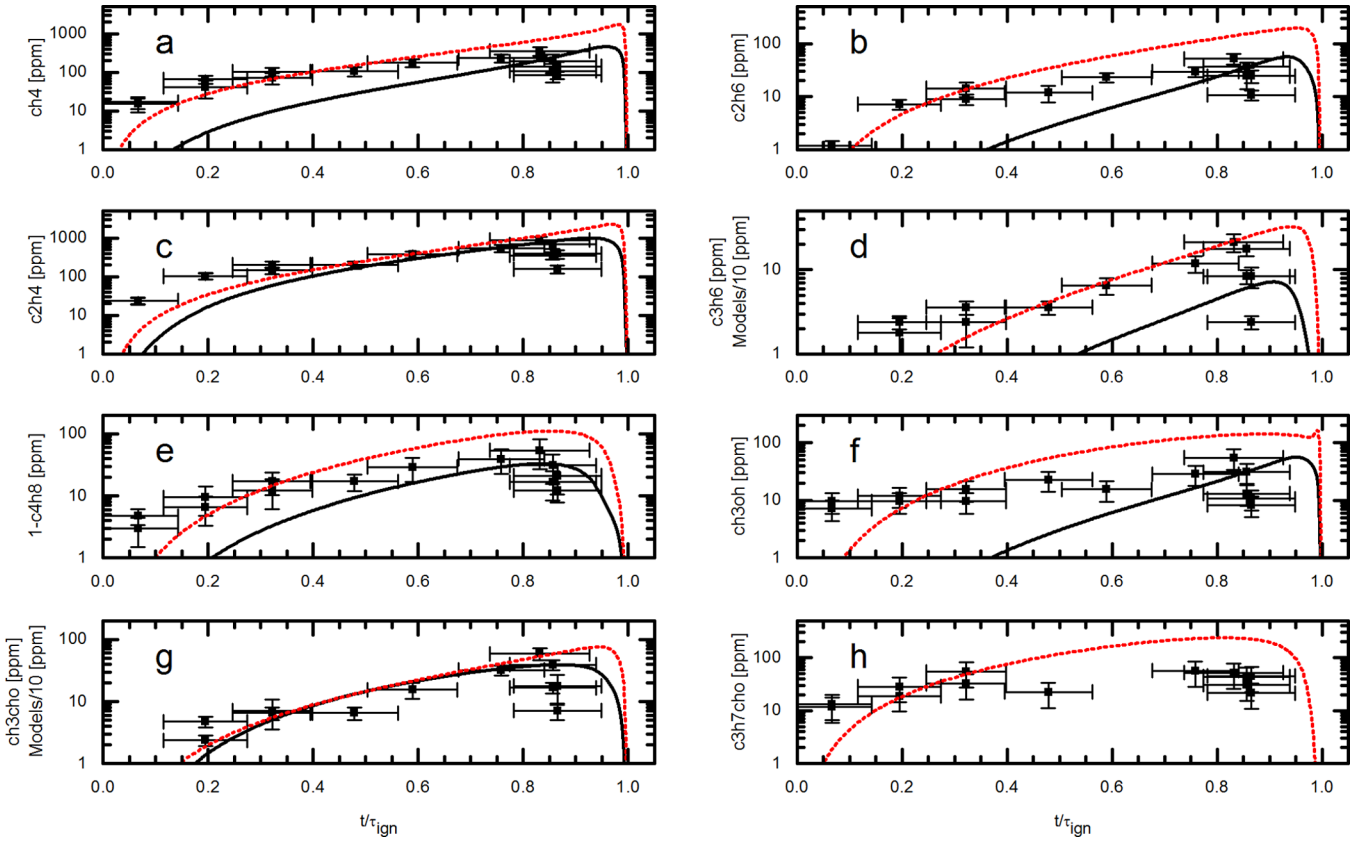

Figure 4. Stable intermediate time histories (mole fraction) during mh3d autoignition: (a) methane, (b) ethane, (c) ethene, (d) propene, (e) 1-butene, (f) methanol, (g) ethanal, and (h) butanal. Results of the current work are represented as symbols (experiments) and the solid line (mechanism), and results using the mechanism by Zhang et al.[39] are shown by the red dotted line. Average conditions for the sampling experiments were P_{eff} = 10.3 atm, T_{eff} = 934 K, ϕ = 0.30, $\chi(O_2)$ = 20.90%, and inert/O_2 = 3.76. In panel h, the predictions from the developed mechanism are not visible on the scale presented (<18 ppb).

4.2. Intermediate Species. The results of the gas-sampling experiments are presented in Figure 3. Figure 3 presents typical gas chromatograms used to identify and quantify intermediate species from mh3d autoignition experiments. Some features of the chromatograms were both identified and quantified. Methane (CH_4) and 1-butene (C_4H_8-1) eluted distinctly across all three GC systems and showed excellent agreement between the measured concentrations. Ethane (C_2H_6), ethene (C_2H_4), ethanal (CH_3CHO), and propene (C_3H_6) eluted distinctly across two of three GC systems and also showed excellent agreement in measured concentrations. Only GC2 was capable of quantifying methanol. Ethyne (C_2H_2), ethanol (C_2H_5OH), propane (C_3H_8), and but-3-en-1-ol (C_4H_7OH) were below the detectable limits (<10 ppm). Butanal (C_3H_7CHO) was found to be most accurately quantified by calibrations using peak response height. A fourth column (DB-WAX, Agilent J&W) via flame ionization detector (FID) was used to identify methyl *trans*-3-hexenoate; however, a reliable calibration could not be determined.

Figure 4 presents the measured results for the stable intermediates, where the time scale has been normalized from t/τ_{ign} = 0 (end of compression) to t/τ_{ign} = 1 (autoignition). The experimental results are the average of the measurements from the two sampling systems and from the multiple columns (where available). The horizontal and vertical error bars represent the uncertainty in the sample time (±1.2 ms) and the measured species (±50%), respectively. The large (±50%) uncertainty associated with the measured species concentrations stems from the effects of the boundary layer in the test section (±16%) and the lack of a reliable calibration for methyl *trans*-3-hexenoate (±25%) for the mixture compositions used in this study. In comparing the experimental data, ethene and methane were formed in the highest concentrations with peak values of over 300 ppm. All of the other measured intermediates were formed at values less than 100 ppm.

The speciation data are compared to predictions from the two reaction mechanisms in Figure 4. A 0D, isometric, adiabatic CHEMKIN simulation was used for the mechanism predictions, where the initial conditions were the average conditions of the sampling experiments: P_{eff} = 10.3 atm, T_{eff} = 934 K, ϕ = 0.29, $\chi(O_2)$ = 20.85%, and inert/O_2 = 3.76. The agreement between the experimental data and the mechanism developed in the current work is generally quite good, typically within a factor of 2 of and within the experimental uncertainties.

For the species that were monitored in the experiments yet below the detectable limits of the GC systems, the mechanism was in good agreement, predicting mole fractions of less than 3 ppm for ethanol and less than 1 ppm for propane. However, the developed mechanism only predicts trace amounts of butanal, less than 18 ppb, which does not agree with the experimental results as shown in Figure 4h. The isomer but-3-en-1-ol was not included in the kinetics model developed, but predictions for isomers but-1-en-1-ol and but-2-en-1-ol remain below 5 ppm each during the ignition delay time. Ethyne mole fractions of over 1500 ppm were predicted by the model, which is

dx.doi.org/10.1021/ef501806s | *Energy Fuels* 2014, 28, 7227−7234

significantly higher than the upper limit determined experimentally of less than 10 ppm.

Model predictions based on the mechanism by Zhang et al.[39] are included in Figure 4. The predictions are consistently higher than the predictions using the reaction mechanism developed in the current work. The level of agreement with the experimental data is generally good (within a factor of 3) with the exception of the peak values predicted from some of the unsaturated species (ethyne and propene) and ethanal, which differ by a factor of 10 or more. Recall that both reaction mechanisms were in good agreement with the experimental data for ignition delay time. Each reaction mechanism indicates that the allylic C−H bonds adjacent to the carbonyl group are weak and the vinylic bonds are strong when compared to the C−H bonds at equivalent sites found in saturated fuels. These agreements and others on the effect of the double bond in mh3d lead to trend-wise agreement in the predicted effects at low and high temperatures (e.g., increased ignition delay times at low temperatures and increased production of unsaturated and oxygenated species at high temperatures). However, there are numerous species and reactions in each mechanism that are absent from the other; i.e., the reaction pathways predicted by each may differ significantly. A complete understanding of the similarities and discrepancies in the two reaction mechanisms for predicting the small intermediates is beyond the scope of the current study and may not yield definitive conclusions. The differences between the predictions of the two mechanisms highlight the complexity and uncertainty of modeling the reaction pathways for forming and consuming these small intermediate species. The results further highlight the importance of ignition delay time and speciation data for providing rigorous targets for understanding reaction pathways and validating chemistry.

The sampled intermediate species (i.e., methane, methanol, ethane, ethene, ethanal, propene, 1-butene, and butanal) account for ∼6.1% of carbon and ∼8.3% of hydrogen late in the ignition delay period (t/τ_{ign} = 0.83). In comparison, the developed mechanism predicts values of ∼5.6% of carbon and ∼6.7% of hydrogen for the same species at the same normalized time. While the species measured do not close the carbon or hydrogen balance in the system, the experimental data provide valuable information on the intermediate reaction pathways important during mh3d autoignition. Figure 5 shows the normalized species time histories predicted for mh3d, CO_2, and CO based on the modified reaction mechanism, where the data are normalized by the amount of carbon in mh3d in the initial mixture. A significant amount of initial mh3d remains well into the ignition delay time period (∼23.2% at 83% of the ignition delay time), while CO and CO_2 formation proceed with less than 15% of m3hd carbon contained in these two species by 90% of the ignition delay time.

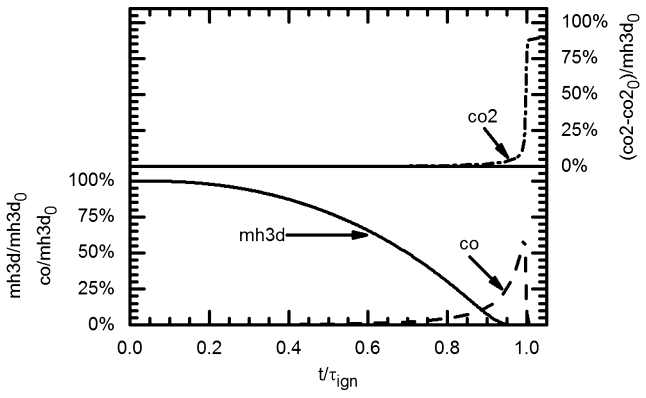

Figure 5. Simulation results for methyl *trans*-3-hexenoate, CO_2, and CO for P = 10.3 atm, T = 934 K, ϕ = 0.30, $\chi(O_2)$ = 20.90%, and inert/O_2 = 3.76. All results are normalized by the amount of carbon in mh3d in the initial mixture.

Figure 6 presents the normalized values for the 15 species with the highest concentrations at the time corresponding to t/τ_{ign} = 0.83. These species account for ∼74.3% of the carbon from the initial mh3d in the mixture. CO_2 from products of combustion accounts for less than 1.0% of carbon from mh3d at 83% of the ignition delay time. The simulations indicate 5 of the top 15 carbon-containing species include unsaturated methyl ester intermediates with two or more alkenyl groups (18.9% of mh35d, mh34d, and mh235d) and some with alkenyl and alkynyl groups (3.5% of mf2d4t and mh3t5d). Aldehydes, such as methanal (CH_2O), ethanal (CH_3CHO), and unsaturated propenal (C_2H_3CHO), compose a significant portion (∼4.5%) of the remaining predicted stable carbon species.

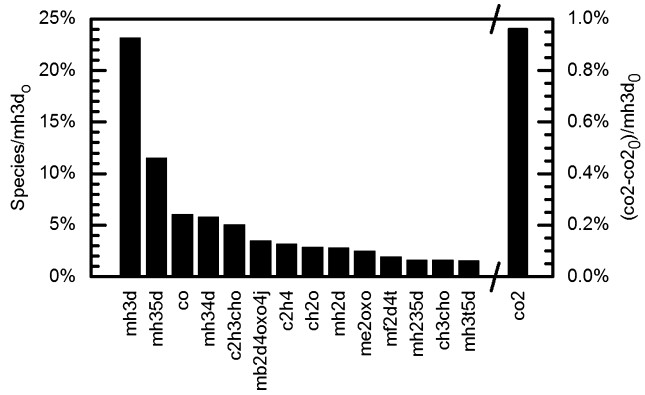

Figure 6. Simulation results at the time corresponding to τ_{ign} = 0.83 for the 15 carbon-containing species with the highest concentrations during ignition for P = 10.3 atm, T = 934 K, ϕ = 0.30, $\chi(O_2)$ = 20.90%, and inert/O_2 = 3.76. All results are normalized by the amount of carbon in mh3d in the initial mixture.

The speciation results of this study provide an interesting new challenge for kinetic modeling that underscores the importance of new studies of unsaturated methyl ester fuels. The first few reactions for fuels with one or more C═C double bonds are not much different from those of saturated fuels, but eventually, smaller fragment species are produced with one or more double bonds. In the present mechanism, it is clear that the intermediate reactions produce too much ethyne, relative to the experimentally measured value, which is evidence that this portion of the reaction mechanism needs further attention. Further studies of unsaturated methyl esters are needed to improve the understanding of the combustion kinetics of these important fuel compounds.

5. CONCLUSION

The current work presents new measurements of methyl *trans*-3-hexenoate ignition delay times and intermediate species formed during mh3d ignition. Such data are vital to understand the effects of unsaturated esters on combustion kinetics. The autoignition data quantify the faster autoignition of the longer

dx.doi.org/10.1021/ef501806s | Energy Fuels 2014, 28, 7227−7234

chain ester compared to other shorter length saturated and unsaturated esters. The study also identifies areas of high uncertainty in the reaction chemistry for unsaturated esters, including the change in the reaction rates of important R + O_2 reactions compared to unsaturated esters, and the reaction pathways involving smaller unsaturated and polyunsaturated stable and radical species. The kinetic features associated with the C=C double bond are important, and these experimental data inform model development and guide further experimental studies to quantify the combustion chemistry of practical biodiesel and related fuels.

■ ASSOCIATED CONTENT

Supporting Information

Description of the GC systems and calibration gases, summary of experimental conditions and results for methyl *trans*-3-hexenoate autoignition (Table S1), and summary of experimental conditions and results for mh3d sampling experiments (Table S2). This material is available free of charge via the Internet at http://pubs.acs.org.

■ AUTHOR INFORMATION

Corresponding Author

*Telephone: 734-763-7470. Fax: 734-647-3170. E-mail: swagnon@umich.edu.

Notes

The authors declare no competing financial interest.

■ ACKNOWLEDGMENTS

This material is based on work supported by the program of the Office of Basic Energy Sciences, Office of Science, U.S. Department of Energy, under Award DE-SC0002645.

■ REFERENCES

(1) Herbinet, O.; Pitz, W. J.; Westbrook, C. K. *Combust. Flame* **2008**, *154*, 507−528.
(2) Herbinet, O.; Pitz, W. J.; Westbrook, C. K. *Combust. Flame* **2010**, *157*, 893−908.
(3) Hoekman, S. K.; Broch, A.; Robbins, C.; Ceniceros, E.; Natarajan, M. *Renewable Sustainable Energy Rev.* **2012**, *16*, 143−169.
(4) Coniglio, L.; Bennadji, H.; Glaude, P. A.; Herbinet, O.; Billaud, F. *Prog. Energy Combust. Sci.* **2013**, *39*, 340−382.
(5) Salooja, K. C. *Combust. Flame* **1968**, *12*, 401−410.
(6) Hughes, R.; Prodhan, A. S. *Combust. Flame* **1973**, *20*, 297−301.
(7) Bounaceur, R.; Warth, V.; Sirjean, B.; Glaude, P. A.; Fournet, R.; Battin-Leclerc, F. *Proc. Combust. Inst.* **2009**, *32*, 387−394.
(8) Hellier, P.; Ladommatos, N.; Allan, R.; Filip, S.; Rogerson, J. *Fuel* **2013**, *105*, 477−489.
(9) Fridlyand, A.; Goldsborough, S. S.; Brezinsky, K.; Merchant, S. S.; Green, W. H. *Proc. Combust. Inst.* **2014**, DOI: 10.1016/j.proci.2014.06.020.
(10) Fisher, E. M.; Pitz, W. J.; Curran, H. J.; Westbrook, C. K. *Proc. Combust. Inst.* **2000**, *28*, 1579−1586.
(11) Walton, S. M.; Wooldridge, M. S.; Westbrook, C. K. *Proc. Combust. Inst.* **2009**, *32*, 255−262.
(12) Parsons, B. I.; Hinshelwood, C. J. *J. Chem. Soc.* **1956**, 1799−1803.
(13) Hoare, D. E.; Ting-Man, L.; Walsh, A. D. *Proc. Combust. Inst.* **1967**, *11*, 879−887.
(14) Gaïl, S.; Thomson, M. J.; Sarathy, S. M.; Syed, S. A.; Dagaut, P.; Diévart, P.; Marchese, A. J.; Dryer, F. L. *Proc. Combust. Inst.* **2007**, *31*, 305−311.
(15) Gaïl, S.; Sarathy, S. M.; Thomson, M. J.; Diévart, P.; Dagaut, P. *Combust. Flame* **2008**, *155*, 635−650.
(16) Sarathy, S. M.; Gaïl, S.; Syed, S. A.; Thomson, M. J.; Dagaut, P. *Proc. Combust. Inst.* **2007**, *31*, 1015−1022.
(17) Metcalfe, W. K.; Dooley, S.; Curran, H. J.; Simmie, J. M.; El-Nahas, A. M.; Navarro, M. V. *J. Phys. Chem. A* **2007**, *111*, 4001−4014.
(18) Farooq, A.; Davidson, D. F.; Hanson, R. K.; Huynh, L. K.; Violi, A. *Proc. Combust. Inst.* **2009**, *32*, 247−253.
(19) Dooley, S.; Curran, H. J.; Simmie, J. M. *Combust. Flame* **2008**, *153*, 2−32.
(20) Hakka, M. H.; Bennadji, H.; Biet, J.; Yahyaoui, M.; Sirjean, B.; Warth, V.; Coniglio, L.; Herbinet, O.; Glaude, P. A.; Billaud, F.; Battin-Leclerc, F. *Int. J. Chem. Kinet.* **2010**, *42*, 226−252.
(21) Akih-Kumgeh, B.; Bergthorson, J. M. *Energy Fuels* **2010**, *24*, 2439−2448.
(22) Hadjali, K.; Crochet, M.; Vanhove, G.; Ribaucour, M.; Minetti, R. *Proc. Combust. Inst.* **2009**, *32*, 239−246.
(23) Osmont, A.; Yahyaoui, M.; Catoire, L.; Gökalp, I.; Swihart, M. T. *Combust. Flame* **2008**, *155*, 334−342.
(24) El-Nahas, A. M.; Navarro, M. V.; Simmie, J. M.; Bozzelli, J. W.; Curran, H. J.; Dooley, S.; Metcalfe, W. *J. Phys. Chem. A* **2007**, *111*, 3727−3739.
(25) Huynh, L. K.; Lin, K. C.; Violi, A. *J. Phys. Chem. A* **2008**, *112*, 13470−13480.
(26) Huynh, L. K.; Violi, A. *J. Org. Chem.* **2008**, *73*, 94−101.
(27) Hayes, C. J.; Burgess, D. R., Jr. *Proc. Combust. Inst.* **2009**, *32*, 263−270.
(28) Walton, S. M.; Karwat, D. M.; Teini, P. D.; Gorny, A. M.; Wooldridge, M. S. *Fuel* **2011**, *90*, 1796−1804.
(29) Lin, C. K.; Lai, J. Y. W; Violi, A. *Fuel* **2012**, *92*, 16−26.
(30) Dayma, G.; Gaïl, S.; Dagaut, P. *Energy Fuels* **2008**, *22*, 1469−1479.
(31) Dayma, G.; Togbé, C.; Dagaut, P. *Energy Fuels* **2009**, *23*, 4254−4268.
(32) Glaude, P. A.; Herbinet, O.; Bax, S.; Biet, J.; Warth, V.; Battin-Leclerc, F. *Combust. Flame* **2010**, *157*, 2035−2050.
(33) Campbell, M. F.; Davidson, D. F.; Hanson, R. K. *Fuel* **2014**, *126*, 271−281.
(34) Wang, W.; Gowdagiri, S.; Oehlschlaeger, M. A. *Energy Fuels* **2013**, *27*, 5527−5532.
(35) Hakka, M. H.; Glaude, P. A.; Herbinet, O.; Battin-Leclerc, F. *Combust. Flame* **2009**, *156*, 2129−2144.
(36) Bax, S.; Hakka, M. H.; Glaude, P. A.; Herbinet, O.; Battin-Leclerc, F. *Combust. Flame* **2010**, *157*, 1220−1229.
(37) Campbell, M. F.; Davidson, D. F.; Hanson, R. K.; Westbrook, C. K. *Proc. Combust. Inst.* **2013**, *34*, 419−425.
(38) Westbrook, C. K.; Naik, C. V.; Herbinet, O.; Pitz, W. J.; Mehl, M.; Sarathy, S. M.; Curran, H. J. *Combust. Flame* **2011**, *158*, 742−755.
(39) Zhang, K.; Togbé, C.; Dayma, G.; Dagaut, P. *Combust. Flame* **2014**, *161*, 818−825.
(40) Donovan, M. T.; He, X.; Zigler, B. T.; Palmer, T. R.; Wooldridge, M. S.; Atreya, A. *Combust. Flame* **2004**, *137*, 351−365.
(41) Donovan, M. T.; He, X.; Zigler, B. T.; Palmer, T. R.; Walton, S. M.; Wooldridge, M. S. *Combust. Flame* **2005**, *141*, 360−370.
(42) Walton, S. M.; He, X.; Zigler, B. T.; Wooldridge, M. S.; Atreya, A. *Combust. Flame* **2007**, *150*, 246−262.
(43) Karwat, D. M. A.; Wagnon, S. W.; Teini, P. D.; Wooldridge, M. S. *J. Phys. Chem. A* **2011**, *115*, 4909−4921.
(44) Karwat, D. M. A.; Wagnon, S. W.; Wooldridge, M. S.; Westbrook, C. K. *Combust. Flame* **2013**, *160*, 2693−2706.
(45) Gaydon, A. G. *The Spectroscopy of Flames*; Wiley: New York, 1957.
(46) McBride, B. J.; Gordon, S.; Reno, M. A. *Coefficients for Calculating Thermodynamic and Transport Properties of Individual Species*; National Aeronautics and Space Administration (NASA): Washington, D.C., 1993; NASA Technical Memorandum 4513.
(47) Walton, S. M. Experimental investigation of the auto-ignition characteristics of oxygenated reference fuel compounds. Ph.D. Dissertation, University of Michigan, Ann Arbor, MI, 2008.
(48) Dayma, G.; Sarathy, S. M.; Togbé, C.; Yeung, C.; Thomson, M. J.; Dagaut, P. *Proc. Combust. Inst.* **2011**, *33*, 1037−1043.

(49) Dayma, G.; Halter, F.; Foucher, F.; Togbé, C.; Mounaim-Rousselle, C.; Dagaut, P. *Energy Fuels* **2012**, *26*, 4735−4748.
(50) Dooley, S.; Dryer, F. L.; Yang, B.; Wang, J.; Cool, T. A.; Kasper, T.; Hansen, N. *Combust. Flame* **2011**, *158*, 732−741.
(51) Yang, B.; Westbrook, C. K.; Cool, T. A.; Hansen, N.; Kohse-Hoinghaus, K. *Phys. Chem. Chem. Phys.* **2011**, *13*, 6901−6913.
(52) Yang, B.; Westbrook, C. K.; Cool, T. A.; Hansen, N.; Kohse-Hoinghaus, K. *Z. Phys. Chem.* **2011**, *225*, 1293−1314.
(53) Westbrook, C. K.; Pitz, W. J.; Sarathy, S. M.; Mehl, M. *Proc. Combust. Inst.* **2014**, *34*, 3049−3056.

THE JOURNAL OF PHYSICAL CHEMISTRY A

Article

pubs.acs.org/JPCA

Effects of New Ab Initio Rate Coefficients on Predictions of Species Formed during *n*-Butanol Ignition and Pyrolysis

Darshan M. A. Karwat,*[,†] Margaret S. Wooldridge,[†,‡] Stephen J. Klippenstein,[§] and Michael J. Davis[§]

[†]Department of Mechanical Engineering and [‡]Department of Aerospace Engineering, University of Michigan, Ann Arbor, Michigan 48109, United States

[§]Chemical Sciences and Engineering Division, Argonne National Laboratory, Argonne, Illinois 60439, United States

Supporting Information

ABSTRACT: Experimental, time-resolved species profiles provide critical tests in developing accurate combustion models for biofuels such as *n*-butanol. A number of such species profiles measured by Karwat et al. [Karwat, D. M. A.; et al. *J. Phys. Chem. A* **2011**, *115*, 4909] were discordant with predictions from a well-tested chemical kinetic mechanism developed by Black et al. [Black, G.; et al. *Combust. Flame* **2010**, *157*, 363]. Since then, significant theoretical and experimental efforts have focused on determining the rate coefficients of primary *n*-butanol consumption pathways in combustion environments, including H atom abstraction reactions from *n*-butanol by key radicals such as HO_2 and OH, as well as the decomposition of the radicals formed by these H atom abstractions. These reactions not only determine the overall reactivity of *n*-butanol, but also significantly affect the concentrations of intermediate species formed during *n*-butanol ignition. In this paper we explore the effect of incorporating new ab initio predictions into the Black et al. mechanism on predictions of ignition delay time and species time histories for the experimental conditions studied by Karwat et al. The revised predictions for the intermediate species time histories are in much improved agreement with the measurements, but some discrepancies persist. A rate of production analysis comparing the effects of various modifications to the Black et al. mechanism shows significant changes in the predicted consumption pathways of *n*-butanol, and of the hydroxybutyl and butoxy radicals formed by H atom abstraction from *n*-butanol. The predictions from the newly revised mechanism are in very good agreement with the low-pressure *n*-butanol pyrolysis product species measurements of Stranic et al. [Stranic, I.; et al. *Combust. Flame* **2012**, *159*, 3242] for all but one species. Importantly, the changes to the Black et al. mechanism show that concentrations of small products from *n*-butanol pyrolysis are sensitive to different reactions than those presented by Stranic et al.

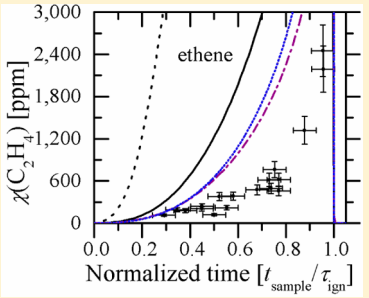

INTRODUCTION

A large portion of recent combustion chemistry research has focused on the combustion chemistry of alcohols given that they can be produced from waste feedstocks and organic material, possibly reducing the demand for fossil-based fuels and/or reducing the overall emissions of carbon dioxide to the atmosphere over the life cycle of the fuel. *n*-Butanol in particular has been widely studied given its thermophysical properties (like vapor pressure and energy density) that make it suitable for a wide range of energy applications, including aviation. As detailed by Sarathy et al.,[4] significant effort has been expended on ab initio kinetics calculations,[5−14] and on experimental measurements of ignition delay times,[1,2,15−17] rate constants,[18] and intermediate species formation at engine-relevant temperatures and pressures.[1,19−23] We direct the interested reader to Sarathy et al.[4] for a comprehensive review of the chemistry of alcohol combustion.

As described by Sarathy et al.,[4] for alcohols, many reaction rates, such as some of the key H atom abstractions, have not yet been measured (and many reaction rates are difficult to measure). Researchers building chemical kinetic mechanisms have thus relied on analogies to hydrocarbon counterparts to estimate the rate coefficients for these reactions. Take, for example, the detailed *n*-butanol chemical kinetic mechanism developed by Black et al.[2] The authors chose key H atom abstraction reaction rates, such as those for *n*-butanol + OH from the 3- and 4-carbon sites of *n*-butanol, to be identical to the corresponding rates for *n*-butane. (For reference, the radicals formed from *n*-butanol by H atom abstraction are denoted as C_4H_8OH-1, C_4H_8OH-2, C_4H_8OH-3, and C_4H_8OH-4, where the radical sites correspond to the carbon sites in *n*-butanol numbered 1−4, with 1 being the carbon atom attached to the OH group and 4 being the carbon furthest from the OH group. The radical formed when an H atom is abstracted from the OH group of *n*-butanol is denoted as PC_4H_9O. This is the same notation used in the mechanism file of Black et al.[2]) Furthermore, abstraction from the 2 site was estimated to be the average of the abstraction rates from the 3 and 4 sites; abstraction from the alcohol group was assumed to be negligible; and abstraction from the 1 site was set to the rate used by Dagaut et al.[22]

Received: September 13, 2014
Revised: January 3, 2015
Published: January 5, 2015

DOI: 10.1021/jp509279d
J. Phys. Chem. A 2015, 119, 543−551

Experiments that measure intermediate species formed during ignition provide stringent tests for chemical kinetic mechanisms. For example, using the University of Michigan Rapid Compression Facility (UM RCF), Karwat et al.[1] measured the intermediate species formed during *n*-butanol ignition, and compared their experimental results to model predictions of the Black et al.[2] mechanism, the most up-to-date mechanism at the time. In Figure 1, the solid black symbols

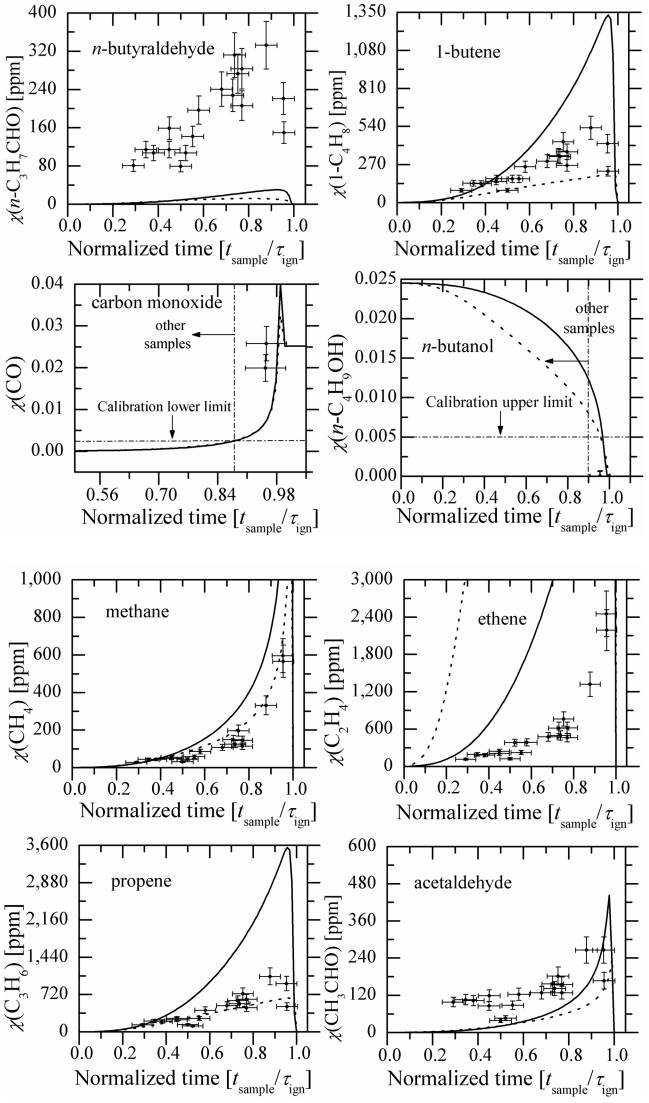

Figure 1. Comparison of experimental data and model predictions for stable intermediate species observed[1] during *n*-butanol ignition. The solid black symbols represent the experimental measurements made by Karwat et al.[1] Predictions using the unmodified reaction mechanism of Black et al.[2] are presented as black solid lines. The effects of using the reaction rates for *n*-butanol + OH recommended by Zhou et al.[5] with the Black et al.[2] mechanism were explored by Karwat et al.[1] and are reproduced here as black dashed lines.

represent the experimental measurements made by Karwat et al.[1] and the solid black lines represent model predictions. All data are presented on a normalized time scale (consistent with Karwat et al.[1]), with 0 representing the end of the compression in the UM RCF and the beginning of the chemical kinetic simulations, and 1 representing the time of ignition, which is the point of maximum rate of pressure rise in the experiment or simulation. All ignition simulations presented in this paper use a mole-basis mixture composition of χ(*n*-butanol) = 0.0245, $\chi(O_2)$ = 0.147, $\chi(N_2)$ = 0.541, and χ(Ar) = 0.2875, and initial conditions of P = 3.25 atm and T = 975 K, which are the average experimental conditions for the speciation experiments presented in Karwat et al.[1] While the Black et al.[2] mechanism predicted the ignition delay time measured by Karwat et al.[1] well (measured = 15.7 ms, predicted = 18.6 ms), several key intermediate species were significantly overpredicted, as illustrated in Figure 1. For example, small alkenes were overpredicted by factors of 2−3 for propene and 4−8 for ethene. These discrepancies pointed to the need for revisions to some of the key elementary reaction rates that dictate *n*-butanol consumption and intermediate species production and consumption.

Karwat et al.[1] explored the effects of incorporating the rates for *n*-butanol + OH recommended by Zhou et al.,[5] which were based on G3-level ab initio calculations. The revision increased the predicted ignition delay (from 18.6 to 21.8 ms) and had contrasting effects on species predictions (as shown by the dashed black lines in Figure 1). While the predictions for methane and propene improved significantly, the discrepancy between the model predictions and experimental measurements for ethene increased dramatically due to increased branching to C_4H_8OH-4, the β-scission of which yields ethene.

Motivated by the importance of the H atom abstractions from *n*-butanol at moderate combustion temperatures (~1000 K), several research groups have recently published new kinetics results for H atom abstractions from *n*-butanol by OH and HO_2 radicals.[5−8,12−14] A theoretical kinetic analysis for the decomposition of *n*-butanol fuel radicals was also presented recently.[9] These state-of-the-art results provide the impetus for the present study, which weaves together the threads of new theoretical ab initio kinetics calculations with those of the well-tested Black et al.[2] chemical kinetic model to explore the effects on predicted species profiles and on reaction pathways at the very beginning stages of *n*-butanol combustion. There are many recent mechanisms[15,22−27] for *n*-butanol that could have been used as the basis for this effort, but to maintain consistency with the previous study by Karwat et al.,[1] we used the Black et al.[2] mechanism.

While experimental measurements like those of Karwat et al.[1] guide the development of detailed chemical kinetic models, this work is not a traditional modeling study in that we are not trying to update a model by fitting model results to experimental data. Instead, we investigate the effects of advances in the physical understanding of key reactions that control *n*-butanol combustion and small radical chemistry. These physical investigations can only happen in the context of detailed chemical kinetic models, which are built using an understanding of reaction classes, insights gained from explorations of individual reaction kinetics, and scientific judgment. Thus, while such studies can yield mechanisms that agree better with experimental data, the primary goal of this study is to understand the changes that arise in mechanism predictions and pathways from physically motivated modifications to a well-tested mechanism.

STUDY METHODOLOGY

We systematically consider the effects of the newly predicted elementary rate coefficients on the Black et al.[2] model predictions of the intermediate species measured by Karwat et al.[1] via sequential substitution of the available sets of

DOI: 10.1021/jp509279d
J. Phys. Chem. A 2015, 119, 543−551

theoretical rate constants. These substitutions were carried out in the following order:

Step 1 is updating old rates for and incorporating new hydroxybutyl and butoxy decomposition reactions[9] into the original Black et al.[2] mechanism.

Step 2 consists of Step 1 + updating rates for H atom abstractions from *n*-butanol by OH[7] and by HO_2.[6,8]

Step 3 includes Step 2 + updating the rate for HO_2 + HO_2.[28]

For each step, we briefly review the incorporated reaction rates and compare the predicted intermediate species concentrations with those presented in Karwat et al.[1] The results of these steps are shown in Figure 2. For Step 3, we also compare the final mechanism predictions for the products of *n*-butanol pyrolysis with the speciation measurements of Stranic et al.[3] and present the results of a sensitivity analysis for the conditions studied by Stranic et al.[3]

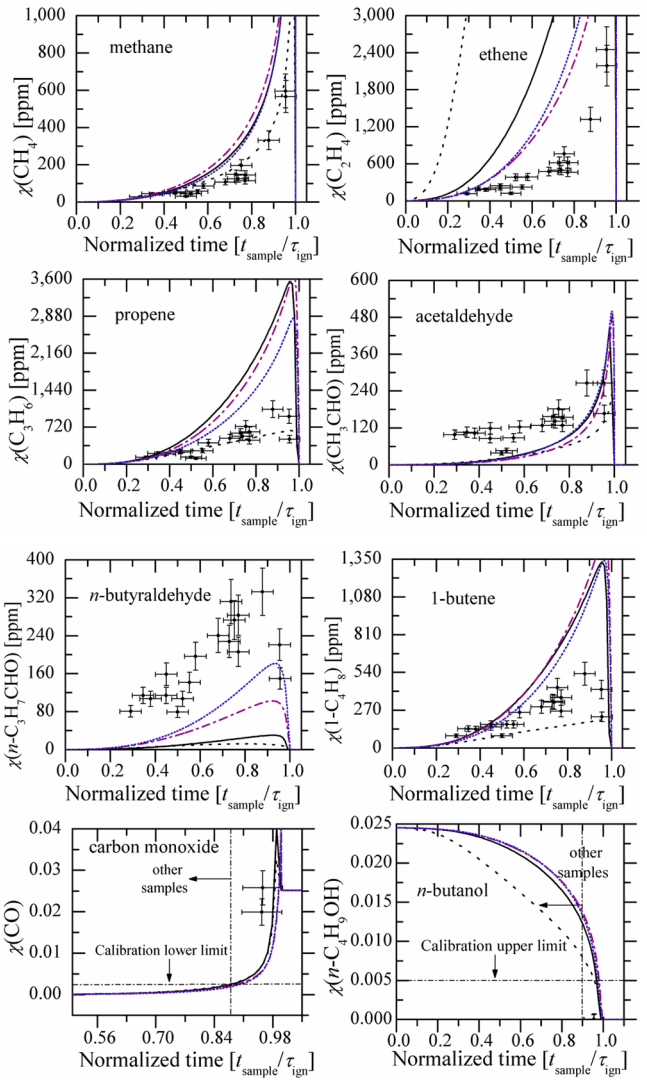

Figure 2. Model predictions based on the three-step revisions to the baseline Black et al.[2] mechanism presented as purple dashed−dotted lines (Step 1), blue dotted lines (Step 2), and dashed orange lines (Step 3; overlapping the Step 2 predictions). All other symbols and lines are the same as detailed in Figure 1.

RESULTS AND DISCUSSION

Step 1. Updating Old Rates for and Incorporating New Hydroxybutyl and Butoxy Decomposition Reactions. Zhang et al.[9] used an ab initio transition-state-theory-based master equation analysis to obtain rate predictions for all hydroxybutyl (C_4H_8OH-1, C_4H_8OH-2, C_4H_8OH-3, and C_4H_8OH-4) and butoxy (PC_4H_9O) radical decomposition and isomerization reactions over a wide range of temperatures (300−2500 K) and pressures (1.3×10^{-3}−100 atm). Their analysis properly treated well-skipping and species-merging phenomena. In contrast, the Black et al.[2] mechanism ignored all pressure effects for these rate coefficients. Zhang et al.[9] showed that the dominant pathway for both C_4H_8OH-4 and PC_4H_9O radical decomposition is a well-skipping pathway that forms propyl + formaldehyde, rather than C_4H_8OH-4 predominantly forming ethene + CH_2CH_2OH as presumed by Black et al.[2] We replaced the original rates in the Black et al.[2] mechanism with the Zhang et al.[9] rates and reactions, and several new reactions determined to be important by Zhang et al.,[9] and listed below, were also incorporated into the Step 1 mechanism. (The reverse rates for the forward reactions[9] were calculated using CHEMKIN algorithms and the thermochemistry of Black et al.[2])

$C_4H_8OH\text{-}1 \leftrightarrow NC_3H_7 + CH_2O$

$C_4H_8OH\text{-}2 \leftrightarrow CH_3 + IC_3H_5OH$

$C_4H_8OH\text{-}2 \leftrightarrow NC_3H_7 + CH_2O$

$C_4H_8OH\text{-}3 \leftrightarrow C_4H_8OH\text{-}4$

$C_4H_8OH\text{-}3 \leftrightarrow NC_3H_7 + CH_2O$

$C_4H_8OH\text{-}4 \leftrightarrow NC_3H_7 + CH_2O$

$C_4H_8OH\text{-}4 \leftrightarrow C_2H_5 + C_2H_3OH$

$PC_4H_9O \rightarrow NC_3H_7 + CH_2O$

$PC_4H_9O \rightarrow C_4H_8OH\text{-}3$

Furthermore, Zhang et al.[9] calculated that several hydroxybutyl decomposition reactions initially included by Black et al.[2] were insignificant (<1%) over the entirety of the temperature and pressure ranges studied, which include essentially all practical combustion conditions. These reactions, listed below, were removed from the Step 1 mechanism.

$C_4H_8OH\text{-}1 \leftrightarrow NC_3H_7CHO + H$

$C_4H_8OH\text{-}1 \leftrightarrow C_4H_7OH1\text{-}1 + H$

$C_4H_8OH\text{-}1 \leftrightarrow C_4H_8OH\text{-}3$

$C_4H_8OH\text{-}2 \leftrightarrow C_4H_7OH2\text{-}1 + H$

$C_4H_8OH\text{-}3 \leftrightarrow C_4H_7OH1\text{-}4 + H$

$C_4H_8OH\text{-}3 \leftrightarrow C_4H_7OH2\text{-}1 + H$

$C_4H_8OH\text{-}4 \leftrightarrow C_4H_8OH\text{-}2$

With these revisions, the Step 1 mechanism predicted a slightly smaller ignition delay time (17.9 ms) than the original Black et al.[2] mechanism (18.6 ms), with significant improvements in the species time history predictions (shown by the purple dashed−dotted lines in Figure 2) for two of the species. The change in the product channel for the C_4H_8OH-4 radical

DOI: 10.1021/jp509279d
J. Phys. Chem. A 2015, 119, 543−551

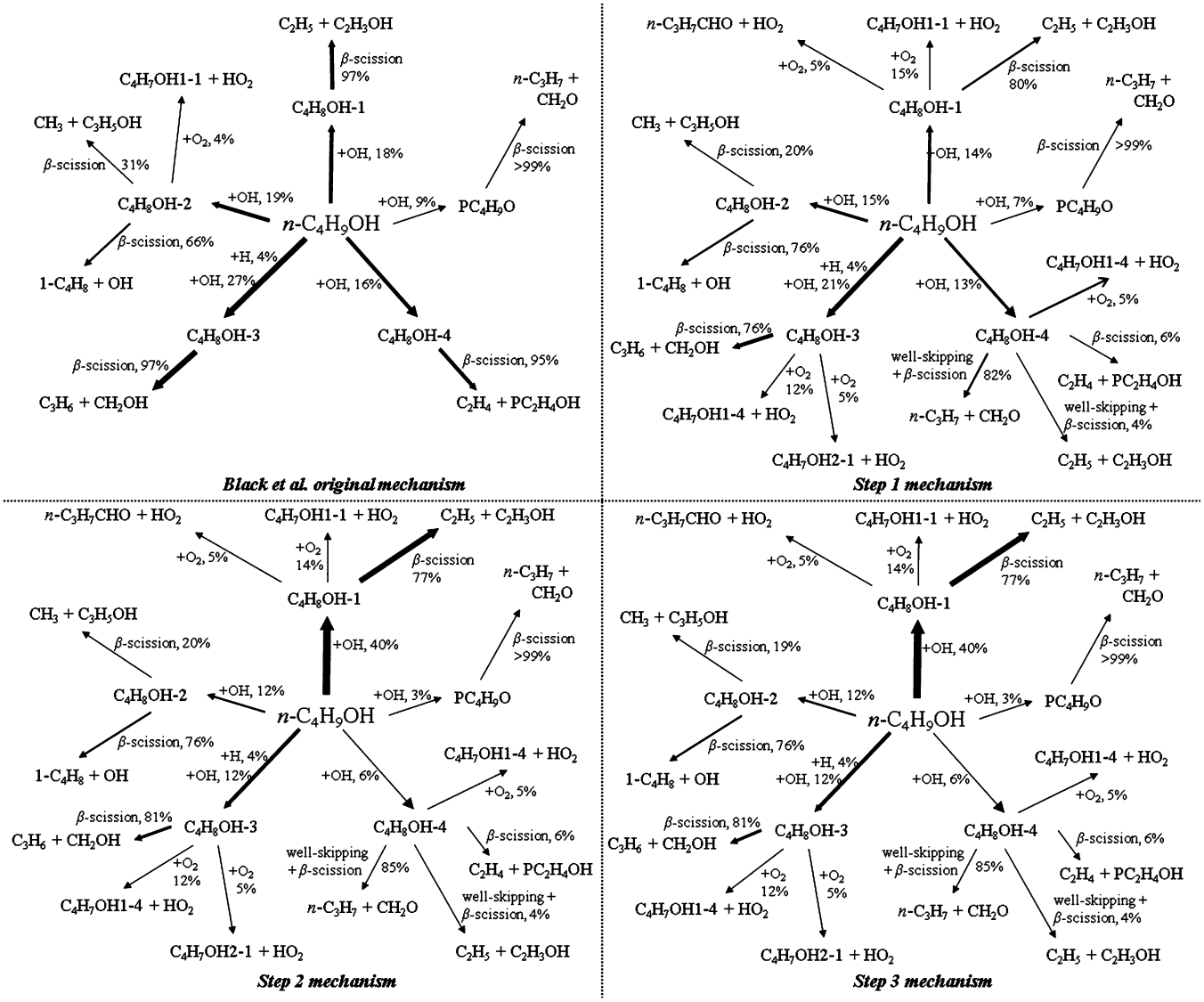

Figure 3. Representations of the rate of production analyses for the original Black et al.,[2] Step 1, Step 2, and Step 3 mechanisms at 75% of the ignition delay time (corresponding to approximately 25% consumption of *n*-butanol), using the simulation conditions described in the paper.

decomposition reaction decreased ethene production, improving the agreement with the experimental observations. The *n*-butyraldehyde predictions improved to within a factor of 4 at the highest measured concentrations. The updated simulation results showed practically no change in the methane, acetaldehyde, propene, 1-butene, and CO predictions, or in *n*-butanol consumption.

Step 2. Step 1 + Updating Rates for *n*-Butanol + OH and *n*-Butanol + HO_2 Reactions. Seal et al.[7] presented multistructural variational transition state theory calculations for all H atom abstractions by OH radicals from *n*-butanol. The calculations employed an analysis of the multidimensional couplings of the torsions and the effects of hydrogen bonding on the kinetics. In contrast, the earlier Zhou et al.[5] results, which Karwat et al.[1] used in their analysis, considered only one-dimensional torsional representations. While the electronic structure methods employed by Zhou et al.[5] and Seal et al.[7] do have many similarities, the M08-HX method used by Seal et al.[7] likely provides better representation of the rovibrational properties, especially for the transition states. Furthermore, the sum of the Seal et al.[7] reaction rates is in reasonable agreement with the sum from experimental measurements of overall *n*-butanol consumption by OH, with a maximum discrepancy of about a factor of 1.6 near room temperature, and a maximum discrepancy at 1000 K of a factor of 1.3−1.4.

McGillen et al.[10] also recently presented a combined experimental and empirical analysis of OH reaction kinetics with all four isomers of butanol. At low temperatures (≤380 K), the extensive experimental data lead to a well-founded representation of the rate coefficient and branching ratios for the *n*-butanol + OH reaction. However, at higher temperatures, the empirical representations likely have limited validity due to the absence of any experimental data for the branching ratios. Thus, the theoretical predictions of Seal et al.[7] are preferred for the high temperature region, and we incorporated these reaction rates into the Step 2 update of the Step 1 mechanism.

In combustion environments, HO_2 radicals, too, are key radicals and the relative importance of HO_2 and OH reactions varies with the thermodynamic conditions and the fuel system. For *n*-butanol ignition under the conditions of interest here, local[1] and global sensitivity analyses[29] (GSA) showed that the ignition delay time has a high sensitivity to the *n*-butanol +

DOI: 10.1021/jp509279d
J. Phys. Chem. A 2015, 119, 543−551

HO_2 reaction kinetics. Indeed, the Zhou et al.[29] GSA showed that the H atom abstractions by *n*-butanol + HO_2 from the carbon sites yielded between 30 and 60% of the variance in the ignition delay time. The GSA performed by Zhou et al.[29] also showed that the sensitivity of the intermediate species concentrations to the HO_2 reactions was much smaller than for the OH reactions. For example, Zhou et al.[29] note that in their simulation of the Karwat et al.[1] experimental conditions, at a normalized ignition delay time of 0.8, two H atom abstractions by OH (at the 3- and 4-carbon sites) account for 67% of the variance for ethylene, while H atom abstraction by HO_2 at the 1-carbon site accounts for only 7.8% of the variance for ethylene. This finding leads us to expect that any changes in HO_2 reaction rates should have a relatively small impact on the species time histories.

The recent study by Alecu et al.[6] (similar to the Seal et al.[7] study of OH radicals) provides high quality multistructural transition-state-theory-based rate predictions for the H atom abstraction by HO_2 from the 1-carbon site of *n*-butanol—by far the most sensitive *n*-butanol + HO_2 H atom abstraction—over the temperature range 250−2000 K. Meanwhile, a related study by Seal et al.[8] predicted the kinetics for the H atom abstraction from the 3-carbon of *n*-butanol by HO_2. These new reaction rates proposed by Alecu et al.[6] and Seal et al.[8] for the *n*-butanol + HO_2 reactions were also substituted into the mechanism from Step 1, giving us the Step 2 mechanism. For the *n*-butanol + OH reactions, and the 1-carbon and 3-carbon H atom abstraction by HO_2, the reverse reaction rates were calculated using CHEMKIN algorithms and the Black et al.[2] thermochemistry.

The Step 2 mechanism predicts a slightly longer ignition delay time of 19.4 ms. Furthermore, as illustrated in Figure 2 (by dotted blue lines), there are practically no changes in the mechanism predictions for methane, acetaldehyde, 1-butene, and carbon monoxide, and in the rate and profile of *n*-butanol consumption compared to the original Black et al.[2] mechanism. However, the predictions for *n*-butyraldehyde are now within a factor of 2−3 of the experimental results. Slight improvements in the propene predictions, and a slight worsening of the ethene predictions, are also observed.

Step 3. Step 2 + Updating the HO_2 + HO_2 Reaction Rate. The local sensitivity analysis performed by Karwat et al.[1] showed the importance of the $H_2O_2 + O_2 \leftrightarrow HO_2 + HO_2$ reaction to the ignition delay time. Given that there were no first-principles calculations of the HO_2 + HO_2 rate coefficient available, Zhou et al.[28] generated a new theoretical rate coefficient appropriate for both low- and high-temperature regimes for the $HO_2 + HO_2 \rightarrow H_2O_2 + O_2$ reaction with statistical rate theory employing properties determined with CASPT2/aug-cc-pVTZ electronic structure calculations. We substituted these new rate coefficients for $HO_2 + HO_2 \rightarrow H_2O_2 + O_2$ into the Step 2 mechanism, leaving the rate for the reverse reaction, $H_2O_2 + O_2 \rightarrow HO_2 + HO_2$, to be calculated by CHEMKIN algorithms and the Black et al.[2] thermochemistry.

The resulting predictions of the intermediate species profiles are presented as dashed orange lines in Figure 2, but the revised species predictions are virtually indistinguishable from the Step 2 mechanism predictions, with less than a 1% difference for a few species. However, the updated rate constant did result in a slight increase in the predicted ignition delay, which increases from 19.4 ms in Step 2 to 19.8 ms in Step 3. This increase is because the high-temperature HO_2 + HO_2 reaction (a reaction that *inhibits* ignition) rate coefficient is smaller than the generally used values presented by Kappel et al.[30]

Rate of Production Analyses of the Modified Mechanisms. In order to gain a better understanding of the impacts of the systematic modifications to the Black et al.[2] mechanism, we performed rate of production (ROP, or flux) analyses at 75% of the ignition delay time for the original Black et al.[2] mechanism and the three modifications for the simulation conditions described above. The results of the ROP analysis are presented in Figure 3. The percentages alongside the arrows in Figure 3 represent the fractional branching of the specific reaction pathways *consuming* each represented species. Results are presented for only those reactions that constitute at least 3% of the species consumption. Even though 75% of the ignition delay time represents slightly different times of analysis for the four cases presented in Figure 3, *n*-butanol consumption was roughly the same—at approximately 25%—for all four cases.

The Step 1 mechanism ROP analysis shows little change from the original Black et al.[2] mechanism in the branching fractions from *n*-butanol. This is expected given that only the hydroxybutyl and butoxy (C_4H_9O) reaction rates were changed. In contrast, the pathways from the five C_4H_9O fuel radicals show some dramatic changes. Most significantly, for C_4H_8OH-4 the products switch from almost completely C_2H_4 + PC_2H_4OH to almost completely *n*-C_3H_7 + CH_2O, with the latter arising from well-skipping via PC_4H_9O. Notably, this change in branching for C_4H_8OH-4 is responsible for the improved agreement with experiment of Step 1 model predictions of C_2H_4 production. β-scission still dominates C_4H_9O and C_4H_8OH-2 consumption, but for the latter there is a significant change in the branching among the two major β-scission channels. Meanwhile, the fractions of C_4H_8OH-1 and C_4H_8OH-3 undergoing β-scission decrease by 17 and 21%, respectively, and there is a corresponding enhanced contribution from reaction with O_2 that effectively yields an H atom abstraction.

Changes in *n*-butanol consumption from the updated H atom abstraction reaction rates introduced in Step 2 are clear when compared to the Step 1 ROP. Specifically, the fraction of *n*-butanol consumed to form C_4H_8OH-1 increases by a factor of 3, while the branching fractions to C_4H_8OH-3, C_4H_8OH-4, and PC_4H_9O decrease by 36, 50, and 60%, respectively. Interestingly, a small fraction of C_4H_8OH-1 isomerizes to C_4H_8OH-4 in the Step 2 mechanism, but there are essentially no significant changes in hydroxybutyl and butoxy radical consumption.

The changes to the HO_2 + HO_2 reaction rate made in Step 3 have no effect on the ROP analysis of Step 2.

Comparing Step 3 Mechanism Predictions to Experimental Measurements by Stranic et al.[3] Stranic et al.[3] presented measurements of the products of *n*-butanol pyrolysis in a low-pressure shock tube. The authors focused on five important small products, namely OH, H_2O, CO, methane, and ethene. They studied the production pathways and conducted sensitivity analyses of the key reactions forming these products using a detailed chemical kinetic mechanism developed by Sarathy et al.[24] Stranic et al.[3] found that, under pyrolysis conditions, H_2O is formed primarily through H atom abstraction from *n*-butanol by OH, and thus H_2O concentrations are extremely sensitive to OH radical formation. The authors suggested that the H_2O production channels also strongly affect those that produce ethene, and that the rate of *n*-

DOI: 10.1021/jp509279d
J. Phys. Chem. A 2015, 119, 543−551

butanol decomposition into n-C_3H_7 + CH_2OH in the Sarathy et al.[24] mechanism is the main cause of the differences between their experimental measurements of CO and mechanism predictions.

We performed simulations of n-butanol pyrolysis using the Step 3 mechanism and compared its predictions with the experimental results presented by Stranic et al.[3] and with the simulation results they presented using the Sarathy et al.[24] mechanism. In the following figures that present these results, the Stranic et al.[3] experimental measurements are represented by the solid lines and the Step 3 mechanism simulation results are presented as dashed lines. All of the Stranic et al.[3] experiments and the simulations used χ(n-butanol) = 0.01 and χ(Ar) = 0.99, and all simulations were at the same temperature, pressure, and constant volume conditions as the corresponding simulations presented in Stranic et al.[3]

We see in Figure 4 (for a temperature of 1477 K and pressure of 1.52 atm) that the Step 3 mechanism predicts an

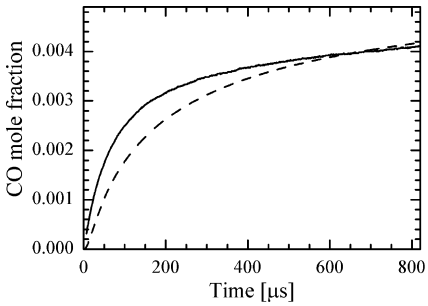

Figure 4. Carbon monoxide mole fractions for 1% n-butanol pyrolysis in argon at 1477 K and 1.52 atm. The solid line represents experimental measurements by Stranic et al.[3] The dashed line represents simulations using the Step 3 mechanism.

initial production of CO that is too slow (particularly for times less than 100 μs), but the simulated and experimentally measured CO concentrations quickly converge, becoming roughly equivalent at 500 μs and beyond. In contrast, as seen in Figure 4 of Stranic et al.,[3] the CO predictions from the Sarathy et al.[24] mechanism converge to the experimental value about a factor of 2 more slowly. The sensitivity analysis of the Sarathy et al.[24] mechanism performed by Stranic et al.[3] implicates a slow rate of H atom abstraction by OH from n-butanol to form C_4H_8OH-3, in addition to a slow rate for thermal decomposition of n-butanol. The former reaction is the very reaction studied by Seal et al.[8] and that was substituted into the original Black et al.[2] mechanism in Step 1 of this study. A sensitivity analysis of the Step 3 mechanism for CO is provided in Figure 5 for 1603 K and 1.36 atm, the same conditions as Figure 6 of Stranic et al.[3] For ease of comparison, the results of the current work use the same color and line formatting for the reactions as used in Stranic et al.[3] The results of the sensitivity analysis based on the Step 3 mechanism show CO is most sensitive to the unimolecular decomposition of n-butanol at early times, similar to Stranic et al.[3] A key difference, however, is that for n-butanol decomposing to CH_3 and C_3H_6OH, the Sarathy et al.[24] mechanism predicts a strong positive sensitivity at very early times that quickly transitions into a negative sensitivity. The Step 3 mechanism, on the other hand, shows a weak positive sensitivity at early times that transitions to a weak negative sensitivity at longer times. Also, the positive sensitivity to n-C_4H_9OH + H ↔ C_4H_8OH-3 + H_2

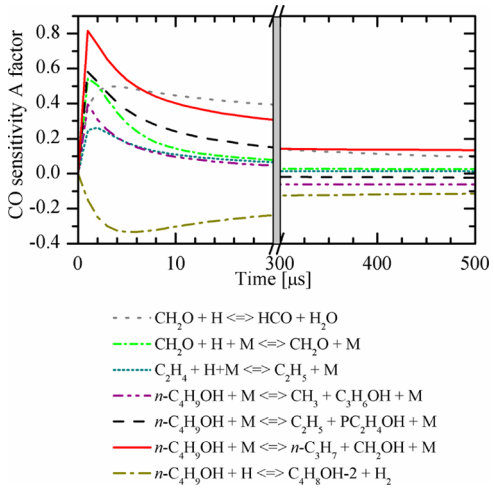

Figure 5. Results of local sensitivity analyses for CO for 1% n-butanol pyrolysis in argon performed at 1603 K and 1.36 atm using the Step 3 mechanism. CO production is affected most positively by the unimolecular decomposition of n-butanol.

for Stranic et al.[3] has been replaced with a negative sensitivity to n-C_4H_9OH + H ↔ C_4H_8OH-2 + H_2.

As illustrated in Figure 6, the Step 3 mechanism provides reasonably satisfactory predictions of the ethene mole fractions

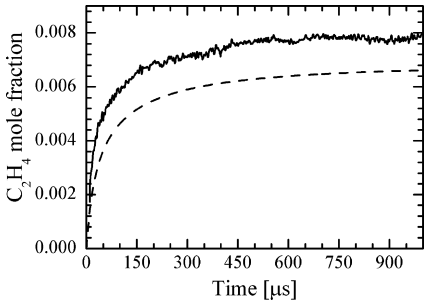

Figure 6. Ethene mole fractions for 1% n-butanol pyrolysis in argon at 1467 K and 1.73 atm. The solid line represents experimental measurements by Stranic et al.[3] The dashed line represents simulations using the Step 3 mechanism, which predicts both the rate of C_2H_4 production and its magnitude very well.

measured by Stranic et al.[3] at 1467 K and 1.73 atm. A local sensitivity analysis for ethene at 1348 K and 1.83 atm, shown in Figure 7, indicates that the Step 3 mechanism predictions are most sensitive to the same reactions as identified in Stranic et al.,[3] and that the sensitivity to most reactions decreases with increasing time.

In Figure 8, the Stranic et al.[3] measurements at 1494 K and 1.46 atm indicate that the methane concentrations rise rapidly for the first 100 μs, but rise much more slowly thereafter. While the initial production of methane is well captured by the Step 3 mechanism, the decrease in the rate of rise is not, leading to a 30% overprediction of methane at the end of the simulation at 1 ms. A sensitivity analysis for methane at 1631 K and 1.5 atm is presented in Figure 9, and indicates that methane production is initially most sensitive to the decomposition of n-butanol to methyl + C_3H_6OH, the decomposition of n-butanol to n-C_3H_7 + CH_2OH, and to n-C_4H_9OH + CH_3 ↔ C_4H_8OH-1 + CH_4. Further, we observe an important difference between our simulations and the results presented by Stranic et al.,[3] namely

DOI: 10.1021/jp509279d
J. Phys. Chem. A 2015, 119, 543−551

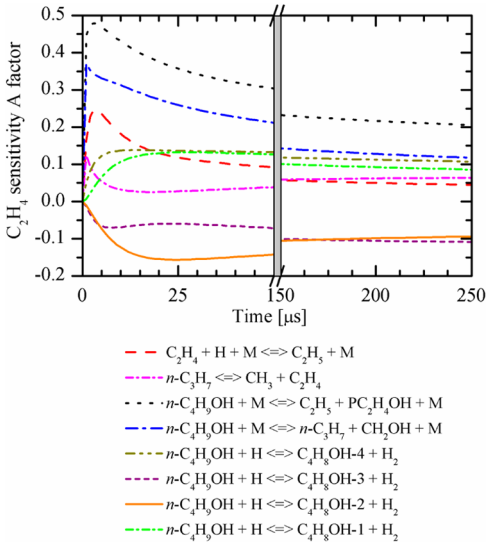

Figure 7. Results of local sensitivity analyses for ethene for 1% *n*-butanol pyrolysis in argon performed at 1348 K and 1.83 atm using the Step 3 mechanism.

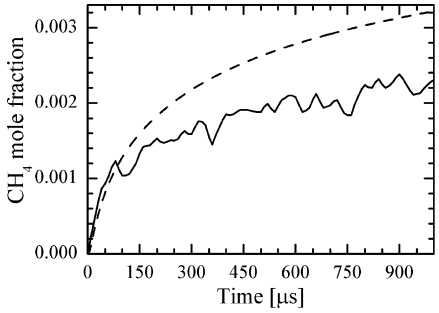

Figure 8. Methane mole fractions for 1% *n*-butanol pyrolysis in argon at 1494 K and 1.46 atm. The solid line represents experimental measurements by Stranic et al.,[3] which show that the rate of increase of methane concentrations decreases sharply at about 100 μs. The dashed line represents simulations using the Step 3 mechanism.

that, according to the Step 3 mechanism, methane production is most strongly sensitive to *n*-butanol decomposition reactions soon after pyrolysis begins, with a significant decrease in sensitivity within the first 20 μs. This is in contrast to the results of Stranic et al.,[3] who found using the Sarathy et al.[24] mechanism that *n*-butanol decomposition plays essentially no role in methane concentrations.

The Step 3 mechanism significantly underpredicts the H_2O profile, as illustrated in Figure 10, for pyrolysis at 1467 K and 1.73 atm, where the predictions are about 30% lower than the experimental results of Stranic et al.[3] The Sarathy et al.[24] mechanism used by Stranic et al.[3] predicts H_2O concentrations within 15% of the experimental measurements. In Figure 11 we see that, at 1348 K and 1.83 atm, *n*-butanol decomposition has the strongest positive sensitivity for H_2O production. We also find that the decomposition of C_4H_8OH-2 is important in this regard, with the two primary decomposition channels having opposite sensitivities, a departure from the findings of Stranic et al.,[3] in which C_4H_8OH-2 was not present in the sensitivity analysis.

Figure 12 shows a comparison between the OH radical concentrations measured by Stranic et al.[3] and predicted by the Step 3 mechanism at 1467 K and 1.73 atm. We see that the

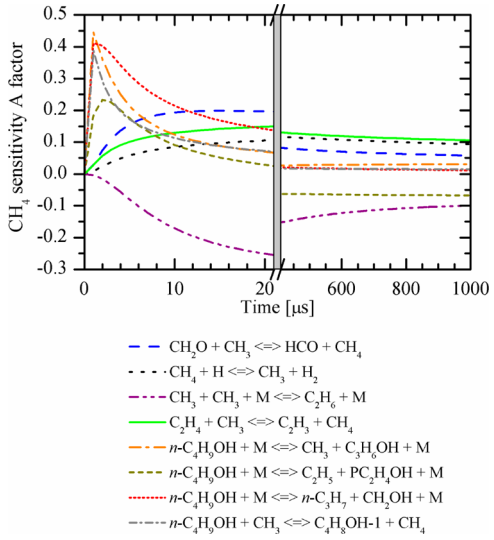

Figure 9. Results of local sensitivity analyses for methane for 1% *n*-butanol pyrolysis in argon performed at 1631 K and 1.5 atm using the Step 3 mechanism. Methane production is most strongly sensitive to *n*-butanol decomposition reactions soon after pyrolysis begins, with a substantial decrease in sensitivity within the first 20 μs.

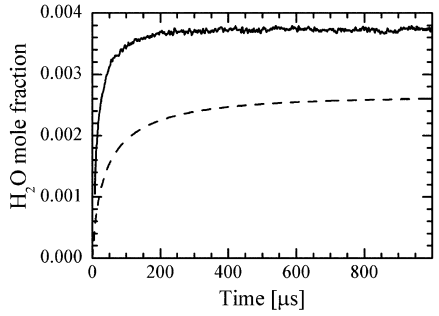

Figure 10. H_2O mole fractions for 1% *n*-butanol pyrolysis in argon at 1467 K and 1.73 atm. The solid line represents experimental measurements by Stranic et al.[3] The dashed line represents simulations using the Step 3 mechanism, which underpredicts the H_2O concentration by about 30%.

Step 3 mechanism underpredicts the initial formation of OH radicals by a factor of 3. The sensitivity analysis of the Step 3 mechanism at 1477 K and 1.52 atm is presented in Figure 13 and indicates that, at pyrolysis conditions, OH concentrations are sensitive not only to small radical chemistry, but also to *n*-butanol unimolecular decomposition as well as the formation of C_4H_8OH-3.

CONCLUSIONS

Significant modifications were made to the Black et al.[2] reaction mechanism on the basis of recent theoretical calculations for the *n*-butanol + OH, *n*-butanol + HO_2, and hydroxybutyl and butoxy decomposition reactions. These changes represent the current state of understanding for these key reactions in *n*-butanol combustion. The changes had little impact on the ignition delay time compared to the original Black et al.[2] mechanism, but predictions for the concentrations of the small alkenes ethene, propene, and 1-butene and of *n*-butyraldehyde were improved. Including an updated rate coefficient for HO_2 + HO_2 increased the ignition delay time compared to the

DOI: 10.1021/jp509279d
J. Phys. Chem. A 2015, 119, 543−551

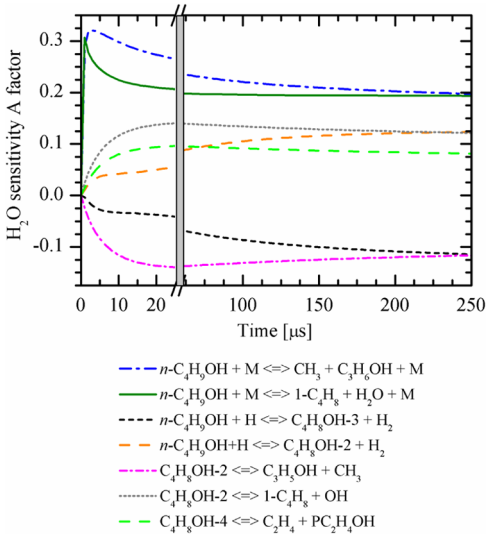

Figure 11. Results of local sensitivity analyses for H_2O for 1% *n*-butanol pyrolysis in argon performed at 1348 K and 1.83 atm using the Step 3 mechanism. The decomposition of C_4H_8OH-2 has both a positive and a negative effect on water production.

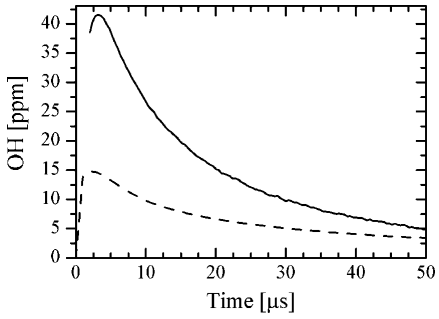

Figure 12. Hydroxyl radical concentrations for 1% *n*-butanol pyrolysis in argon at 1467 K and 1.73 atm. The solid line represents experimental measurements by Stranic et al.[3] The dashed line represents simulations using the Step 3 mechanism, which underpredicts the initial formation of OH radicals by a factor of 3.

experimental measurements from 15.7 to 19.8 ms, but did not impact species predictions.

These revisions significantly changed the consumption pathways of *n*-butanol and the products of the H atom abstractions from *n*-butanol—namely hydroxybutyl and butoxy radicals—under combustion conditions. Even though *β*-scission still consumes a large fraction of these radicals, the systematic changes introduced in the mechanism are the very changes that led to improved species predictions. Additionally, these changes to the Black et al.[2] mechanism also result in mostly satisfactory predictions of the products of the low-temperature pyrolysis of *n*-butanol when compared to the experimental measurements made by Stranic et al.[3] These revisions suggest the importance of certain unimolecular decomposition reactions of *n*-butanol and hydroxybutyl formation and consumption to small pyrolysis products. Further multistructural torsion-based theoretical studies may help reduce the remaining discrepancies. For example, studies of the n-C_4H_9OH and C_4H_9O partition functions would provide interesting insights into the effect of uncertainties in thermochemistry, and Zheng et al.[31] have very recently published a study to this end.

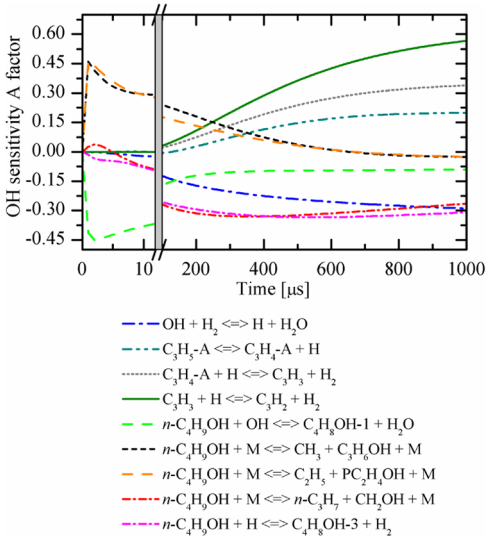

Figure 13. Results of local sensitivity analysis for OH radicals for 1% *n*-butanol pyrolysis in argon performed at 1477 K and 1.52 atm using the Step 3 mechanism. At pyrolysis conditions, OH concentrations are sensitive not only to small radical chemistry, but also to *n*-butanol unimolecular decomposition as well as the formation of C_4H_8OH-3.

Our observations highlight the utility of theoretical chemical kinetics studies for combustion modeling. The uncertainties and inaccuracies in current state-of-the-art mechanisms may be so large that even the key sensitivites may not be accurate, as illustrated by the changes observed in this study. Theoretical studies provide physically based improvements for the key reactions in the mechanism, and an improved understanding of the uncertainties in the theoretical predictions would be valuable in refining detailed chemical kinetic mechanisms. In the present study, theoretically driven modifications yield a significant improvement in the global predictions. Yet some discrepancies between the species measurements and the model predictions remain, and this fact, coupled with the changes to the sensitivities observed in this study, provide fodder for further research, which may be either theoretical or experimental in nature.

■ ASSOCIATED CONTENT

Ⓢ Supporting Information

Modified chemical kinetic mechanisms. This material is available free of charge via the Internet at http://pubs.acs.org.

■ AUTHOR INFORMATION

Corresponding Author

*Fax: 734-647-3170. Tel.: 734-763-7470. E-mail: dippind@umich.edu.

Notes

The authors declare no competing financial interest.

■ ACKNOWLEDGMENTS

This material is based on work supported by the U.S. Department of Energy, Office of Science, Office of Basic Energy Sciences, Division of Chemical Sciences, Geosciences, and Biosciences. The work at the University of Michigan was supported under Contract No. DE-SC0002645. The work at Argonne was supported under Contract No. DE-AC02-06CH11357, with the work of S.J.K. performed under the

DOI: 10.1021/jp509279d
J. Phys. Chem. A 2015, 119, 543−551

auspices of the Combustion Energy Frontier Research Center under Award No. DE-SC0001198.

REFERENCES

(1) Karwat, D. M. A.; Wagnon, S. W.; Teini, P. D.; Wooldridge, M. S. On the chemical kinetics of n-butanol: ignition and speciation studies. *J. Phys. Chem. A* **2011**, *115*, 4909−4921.
(2) Black, G.; Curran, H. J.; Pichon, S.; Simmie, J. M.; Zhukov, V. Bio-butanol: Combustion properties and detailed chemical kinetic model. *Combust. Flame* **2010**, *157*, 363−373.
(3) Stranic, I.; Pyun, S. H.; Davidson, D. F.; Hanson, R. K. Multi-species measurements in 1-butanol pyrolysis behind reflected shock waves. *Combust. Flame* **2012**, *159*, 3242−3250.
(4) Sarathy, S. M.; Oßwald, P.; Hansen, N.; Kohse-Höinghaus, K. Alcohol combustion chemistry. *Prog. Energy Combust. Sci.* **2014**, *44*, 40−102.
(5) Zhou, C.-W.; Simmie, J. M.; Curran, H. J. Rate constants for hydrogen-abstraction by OH from *n*-butanol. *Combust. Flame* **2011**, *158*, 726−731.
(6) Alecu, I. M.; Zheng, J.; Papajak, E.; Yu, T.; Truhlar, D. G. Biofuel Combustion. Energetics and Kinetics of Hydrogen Abstraction from Carbon-1 in *n*-Butanol by the Hydroperoxyl Radical Calculated by Coupled Cluster and Density Functional Theories and Multistructural Variational Transition-State Theory with Multidimensional Tunneling. *J. Phys. Chem. A* **2012**, *116*, 12206−12213.
(7) Seal, P.; Oyedepo, G.; Truhlar, D. G. Kinetics of the Hydrogen Atom Abstraction Reactions from 1-Butanol by Hydroxyl Radical: Theory Matches Experiment and More. *J. Phys. Chem. A* **2013**, *117*, 275−282.
(8) Seal, P.; Papajak, E.; Truhlar, D. G. Kinetics of the Hydrogen Abstraction from Carbon-3 of 1-Butanol by Hydroperoxyl Radical: Multi-Structural Variational Transition-State Calculations of a Reaction with 262 Conformations of the Transition State. *J. Phys. Chem. Lett.* **2012**, *3*, 264−271.
(9) Zhang, P.; Klippenstein, S. J.; Law, C. K. Ab initio kinetics for the decomposition of hydroxybutyl and butoxy radicals of *n*-butanol. *J. Phys. Chem. A* **2013**, *117*, 1890−1906.
(10) McGillen, M. R.; Baasandorj, M.; Burkholder, J. B. Gas-Phase Rate Coefficients for the OH + *n*-, *i*-, *s*-, and *t*-Butanol Reactions Measured Between 220 and 380 K: Non-Arrhenius Behavior and Site-Specific Reactivity. *J. Phys. Chem. A* **2013**, *117*, 4636−4656.
(11) Welz, O.; Zádor, J.; Savee, J. D.; Sheps, L.; Osborn, D. L.; Taatjes, C. A. Low-Temperature Combustion Chemistry of *n*-Butanol: Principal Oxidation Pathways of Hydroxybutyl Radicals. *J. Phys. Chem. A* **2013**, *117*, 11983−12001.
(12) Zhou, C.; Simmie, J. M.; Curran, H. J. Rate Constants for Hydrogen HO_2 from *n*-Butanol. *Int. J. Chem. Kinet.* **2012**, *44*, 155−164.
(13) Moc, J.; Simmie, J. M. Hydrogen Abstraction from *n*-Butanol by the Hydroxyl Radical: High Level Ab Initio Study of the Relative Significance of Various Abstraction Channels and the Role of Weakly Bound Intermediates. *J. Phys. Chem. A* **2010**, *114*, 5558−5564.
(14) Black, G.; Simmie, J. M. Barrier Heights for H-Atom Abstraction by HO_2 from *n*-Butanol—A Simple Yet Exacting Test for Model Chemistries? *J. Comput. Chem.* **2009**, *31*, 1236−1248.
(15) Grana, R.; Frassoldati, A.; Faravelli, T.; Niemann, U.; Ranzi, E.; Seiser, R.; Cattolica, R.; Seshadri, K. An experimental and kinetic modeling study of combustion of isomers of butanol. *Combust. Flame* **2010**, *157*, 2137−2154.
(16) Noorani, K. E.; Akih-Kumgeh, B.; Bergthorson, J. M. Comparative High Temperature Shock Tube Ignition of C1-C4 Primary Alcohols. *Energy Fuels* **2010**, *24*, 5834−5843.
(17) Vranckx, S.; Heufer, K. A.; Lee, C.; Olivier, H.; Schill, L.; Kopp, W. A.; Leonhard, K.; Taatjes, C. A.; Fernandes, R. X. Role of peroxy chemistry in the high-pressure ignition of *n*-butanol—Experiments and detailed kinetic modelling. *Combust. Flame* **2011**, *158*, 1444−1455.
(18) Pang, G. A.; Hanson, R. K.; Golden, D. M.; Bowman, C. T. Rate constant measurements for the overall reaction of OH + 1-butanol → products from 900 to 1200 K. *J. Phys. Chem. A* **2012**, *116*, 2475−2483.
(19) Sarathy, S. M.; Thomson, M. J.; Togbé, C.; Dagaut, P.; Halter, F.; Mounaim-Rousselle, C. An experimental and kinetic modeling study of *n*-butanol combustion. *Combust. Flame* **2009**, *156*, 852−864.
(20) Veloo, P. S.; Wang, Y. L.; Egolfopoulos, F. N.; Westbrook, C. K. A comparative experimental and computational study of methanol, ethanol, and *n*-butanol flames. *Combust. Flame* **2010**, *157*, 1989−2004.
(21) Zhang, J.; Niu, S.; Zhang, Y.; Tang, C.; Jiang, X.; Hu, E.; Huang, Z. Experimental and modeling study of the auto-ignition of *n*-heptane/*n*-butanol mixtures. *Combust. Flame* **2013**, *160*, 31−39.
(22) Dagaut, P.; Sarathy, S. M.; Thomson, M. J. A chemical kinetic study of *n*-butanol oxidation at elevated pressure in a jet stirred reactor. *Proc. Combust. Inst.* **2009**, *32*, 229−237.
(23) Hansen, N.; Harper, M. R.; Green, W. H. High-temperature oxidation chemistry of *n*-butanol—experiments in low-pressure premixed flames and detailed kinetic modeling. *Phys. Chem. Chem. Phys.* **2011**, *13*, 20262−20274.
(24) Sarathy, S. M.; Vranckx, S.; Yasunaga, K.; Mehl, M.; Oßwald, P.; Metcalfe, W. K.; Westbrook, C. K.; Pitz, W. J.; Kohse-Höinghaus, K.; Fernandes, R. X.; et al. A comprehensive chemical kinetic combustion model for the four butanol isomers. *Combust. Flame* **2012**, *159*, 2028−2055.
(25) Moss, J. T.; Berkowitz, A. M.; Oehlschlaeger, M. A.; Biet, J.; Warth, V.; Glaude, P.-A.; Battin-Leclerc, F. An Experimental and Kinetic Modeling Study of the Oxidation of the Four Isomers of Butanol. *J. Phys. Chem. A* **2008**, *112*, 10843−10855.
(26) Van Geem, K. M.; Pyl, S. P.; Marin, G. B.; Harper, M. R.; Green, W. H. Accurate High-Temperature Reaction Networks for Alternative Fuels: Butanol Isomers. *Ind. Eng. Chem. Res.* **2010**, *49*, 10399−10420.
(27) Harper, M. R.; Van Geem, K. M.; Pyl, S. P.; Marin, G. B.; Green, W. H. Comprehensive reaction mechanism for *n*-butanol pyrolysis and combustion. *Combust. Flame* **2011**, *158*, 16−41.
(28) Zhou, D. D. Y.; Han, K.; Zhang, P.; Harding, L. B.; Davis, M. J.; Skodje, R. T. Theoretical Determination of the Rate Coefficient for the $HO_2 + HO_2 \rightarrow H_2O_2 + O_2$ Reaction: Adiabatic Treatment of Anharmonic Torsional Effects. *J. Phys. Chem. A* **2012**, *116*, 2089−2100.
(29) Zhou, D. D. Y.; Davis, M. J.; Skodje, R. T. Multitarget global sensitivity analysis of *n*-butanol combustion. *J. Phys. Chem. A* **2013**, *117*, 3569−3584.
(30) Kappel, C.; Luther, K.; Troe, J. Shock wave study of the unimolecular dissociation of H2O2 in its falloff range and of its secondary reactions. *Phys. Chem. Chem. Phys.* **2002**, *4*, 4392−4398.
(31) Zheng, J.; Truhlar, D. G. Quantum Thermochemistry: Multistructural Method with Torsional Anharmonicity Based on A Coupled Torsional Potential. *J. Chem. Theory Comput.* **2013**, 1356−1367.

DOI: 10.1021/jp509279d
J. Phys. Chem. A 2015, 119, 543−551

THE JOURNAL OF PHYSICAL CHEMISTRY A

Article

pubs.acs.org/JPCA

Effects of Bond Location on the Ignition and Reaction Pathways of *trans*-Hexene Isomers

Scott W. Wagnon,*[,†] Cesar L. Barraza-Botet,[†] and Margaret S. Wooldridge[†,‡]

[†]Department of Mechanical Engineering, University of Michigan, Ann Arbor, Michigan 48109, United States

[‡]Department of Aerospace Engineering, University of Michigan, Ann Arbor, Michigan 48109, United States

Supporting Information

ABSTRACT: Chemical structure and bond location are well-known to impact combustion reactivity. The current work presents new experimental autoignition and speciation data on the three *trans*-hexene isomers (1-hexene, *trans*-2-hexene, and *trans*-3-hexene), which describe the effects of the location of the carbon−carbon double bond. Experiments were conducted with the University of Michigan rapid compression facility to determine ignition delay times from pressure time histories. Stoichiometric (ϕ = 1.0) mixtures at dilution levels of buffer gas:O_2 = 7.5 (mole basis) were investigated at an average pressure of 11 atm and temperatures from 837 to 1086 K. Fast gas sampling and gas chromatography were also used to quantitatively measure 13 stable intermediate species formed during the ignition delay period of each isomer at a temperature of ∼900 K. The measured ignition delay times and species measurements were in good agreement with previous experimental studies at overlapping conditions. The results were modeled using a gasoline surrogate reaction mechanism from Lawrence Livermore National Laboratory, which contains a submechanism for the *trans*-hexene isomers. The model predictions captured the overall autoignition characteristics of the hexene isomers well (within a factor of 2), as well as the time histories of several of the intermediate species (e.g., propene). However, there were discrepancies between the model predictions and the experimental data for some species, particularly for the 3-hexene isomer.

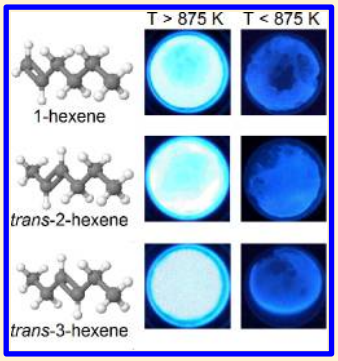

INTRODUCTION

Alkenes are an important class of species that are critical to accurate predictions of combustion reactivity and emissions for all hydrocarbon fuels. Historically, alkanes have received more attention in the literature; however, more recently, computational and experimental studies have focused on alkenes to build an understanding of the effects of fuel structure on reactivity, due to their presence in real fuels and the increasing (although currently limited) use in fuel surrogates. Despite the increased attention on alkenes, there remain significant gaps in the literature for studies of larger, ≥C_5 compounds. The research on alkene combustion can be categorized as studies focusing on smaller, <C_5 alkenes such as ethylene and propene[1−3] and larger species (excluding ring compounds). Of the larger linear species, investigations often concentrate on 1-alkenes (e.g., 1-pentene, 1-hexene, and 1-heptene) as important intermediate species and as components of surrogates and real fuels.[4−6] The results of these studies have greatly informed theory on the effects of the carbon double bond chemical structure on combustion reactions. However, there are still few experimental studies that provide details on the differences in reaction pathways between isomer alkene species. Such data provide quantitative information on the reactivity of these important species as well as inform combustion theory to improve the development of reaction rules for different classes of fuel compound structures.

The objective of the current work was to quantify the reactivity and reaction pathways of three hexene isomers via ignition and speciation measurements and to compare the results with a current understanding of the effects of the location of the carbon−carbon double bond. Hexene ignition has been studied previously for a very limited range of conditions. Vanhove et al.[7] completed an experimental study of the linear hexene isomers at stoichiometric, air dilution (buffer gas:O_2 = 3.76) conditions, moderate pressures (6.7−8.4 atm), and low temperatures (630−850 K) using a rapid compression machine. The authors concluded the behavior of the isomers at low temperatures is driven by the position of the double bond, and the double bond position results in competition between the reaction pathways of the component alkyl chains and alkenyl chains.

Yahyaoui et al.[8,9] conducted high temperature (1270−1700 K) shock tube studies of ignition of 1-hexene in O_2 and argon mixtures, as well as flow reactor oxidation studies of 1-hexene with species measurements. The flow reactor conditions included low temperatures (from 780 to 1100 K, 10 atm) of a range of equivalence ratios for dilute (0.1%) mixtures of 1-hexene in N_2.

Special Issue: 100 Years of Combustion Kinetics at Argonne: A Festschrift for Lawrence B. Harding, Joe V. Michael, and Albert F. Wagner

Received: January 31, 2015
Revised: March 6, 2015
Published: April 2, 2015

DOI: 10.1021/acs.jpca.5b01029
J. Phys. Chem. A 2015, 119, 7695−7703

Touchard et al.[10] developed a process for creating detailed reaction mechanisms to represent the oxidation of alkenes at temperatures from 600 to 900 K, highlighting the differences in alkane and alkene oxidation pathways, as well as specific differences in the two alkenes they studied: 1-hexene and 1-pentene. The proposed reaction mechanisms were validated and the process was enabled by the availability of both ignition data and measurements of intermediate species for 1-pentene. Only ignition data were available for 1-hexene at the time for stoichiometric conditions between temperatures of 615−850 K and pressures of 6.8−10.9 bar.

Mehl et al.[11] conducted computational studies of the linear hexene isomers, validating the reaction mechanism with ignition and speciation data from Vanhove et al.[7] and with the shock tube and flow reactor data from Yahyaoui et al.[8,9] Mehl et al.[11] found at high temperatures ($T \sim 1360$ K) internal isomerizations cause the three isomers to produce similar intermediates despite the double bond position. At lower temperatures ($T \sim 710$ K), Mehl et al.[11] proposed that radical additions to the double bond effectively trapped the radicals and prevented low-temperature isomerization pathways that increase reactivity.

The computational study of the linear hexene and heptene isomers by Bounaceur et al.[12] validated model predictions with experimental data for hexene from Vanhove et al.[7] and Yahyaoui et al.[9] and heptene ignition data from Tanaka et al.[13] Bounaceur et al.[12] observed that cis−trans isomers are important in modeling species with a double bond at low temperatures. Alkenes form alkenyl and alkenyl peroxy radicals that can undergo isomerization pathways (involving cis−trans conformations), which can alter reactivity and intermediates according to Bounaceur et al.[12]

More recently, Mehl et al.[14] completed an experimental shock tube ($\phi = 1$, buffer gas:$O_2 = 3.7$, $P = 11$ atm, $T = 990$−1770 K) and computational study of the linear hexene isomers. The authors concluded that at higher temperatures oxidation is driven by initiation and allyl radicals are preferentially formed due to the double bond, while at lower temperatures the length of the alkyl chain determines reactivity.

These previous studies highlight the transition in reaction behavior that occurs in alkenes from low-to-high temperatures. The studies also emphasize the dearth of data, including more rigorous metrics like species time histories that exist for validating and refining our understanding of this important class of alkene compounds. This study presents new quantitative experimental ignition delay time and species measurements that highlight the effects of the carbon−carbon double bond at temperature conditions where the transition in reaction behavior occurs; nominally, $P = 11$ atm and $T = 850$−1050 K.

EXPERIMENTAL APPROACH

All experiments were conducted using the University of Michigan rapid compression facility (UM RCF). Ignition and speciation experiments were conducted for the three linear isomers of hexene. The structures of the isomers are presented in Figure 1. A detailed description of the equipment and characterization of the UM RCF can be found in previous literature.[15−17] Brief descriptions of the different components and methods used in this study are provided here. All reactant mixtures used high purity gases (cryogenic gases: 99.994% O_2, 99.999% N_2, 99.995% CO_2, and 99.999% Ar) and liquids

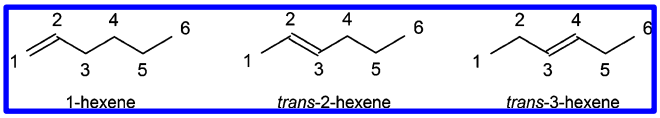

Figure 1. Molecular structures of 1-hexene (left), *trans*-2-hexene (middle), and *trans*-3-hexene (right) with carbon atoms numbered from left to right.

(Sigma-Aldrich; ≥99% 1-hexene, 97% *trans*-2-hexene, and ≥99% *trans*-3-hexene).

Ignition and High Speed Imaging. The UM RCF consists of five sections: the driver section, the driven section, the test section, the sabot and nosecone assembly, and the hydraulic globe valve assembly. Mixtures of fuel, oxygen, and buffer gases are prepared manometrically in a dedicated mixing tank with a magnetically driven stirrer. Prepared mixtures are used to fill the evacuated (filled: < approximately 1.6×10^{-1} atm, evacuated: < approximately 3.3×10^{-4} atm) driven section (stainless steel, 2.74 m × 101.2 mm i.d.) after the sabot is positioned adjacent to the globe valve assembly. A sheet of polyester film (<5.1×10^{-2} mm thickness) is placed between the sabot and globe valve assembly to ensure the integrity of the vacuum and mixture, and a polycarbonate plate is used to seal the test section while allowing optical access. High pressure air (∼10−25 psig) is utilized to fill the driver section. The sabot (Delrin) is propelled down the driven section when the globe valve is actuated. During the compression stroke, colder boundary layer gases are trapped via the annular interference fit of the nosecone (ultra high molecular weight polyethylene) and a convergent section that bridges the driven section and the test section. The interference fit also prevents mass transfer from the trapped region into the test section and thereby helps maintain uniform state conditions after the end of compression.

A piezoelectric transducer (Kistler 6045A) in series with a charge amplifier (Kistler 5010B) is used to measure the pressure in the test section. Chemiluminescence from ignition is recorded with a high speed digital color camera (Vision Research Phantom v711 camera) through the transparent end wall. Experiments are recorded with a fixed exposure time of 38 μs and at a rate of 26000 frames per second. The camera is equipped with a fast 50 mm lens (f/0.95, Navitar) with a c-mount extension tube.

Fast Gas Sampling and Analysis. A detailed description of the fast gas sampling system and gas chromatography techniques applied in this study are provided in Karwat et al.[17] For gas sampling experiments, the polycarbonate end plate is replaced with a stainless steel plate to which two independently actuated sampling systems are mounted. Stainless steel tubes extend (10 mm) from the stainless steel plate beyond the cold boundary layer of the test section to sample the reactive mixture. Each sampling system includes the following components: a fast sampling valve (Festo MHE3-MS1H-3/26−1/8, stock response 3 ms), a sampling chamber (4.5 ± 0.5 mL), a piezoresistive pressure transducer (Kistler 4045A2) and charge amplifier (Kistler 4618A0), a septum port (VICI Valco, low-bleed), and an isolation valve. The sampling valves are actuated by a trigger signal from a pulse generator (Stanford Research Systems DG535) and have a modified response time of ∼1.5 ms. Samples are acquired from the test section and quenched upon expansion into the evacuated sampling chamber. A syringe (Hamilton Gastight no. 1010, 10 mL) is inserted into the septum port to obtain a gas sample for

DOI: 10.1021/acs.jpca.5b01029
J. Phys. Chem. A 2015, 119, 7695−7703

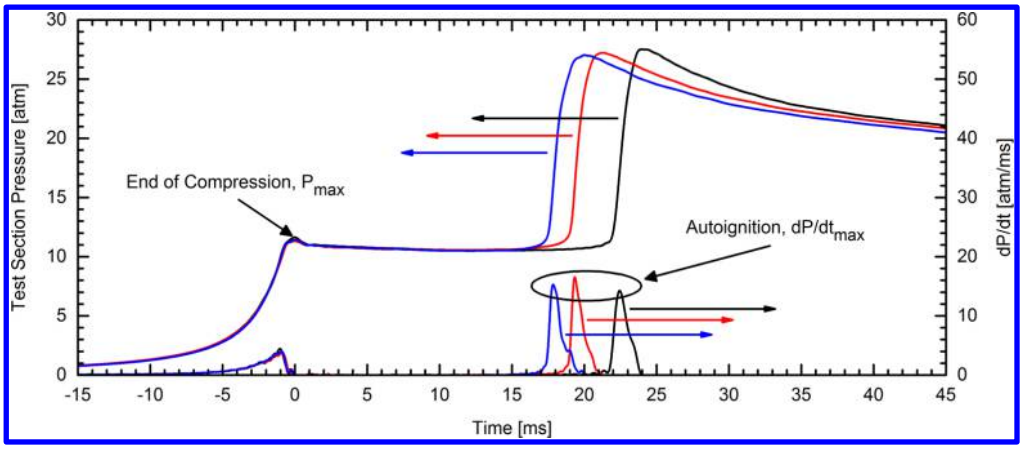

Figure 2. Typical pressure and pressure derivative time histories for ignition experiments of each of the three linear hexene isomers. Experimental conditions for the three isomers were ϕ = 1.0, buffer gas:O_2 = 7.5, P_{eff} = 10.8 atm; 1-hexene: T_{eff} = 900 K, τ_{ign} = 22.5 ms; *trans*-2-hexene: T_{eff} = 897 K, τ_{ign} = 19.4 ms; *trans*-3-hexene: T_{eff} = 896 K, τ_{ign} = 17.9 ms. The end of compression is set at t = 0 ms, as defined by P_{max}.

injection into the gas chromatographs which are equipped with columns for identifying and quantifying stable intermediates.

Four GCs (PerkinElmer Autosystem) and columns allowed the stable intermediate species to be identified and quantified. GC−OHC used a flame ionization detector (FID) with a Varian CP-Porabond Q capillary column to target hydrocarbon species up to C_6, including oxygenates. GC-C5 used a FID with a Varian CP-Al_2O_3/Na_2SO_4 capillary column to target species smaller than C_5. GC-LVHC was equipped with a FID with a Varian DB-Wax capillary column to target low volatility and high polarity species. GC-PG utilized a thermal conductivity detector (TCD) and a Restek ShinCarbon ST packed column to target permanent gases and light hydrocarbon species. Helium was used as the carrier gas in all the GCs. The temperature methods applied for each of the columns used in this study are provided in the Supporting Information.

High purity gases and vapor from high purity liquids were used to determine calibration standards for 29 stable intermediates and mixture components. The calibrated species, purities, and suppliers used in this study are provided in the Supporting Information. Signals from the gas chromatographs were captured using a high-resolution data acquisition system (NI PXI 4472) at a rate of 8 Hz. Species were calibrated and quantified using the area under the response peak unless otherwise noted.

■ COMPUTATIONAL APPROACH

Computational simulations were carried out using the CHEMKIN suite (version 10131, x64)[18] and assuming a closed zero-dimensional homogeneous batch reactor at adiabatic, constant volume conditions. The appropriateness of these modeling assumptions has been considered previously for UM RCF experiments[17,19] and by others[20] and were evaluated using the same methods as described in He et al.[21] and Mansfield and Wooldridge.[19] Specifically, reaction during compression is typically negligible for experiments with ignition delay times τ_{ign} > approximately 5 ms, and heat transfer effects are well-represented by the "effective" or average thermodynamic state conditions (defined below) for τ_{ign} < approximately 50 ms. Other methods to model heat losses in RCF experiments exist, such as including the compression stroke and representing heat transfer losses as a virtual expansion stroke after the end of mechanical compression. Such an approach leads to minor differences (< approximately 15%) in ignition delay times between the methods used in this study. Moreover, the use of effective state conditions for reporting the experimental data and for the model simulations provide greater transparency and clarity in understanding the effect of state conditions, and consequently, the time-integrated effective conditions were used here. Default values from CHEMKIN were used for the solver tolerances and solver time steps.

Autoignition simulations of the hexene isomers were conducted using the Lawrence Livermore National Laboratory (LLNL) gasoline surrogate chemical kinetic mechanism developed by Mehl et al.[22] The LLNL reaction mechanism was selected due to the maturity and extensive validation that has been previously completed on the reaction chemistry. No modifications to reaction rates were made to the mechanism considered in this study. The mechanism does not consider NO_x chemistry.

The LLNL gasoline surrogate mechanism was developed to incorporate several submechanisms, including a set of reaction chemistry for the three linear hexene isomers considered in this study. The LLNL gasoline surrogate mechanism consists of four submechanisms, with the first submechanism describing small hydrocarbons ($\leq C_4$). The three remaining submechanisms describe the main reaction pathways for linear saturated and unsaturated hydrocarons ($\leq C_7$), branched hydrocarbons ($\leq C_8$), and aromatics. The reaction pathways for the linear hexene isomers in the gasoline surrogate mechanism were based on work by Mehl et al.[11,14] With regard to the hexene reaction pathways in the gasoline surrogate mechanisms, Mehl et al.[22] reported satisfactory validation of 1-hexene simulations with the low-temperature ignition delay time measurements of Vanhove et al.,[7] and previous validation work by Mehl et al.[14] reported satisfactory agreement with the additional hexene validation targets from the shock tube and reactor studies by Yahyaoui et al.[8,9]

■ RESULTS AND DISCUSSION

Ignition Delay Times. Experimental pressure and pressure-derivative data for ignition delay time measurements of the three hexene isomers (1-hexene, *trans*-2-hexene, and *trans*-3-hexene) are plotted in Figure 2. Thermodynamic state conditions used in this study are the effective pressure (P_{eff}) and the corresponding effective temperature (T_{eff}). Effective pressure is defined as the integrated time averaged pressure, beginning at the local maximum in pressure at the end of

DOI: 10.1021/acs.jpca.5b01029
J. Phys. Chem. A 2015, 119, 7695−7703

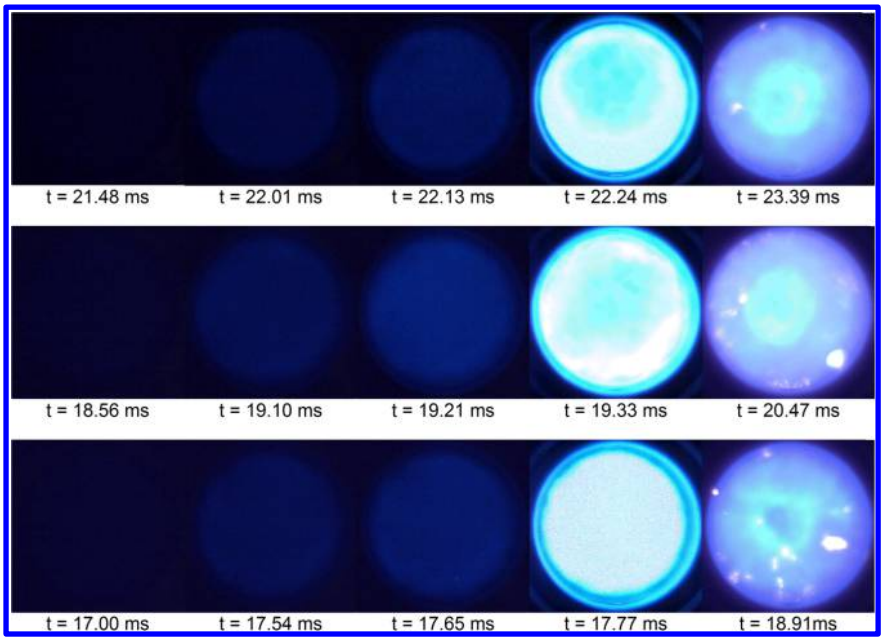

Figure 3. Typical still images from the high-speed imaging of the 1-hexene (top row), *trans*-2-hexene (middle row), and *trans*-3-hexene (bottom row) UM RCF experiments presented in Figure 2.

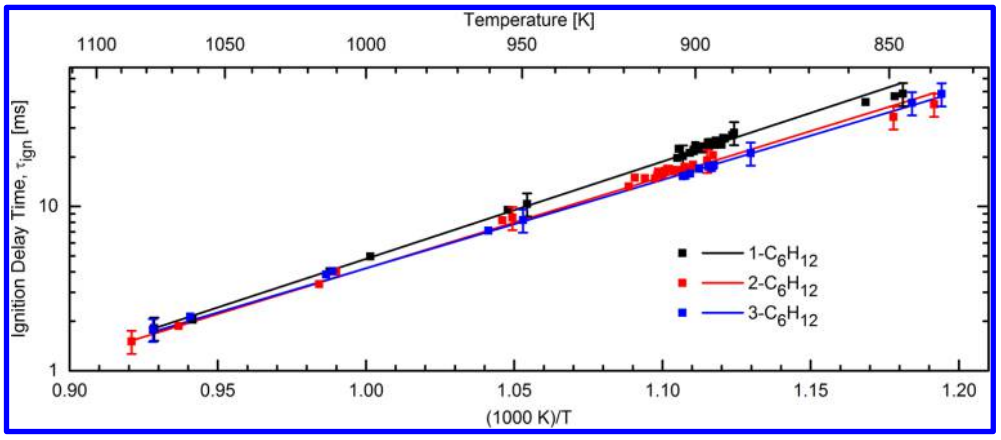

Figure 4. Arrhenius plot of the UM RCF measurements of ignition delay times of 1-hexene (black symbols), *trans*-2-hexene (red symbols), and *trans*-3-hexene (blue symbols). Temperature-dependent regressions of the experimental data are provided as lines. All experimental data have been normalized to conditions of buffer gas:O_2 = 7.5 and P = 11 atm.

compression (P_{max}) and ending at the maximum in the pressure derivative (dP/dt_{max}), shown in Figure 2. Effective temperature is calculated from the effective pressure using isentropic relations. The ignition delay time corresponds to the time between P_{max} and dP/dt_{max}.

Typical still images from the high-speed imaging taken during the experiments are presented in Figure 3. The images shown correspond to the experimental data presented in Figure 2. Blue emission from chemiluminescence was homogeneous (i.e., occurring simultaneously throughout the test volume) for all ignition experiments with T_{eff} > 875 K. At the lowest temperatures (<875 K), the imaging data from 1-hexene and *trans*-2-hexene showed some spatial progress to the chemiluminescence during ignition (over a very short duration, <1 ms). This behavior may be due to transition of the reaction chemistry into negative temperature dependence. The pressure time history and corresponding still images from typical low-temperature experiments are provided in the Supporting Information.

Experimental conditions for each fuel were fixed at a stoichiometric fuel-to-O_2 equivalence ratio (ϕ = 1) and dilution of buffer gas:O_2 = 7.5 (molar basis). Buffer gas composition was varied between Ar, CO_2, and N_2 to control the end of compression thermodynamic state conditions. Changes in the buffer gas composition are expected to have negligible effect on the ignition delay times and intermediate species measured in this work based on comparison with previous buffer gas studies.[20,23] The hexene ignition data focused on a limited range of effective pressures (from P_{eff} = 10.4 to 12.1 atm with an average value of P_{eff} = 11.1 atm) and effective temperatures from T_{eff} = 837 to T_{eff} = 1086 K. A summary of the measured ignition delay times for the three hexene isomers is presented in Figure 4. Tables of the experimental conditions and results are provided in the Supporting Information. The experimental data of Figure 4 have been scaled to the molar dilution ratio of 7.5 and P = 11 atm, assuming ignition delay times scale inversely with pressure (i.e., as P^{-1}) and proportionally with dilution based on the molar ratio of buffer gas:O_2 [e.g., $\tau_{ign} \propto$ (the ratio

DOI: 10.1021/acs.jpca.5b01029
J. Phys. Chem. A 2015, 119, 7695−7703

of the mole fraction of the inert gases to the mole fraction of the O_2 in the reactant mixture)]. The scaling rules are based on trends observed in previous ignition studies[17,23,24] and are considered reasonably accurate for data outside the negative coefficient region of the fuels. For the experiments presented here, the dilution levels ranged from ratios of 7.45:1 to ratios of 7.51:1 and the scaling for dilution is not expected to be a significant source of error for comparing the reactivity of the three isomers. The recommended uncertainty of ±16% in the ignition delay times is shown as the error bars in Figure 4 and is attributed primarily to the accuracy of the test section pressure transducer (± <0.4% FSO).

The results in Figure 4 show the three hexene isomers exhibited virtually identical reactivity (within the uncertainty of the measurements) at the conditions studied. Arrhenius behavior was observed for 2-hexene and 3-hexene throughout the range of temperatures studied and for temperatures above 875 K for 1-hexene. The lowest temperature data (<875 K) show a slight increase in reactivity and decrease in activation energy for 1-hexene, consistent with theory and previous studies, indicating the possible onset of non-Arrhenius behavior at these conditions. Regression correlations of the form $\tau_{ign} = A \exp(E_a/\bar{R}T)$ were determined from the data using best-fit analysis, and the results of the correlations are shown in Figure 4 as solid lines. The R^2 values and the correlation parameters are provided in Table 1.

Table 1. Best-Fit Parameters from the Correlations for Ignition Delay Time from the Data of the Current Study for 1-Hexene, *trans*-2-Hexene, and *trans*-3-Hexene at Conditions of ϕ = 1.0, Buffer Gas:O_2 = 7.5 and P = 11 atm[a]

fuel	A (ms)	E_a (cal/mol K^{-1})	T (K)	R^2
1-hexene	5.8×10^{-6}	27100	847−1077	0.992
trans-2-hexene	1.1×10^{-5}	25500	839−1086	0.992
trans-3-hexene	1.8×10^{-5}	24600	837−1077	0.997

[a]Regression correlations are in the form of $\tau_{ign} = A \exp(E_a/\bar{R}T)$.

Figure 5 presents a comparison of the results of the current work with the results from Vanhove et al.[7] and from Mehl et al.[14] All data were acquired at stoichiometric conditions and have been scaled to the dilution and pressure of the current work (buffer gas:O_2 = 7.5 and P = 11 atm) as described earlier, assuming ignition delay time scales inversely with pressure and proportionally with the molar dilution level of the initial reactant mixture (i.e., the ratio of the inert gas mole fraction to the O_2 mole fraction). Recall the data from Vanhove et al.[7] spanned pressures of 6.7−8.4 atm and used dilution levels of 3.76:1. The data from Mehl et al.[14] were measured at a pressure of 11 atm and used a dilution level of 3.7:1. The combined data sets span 3 orders of magnitude in ignition delay time and emphasize the value in multiple experimental methods to cover high and low temperature ignition regimes. At high temperatures, there is excellent agreement (within the scatter of the data sets) with the results of the current work and the data of Mehl et al.[14] Where the data overlap at low temperatures, there is reasonable agreement between the results of the current work and the data of Vanhove et al.,[7] within a factor of 2; however, the two data sets indicate opposite order of reactivity for the three isomers. Differences in the order of magnitude of the ignition delay times at low temperatures may be due to different reporting practices (i.e., the use of T_{eff} versus $T_{end\text{-}of\text{-}compression}$) and differences in heat losses which become more significant at the long test times required at low temperatures. The scaling rules are also expected to be less appropriate at the low temperature conditions that are in the non-Arrhenius region. However, the relative trends of reactivity for the three isomers are not expected to be affected by these uncertainties. The trends observed in the two studies may therefore represent the transition from high-to-low temperature hexene isomer chemistry, and this transition region is an excellent area for future work.

CHEMKIN simulation results (ϕ = 1, buffer gas:O_2 = 7.5, P = 11 atm) using the Mehl et al.[22] mechanism are presented in Figure 5 as solid lines. The simulations considered initial

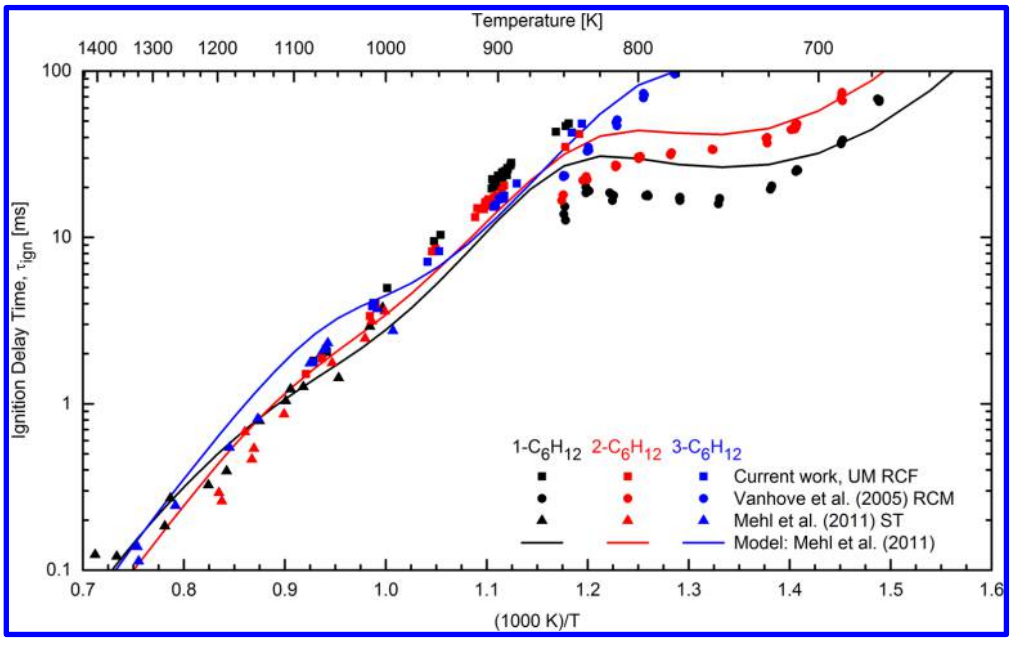

Figure 5. Comparison of results from the current work with data from previous ignition studies of the linear hexene isomers.[7,14,22] Predicted results for ignition delay time are shown as the solid lines. All experimental data have been normalized to ϕ = 1, buffer gas:O_2 = 7.5 and P = 11 atm.

DOI: 10.1021/acs.jpca.5b01029
J. Phys. Chem. A 2015, 119, 7695−7703

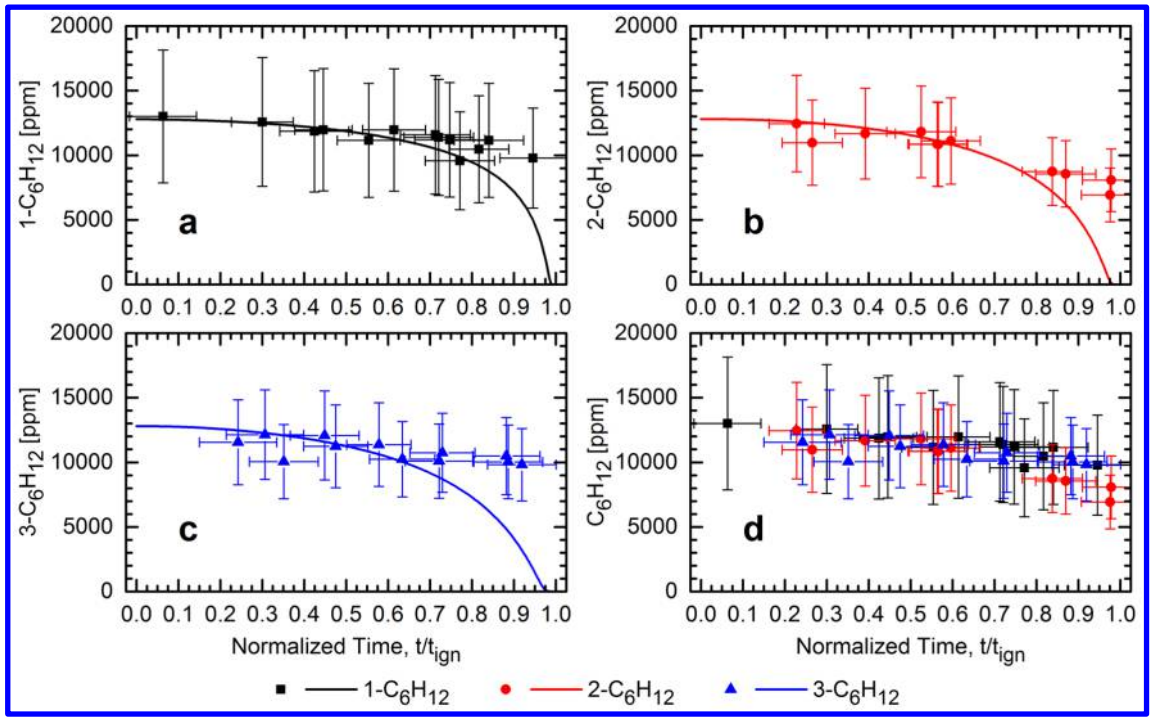

Figure 6. Measured (symbols) and predicted (lines) fuel time histories during autoignition of the three hexene isomers. Results are presented for mixtures of (a) 1-hexene, (b) *trans*-2-hexene, (c) *trans*-3-hexene, and (d) all three hexene isomers. Simulations used the Mehl et al.[22] mechanism at the average compositions and conditions of the experiments.

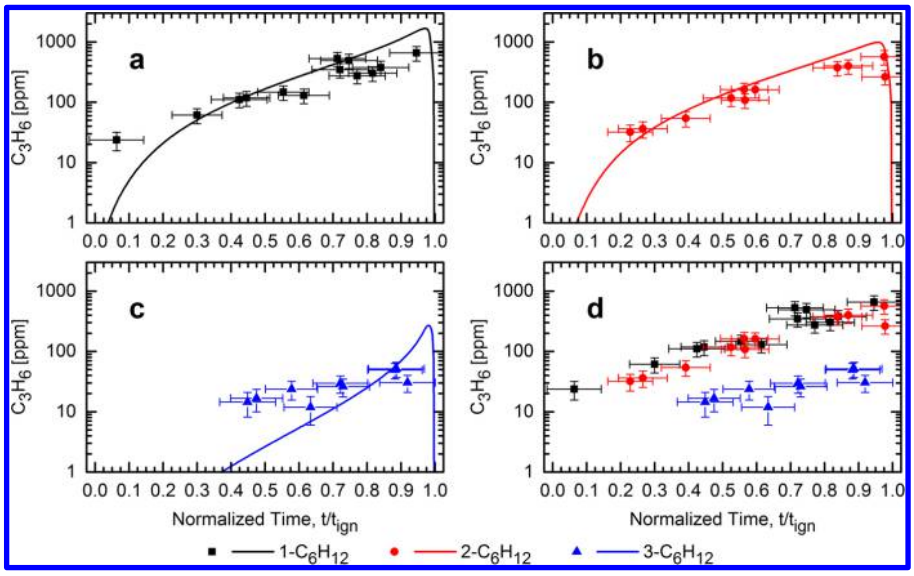

Figure 7. Measured (symbols) and predicted (lines) propene (C_2H_2) time histories during autoignition of the three hexene isomers. Results are presented for mixtures of (a) 1-hexene, (b) *trans*-2-hexene, (c) *trans*-3-hexene, and (d) all three hexene isomers. Simulations used the Mehl et al.[22] mechanism at the average compositions and conditions of the experiments.

temperatures ranging from 600 to 1500 K in 25 K increments for each of the three hexene isomers. Nitrogen was used as the buffer gas in the simulations. There is excellent qualitative and quantitative agreement between the three experimental data sets and the simulation results. Specifically, the model predicts no differences in reactivity for the three isomers at temperatures above 875 K, in the temperature range of the current study. There is some unusual behavior predicted for 3-hexene at ~1100 K, but the agreement with the experimental data is likely within the uncertainty of the reaction mechanism. The slight differences in the agreement of the model predictions with the experimental data below 850 K may be due to effects from heat transfer, differences in buffer gas composition, and weak ignition phenomena which can affect lower temperatures, as well as uncertainty in the reaction mechanism.

Intermediate Species. Results from the fast gas sampling for the three hexene fuels are shown in Figures 6–8 for hexene, propene, and propanal, respectively. Additional stable intermediate species measurements are provided in the Supporting Information for carbon monoxide, methane, methanol, ethyne (acetylene), ethene, ethane, ethanal (acetaldehyde), 1-butene, 1,3-butadiene, and 1-pentene. Presented in Figure 6 are the

DOI: 10.1021/acs.jpca.5b01029
J. Phys. Chem. A 2015, 119, 7695−7703

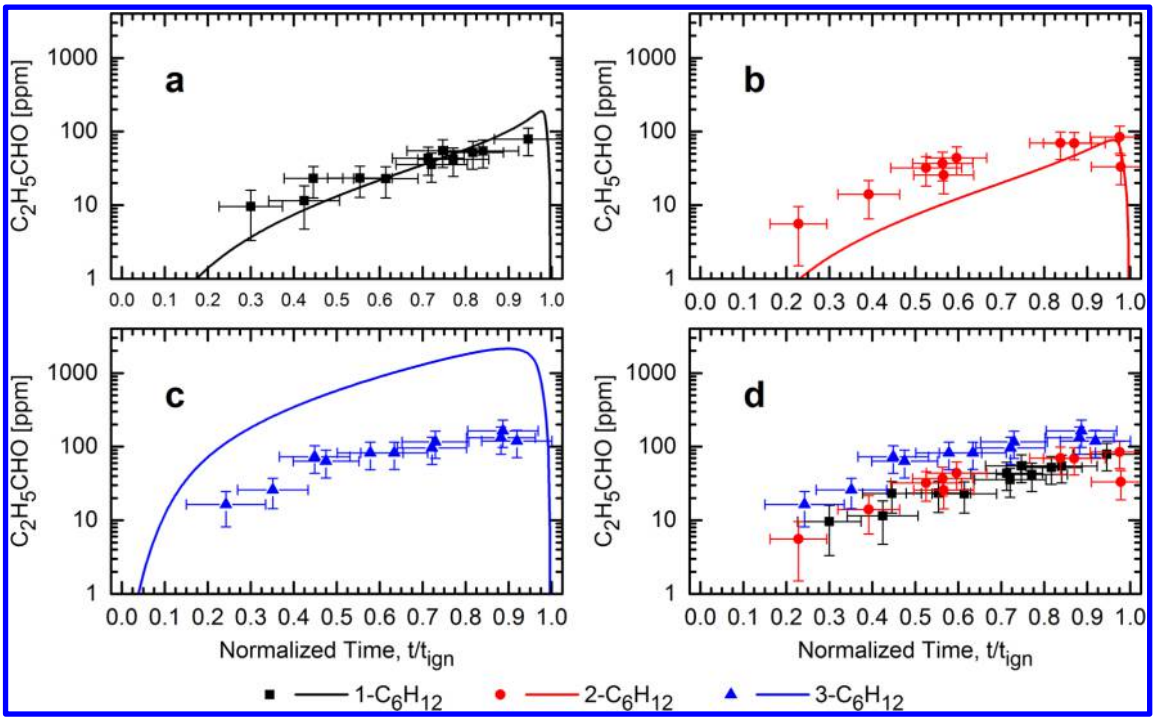

Figure 8. Measured (symbols) and predicted (lines) propanal (C_2H_5CHO) time histories during autoignition of the three hexene isomers. Results are presented for mixtures of (a) 1-hexene, (b) *trans*-2-hexene, (c) *trans*-3-hexene, and (d) all three hexene isomers. Simulations used the Mehl et al.[22] mechanism at the average compositions and conditions of the experiments.

measured concentrations of the hexene fuels where the horizontal and vertical error bars represent the uncertainty in sample duration and timing (±1.8 ms) and measured concentration (±40%). The timescale in Figure 6 has been normalized such that end of compression corresponds to t/τ_{ign} = 0 and autoignition to t/τ_{ign} = 1 (the normalized pressure time histories from the corresponding experiments are provided in the Supporting Information). The experimental data for the hexene fuels indicate that the rate of consumption is similar for all three isomers, with a rapid increase in the rate of consumption late in the ignition delay time period (t/τ_{ign} > 0.9).

Model predictions using the Mehl et al.[22] mechanism are also shown in Figures 6−8. The initial conditions and compositions for the 0D, isometric, adiabatic CHEMKIN simulation were the average conditions of the fast gas sampling experiments: 1-hexene (P_{eff} = 11.1 atm, T_{eff} = 896 K, ϕ = 1.0, $\chi(O_2)$ = 11.63%, and buffer gas:O_2 = 7.5), *trans*-2-hexene (P_{eff} = 11.3 atm, T_{eff} = 905 K, ϕ = 1.0, $\chi(O_2)$ = 11.62%, and buffer gas:O_2 = 7.5), and *trans*-3-hexene (P_{eff} = 11.2 atm, T_{eff} = 899 K, ϕ = 1.0, $\chi(O_2)$ = 11.63%, and buffer gas:O2 = 7.5). Agreement between the experimental data and the model is generally excellent and within 20% for the majority of the time history of the hexenes; however, the model does predict faster consumption rates for all three isomers. Specifically, the experimental measurements show ∼25% consumption for 1-hexene and *trans*-3-hexene and ∼35% consumption for *trans*-2-hexene at ∼90% of the ignition delay times. The model predicts consumption ∼2−3× higher at ∼90% of the ignition delay times (∼45% consumption for 1-hexene, ∼60% for *trans*-2-hexene, and ∼70% for *trans*-3-hexene). This comparison indicates the initial abstraction reactions for the hexene isomers are good candidate reactions for future studies. Note that reducing the initiation reaction rates may impact the intermediate species time histories, as discussed below. At later times (t/τ_{ign} greater than ∼0.9) during the ignition delay period, the model overpredicts the rate of consumption of *trans*-3-hexene. For the majority of the ignition delay period (t/τ_{ign} less than ∼0.9), the hexene concentrations and the measured stable intermediates account for greater than 80% of the carbon initially in the test mixtures.

Figure 7 shows the measurements and model predictions for propene (C_3H_6). The model and experimental data are in good agreement, within a factor of 3, for much of the ignition delay period. The experimental data also indicate that a longer alkyl chain promotes significantly increased propene production (a factor of ∼5 increase in propene comparing *trans*-3-hexene and 1-hexene at t/τ_{ign} ∼0.93), and this trend is well predicted by the mechanism simulations.

Figure 8 shows the measurements and model predictions for propanal (C_2H_5CHO). For 1-hexene and *trans*-2-hexene, the experimental data and the simulations are in excellent agreement, within a factor of 2. Unlike propene, the experimental measurements indicate propanal production decreases for the longer alkyl chain isomers and exhibits less sensitivity to the double bond position (a factor of ∼2 decrease in propanal comparing *trans*-3-hexene and 1-hexene at t/τ_{ign} ∼0.93). However, the simulations overpredict the experimental measurements for propanal during 3-hexene ignition by more than a factor of 10. While the overprediction of the propanal (and potentially other intermediate species) may be related to the higher hexene consumption rates predicted by the model as discussed above, that would not explain the overprediction at times earlier than ∼50% of the ignition delay time. Additional figures are provided in the Supporting Information, which show how reductions to the initiation reaction rates would influence *trans*-3-hexene consumption, production of propene, and production of propanal.

DOI: 10.1021/acs.jpca.5b01029
J. Phys. Chem. A 2015, 119, 7695−7703

Not shown here, but available in the Supporting Information, are several additional species and comparisons with the model predictions. Because they are formed late in the ignition process, there are few experimental data for carbon monoxide, ethyne, and 1-pentene; however, the results are in excellent agreement with the model predictions. Methanol is under-predicted for all three isomers. The experimental data and the model predictions are in excellent agreement (within the experimental uncertainty) for ethene, ethanal, and 1,3 butadiene for 1-hexene and 2-hexene. However, the model significantly overpredicts the formation of these species for 3-hexene. The model under-predicts the formation of 1-butene for 1-hexene with reasonable agreement with the other hexene isomers. The methane and ethane data agree within a factor of 2 for all hexene isomers.

The trends for the intermediate species measurements indicates the small alkene and small alkane chemistry is generally well-represented in the LLNL reaction mechanism for 1-hexene and 2-hexene; however, some reaction pathways for 3-hexene differ significantly with the experimental measurement [e.g., ethanal (acetaldehyde), propanal, and 1,3-butadiene]. As described in Vanhove et al.[7] and Mehl et al.,[14] alkene chemistry undergoes a transition from low temperatures where allyl radical reactions dominate to higher temperatures (>900 K) where β-decomposition of alkenyl radicals dominate. The species measurements of Vanhove et al.[7] were made at end-of-compression temperatures of 710 K, compared to the ~900 K conditions studied here. Thus, the two sets of species measurements are expected to be representative of the low temperature (Vanhove et al.[7]) and high/transition temperature (current work) regimes. Some species were identified and quantified in both studies, including ethanal and propanal. Vanhove et al.[7] found relative selectivities or proportions during ignition for ethanal of 2-hexene > 1-hexene > 3-hexene and for propanal of 3-hexene > 1-hexene > 2-hexene. In the current work, the same relative orders were found for ethanal and propanal, for example, ethanal was formed at the highest levels during 2-hexene ignition and the lowest levels during 3-hexene ignition. Vanhove et al.[7] propose a primary path for propanal formation during 3-hexene ignition is from the reaction sequence initiated by OH addition to the double bond of 3-hexene, as well as through subsequent fuel fragment reactions. Rate of production analysis conducted here and provided in the Supporting Information supports that the propanal reaction is the only active channel for 3-hexene + OH. The overprediction of the LLNL reaction mechanism for propanal indicates the OH addition to the double bond of 3-hexene is too fast and would be a good candidate reaction for further experimental and computational studies.

CONCLUSIONS

The new ignition delay time data for the three linear hexene isomers presented in this work show negligible sensitivity to the location of the carbon−carbon double bond for the temperatures considered, consistent with expectations for alkenes at high temperatures (>900 K). However, the measurements of stable intermediates showed significant differences in the isomer reaction pathways. Measurements of the three hexene fuels indicate the initial oxidation of the three hexene isomers proceeds at similar rates. However, the length of the alkyl chain leads to differentiation in the stable intermediates produced and the reaction pathways. The ignition delay results from this study are in good agreement with previous experimental studies at higher and lower temperatures. Model predictions for the ignition delay times and intermediate species were in generally good agreement with the experimental data; however, the reaction chemistry for 3-hexene significantly overpredicts the formation of the small aldehyde (C_2 and C_3) species. The results of the current work emphasize the value of bulk reactivity data (e.g., ignition delay time) and species measurements as important methods to identify similarities and differences in reactivity and reaction pathways, which are particularly vital toward developing reaction rate rules for classes of fuel compounds. In particular, the results of the current work are the first species measurements in the high/transition temperature regime for this important alkene.

ASSOCIATED CONTENT

Supporting Information

Tables of the ignition delay data, calibration gases, and gas chromatography methods; pressure-time histories and corresponding images at low temperature (~850 K) conditions for each of the hexene isomers; additional stable species-time histories from the gas sampling experiments; and reaction pathways based on rate of production analysis for propanal. This material is available free of charge via the Internet at http://pubs.acs.org.

AUTHOR INFORMATION

Corresponding Author

*Address: University of Michigan Department of Mechanical Engineering 2350 Hayward Street, Ann Arbor, Michigan 48109-2125, United States. E-mail: swagnon@umich.edu. Tel: 734-763-7470. Fax: 734-647-3170.

Author Contributions

The manuscript was written through contributions of all authors. All authors have approved the final version of the manuscript.

Notes

The authors declare no competing financial interest.

ACKNOWLEDGMENTS

The authors would like to thank the Division of Chemical Sciences, Geosciences, and Biosciences, Office of Basic Energy Sciences, U.S. Department of Energy for their financial support via Contract DE-SC0002645.

REFERENCES

(1) Heyberger, B.; Belmekki, N.; Conraud, V.; Glaude, P. A.; Fournet, R.; Battin-Leclerc, F. Oxidation of Small Alkenes at High Temperature. *Int. J. Chem. Kinet.* **2002**, *34*, 666−677.

(2) Saxena, S.; Kahandawala, M. S. P.; Sidhu, S. S. A Shock Tube Study of Ignition Delay in the Combustion of Ethylene. *Combust. Flame* **2011**, *158*, 1019−1031.

(3) Qin, Z.; Yang, H.; Gardiner, W. C. Measurement and Modeling of Shock-Tube Ignition Delay for Propene. *Combust. Flame* **2001**, *124*, 246−254.

(4) Perez, P. L.; Boehman, A. L. Effects of the Chemical Structure and Composition of Surrogate Gasoline Fuels on Homogeneous Charge Compression Ignition Combustion in a Single-Cylinder Engine. *Energy Fuels* **2014**, *28*, 3377−3390.

(5) Luo, J.; Yao, M.; Liu, H. A Reduced Chemical Kinetic Mechanism for Low Temperature Diesel Combustion and Soot Emissions. *Combust. Sci. Technol.* **2014**, *186*, 1975−1990.

(6) Perez, P. L.; Boehman, A. L. Experimental Investigation of the Autoignition Behavior of Surrogate Gasoline Fuels in a Constant-

DOI: 10.1021/acs.jpca.5b01029
J. Phys. Chem. A 2015, 119, 7695−7703

Volume Combustion Bomb Apparatus and Its Relevance to HCCI Combustion. *Energy Fuels* **2012**, *26*, 6106−6117.
(7) Vanhove, G.; Ribaucour, M.; Minetti, R. On the Influence of the Position of the Double Bond on the Low-Temperature Chemistry of Hexenes. *Proc. Combust. Inst.* **2005**, *30*, 1065−1072.
(8) Yahyaoui, M.; Debaili-Chaumeix, N.; Paillard, C.-E.; Touchard, S.; Fournet, R.; Glaude, P. A.; Battin-Leclerc, F. Experimental and Modeling Study of 1-Hexene Oxidation Behind Reflected Shock Waves. *Proc. Combust. Inst.* **2005**, *30*, 1137−1145.
(9) Yahyaoui, M.; Debaili-Chaumeix, N.; Dagaut, P.; Paillard, C.-E.; Gail, S. Kinetics of 1-Hexene Oxidation in a JSR and a Shock Tube: Experimental and Modeling Study. *Combust. Flame* **2006**, *147*, 67−78.
(10) Touchard, S.; Fournet, R.; Glaude, P. A.; Warth, V.; Battin-Leclerc, F.; Vanhove, G.; Ribaucour, M.; Minetti, M. Modeling of the Oxidation of Large Alkenes at Low Temperature. *Proc. Combust. Inst.* **2005**, *30*, 1073−1081.
(11) Mehl, M.; Vanhove, G.; Pitz, W. J.; Ranzi, E. Oxidation and Combustion of the *n*-Hexene Isomers: A Wide Range Kinetic Modeling Study. *Combust. Flame* **2008**, *155*, 756−772.
(12) Bounaceur, R.; Warth, V.; Sirjean, B.; Glaude, P. A.; Fournet, R.; Battin-Leclerc, F. Influence of the Position of the Double Bond on the Autoignition of Linear Alkenes at Low Temperature. *Proc. Combust. Inst.* **2009**, *32*, 387−394.
(13) Tanaka, S.; Ayala, F.; Keck, J. C.; Heywood, J. B. Two-Stage Ignition in HCCI Combustion and HCCI Control by Fuels and Additives. *Combust. Flame* **2003**, *132*, 219−239.
(14) Mehl, M.; Pitz, W. J.; Westbrook, C. K.; Yasunaga, K.; Conroy, C.; Curran, H. J. Autoignition Behavior of Unsaturated Hydrocarbons in the Low and High Temperature Regions. *Proc. Combust. Inst.* **2011**, *33*, 201−208.
(15) Donovan, M. T.; He, X.; Zigler, B. T.; Palmer, T. R.; Wooldridge, M. S.; Atreya, A. Demonstration of a Free-Piston Rapid Compression Facility for the Study of High Temperature Combustion Phenomena. *Combust. Flame* **2004**, *137*, 351−365.
(16) Walton, S. W.; He, X.; Zigler, B. T.; Wooldridge, M. S.; Atreya, A. An Experimental Investigation of *iso*-Octane Ignition Phenomena. *Combust. Flame* **2007**, *150*, 246−262.
(17) Karwat, D. M. A.; Wagnon, S. W.; Wooldridge, M. S.; Westbrook, C. K. Low-Temperature Speciation and Chemical Kinetic Studies of *n*-Heptane. *Combust. Flame* **2013**, *160*, 2693−2706.
(18) *CHEMKIN Release 10131 (x64)*; Reaction Design: San Diego, 2013.
(19) Mansfield, A. B.; Wooldridge, M. S. High-Pressure Low-Temperature Ignition Behavior of Syngas Mixtures. *Combust. Flame* **2014**, *161*, 2242−2251.
(20) Wurmel, J.; Silke, E. J.; Curran, H. J.; Conaire, M. S. Ó.; Simmie, J. M. The Effect of Diluent Gases on Ignition Delay Times in the Shock Tube and in the Rapid Compression Machine. *Combust. Flame* **2007**, *151*, 289−302.
(21) He, X.; Walton, S. M.; Zigler, B. T.; Wooldridge, M. S.; Atreya, A. Experimental Investigation of the Intermediates of Isooctane During Ignition. *Int. J. Chem. Kinet.* **2007**, *39*, 498−517.
(22) Mehl, M.; Pitz, W. J.; Westbrook, C. K.; Curran, H. J. Kinetic Modeling of Gasoline Surrogate Components and Mixtures Under Engine Conditions. *Proc. Combust. Inst.* **2011**, *33*, 193−200.
(23) Wagnon, S. W.; Wooldridge, M. S. Effects of Buffer Gas Composition on Autoignition. *Combust. Flame* **2014**, *161*, 898−907.
(24) Davidson, D. F.; Haylett, D. R.; Hanson, R. K. Development of an Aerosol Shock Tube for Kinetic Studies of Low-Vapor-Pressure Fuels. *Combust. Flame* **2008**, *155*, 108−117.

DOI: 10.1021/acs.jpca.5b01029
J. Phys. Chem. A 2015, 119, 7695−7703

Combustion and Flame 163 (2016) 79–89

Contents lists available at ScienceDirect

Combustion and Flame

journal homepage: www.elsevier.com/locate/combustflame

A numerical study of the effects of primary reference fuel chemical kinetics on ignition and heat release under homogeneous reciprocating engine conditions

Mohammad Fatouraie [a,*], Darshan M.A. Karwat [a], Margaret S. Wooldridge [a,b]

[a] Department of Mechanical Engineering, University of Michigan, 2350 Hayward Street, Ann Arbor, Michigan 48109-2125, USA
[b] Department of Aerospace Engineering, University of Michigan, Ann Arbor, MI 48109-2125, USA

ARTICLE INFO

Article history:
Received 14 May 2015
Revised 31 August 2015
Accepted 2 September 2015
Available online 23 October 2015

Keywords:
iso-octane
n-heptane
Primary reference fuel blends
Detailed chemical kinetics
Numerical simulation

ABSTRACT

In the current work, numerical simulations are used to evaluate the effects of detailed reaction chemistry of different primary reference fuel (PRF) blends of *iso*-octane and *n*-heptane on heat release in one-dimensional engine simulations. A simplified slider-crank model was used to represent the engine cycle. The contributions of specific reaction classes to ignition and heat release were quantified. Maps of ignition phasing and heat release were created as a function of pressure and temperature to indicate the change in reactivity (defined by the first and second stages of ignition) as a function of state conditions as well as the fraction of heat release associated with the two stages of ignition. For the conditions studied, the reactivity of the second stage of ignition always increased with increasing temperature, i.e. the phasing of autoignition advanced with increasing temperature, whereas the reactivity of the first stage of ignition exhibited negative temperature dependence where increasing temperature delayed the first stage of ignition and decreased the heat release at the first stage of ignition for some conditions. The results show low-temperature chemistry radicals like C_7 RO_2 species are not uniquely indicative of low-temperature heat release, but they are formed at earlier times, higher rates and higher concentrations with PRF blends with higher fractions of *n*-heptane. A modified approach to the Livengood–Wu integral is presented to capture the integrated effects of the compression stroke on the potential for using the first stage of ignition to distribute heat release. The results of the modified ignition integral analysis are presented as a function of engine speed and fuel/air preheat temperature and demonstrate the utility of the approach to design and interpret fueling strategies of fuel blends.

1. Introduction

Modern internal combustion engines operate at low temperatures and with high levels of dilution, conditions where heat release is often affected by low-temperature fuel chemistry. In particular, homogeneous charge compression ignition (HCCI) is a low temperature combustion strategy that has successfully yielded high thermal efficiencies and low emissions [1 and references therein]. Relying on fuel chemical kinetics rather than a spark for ignition, HCCI remains difficult to control [1–4] and therefore difficult to develop for commercial powertrains. But the HCCI operating mode provides an opportunity to consider fuel chemistry effects on engine performance at conditions particularly sensitive to combustion chemistry and where chemistry dominates the rate of heat release, as compared with strategies in which heat release rate is controlled by fuel/air mixing and flame propagation convolved with reaction chemistry. The results of autoignition studies also provide understanding of pre-ignition and end-gas knock phenomena.

Many studies have considered the effects of primary reference fuel (PRF) blends of *n*-heptane and *iso*-octane on HCCI engine performance [1 and references therein] and on the relationship between PRF blends, octane number, and engine knock [5]. Some outcomes of these studies demonstrate sensitivity to PRF blends that are attributed to differences in the reaction pathways important for *n*-heptane (PRF0) and *iso*-octane (PRF100). For example, blends with low PRF number (i.e. large fractions of *n*-heptane in the fuel blend, where the PRF number indicates the volume fraction of *iso*-octane in the binary fuel blend), which exhibit more low-temperature heat release (LTHR), have been found to be more sensitive to partial fuel stratification, and are thus more effective at decreasing the rate of pressure rise during the HCCI [6,7].

Simultaneous to the development of the understanding of PRF engine performance at HCCI operating conditions, the elementary chemical kinetics of *n*-heptane and *iso*-octane have been explored at

* Corresponding author. Fax: +1 734 647 3170.
E-mail address: mohfat@umich.edu (M. Fatouraie).

http://dx.doi.org/10.1016/j.combustflame.2015.09.002
0010-2180/

length using many experimental and computational methods [e.g., [8–20], and references therein]. These studies have carefully and systematically elucidated the reactions controlling low- and high-temperature heat release, as well as the reactions responsible for negative temperature coefficient (NTC) behavior. While several studies present chemical kinetics simulations performed using detailed reaction mechanisms, what remains elusive are the connections between elementary reaction chemistry and engine performance metrics. Some key contributions to the literature on this topic include the work by Silke et al. [2] and Mehl et al. [16–19]. In one of the earlier studies by Mehl and co-workers [16], the authors used detailed reaction chemistry and a simplified engine model for several pentane and pentene fuel blends to study the effects of a range of research and motoring octane numbers on fuel reactivity. Importantly, Mehl et al. [16] superimposed pressure–temperature trajectories for different engine conditions on reactivity maps (defined by ignition delay times), providing insight into when state conditions in the engine overlap with NTC regions of the fuels. In Silke et al. [2], detailed reaction chemistry was used to quantify low temperature heat release as a function of boosted intake air pressure and compared with HCCI engine data for a PRF80 fuel blend. Reaction path and sensitivity analyses were used to identify the classes of reactions important for forming OH and for phasing of the low-temperature heat release. In Mehl et al. [17], measured intermediate species were well predicted using detailed chemistry for PRF20 blends. In another study, Mehl et al. [18] compared predicted and measured phasing to low temperature heat release using detailed chemistry for a range of PRF blends and for different generations of PRF reaction mechanisms.

Because reciprocating engines create wide-ranging trajectories of temperature and pressure conditions during their cyclical operation, it is challenging to extrapolate the results of the many high-quality isothermal and/or isobaric studies of PRF reaction chemistry to engine behavior. Building on the methods used in the simplified HCCI engine modeling studies like those by Silke et al. [2] and Mehl et al. [16], the objective of this work was to identify links between elementary reaction chemistry for PRF blends and engine performance metrics using a simplified engine modeling approach and focusing on the cumulative effects of the temperature/pressure trajectories on heat release at chemically limited operating conditions. A simplified slider/crank model was used with a detailed chemical kinetic model for PRF blends to simulate a reciprocating engine compression process. The results were analyzed to determine the relative effects of individual as well as groups of chemical reactions on engine performance metrics such as ignition phasing. Additionally the behavior of the combustion intermediates was evaluated to determine if sentinel species could be identified as proxies for low-temperature heat release.

2. Technical approach

As noted above, significant efforts have been made for developing detailed chemical kinetic mechanisms for the primary reference fuels *n*-heptane and *iso*-octane, and several mechanisms focus on high-temperature chemistry (see, for example, [20]). Many mechanisms incorporate low-temperature kinetic schemes making them applicable over wider temperature ranges. Comprehensive explanations of the development and validation of these reaction mechanisms can be found elsewhere (see, for example, [8–10,14,15,18,19] among others). Researchers at Lawrence Livermore National Laboratories (LLNL) have recently incorporated the detailed kinetics of large linear alkenes into their PRF mechanism [19], and have also added cross-reactions between large fuel molecules and fuel fragments (for example, *n*-heptyl + *iso*-octane). Research by Vanhove et al. [21] and others has shown these cross reactions between fuel fragments and fuel molecules are important determinants of whether detailed mechanisms can adequately represent global reactivity of fuel/oxidizer mixtures. Consequently, the LLNL reaction mechanism was selected for the present study.

The LLNL mechanism consists of a C_1–C_4 detailed mechanism core with three additional blocks of reactions, including reaction pathways for saturated and unsaturated linear hydrocarbons through C_7, as well as similar reactions for branched hydrocarbons from C_5 to C_8, along with aromatic hydrocarbon reactions. Reactions of small radicals with alkyl (R) and alkylperoxy radicals (RO_2) from different fuels are also included. These reactions determine the low-temperature reactivity of PRFs (see, for example, [8–10,14,15 among numerous other references].

The LLNL mechanism has been built gradually and improved upon consistently with the availability of new computational chemistry studies and new experimental data for validation and verification. (For details on this continuous improvement, please see [22].) The mechanism has been validated over a range of conditions and for diverse data sets. The goal of this work was not to further validate the detailed chemical kinetic model, but rather to use our understanding of detailed reaction schemes represented in the model to understand the sensitivity of the engine simulations to various PRF blends and engine operating conditions.

The CHEMKIN suite of software (version 10131, x64 [23]) was used for the two categories of simulations performed and presented in this paper. First, adiabatic constant volume simulations were used to quantify the ignition characteristics of the fuel blends, and second, adiabatic variable volume simulation using the dynamic state conditions for the crank-slider approach of engine simulations were used to study the effects of fuel blends on engine performance. The results of these simulations are presented below.

3. Results and discussion

3.1. Constant volume autoignition characteristics of PRF blends

Calculations of constant volume, adiabatic ignition delay times provide a baseline understanding of the ignition characteristics of the fuels as a function of temperature, pressure and mixture conditions. While many such results can be found in the literature, the trends are briefly reviewed here to provide a basis of comparison with the results of the variable volume simulations. The ignition delay time characteristics of four PRF blends—PRF0, PRF60, PRF88 and PRF100—over the temperature range of 625–1200 K, at pressures of 10 and 25 bar with an equivalence ratio (ϕ) of 0.33 and inert/O_2 ratio of 3.76 are presented in Fig. 1. The lean equivalence ratio was selected due to the relevance to HCCI engine operation [1]. CO_2 and H_2O comprised a total of 5% of the diluent gas composition for all simulations to incorporate the effect of internal exhaust gas recirculation (EGR) of an engine. The balance of the diluent gas composition was N_2. The EGR values were selected based on estimates for internal residual for a single-cylinder cooperative fuel research (CFR) engine [24]. The pressures of the calculations span the range expected during the compression stroke of wide-open-throttle operation of an engine with a compression ratio of 12:1.

As expected and as seen in Fig. 1, the ignition of PRF100 is significantly slower than that of PRF0 at the same pressure for temperatures below ~1000 K. The results in Fig. 1 also demonstrate the predicted magnitude of non-Arrhenius behavior of the blends at different state conditions. For some fuel blends and conditions, the non-Arrhenius behavior is significant and negative temperature coefficient trends are predicted, i.e. where increasing temperature results in lower fuel reactivity. The NTC regime occurs at lower temperatures for *iso*-octane compared with *n*-heptane, and the NTC region shifts to higher temperatures with increasing pressure. Two stages of heat release are observed in the low temperature portion of the non-Arrhenius regions. For these cases, the first stage of ignition is defined by the first local maximum in the rate of pressure rise in the

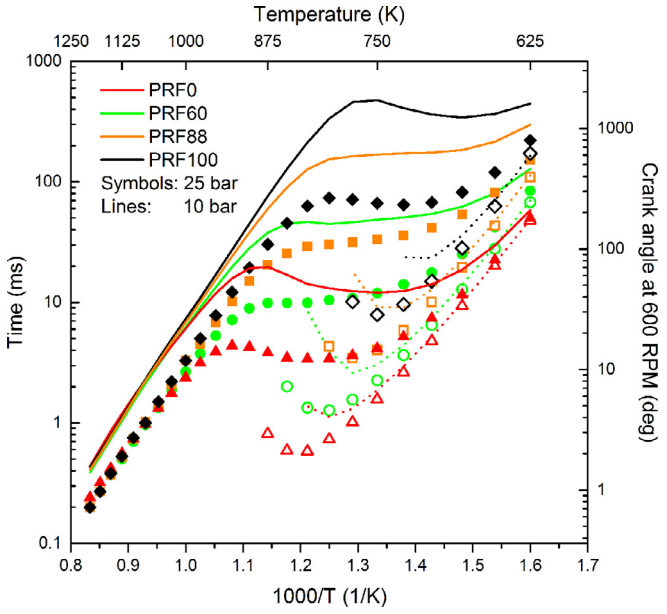

Fig. 1. Adiabatic constant volume simulation results for ignition delay time for PRF blends. Lines represent 10 bar and symbols represent 25 bar simulations. When two stages of ignition were observed, the open symbols and dotted lines indicate the first stage of ignition and closed symbols and solid lines indicate the second stage of ignition. The equivalent time in crank angle degrees is shown on the right axis for an engine speed of 600 RPM.

simulations and is represented by open symbols and dotted lines in the figure. The second stage of ignition, also referred to as autoignition in this work, is defined by the maximum rate of pressure rise in the simulations and is represented by closed symbols and solid lines. Two stage ignition is generally observed at temperatures less than 875 K. Definitions of the first and second stages of ignition for typical simulation time histories are provided in the supplementary material. Importantly, the time difference between the first and second stage of ignition is not constant in the NTC region, and the temperature corresponding to the maximum time difference is different for each pressure and fuel blend. As seen in Fig. 1, adding *iso*-octane to the PRF blend not only increases the overall ignition delay time non-linearly, but also non-linearly increases the difference between the first and second stages of ignition. These results are attributed to the high degree of branching in *iso*-octane, which increases the number of primary carbon sites in the molecule, thus decreasing the availability of lower energy secondary and tertiary C–H bonds that promote low-temperature chemistry, as described below.

The NTC behavior of fuel species like *n*-heptane and *iso*-octane is attributed to low-temperature reaction kinetics. These kinetic pathways produce a large number of radicals at low temperatures, thereby accelerating fuel consumption and global ignition. Several papers (such as [8,9]) articulate the kinetics comprehensively. Figure 2, based on the work by Curran et al. [8], is a schematic of the high- and low-temperature chemistry pathways that lead to two-stage ignition and faster global reactivity at lower temperatures. The brief discussion below pertains to PRF0 at 10 bar (solid red line) presented in Fig. 1. Analogous descriptions of PRF100 can be made, and at a very high level, any mixture of *n*-heptane and *iso*-octane, i.e. any PRF blend other than PRF0 or PRF100, can be described by the individual *n*-heptane and *iso*-octane reaction pathways, except for the addition of the cross reactions between fuel fragments. See for example the work of Vanhove et al. [21].

At high temperatures (above approximately 875 K for PRF0 at 10 bar), *R* (alkyl) radicals formed during early times undergo β-scission. β-scission is the breaking of the C–C bond one removed from the radical carbon site. Taking C_7H_{15}-2, for example, the second C

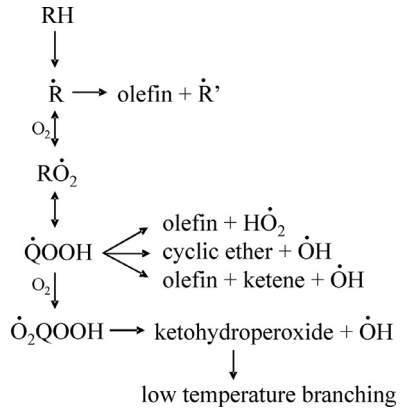

Fig. 2. Schematic describing the reaction pathway behavior of alkanes, after the work by Curran et al.[8]. The low temperature pathway is represented by the bottom portion of the schematic which either leads to chain propagation or low temperature branching.

atom in the alkyl chain is missing a hydrogen atom. At high temperatures, β-scission of C_7H_{15}-2 yields propene and the radical PC_4H_9. β-scission is a chain-propagating reaction pathway, and the main chain branching reaction at high temperatures is $H + O_2 = O + OH$. This general reaction pathway is represented in the top part of Fig. 2.

In the low temperature region, (temperatures below ~700 K for PRF0 at 10 bar), O_2 molecules add to the *R* radical site, and internal isomerization of 5-, 6-, and 7-member transition state rings leads to the formation of QOOH radicals. For example, C_7H_{15}-2 radicals may combine with O_2 to yield $C_7H_{15}O_2$-2 radicals, which then isomerize to form C_7H_{14}OOH2-1, C_7H_{14}OOH2-3, C_7H_{14}OOH2-4, C_7H_{14}OOH2-5, or C_7H_{14}OOH2-6. The QOOH radicals decompose to yield stable compounds (olefins, cyclic ethers, ketenes) and a radical (HO_2 or OH). These low-temperature reaction kinetics are chain propagating.

In the NTC region or between ~700 K and 875 K for PRF0 at 10 bar, QOOH radicals do not undergo chain propagating reactions, but rather add O_2 to the radical site, forming O_2QOOH radicals. These radicals then decompose through a transition-state ring to produce a ketohydroperoxide and an OH radical. The decomposition of the ketohydroperoxide forms another OH radical and a carbonyl radical, and thus, crucially, reaction kinetics in this intermediate temperature range are chain *branching* rather than chain *propagating*. For example, C_7H_{14}OOH2-1 radicals combine with O_2 to yield C_7H_{14}OOH2-1O_2, forming NC_7KET21 + OH. NC_7KET21 then decomposes, eventually forming CH_3COCH_2 and OH. The chain branching accelerates fuel and fuel fragment oxidation. It is also important to note that the exothermicity of this reaction pathway increases the temperature of the system, demarking the first stage of ignition. The increase in temperature also slows the reactions that form ketohydroperoxides. Between the first and second stages of ignition, an accumulation of H_2O_2 radicals occurs, and the decomposition of H_2O_2 creates two OH radicals, which then lead to thermal runaway and autoignition.

As in the modeling studies by Yates et al. [25] and Mehl et al. [16], the data of Fig. 1 can be converted to contour maps of the ignition delay time as a function of pressure and temperature for the different fuel blends. Figure 3 presents the contour surfaces for PRF0 and PRF100 where the top panels present the data for the first stage of ignition and the bottom panels present the data for autoignition. In order to generate the contours, a series of simulations for a range of temperatures and pressures were performed. The pressure was varied from 5 bar to 25 bar using 5 bar intervals and the temperature was varied from 600 K to 1200 K using 25 K intervals. The conditions yielding ignition delay times longer than 600 ms were eliminated. Presenting the data in this manner allows the trajectory of a compression stroke to be superimposed on the ignition delay time data,

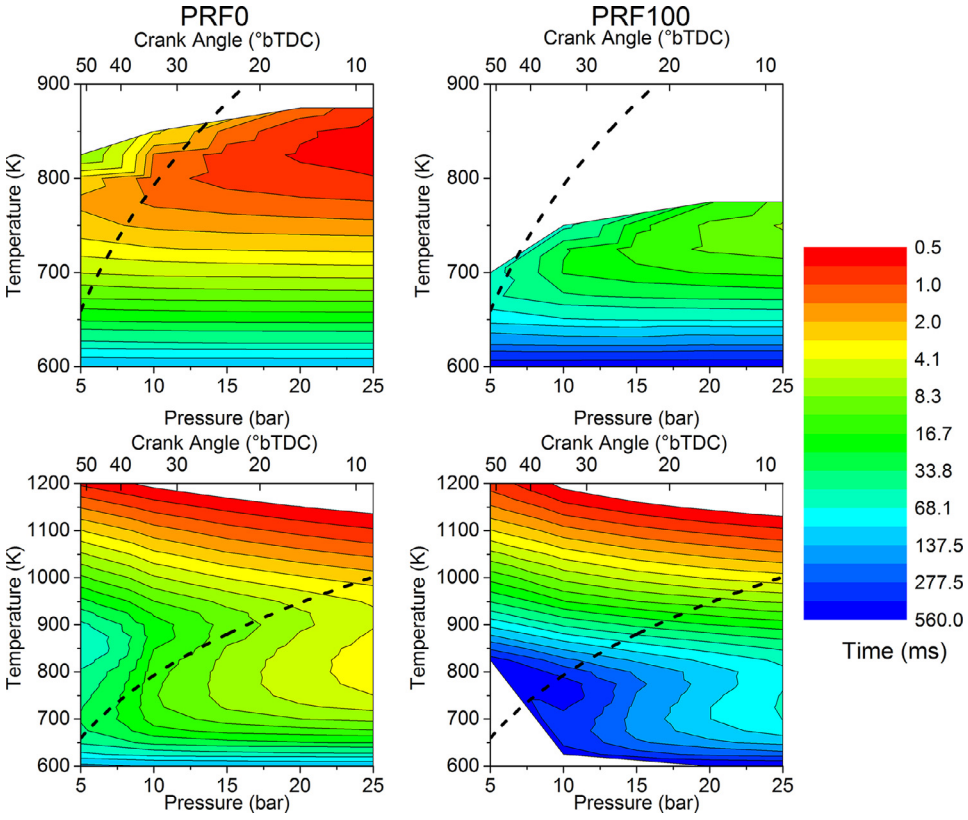

Fig. 3. Reactivity contour maps of ignition times for PRF0 (left) and PRF100 (right) fuels. The top and bottom panels present the first and second stages of ignition, respectively. The dashed line represents the range of pressures and temperatures experienced during a compression stroke for CR = 12, T_{in} = 423 K and P_{in} = 1 bar, assuming isentropic compression for a fuel/air mixture with $\phi = 0.33$.

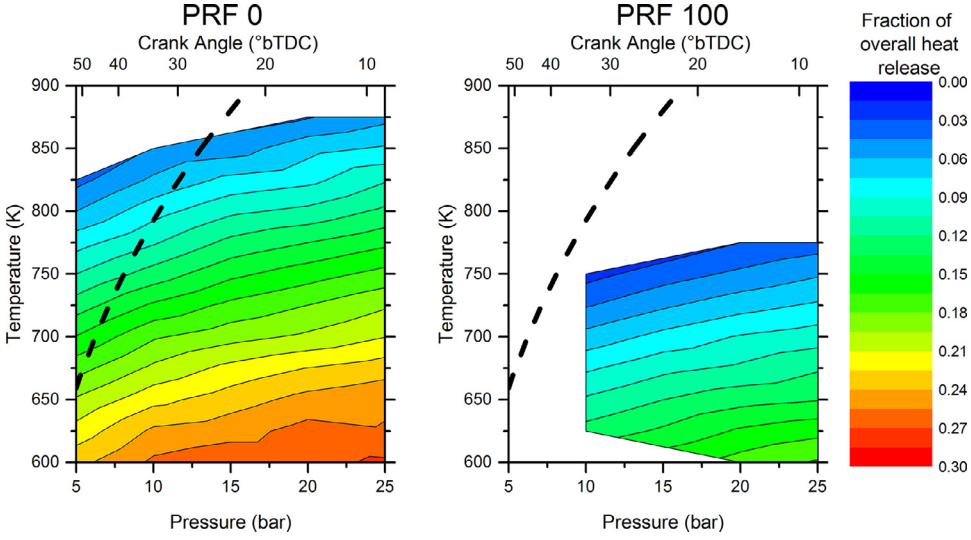

Fig. 4. Contour maps of the fractional heat release associated with the first stage of ignition for PRF0 (left) and PRF100 (right) for the simulation conditions and compression stroke of Fig. 3.

as depicted by the dashed line in Fig. 3. The compression stroke shows the trajectory of states that occurs during isentropic compression, in this case for a fuel/air mixture with $\phi = 0.33$, an intake temperature of T_{in} = 423 K, an intake pressure of P_{in} = 1 bar and for a compression ratio CR = 12. (High levels of air preheat are necessary for appropriate HCCI engine phasing.) As seen in the bottom panels for both PRF0 and PRF100, at every point along the CR = 12 trajectory, increasing compression decreases the autoignition delay time. However, the trajectory passes through thermodynamic states in which PRF0 exhibits NTC behavior, where increasing compression (and therefore temperature and pressure) increases the time to the first stage of ignition. PRF100 shows very little NTC or two stage ignition behavior along the CR = 12 trajectory.

In engines, the amount of heat release at the first stage of ignition affects the load range of HCCI combustion by distributing the heat release and reducing the rate of pressure rise [6]. Figure 4 presents the fractional heat release at the first stage of ignition for PRF0 and PRF100 using contour maps similar to Fig. 3 and including the compression stroke trajectory of Fig. 3. The fraction of the total heat release was calculated at the midpoint of the time between the first and second stages of ignition. The figures show for a constant temperature, the amount of heat released during the first stage of

ignition increases as pressure increases. The results also show a maximum of 30% of the total heat release can occur at the first stage of ignition for PRF0 and a maximum of 18% can occur with the first stage of ignition for PRF100. However, when the compression stroke is considered, less than 18% of the overall heat release is associated with the first stage of ignition for PRF0. The value of 18% represents an upper limit for PRF0 for the heat release, since the fuel/air mixture would need sufficient residence time at the NTC temperature and pressure conditions for reaction to occur. For PRF100, negligible heat release is associated with the first stage of ignition for the compression stroke considered here and using the definition for measuring heat release based on the midpoint in time between the first and second stages of ignition.

3.2. Variable volume autoignition characteristics of PRF blends

In this section, the results of a simple slider-crank model with detailed chemistry are used to understand the cumulative effects of compression and finite reaction times on ignition phasing and heat release. Heat transfer and turbulence effects are neglected to isolate the chemical effects of the PRF blends, and the results thus represent the effects of fuel chemistry at the limiting conditions of fully premixed fuel/air mixtures.

The dimensions of a CFR engine with a 83 mm bore and a 114 mm stroke (as used in the HCCI engine study by Rapp et al. [26]) were used to simulate a range of compression ratios and intake temperatures for a fixed intake pressure of 1 bar with equivalence ratio of $\phi = 0.33$ and air dilution including 5% EGR, as described earlier. The engine speed was set to 600 RPM (unless otherwise noted), a standard operating condition for research octane number (RON) rating exercises. The simulations were initiated using the temperature and pressure conditions expected in the CFR engine configuration at intake valve closing (IVC). The volume profile was derived using the compression ratio specified at the beginning of the simulation.

First, the slider-crank model predictions were evaluated to ensure the results reproduced experimentally observed trends from the HCCI engine study of primary reference fuels by Rapp et al. [26]. In Rapp et al. [26], the compression ratio of the engine was varied for each PRF blend to determine the time of 50% of the total heat release. This time is defined as CA50 and is reported in crank angle degrees. CA50 is typically determined using in-cylinder pressure time history measurements and heat release analysis [27], and is often used as a metric to gauge optimum timing for heat release rate and as a measure of the ignition delay time for HCCI operating conditions. Figure 5 compares the results of CA50 values from Rapp et al. [26] with the simulation results. The simulation results exhibited almost instantaneous heat release at the second stage of ignition, making the CA50 and the phasing of peak pressure rise rate, $dP/d\theta_{max}$ equivalent for the simulations.

Both the modeling and the experimental results show maintaining combustion phasing within a narrow range of crank angle degree (CAD) while increasing the PRF number requires increasing the CR, which is expected given the slower reactivity of *iso*-octane compared with *n*-heptane. The experimental trends are well reproduced by the simplified model for the range of PRF blends studied, with the exception of the more advanced ignition predicted by the simulations for PRF88 compared with PRF85. The experimental trend indicates comparable ignition timing for PRF88 and PRF 85. Differences between the absolute values for the experimental data and the model results are expected, since the model neglects heat losses, friction, turbulence-kinetic interactions, and stratification, to name a few physical phenomena important in the engines studies. At higher compression ratios, the friction and heat losses will increase considerably in the engine which may be the source of the discrepancy between the model predictions and the experimental data for PRF88.

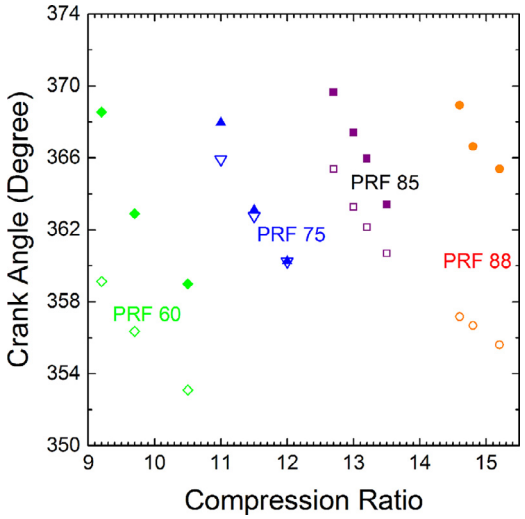

Fig. 5. Comparison of experimental and computational results for combustion phasing for different PRF blends. Solid symbols represent CA50 determined from experiments by Rapp et al. [26] and open symbols represent the $dP/d\theta_{max}$ results from the slider-crank simulations.

Having verified that the model can reasonably reproduce the experimental trends observed in the literature, the following sections examine the contributions of the detailed reaction chemistry to the engine model predictions. Figure 6 presents the model predictions for the time-histories of pressure, accumulated heat release, temperature, and fraction of fuel consumed for a range of PRF blends for CR = 12, $T_{in} = 423$ K, $P_{in} = 1$ bar, $\phi = 0.33$, and air level of dilution including 5% EGR. A first stage of ignition was identified for a PRF blend if there was a 5% increase in pressure during compression compared to a motoring (i.e. non-reacting) baseline. Autoignition (second stage of ignition) was determined based on the peak rate of pressure rise. As the amount of *n*-heptane in the fuel blend decreases with increasing PRF number, the heat release associated with the first stage of ignition decreases and is more distributed in time. Further, the results of the slider-crank simulations highlight the effects of the finite reaction and compression time compared with the constant volume results. Recall, Fig. 4 indicates a maximum of 18% of the heat release associated with the first stage of ignition for PRF0 and the CR = 12 trajectory for fixed state conditions. The engine simulations show only half of the maximum heat release, ~9%, occurs for PRF0, and this heat release corresponds to consumption of 70% of the *n*-heptane. For PRF100, fuel consumption begins close to top dead center (TDC), and consequently the expansion stroke essentially quenches the reactivity of PRF100, limiting fuel consumption to around 40% and resulting in no significant heat release.

For all the PRF blends, the fraction of *n*-heptane consumed (solid lines) at the first stage of ignition is systematically higher than the fraction of *iso*-octane consumed (dashed lines). As seen in Fig. 3 and as indicated by the PRF100 data in Fig. 6, *iso*-octane has very low reactivity at these conditions. Thus the consumption of *iso*-octane in the blends is attributed to the radical pool developed by the consumption of *n*-heptane. Such synergistic fuel interactions have been observed with constant volume studies with other binary blends of fuels of different reactivity (e.g., Vanhove et al. [21] and Karwat et al. [28]), where the radicals produced by the more reactive fuel induce the other fuel to react at conditions where it would normally be non-reactive. For the blends, the accumulated heat release at the first stage of ignition decreases with increasing PRF number. Increasing the amount of *iso*-octane in the fuel blend decreases the rate of fuel consumption, and when CA50 occurs after TDC, the cooling effect of expansion stroke further slows the rate of fuel consumption and distributes the heat release over a longer duration.

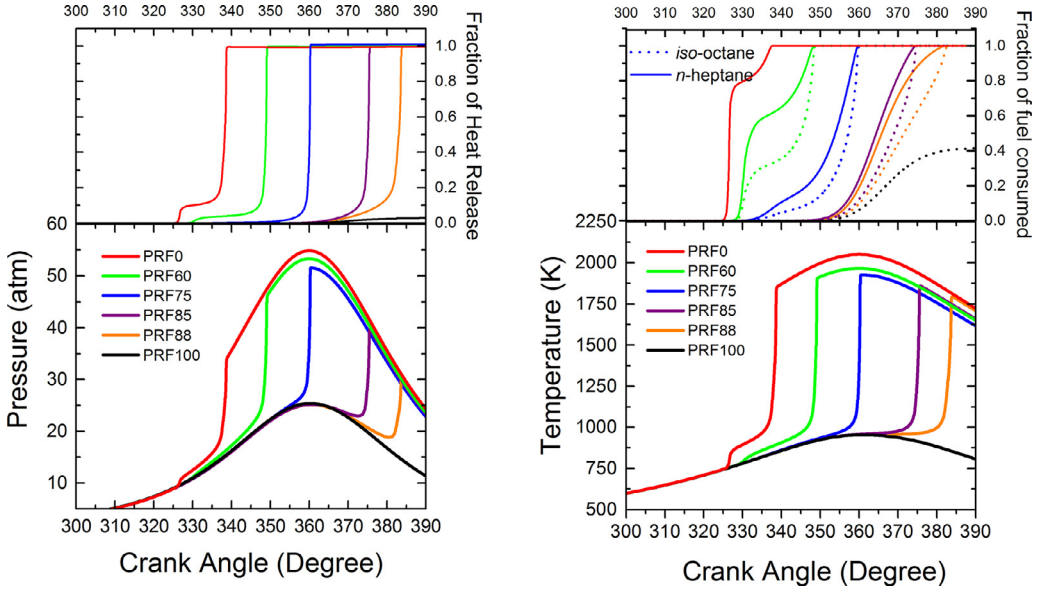

Fig. 6. Model predictions for pressure and accumulated heat release (left panel) and temperature and fraction of fuel consumption (right panel) of PRF blends with CR = 12, T_{in} = 423 K, P_{in} = 1 bar.

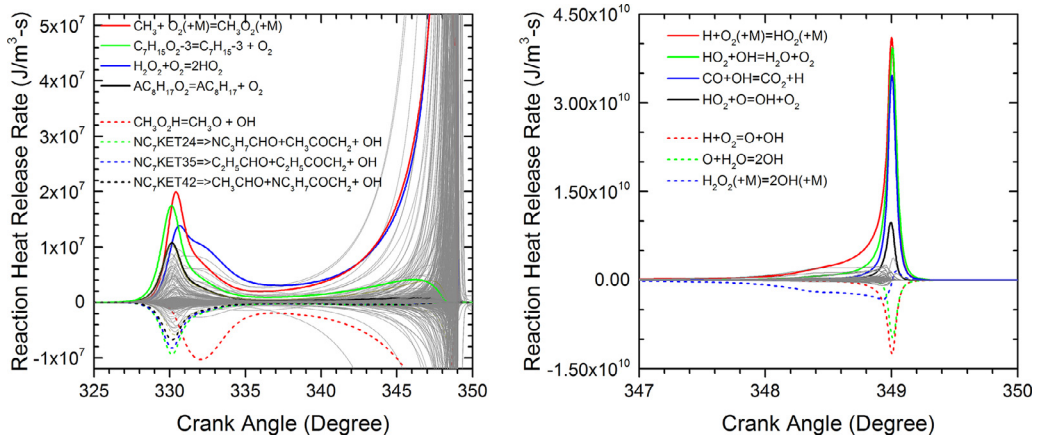

Fig. 7. Model predictions for heat production and heat removal per reaction for PRF60 for the model conditions of Fig. 6. The left panel highlights the time associated with the first stage of ignition, and the right panel presents the heat release at autoignition.

The trends for heat release can be explained by the reaction pathways that dominate for the different PRF blends. While the reaction pathways for *n*-heptane and *iso*-octane are broadly analogous given that they are both alkanes, their respective rates of low-temperature chemistry reactions, described above, are functions of the number of primary, secondary and tertiary bonds in each molecule. More primary C–H bonds leads to a lower amount of low-temperature chemistry at a given temperature and pressure. In Fig. 7, the heat production per reaction is presented for the PRF60 blend simulation of Fig. 6. All reactions are included in the figure and the four most exothermic and endothermic reactions are highlighted. The left and right panels present the data for the first and second stages of ignition, respectively. At the first stage of ignition, the interplay between exothermic reactions like $C_7H_{15}O_2$-3 = C_7H_{15} + O_2 and endothermic reactions like NC_7KET24 = CH_2O + CH_3COCH_2 + OH dictate the magnitude of the low-temperature chemistry and the low-temperature heat release. The left panel of Fig. 7 confirms the low-temperature chemistry of *n*-heptane that plays a more dominant role in low-temperature heat release in engine conditions. As described above, the heat release at the first stage of ignition suppresses the RO_2 and QOOH chemistry, and, as seen in the right panel of Fig. 7, it is small radical chemistry that leads to the heat release and chain branching necessary for autoignition. In comparison, only a single stage of heat release and ignition is observed for PRF88 (see Fig. 6), and the reactions controlling heat release for PRF88 (not shown here) were the same as those for heat release of autoignition of PRF60, i.e. the reactions found in the right panel of Fig. 7.

Figure 8 presents the predicted time histories of the radical species and small intermediates for the model results presented in Fig. 6. Shown specifically are the sum of key radical species that are associated with the low-temperature chemistry pathways of the large fuel alkyl radicals—*n*-heptyl and *iso*-octyl— specifically alkylperoxy (RO_2) and ketohydroperoxide (QOOH) radicals, as well as small species that promote low-temperature chemistry and autoignition, OH, HO_2, H_2O_2. The results show the radicals and small intermediates are crucial for not only fuel reactivity and autoignition, but also for releasing heat at the first stage of ignition. For example, as seen in Fig. 7, RO_2 and HO_2 formation through bimolecular addition are key low-temperature reactions releasing heat at the first stage of ignition. Figure 8 shows the shift from high levels of C_7 and C_8 RO_2 intermediates for PRF60 during the first stage of ignition to orders of magnitude lower levels of these species for PRF88 at early times in the cycle. The concentrations of radicals like RO_2 are thus limited proxies for the heat release at the first stage of ignition.

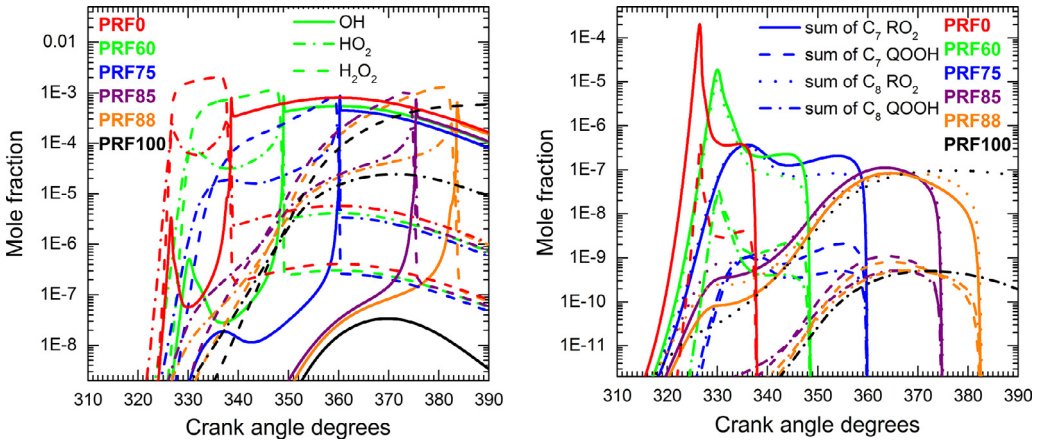

Fig. 8. Model predictions of important intermediate and radical species of PRF blends for CR = 12, T_{in} = 423 K, P_{in} = 1 bar.

There is no distinct first stage of ignition for PRF85 and PRF88, and the species time histories for these blends are similar. PRF100 did not exhibit autoignition at the conditions simulated. Yet, as observed in Fig. 8, low-temperature chemistry radicals are formed nonetheless for these blends, showing that even small amounts of fuels that exhibit low-temperature chemistry like *n*-heptane, when present in the PRF blends, will pass through these low-temperature pathways at conditions relevant to HCCI engines. It can be seen that the radical formation for PRF100 follows PRF88, but despite reaching the same concentrations, the slower high temperature chemistry coupled with the reduction of the temperatures after TDC prohibits the thermal runaway and autoignition. In comparison with PRF85 and PRF88, PRF75 shows a significant increase in the concentrations of small radical species formed by low-temperature chemistry, such as HO_2 and H_2O_2. H_2O_2 decomposition results in the production of OH radicals that cause thermal runaway and autoignition. For PRF60 and PRF0 the local maximum concentration of OH radicals corresponds to the low-temperature heat release associated with the first stage of ignition.

The concentrations of RO_2 radicals for both C_7 and C_8 correlate with each other in shape and in value for each PRF blend. This is particularly interesting because (1) *iso*-octane is much less reactive than *n*-heptane at low-temperatures; (2) the concentration of *n*-heptane is much lower than the concentration of *iso*-octane; and (3) the fraction of fuel consumed at the first stage of ignition, as observed for PRF60 in Fig. 6, for *iso*-octane is half that of *n*-heptane. These results provide evidence of the synergism of reactivity, as described by Vanhove et al. [21] and Karwat et al. [28], in which a highly reactive fuel promotes the reactivity of a less reactive fuel, and, conversely, in which a less reactive fuel non-linearly suppresses the reactivity of a highly reactive fuel.

As expected, the amount of *n*-heptane in the PRF blend is a key determinant of the magnitude of the low-temperature chemistry. If the concentrations of the low-temperature chemistry radicals were normalized by the amount of the respective fuel source in the binary blend, the results would show the fraction is much higher for *n*-heptane than for *iso*-octane, indicating a larger fraction of the *n*-heptane participates in the low temperature reaction pathways compared with *iso*-octane. Changing the blend ratio changes the absolute concentration as well as the shape of the evolution of RO_2 and QOOH species, and *n*-heptane concentrations therefore control the distribution of heat release and phasing of PRFs.

3.3. Effects of intake temperature and pressure on PRF blends

As the amount of *iso*-octane in the PRF blend increases, the ignition delay time increases, as seen in Fig. 1. When coupled with the temperature decrease that occurs during the expansion stroke after TDC, increasing the *iso*-octane content in the blend causes the combustion phasing in the engine simulation to be significantly later even for small changes in the PRF blend, as seen in Fig. 6 (e.g. for PRF85 and PRF88). Since the fuel consumption is more distributed in time as the amount of *iso*-octane in the PRF blend increases (seen in Fig. 6), or, in other words, since less of the fuel is consumed quickly with increasing amounts of *iso*-octane in the PRF blend, small changes in thermodynamic conditions can lead to large changes in phasing after TDC for PRF blends with high fractions of *iso*-octane.

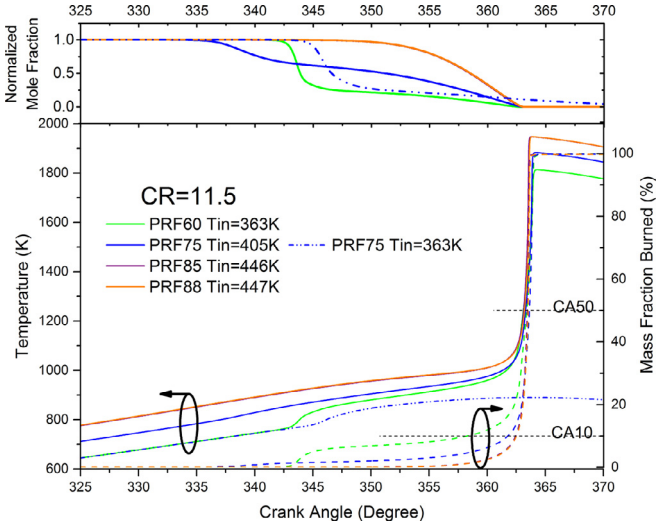

Fig. 9. Model predictions for *T* and heat release fraction (bottom panel) and normalized *n*-heptane mole fraction of PRF blends (top panel) with the same combustion phasing. The combustion phasing was set by changing the intake temperature for each fuel for CR = 11.5, P_{in} = 1 bar, and ϕ = 0.33. The simulation results for PRF 85 and 88 are nearly identical and result in nearly superimposed lines.

In order to understand the effects of temperature and pressure on fuel chemistry at realistic and fixed phasing conditions for a reciprocating engine, simulations with fixed combustion phasing, specifically CA50 (which is the second stage of ignition for all practical purposes) set at 3.5° after top-dead center (aTDC), were conducted. The simulations used a compression ratio of CR = 11.5, intake pressure of P_{in} = 1 bar, equivalence ratio of ϕ = 0.33 with air dilution and 5% EGR for all cases. Fixing CA50 required changing the intake temperature for each PRF blend where the intake temperature was adjusted from T_{in} = 363 K for PRF60 to T_{in} = 447 K for PRF88.

Figure 9 presents the results of the simulations. The top panel shows the normalized mole fraction of *n*-heptane as a function of

time in the system. A significant amount (~70%) of *n*-heptane in PRF60 is consumed at the first stage of ignition over a very short period of time (<3 CAD). As seen in the bottom panel, the fuel consumption occurs in the NTC temperature window, starting at ~760 K and ending at ~840 K, with 6% of the overall heat release occurring in the first stage of ignition. For fuel blends above PRF75, there is negligible heat release at low temperatures, and only the autoignition event is observed. High intake temperatures are required for the high PRF blends to maintain the combustion phasing at 3.5° aTDC. The Arrhenius diagram presented in Fig. 1 shows that at engine relevant conditions of approximately 10 bar, the highest temperature at which low-temperature chemistry occurs for these blends is ~775 K, and the difference between the second and first stages of ignition for PRF88 at these conditions is ~47 ms, which is too long to observe first stage heat release at the engine simulation conditions.

The results of Fig. 9 can also be compared with expectations based on the temperature and pressure trajectories superimposed on the *P–T-heat release* diagrams for PRF0 and PRF100 shown in Fig. 4. Based on the data of Fig. 4, PRF100 would not experience any heat release during the first stage of ignition for T_{in} = 423 K, and higher intake temperatures would shift the T–P trajectory toward the top left corner of the diagram and further away from the NTC region. For PRF0, the data of Fig. 4 indicate a maximum heat release during the first stage of ignition of 18%. The simulation results of Fig. 9 show the finite reaction time during compression as well as the lower *n*-heptane concentration for PRF60 yields heat release of ~9% during the first stage of ignition.

For sake of comparison, simulation results for PRF75 at the same intake temperature of 363 K as PRF60 are also presented in Fig. 9 as the dot–dot-dashed lines. The results for PRF75 with T_{in} = 363 K show the first stage of ignition occurs at ~770 K, but the decreased amount of *n*-heptane in the fuel blend and the suppression of the low-temperature chemistry pathways due to the higher *iso*-octane concentration extends the duration of the second stage of ignition too much to maintain the phasing at 3.5° aTDC. The reactions are quenched during the expansion stroke and consequently, autoignition never occurs for PRF75 with T_{in} = 363 K. Instead, the intake temperature must be increased to 405 K for PRF75 to maintain phasing at 3.5° aTDC, which significantly reduces the heat release during the first stage of ignition, as depicted by the significantly longer consumption of *n*-heptane in the top panel of Fig. 9.

Karwat et al. [14] found in their experimental and computational work for *n*-heptane that (1) the amount of fuel consumed at the first stage of ignition and the amount of heat released at the first stage of ignition decreases with increasing temperature, and that (2) the higher the initial temperature, the longer the time between the first and second stages of ignition, until two-stage behavior disappears. From an engine operation standpoint that targets distributed heat release at a fixed engine speed, the intake temperature should be such that low temperature heat release occurs early enough before TDC to allow the low-temperature chemistry time for heat release associated with two-stage ignition to occur. However, as the amount of *n*-heptane decreases with increasing PRF number, the intake temperature needs to be increased to accelerate the second stage of ignition, which tends to increase the time required for heat release at the first stage of ignition.

The effects of the low-temperature chemistry are also apparent in the time histories of the intermediate and radical species. Specifically, the RO_2 radicals for the fixed ignition phasing simulations, represented in Fig. 9, are compared with the results for the cases with higher compression ratio and fixed intake temperature (CR = 15, T_{in} = 423 K, P_{in} = 1 bar) in Fig. 10 for PRF60, PRF75, and PRF88. The temperature profiles are also presented to highlight the temperature interval in which the radical species are being formed and consumed. Since PRF85 and PRF88 exhibited very similar trends, only PRF88 results are shown. The RO_2 radicals for both C_7 and C_8 correlated with

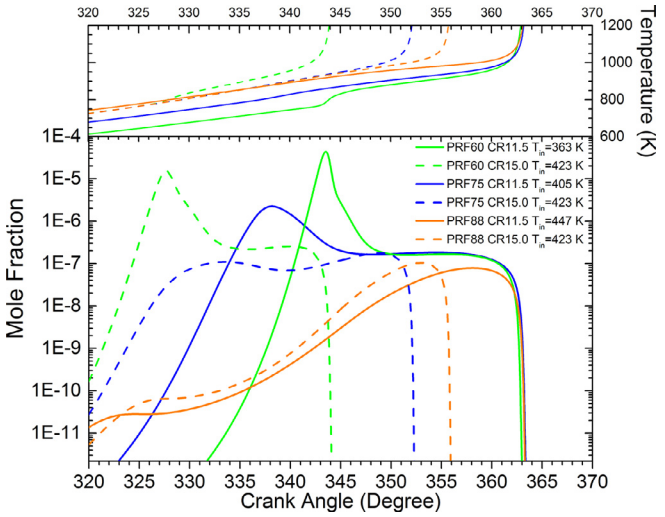

Fig. 10. Comparison of model predictions of C_7 *RO*2 intermediate speicies for PRF60, PRF75, and PRF88. Solid lines represent the blends with the same combustion phasing at CR = 11.5 and P_{in} = 1 bar and the dashed lines represent blends with CR = 15, T_{in} = 423 K, P_{in} = 1 bar.

each other in shape and in value for each PRF blend, as shown in Fig. 8, therefore only C_7 RO_2 are presented in Fig. 10. The results show the lower compression ratio CR = 11.5 and lower intake temperatures (T_{in} = 363 K for PRF60 and T_{in} = 405 K for PRF75) yield higher peak concentrations of RO_2 radicals compared with the higher compression ratio and higher intake temperature conditions of T_{in} of 423 K for CR = 15. The lower T_{in} for CR = 11.5 increases the low-temperature reactivity of PRF60 and PRF75. The timing of these concentration peaks align with the temperature increases due to LTHR and this sharp increase in the temperature pushes the charge out of NTC region and the chain branching reactions stop. In comparison, PRF 88 does not exhibit a peak in the early stages of reactivity and the concentration of the radicals increase monotonically until the thermal runaway and autoignition. The increases in intake temperature and compression ratio only affected the overall reaction kinetics of fuel consumption and the timing of ignition. The peak concentrations of C8 RO_2 and QOOH radicals (not shown here) did not change significantly.

Higher engine speeds reduce the residence time of the fuels at high temperatures and pressures, which dramatically changes the chemistry exhibited by the PRF blends. Simulations were performed at a higher engine speed conditions of 1800 RPM while maintaining the ignition phasing at 3.5° aTDC by varying the intake temperature. As can be deduced from Fig. 1, decreasing the residence time of fuel/air mixtures requires higher intake temperatures and/or pressures to maintain fixed ignition timing. Furthermore, Fig. 1 shows *n*-heptane and *iso*-octane have the same reactivity at high temperatures, regardless of pressure. For the 1800 RPM simulations, the intake temperatures required to fix the phasing at 3.5° aTDC was virtually the same for all PRF blends, T_{in} = 484–488 K. The significantly reduced residence time in the NTC region at 1800 RPM and the higher intake temperatures resulted in no observable first stage of ignition for any fuel blend, including PRF60. Sjöberg and Dec [29] have observed similar trends in their experimental studies of PRF fuels during HCCI engine operation where increasing engine speed decreased the "cool-flame activity" or the low-temperature chemistry of the PRF fuel blends. Sjöberg and Dec [29] conjectured that there was a limiting engine speed above which there would be no observable effects of low-temperature chemistry (~3000 RPM for PRF60).

3.4. Additional implications of simulation results

In dynamic thermodynamic environments like reciprocating engines, autoignition events are outcomes of the cumulative effects of

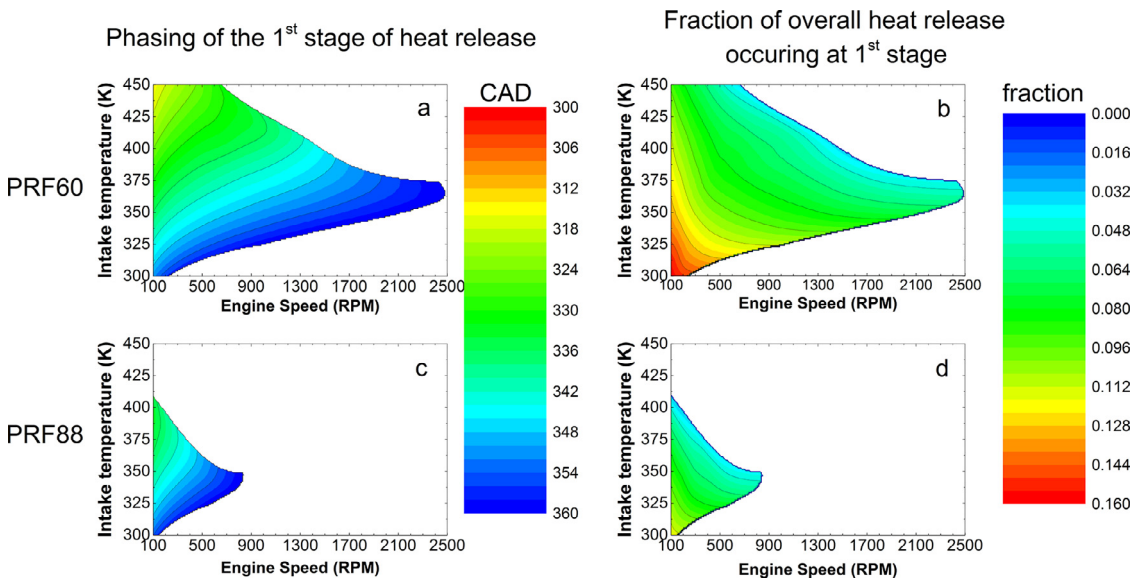

Fig. 11. Model predictions for the phasing of the first stage of heat release and the fraction of the first stage to overall heat release based on the modified Livengood–Wu autoignition integral for PRF60 and PRF88. Simulation conditions of CR = 11.5, $\phi = 0.33$, and $P_{in} = 1$ bar.

temperature and pressure on fuel/air mixtures. This is in contrast to studies conducted to examine the combustion kinetics at constant temperatures and pressures of fuel/air mixtures, like ignition experiments conducted in shock tubes and rapid compression facilities, in which dynamic thermodynamic conditions are intentionally minimized. It is valuable to understand the cumulative and integrated effects of state conditions on fuel reactivity, particularly for chemical kinetic models that have been deeply influenced by shock tube and rapid compression facility chemical kinetic studies. The Livengood–Wu autoignition integral [30] is a method that has been developed to include the effects of dynamic state conditions on ignition timing. As shown in Eq. (1), ignition is calculated by integrating the cumulative effects of fuel reactivity at each temperature and pressure condition that the fuel/air mixture experiences prior to autoignition.

$$1 = \int_{t=0}^{t=t_{IGN}} \frac{dt}{\tau(T,P)} \tag{1}$$

For fuels with single stage heat release, this metric can be an effective way of predicting the autoignition event in engine environments [31]. But the method, as it stands, does not account for fuels that exhibit low-temperature chemistry and two-stage heat release.

In order to provide a more clear understanding of the effect of the range of intake temperatures that will allow different PRF blends to exhibit LTHR before TDC, the Livengood–Wu autoignition integral was adapted in this work to estimate the onset of the first stage of ignition and the heat release fraction associated with the first stage of ignition. The results quantify the sensitivity of low-temperature chemistry to intake temperature and residence time. The autoignition integral was evaluated for an adiabatic motoring trace for CR = 11.5, using the ignition delay values (previously calculated using the detailed reaction mechanism for the first stage of ignition, τ_1, for a large range of PRF blends, temperatures and pressures), to identify the timing of the first stage of ignition $\boldsymbol{\theta_{IGN,1}}$, at which the integral approaches unity, and the temperature at this onset of LTHR. The engine speed is scaled by the $\frac{dt}{d\theta}$, where θ is in crank angle degrees and the resulting expression is given in Eq. (2).

$$\frac{dt}{d\theta} \cdot \int_{\theta=IVC}^{\theta=\theta_{IGN,1}} \frac{1}{\tau_1(T,P)} d\theta = 1 \tag{2}$$

The heat release fraction of the LTHR is calculated using the same method described earlier to develop the results presented in Fig. 4.

The results for the modified autoignition integral are presented in Fig. 11 for PRF60 and PRF88 as a function of engine speed and T_{in} for a fixed compression ratio of CR = 11.5, $P_{in} = 1$ bar, and $\phi = 0.3$. The regions in white represent the conditions in which the first stage of ignition would not occur before TDC. For PRF60 at an engine speed of 1300 RPM, Fig. 11 shows LTHR does not occur until T_{in} is approximately 325 K, and the first stage of ignition occurs close to TDC at this T_{in}. As T_{in} is increased at 1300 RPM, the first stage of ignition advances in time, until at T_{in} of ~400 K, the first stage of ignition ceases to occur. The results indicate for PRF60, the first stage of ignition at 1300 RPM for $T_{in} = 400$ K can produce a first stage heat release fraction of < 8%. The changes in the characteristics and limits of the first state of ignition as a function of increased T_{in} are due to the changing reaction kinetics as seen in Fig. 1; as the temperature increases, the reaction chemistry moves out of the NTC region. The timing of the first stage of ignition is a non-linear function of residence time, and so is the amount of heat release at the first stage of ignition as seen in Fig. 11.

In essence, the contours of Fig. 11 depict the non-Arrhenius NTC behavior of Fig. 1 in metrics important to practical engine operation. As the engine speed increases, the residence time at each temperature decreases. And, as the PRF number increases, the concentration of *iso*-octane, which is much slower to react than and shows less NTC behavior compared to *n*-heptane, increases. Thus, as engine speed increases, LTHR occurs for a much wider engine operating range for PRF60 compared with PRF88. Further, at the same intake temperature and engine speed, the first stage of ignition moves closer to TDC for PRF88 when compared to PRF60. Figure 11 provides a clear picture of the operating conditions within which multi-stage ignition can be used to maximize HCCI performance.

4. Conclusions

The results of the current work provide new understanding for trends observed in previous experimental studies of primary reference fuels at conditions where ignition is controlled by ignition chemistry, and provide a novel method to guide for future strategies to control heat release using ignition chemistry. This work focuses on *iso*-octane and n-heptane since there is a high degree of confidence in the chemical kinetic mechanisms of these two hydrocarbons. Extension of these methods to more complex fuels is necessary and a

valuable area for future work. The primary conclusions of the study are as follows.

The fixed phasing simulations indicate that for low PRF number blends (e.g. PRF60), more low-temperature chemistry, i.e. lower intake air temperature, is required to fix phasing at an optimum CAD. This result is consistent with experimental observations by Sjöberg and Dec [29], who found intake temperatures had to be "decreased drastically" as low temperature chemistry increased with lower PRF number blends to maintain combustion phasing in their HCCI engine study. For higher PRF number blends (e.g. PRF75), higher intake temperatures are required to move the reaction kinetics of the fuel into the high temperature regime in order to fix the phasing at CAD suitable for practical engine operation. Interestingly, given nominal temperature and pressure trajectories experienced by PRF blends in an engine, it may be that only the first stage of ignition exhibits the non-linearity observed in the negative temperature coefficient region, while the timing of the autoignition event monotonically advances with the increasing temperatures and pressures cause by the compression process. Increasing intake temperature conditions to ensure adequate combustion phasing will decrease low-temperature heat release from both PRF components, thus making it difficult to distribute heat release in time using low-temperature heat release chemistry.

Generally, fuel components that exhibit low-temperature chemistry within practical engine operating conditions must be present to distribute heat release in an engine operating at kinetically limited and not mixing limited conditions. At the conditions important for HCCI engine operation, the interplay between reactions that are exothermic and endothermic dictates low-temperature chemistry and two-stage ignition. For example, alkylperoxy and hydroperoxy radical formation through bimolecular addition are key low-temperature reactions that release heat at the first stage of ignition for *n*-heptane and low PRF number blends. Yet these species are also formed by high PRF number blends that do not display low-temperature heat release or multi-stage ignition behavior during compression. Thus, low temperature chemistry radicals like alkylperoxy radicals formed from n-heptane are not uniquely indicative of low-temperature heat release, but they are formed at earlier times, higher rates and higher concentrations with PRF blends with higher fractions of *n*-heptane.

As in the current work and previous studies such as Mehl et al. [16], superimposing temperature and pressure trajectories expected in engines onto P–T-ignition delay time and P–T-heat release maps generated at constant state conditions provides limiting values for ignition timing and the heat release. However, the modified Livengood–Wu integral introduced in this work provides more appropriate limiting values (since the data include the integrated effects of the state conditions) for the first stage of ignition as a function of engine operating parameters. The results of the modified Livengood–Wu analysis presented in this work show that the effectiveness of low temperature heat release is limited to lower engine speeds (e.g. 5% overall heat release in the first stage of ignition requires speeds < 2500 RPM) and lower PRF number blends (PRF60 and below). Further, the modified Livengood–Wu integral approach can be easily applied to quantify the effects of different fuel chemistries on low-temperature heat release to enable the design and interpretation of fueling strategies of fuel blends.

Acknowledgments

The authors would like to thank Dr. Vi Rapp for sharing her experimental HCCI engine data and Dr. George Lavoie and Dr. Scott Wagnon for their thoughtful discussions on this subject. The authors acknowledge the generous financial support of the U.S. Department of Energy, Office of Basic Energy Sciences, Contract No. DE-SC0002645.

Supplementary materials

Supplementary material associated with this article can be found, in the online version, at doi:10.1016/j.combustflame.2015.09.002.

References

[1] S. Saxena, I.D. Bedoya, Fundamental phenomena affecting low temperature combustion and HCCI engines, high load limits and strategies for extending these limits, Prog. Energy Combust. Sci. 39 (2013) 457–488.
[2] E.J. Silke, W.J. Pitz, C.K. Westbrook, M. Sjöberg, J.E. Dec, Understanding the chemical effects of increased boost pressure under HCCI conditions, SAE Int. J. Fuels Lubr. 1 (2008) 12–25.
[3] G.T. Kalghatgi, R.A. Head, Combustion limits and efficiency in a homogeneous charge compression ignition engine, Int. J. Engine Res. 7 (2006) 215–236.
[4] A. Lewis, E. Ortiz-Soto, G. Lavoie, D.N. Assanis, Scaling and dimensional methods to incorporate knock and flammability limits in models of high-efficiency gasoline and ethanol engines, Int. J. Engine Res. 16 (2015) 181–196.
[5] C.K. Westbrook, W.J. Pitz, W.R. Leppard, The Autoignition Chemistry of Paraffinic Fuels and Pro-Knock and Anti-Knock Additives: A Detailed Chemical Kinetic Study, 1991, paper 912314.
[6] Y. Yang, J.E. Dec, N. Dronniou, M. Sjöberg, W. Cannella, Partial fuel stratification to control HCCI heat release rates: Fuel composition and other factors affecting pre-ignition reactions of two-stage ignition fuels, SAE Int. J. Engines 4 (2011) 1903–1920.
[7] Y. Yang, J.E. Dec, N. Dronniou, W. Cannella, Boosted HCCI combustion using low-octane gasoline with fully premixed and partially stratified charges, SAE Int. J. Engines 5 (2012) 1075–1088.
[8] H.J. Curran, P. Gaffuri, W.J. Pitz, C.K. Westbrook, A comprehensive modeling study of n-heptane oxidation, Combust. Flame 114 (1998) 149–177.
[9] H.J. Curran, P. Gaffuri, W.J. Pitz, C.K. Westbrook, A comprehensive modeling study of iso-octane oxidation, Combust. Flame 129 (2002) 253–280.
[10] H.J. Curran, W.J. Pitz, C.K. Westbrook, G.V. Callahan, F.L. Dryer, Oxidation of automotive primary reference fuels at elevated pressures, Symp. (Int.) Combust. 27 (1998) 379–387.
[11] P. Dagaut, M. Reuillon, M. Cathonnet, Experimental study of the oxidation of n-heptane in a jet stirred reactor from low to high temperature and pressures up to 40 atm, Combust. Flame 101 (1995) 132–140.
[12] P.A. Glaude, V. Conraud, R. Fournet, F. Battin-Leclerc, G.M. Côme, G. Scacchi, P. Dagaut, M. Cathonnet, Modeling the oxidation of mixtures of primary reference automobile fuels, Energy & Fuels 16 (2002) 1186–1195.
[13] P. Dagaut, M. Reuillon, M. Cathonnet, High-pressure oxidation of liquid fuels from low to high-temperature. 1. N-Heptane and isooctane, Combust. Sci. Technol. 95 (1994) 233–260.
[14] D.M.A. Karwat, S.W. Wagnon, M.S. Wooldridge, C.K. Westbrook, Low temperature chemical kinetic and speciation studies of n-heptane, Combust. Flame 160 (2013) 2693–2706.
[15] C.K. Westbrook, W.J. Pitz, O. Herbinet, H.J. Curran, E.J. Silke, A comprehensive detailed chemical kinetic reaction mechanism for combustion of n-alkane hydrocarbons from n-octane to n-hexadecane, Combust. Flame 156 (2009) 181–199.
[16] M. Mehl, T. Faravelli, F. Giavazzi, E. Ranzi, P. Scorletti, A. Tardani, D. Terna, Detailed chemistry promotes understanding of octane numbers and gasoline sensitivity, Energy & Fuels 20 (2006) 2391–2398.
[17] M. Mehl, T. Faravelli, E. Ranzi, D. Miller, N. Cernansky, Experimental and kinetic modeling study of the effect of fuel composition in HCCI engines, Proc. Combust. Inst. 32 (2009) 2843–2850.
[18] M. Mehl, W.J. Pitz, M. Sjöberg, J.E. Dec, Detailed Kinetic Modeling of Low-Temperature Heat Release for PRF Fuels in an HCCI Engine, SAE Tech. Pap., 2009, paper 2009–01–1806.
[19] M. Mehl, W.J. Pitz, C.K. Westbrook, H.J. Curran, Kinetic modeling of gasoline surrogate components and mixtures under engine conditions, Proc. Combust. Inst. 33 (2011) 193–200.
[20] H. Wang, E. Dames, B. Sirjean, D.A. Sheen, R. Tango, A. Violi, J.Y.W. Lai, F.N. Egolfopoulos, D.F. Davidson, R.K. Hanson, C.T. Bowman, C.K. Law, W. Tsang, N.P. Cernansky, D.L. Miller, R.P. Lindstedt, A high-temperature chemical kinetic model of n-alkane (up to n-dodecane), cyclohexane, and methyl-, ethyl-, n-propyl and n-butyl-cyclohexane oxidation at high temperatures, JetSurF version 2.0, Retrieved from: http://web.stanford.edu/group/haiwanglab/JetSurF/JetSurF2.0/index.html.
[21] G. Vanhove, G. Petit, R. Minetti, Experimental study of the kinetic interactions in the low-temperature autoignition of hydrocarbon binary mixtures and a surrogate fuel, Combust. Flame 145 (2006) 521–532.
[22] Gasoline Surrogate Mechanism, Lawrence Livermore National Laboratory. Retrieved from: https://combustion.llnl.gov/mechanisms/surrogates/gasoline-surrogate.
[23] CHEMKIN, "Reaction Design CHEMKIN." 2013.
[24] I. Truedsson, M. Tuner, B. Johansson, W. Cannella, Pressure sensitivity of HCCI auto-ignition temperature for primary reference fuels, SAE Int. J. Engines 5 (2012) 1089–1108.
[25] A.D.B. Yates, A. Swarts, C.L. Viljoen, Correlating Auto-Ignition Delays And Knock-Limited Spark- Advance Data For Different Types Of Fuel, SAE Tech. Pap., 2005, paper 2005-01-2083.
[26] V.H. Rapp, W.J. Cannella, J.Y. Chen, R.W. Dibble, Predicting fuel performance for future HCCI engines, Combust. Sci. Technol. 185 (2013) 735–748.

[27] J.B. Heywood, Internal Combustion Engine Fundamentals, McGraw-Hill, 1988.
[28] D.M.A. Karwat, S.W. Wagnon, M.S. Wooldridge, C.K. Westbrook, On the combustion chemistry of n-heptane and n-butanol blends, J. Phys. Chem. A 116 (2012) 12406–12421.
[29] M. Sjöberg, J.E. Dec, Combined Effects of Fuel-Type and Engine Speed on Intake Temperature Requirements and Completeness of Bulk-Gas Reactions for HCCI Combustion, SAE Tech. Pap., 2003, paper 2003-01-3173.
[30] J.C. Livengood, P.C. Wu, Correlation of autoignition phenomena in internal combustion engines and rapid compression machines, Symp. (Int.) Combust. 5 (1955) 347–356.
[31] A. Babajimopoulos, G.A. Lavoie, D.N. Assanis, On the role of top dead center conditions in the combustion phasing of homogeneous charge compression ignition engines, Combust. Sci. Technol. 179 (2007) 2039–2063.

THE JOURNAL OF PHYSICAL CHEMISTRY A

Article

pubs.acs.org/JPCA

Combustion Chemistry of Ethanol: Ignition and Speciation Studies in a Rapid Compression Facility

Cesar L. Barraza-Botet,[†] Scott W. Wagnon,[†,§] and Margaret S. Wooldridge*[,†,‡]

[†]Department of Mechanical Engineering and [‡]Department of Aerospace Engineering, University of Michigan, Ann Arbor, Michigan 48109, United States

Supporting Information

ABSTRACT: Ethanol remains the most important alternative fuel for the transportation sector. This work presents new experimental data on ethanol ignition, including stable species measurements, obtained with the University of Michigan rapid compression facility. Ignition delay times were determined from pressure histories of ignition experiments with stoichiometric ethanol−air mixtures at pressures of ∼3−10 atm. Temperatures (880−1150 K) were controlled by varying buffer gas composition (Ar, N_2, CO_2). High-speed imaging was used to record chemiluminescence during the experiments, which showed homogeneous ignition events. The results for ignition delay time agreed well with trends on the basis of previous experimental measurements. Speciation experiments were performed using fast gas sampling and gas chromatography to identify and quantify ethanol and 11 stable intermediate species formed during the ignition delay period. Simulations were carried out using a chemical kinetic mechanism available in the literature, and the agreement with the experimental results for ignition delay time and the intermediate species measured was excellent for the majority of the conditions studied. From the simulation results, ethanol + HO_2 was identified as an important reaction at the experimental conditions for both the ignition delay time and intermediate species measurements. Further studies to improve the accuracy of the rate coefficient for ethanol + HO_2 would improve the predictive understanding of intermediate and low-temperature ethanol combustion.

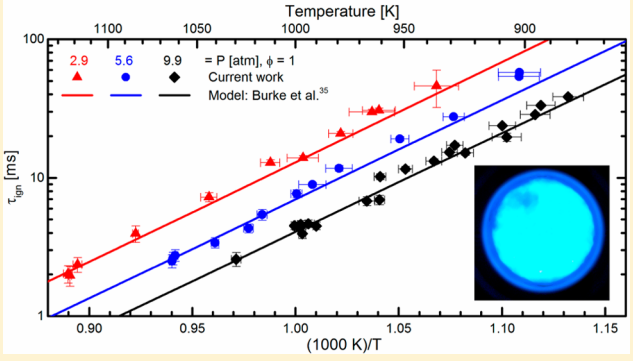

INTRODUCTION

Ethanol is the leading biofuel in the transportation sector, where it is mainly used in reformulated gasoline in the U.S. and as primary transportation fuel in Brazil.[1] The study of the impact of ethanol on internal combustion engine (ICE) technologies and strategies is of high interest from scientific, industrial, and environmental perspectives. Gasoline−ethanol blends used in ICEs enhance the octane number and octane sensitivity for knock control, can reduce pollutant emissions including soot particulates, and potentially stimulate the sustainable production of fuels.[2−5]

In spite of the well-known relevance of ethanol, there are still a limited number of experimental studies on ethanol autoignition behavior at conditions expected in ICE applications and there are even fewer studies where intermediate species have been quantified. Ignition studies, particularly when coupled with species measurements, allow a deeper understanding of oxidation and emissions chemistry and related heat release rates. To date, there are two major groups of experimental conditions for ethanol ignition reported in the literature. Many of the experimental data in the literature are from shock tube studies and include mixtures dilute in argon with fuel-to-oxygen equivalence ratios of ϕ = 1.0, 0.5, and 2, pressures from 1 atm to slightly higher than 10 atm, and temperatures >1100 K.[6−9] For ethanol−air mixtures at stoichiometric conditions, ignition delay time results for pressures higher than 10 atm and temperatures from 750 to 1400 K are available from shock tube studies[4,10,11] and rapid compression machines.[3,4] Ethanol speciation data are available in the literature from low-pressure flames and flow and jet-stirred reactors, mainly at high temperatures;[12−23] however, no species measurements are currently available at intermediate pressures, and intermediate and low temperatures. From the elementary reaction studies involving ethanol, most experiments have focused on hydrogen abstraction from the ethanol α-carbon by hydroxyl radicals and ethanol molecular decomposition using several diagnostic techniques at different conditions, as summarized by Sarathy et al.[2] Additionally, several detailed chemical kinetic mechanisms can be found in the literature for ethanol[4,6,14,19,24−27] and for multicomponent fuel mixtures including ethanol.[2,3,8,28−35]

The aim of this work is to provide new experimental ignition and speciation data on ethanol−air mixtures from a single facility [the University of Michigan rapid compression facility

Received: July 5, 2016
Revised: August 26, 2016

DOI: 10.1021/acs.jpca.6b06725
J. Phys. Chem. A XXXX, XXX, XXX−XXX

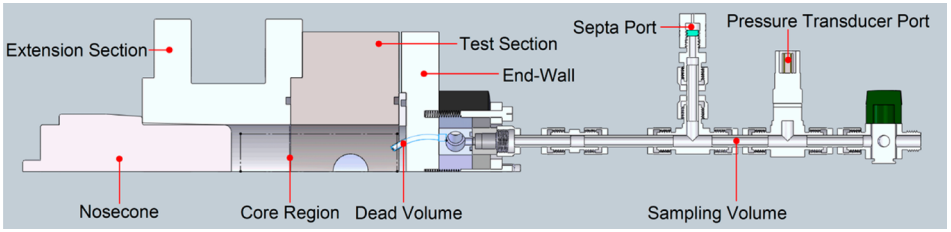

Figure 1. Cross-section schematic of the top half of the axi-symmetric components of the fast gas sampling system and the rapid compression facility assembly for speciation experiments. The second sampling system is a mirror-image across the RCF centerline axis of this schematic.

(UM-RCF)] at conditions that complement and expand on prior studies in the literature. The current work considers stoichiometric ethanol−oxygen mixtures at moderate levels of dilution using Ar, N_2, and CO_2 as buffer gases, pressures from 3 to 10 atm, and temperatures from 880 to 1150 K. Simulations were carried out using an updated version of the AramcoMech kinetic model modified by Burke et al.[34,35] High-speed imaging was used to record chemiluminescence during ignition, and fast-gas sampling coupled with gas chromatography was used to identify and quantify stable species during the ignition delay time of stoichiometric ethanol−air mixtures at 10 atm and 930 K.

EXPERIMENTAL METHODS

Ignition delay times (τ_{ign}) from the UM RCF provide direct quantification of the global reactivity of reference compounds and their parametric correlation with a wide range of thermodynamic state conditions. Stable intermediate species concentrations assist in identifying important reaction pathways and improving predictive chemical kinetic models. A broad variety of fuels and a wide range of experimental conditions can be studied using the UM RCF. Pressures and temperatures typically in the ranges 0.5−30 atm and 500−1800 K and test times of 1−50 ms can be reached in the UM RCF by modifying the compression ratio between 16 and 37.[36]

Ignition and High Speed Imaging. The five main components of the UM RCF are the stainless steel driver, driven and test sections, the sabot (free piston), and the hydraulic control valve system. The working principle of the facility is based on the driver and driven sections being initially separated by the hydraulic control valve while the driver section is filled with high-pressure air and the driven section is filled with the test gas mixture at low pressure. Extra isolation between the hydraulic control valve assembly and the driven section is provided by a thin polyester (Mylar) film. The sabot is a two-piece assembly consisting of a brass counterweighted body (Delrin) in contact with the driven section internal walls and a deformable ultrahigh molecular weight polyethylene nosecone. The test gas mixtures are prepared in a dedicated mixing tank on the basis of the partial pressures of high-purity grade ethanol (C_2H_5OH, Decon Laboratories, 200 proof, 100%, anhydrous), oxygen (O_2, PurityPlus 4.3, 99.993%), argon (Ar, PurityPlus 5.0, 99.999%), carbon dioxide (CO_2, PurityPlus Laser grade 4.5, 99.995%), and nitrogen (N_2, PurityPlus 5.0, 99.999%) for a predefined mixture composition determined by the target values of molar equivalence ratio, molar dilution ratio, pressure, and temperature. An intake manifold is used to prepare the mixture by measuring the partial pressures with a capacitance diaphragm gauge (MKS High Accuracy Baratron Type 690A). After the driver and driven section have been filled, the hydraulic control valve is rapidly opened, allowing the high-pressure air to break the polyester film and accelerate the sabot down the driven section toward the test section. After a compression period of ∼100 ms,[36] the nosecone seats in an annular interference fit, sealing the test gas mixture in the test section. The shape of the sabot and the nosecone permits the colder boundary layer gases to be trapped outside of the test section, reducing cold boundary layer and fluid mixing effects on the test gas mixture. The end-wall of the test section is sealed using either a polycarbonate sheet that allows optical access for high-speed imaging or a stainless steel plate instrumented with the fast-gas sampling system, described below. A further detailed description of the UM RCF components, dimensions, procedures, and characterization is provided by Donovan et al.[36,37]

Piezoelectric transducers (Kistler 6045A and B, and Kistler 6125A and C) coupled with a charge amplifier (Kistler 5010B) were used to measure the pressure histories for the experiments, and the data were collected using a 32-bit data acquisition system (National Instruments cDAQ-9172) and a user data-acquisition program developed in LabView. Chemiluminescence emitted during ignition was recorded using a high-speed color camera (Vision Research Phantom v7.1) and a Navistar 50 mm lens (f/0.95). Proprietary software (Phantom v. 675.2) was used to collect the optical data at a resolution of 512 × 512 pixels, a sample rate of 25 000 frames per second and an exposure time of 39.6 μs. Further details about camera specifications and settings can be found in Walton et al.[38]

Fast Gas Sampling and Analysis. For speciation experiments, the polycarbonate sheet is replaced with a stainless steel end-wall equipped with two symmetrically positioned fast gas sampling systems used to collect samples of the reacting gases during discrete time intervals within the ignition delay time. The main components of the sampling systems assembled with the RCF are shown in Figure 1. Each sampling system consists of a sampling tube (inner diameter/outer diameter, ID/OD = 0.20/0.32 cm) extending ∼10 mm into the volume of the test section, a fast sampling valve (a modified Festo MHE3 valve with a stock response time of 3 ms, 3 mm orifice), a sampling chamber (4.5 ± 0.5 mL) with a septum port (VICI Valco, low bleed), a piezoresistive pressure transducer (Kistler 4045A2) coupled with an amplifier (Kistler 4618A0), and an isolation valve. Sample collection into the pre-evacuated sampling chamber is achieved by a custom-made triggering system connected to a pulse generator (Stanford Research Systems DG535). Pre-evacuation of the sampling chamber quenches the reacting mixture during sample acquisition (due to the rapid expansion of the sample gases from the test section to the sampling chamber) and minimizes sample dilution with residual gases in the sample chamber. To construct concentration−time histories, successive ignition experiments are conducted targeting the same thermodynamic

DOI: 10.1021/acs.jpca.6b06725
J. Phys. Chem. A XXXX, XXX, XXX−XXX

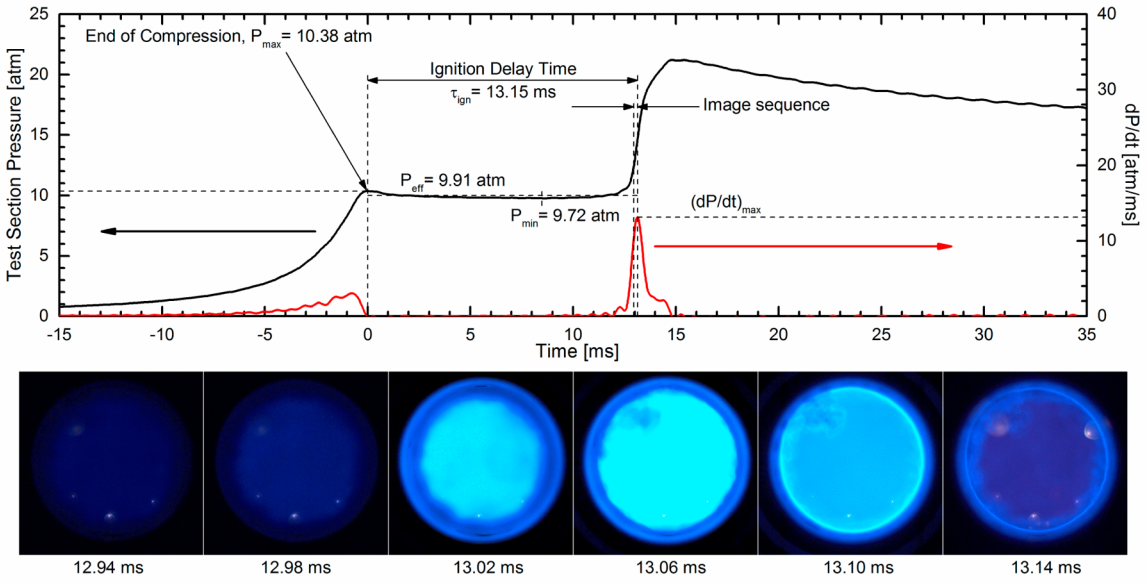

Figure 2. Typical pressure (black lines) and pressure derivative (red lines) time histories in the test section for an ignition experiment using high-speed imaging. The bottom panels show the sequence of still images from the high-speed camera at the time near ignition. Conditions for the experiment were P_{eff} = 9.91 atm, T_{eff} = 937 K, ϕ = 0.99, inert/O_2 ratio = 8.29, C_2H_5OH = 3.43%, O_2 = 10.4%, N_2 = 86.17%, Ar = 0.01%, τ_{ign} = 13.15 ms.

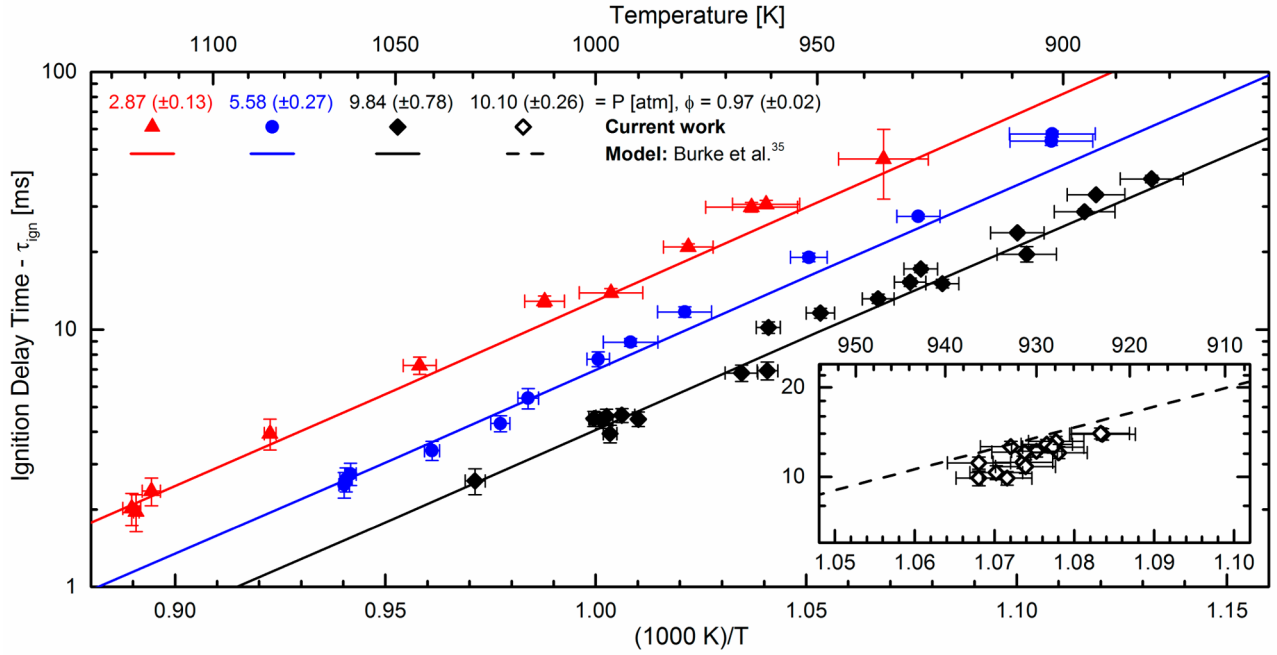

Figure 3. Experimental and modeling results for ethanol ignition delay time. Results of the ignition measurements in the UM RCF were for near stoichiometric conditions (ϕ = 0.97) and average dilution levels of inert/O_2 ratios of 8.2 for imaging (main figure) and 7.5 for speciation (inset) experiments. Model predictions (lines) are based on the reaction mechanism by Burke et al.[35]

state conditions while changing the sample trigger timing. Constant trigger pulse widths of Δt = 1.5 ms were used to obtain good temporal resolution ($\Delta t/\tau_{ign}$ = 0.18 ± 0.02) of the stable species while collecting sufficient volume for analysis. After every experiment, a syringe (Hamilton Gastight #1010, 10 mL) for each sampling chamber was used to remove the quenched gas through the septum port for injection into the gas chromatograph (GC) systems for analysis. Further descriptions of the fast-gas sampling systems can be found in Karwat et al.,[39] and the GC standard calibration procedure followed and compounds used in this work are included in Wagnon et al.[40] and Wagnon et al.[41] System specifications on the GCs are provided in Table S.1 of the Supporting Information.

RESULTS AND DISCUSSION

Ignition Delay Times. Figure 2 shows a plot of the typical pressure and pressure derivative time histories from ethanol ignition experiments carried out in this study. As a result of compression by the sabot, the pressure of the test gas mixture increases to a local maximum (P_{max}) at the end of compression,

DOI: 10.1021/acs.jpca.6b06725
J. Phys. Chem. A XXXX, XXX, XXX−XXX

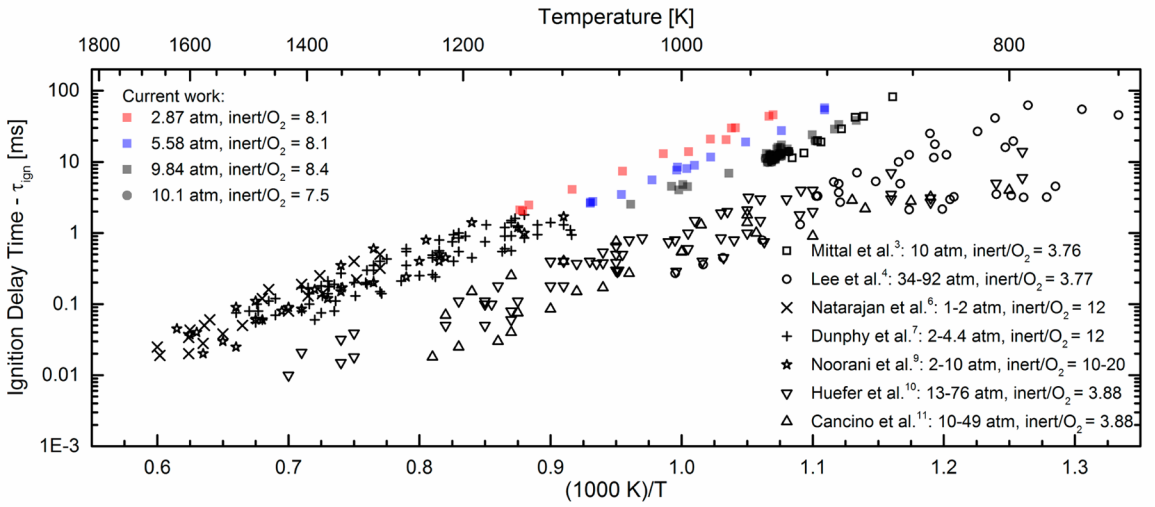

Figure 4. Summary of results of ignition delay time for stoichiometric mixtures of ethanol studied in this work and available in the literature. All data are presented as reported in the literature. No scaling was used to create this figure.

corresponding to the time when the nosecone seats. The time at the end of compression when the pressure reaches P_{max} is set as zero (t = 0 ms). The gas mixture pressure slightly decreases after the end of compression as heat is transferred to the walls of the test and extension sections and, to a lesser extent, due to endothermic fuel pyrolysis. After a period of time, the pressure rapidly increases due to autoignition of the test gas mixture. The ignition delay time, τ_{ign}, for each experiment was defined as the time from the end of compression, where $P = P_{max}$, to the maximum rate of change in the pressure history, i.e., $(dP/dt)_{max}$. All data exhibited similar features of a smooth compression process, followed by relatively constant pressure before ignition.

Effective pressure (P_{eff}) and effective temperature (T_{eff}) for each experiment in this study were defined as in He et al.,[42] a method that has been successfully used in many previous UM RCF studies to represent the experimental state conditions.[38−41,43−45] The effective pressure was calculated as the time-averaged integrated pressure from P_{max} to P_{min}, i.e., the minimum pressure before ignition, to account for heat transfer effects. T_{eff} was determined by numerically integrating isentropic compression relations using P_{eff}, the initial mixture pressure and temperature, and the gas mixture thermophysical properties as in Karwat et al.[45] The appropriateness of modeling the UM RCF compression process as isentropic has been experimentally verified by Donovan et al.[36] The use of average conditions further removes some of the bias toward higher temperatures and pressures that occurs under end-of-compression conditions, particularly when results are presented on Arrhenius diagrams, which typically assume isobaric and isothermal reporting.

A set of still images from the high-speed imaging corresponding to the ignition experiment is included in Figure 2. The chemiluminescence emission showed homogeneous ignition in the test volume, with no indication of local ignition events, propagation of flames or reaction fronts, or other spatial irregularities. As seen in Figure 2, the intensity of the emission increased to the maximum at t = 13.06 ms, which corresponded to the time of the maximum pressure derivative, i.e., τ_{ign} = 13.15 ms. The observations of homogeneous chemiluminescence were typical for all the imaging experiments and provided confidence in local sampling as being representative of the overall mixture conditions.

Summaries of the results for τ_{ign} are presented in Figure 3 and Table S.2 of the Supporting Information. The imaging and sampling experiments used average inert/O_2 ratios of 8.2 and 7.5, respectively. In the figure, the symbols represent the results of the current work. The experimental uncertainties of the measurements are represented as error bars in Figure 3 with an average value of ±6.7% for τ_{ign}. The horizontal error bars for temperature were calculated as the standard deviation of the temperatures deduced from measured pressure history data. The vertical error bars represent the uncertainty in determining the ignition delay time based on the pressure data. Filled symbols in Figure 3 correspond to ignition experiments that used high-speed imaging and open symbols correspond to speciation experiments. In Figure 3, the vertical error bars are included for all data, but they are sometimes smaller than the size of the symbols. Both data sets exhibited excellent repeatability and low scatter. The results for τ_{ign} exhibited the expected trends of increasing reactivity with increasing pressure and temperature, with clear Arrhenius behavior at each pressure.

The UM RCF results provide new ignition data at conditions where no previous studies have been reported, specifically for temperatures below 1200 K and pressures of 10 atm and below, as seen in Figure 4, which presents a summary of the results of the current work and previous studies of ignition delay time for stoichiometric mixtures of ethanol. The results of the current work are in good agreement with the larger body of data which include high-temperature conditions. In particular, the current work agrees with the higher temperature studies by Natarajan et al.,[6] Dunphy et al.[7] and Noorani et al.,[9] which were conducted at slightly higher levels of dilution (inert/O_2 = 10−20), but comparable pressures (1−10 atm). The other intermediate and low-temperature studies were conducted at approximately air levels of dilution and higher pressures and show clear trends of increasing reactivity with increasing pressure and higher O_2 concentrations.

The large body of data available for ethanol ignition delay time presented the opportunity to explore regression analysis over the wide range of conditions and mixtures studied to see if the data could be represented by a single, simple correlation as a function of P, T, and dilution. The composite data presented

DOI: 10.1021/acs.jpca.6b06725
J. Phys. Chem. A XXXX, XXX, XXX−XXX

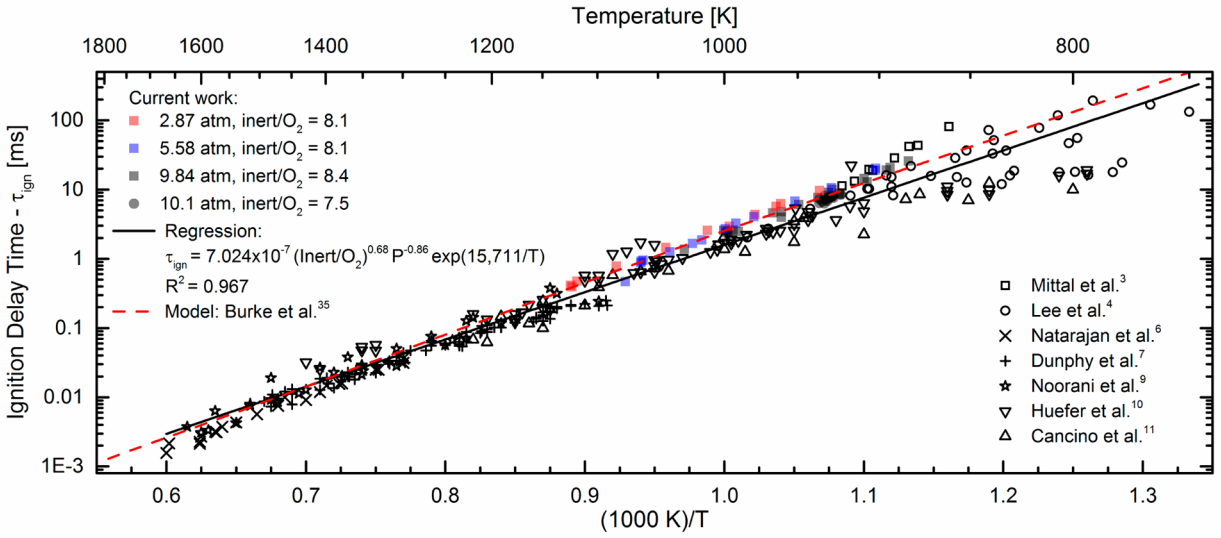

Figure 5. Summary of the normalized ignition delay time data for stoichiometric mixtures of ethanol studied in this work and available in the literature. All data were normalized to P = 10 atm and Inert/O_2 = 3.76 (air level of dilution) using Equation 1. Model predictions (red dashed line) based on the reaction mechanism by Burke et al.[35] and Equation 1 (black solid line) are included.

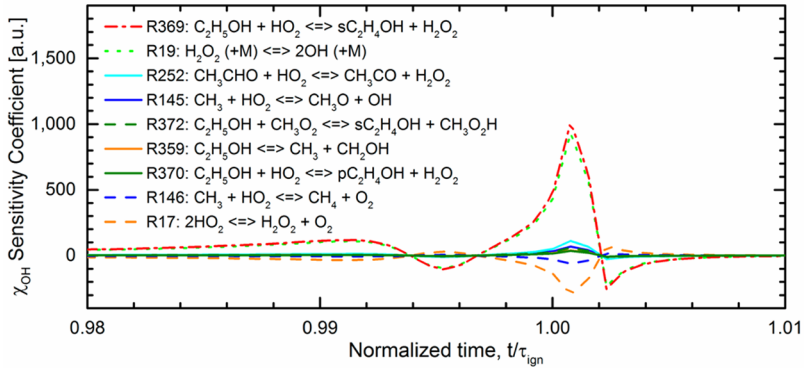

Figure 6. Results of CHEMKIN sensitivity analysis for OH based on the reaction mechanism by Burke et al.[35] at simulation conditions of P = 10.1 atm, T = 930 K, ϕ = 1, and (inert/O_2) = 7.5. The top 10 reactions are included in the figure.

in Figure 4 were used to determine the following best-fit correlation for ignition delay time (ms):

$$\tau_{ign} = 7.024 \times 10^{-7}(\text{Inert}/O_2)^{0.68} P^{-0.86} \exp(15711/T) \quad (1)$$

Equation 1 was developed for data that span the range of the conditions of ϕ = 1.0, P = 1.0−91.5 atm, molar dilution of inert/O_2 = 3.76−25.33, and T = 750−1670 K. The quality of the correlation at representing the data was excellent as indicated by the R^2 value of 0.967. The correlation was used to normalize the experimental data to air levels of dilution and 10 atm, and the results are presented in Figure 5. Equation 1 is included in the figure. The extended data set collapses well to a single trend-line for temperatures above 900 K, with slightly increasing scatter for temperatures below 900 K.

The experimental results were compared with model predictions using detailed reaction chemistry. The pressures, temperatures, and mixture composition from the UM RCF experiments were used as initial conditions for 0-dimensional adiabatic constant-volume CHEMKIN simulations, and the time from the start of the simulation to the maximum $(dP/dt)_{max}$ was defined as τ_{ign}. Model predictions are shown in Figure 3 as lines for the mechanism by Burke et al.,[35] which is a detailed mechanism for C_1−C_3 hydrocarbon and oxygenated species oxidation. The mechanism contains 1831 elementary reactions, including ethanol reaction chemistry, and has been validated by comparison with several experimental data sets.[3,30,34,35] As seen in Figure 3, the predictions using the mechanism by Burke et al.[35] are in excellent agreement with the current results, generally falling within the uncertainty of the experimental data for all pressures and temperatures presented. The model predictions also agreed well with Equation 1 and the extended data set, as seen in Figure 5.

The excellent level of agreement between the experimental data and the model predictions provided confidence in using the reaction mechanism to interpret the reaction pathways controlling ethanol ignition at the conditions of the UM RCF study. For this purpose, the OH radical concentration was used as a surrogate for τ_{ign} to conduct CHEMKIN sensitivity analysis using the mechanism by Burke et al.[35] The results for the OH sensitivity coefficients at the average conditions of the speciation experiments, i.e., P = 10.1 atm, T = 930 K, ϕ = 0.99, and (Inert/O_2) = 7.5 are presented in Figure 6. Two elementary reactions control ethanol ignition at these conditions:

$$H_2O_2(+M) \leftrightarrow 2OH(+M) \quad (R19)$$

DOI: 10.1021/acs.jpca.6b06725
J. Phys. Chem. A XXXX, XXX, XXX−XXX

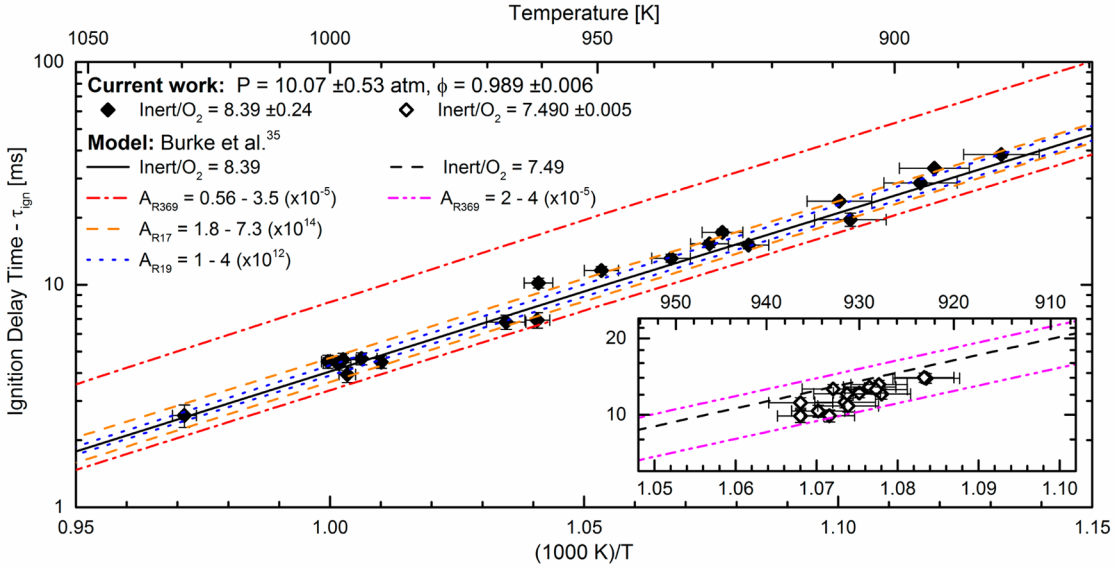

Figure 7. Experimental data for stoichiometric ethanol experiments at 10.1 atm and inert/O_2 ratio of 8.4 (main figure) and 7.5 (inset) compared with model predictions using the reaction mechanism of Burke et al.,[35] and the effects of modifying the pre-exponential factors of reactions R17, R19, and R369.

$$C_2H_5OH + HO_2 \leftrightarrow sC_2H_4OH + H_2O_2 \quad (R369)$$

and to a lesser extent the reaction

$$2HO_2 \leftrightarrow H_2O_2 + O_2 \quad (R17)$$

where the reaction numbers are according to the Burke et al. mechanism.[35] The hydrogen abstraction from the ethanol α-carbon site by hydroperoxyl radical (R369) was included in an earlier version of this mechanism by Metcalfe et al.[30] who used an analogy of the rate constants calculated by Zhou et al.[46] for *n*-butanol with a factor of 2.5 as the estimated uncertainty. Mittal et al.[3] later adjusted the pre-exponential factor, which improved the prediction capabilities of the mechanism for τ_{ign} for their experimental data. Rate coefficients derived by Troe[47] for the chain-branching thermal dissociation of hydrogen peroxide (R19) and by Hippler et al.[48] for the inhibiting self-reaction of HO_2 radicals (R17) each have uncertainties of ± a factor of 2.

A CHEMKIN parametric study was carried out to quantify the effects of independently changing the pre-exponential factors (A) of these three reactions on τ_{ign} of stoichiometric ethanol mixtures at 10.1 atm and inert/O_2 ratios of 8.4 and 7.5 for the temperature range studied experimentally. Figure 7 shows that changes in the A-factors within the reported uncertainties for reactions R17[48] and R19[47] produced relatively small variations on τ_{ign}, and the model predictions still fell within the experimental uncertainties. Only reaction R369 showed a significant effect on τ_{ign} when the pre-exponential factor was changed by a factor of 2.5 (based on the original estimate by Zhou et al.[46] for *n*-butanol). The uncertainty bounds for reaction R369 include the fact that Mittal et al.[3] increased the Zhou et al.[46] A-value by a factor of 1.75 (to $A_{R369} = 2.45 \times 10^{-5}$) but kept the original uncertainty values unmodified. As presented in the inset of Figure 7, both experimental repeatability and uncertainty are well captured by A_{R369} values ranging from 2×10^{-5} to 4×10^{-5}, which suggests that uncertainty factors lower than ±2.5 could be assigned to A in reaction R369.

Modification of the pre-exponential factor of ethanol + HO_2 by Mittal et al.[3] improved the level of agreement with the experimental results presented by Mittal et al.[3] and in this work; however, fundamental studies of the ethanol + HO_2 elementary reaction will help reduce empiricism and improve the fundamental understanding of this important reaction. Such future efforts will benefit from the high sensitivity of the results of this study to the ethanol + HO_2 reaction, as these data can help to develop strategies to measure and validate elementary reaction rates for ethanol + HO_2.

Intermediate Species. Figure 8 shows the pressure histories for the test section and sampling volumes as well as the pressure derivative for the test section data of a typical speciation experiment. The ignition delay time data derived from the sampling experiments were presented in Figures 3, 4, 5, and 7 and agreed well with the trends of other experimental data and with model predictions, indicating that the collection of two samples did not affect the ignition process. Sample times

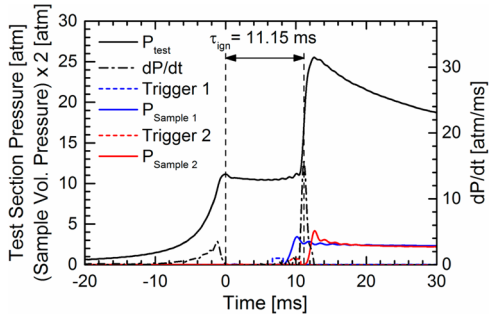

Figure 8. Typical pressure (solid black line) and pressure derivative (dashed black line) histories in the test section for an ignition experiment using fast gas sampling. Pressure histories for sampling volumes 1 (solid blue line) and 2 (solid red line) and corresponding valve triggering signals (colored dashed lines) are included. Conditions for the experiment were P_{eff} = 10.6 atm, T_{eff} = 936 K, ϕ = 0.99, inert/O_2 ratio = 7.47, C_2H_5OH = 3.74%, O_2 = 11.36%, N_2 = 79.6%, Ar = 5.3%, τ_{ign} = 11.15 ms.

DOI: 10.1021/acs.jpca.6b06725
J. Phys. Chem. A XXXX, XXX, XXX−XXX

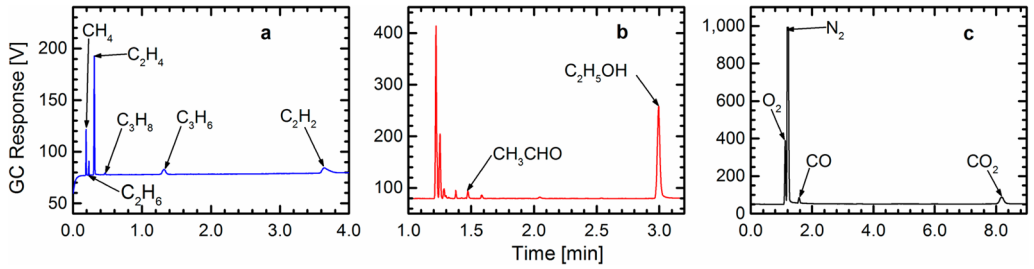

Figure 9. Chromatograms corresponding to Sample 2 of Figure 8 from (a) GC-2/FID, (b) GC-3/FID and (c) GC-3/TCD. See Table S.1 for specific technical information on each GC configuration.

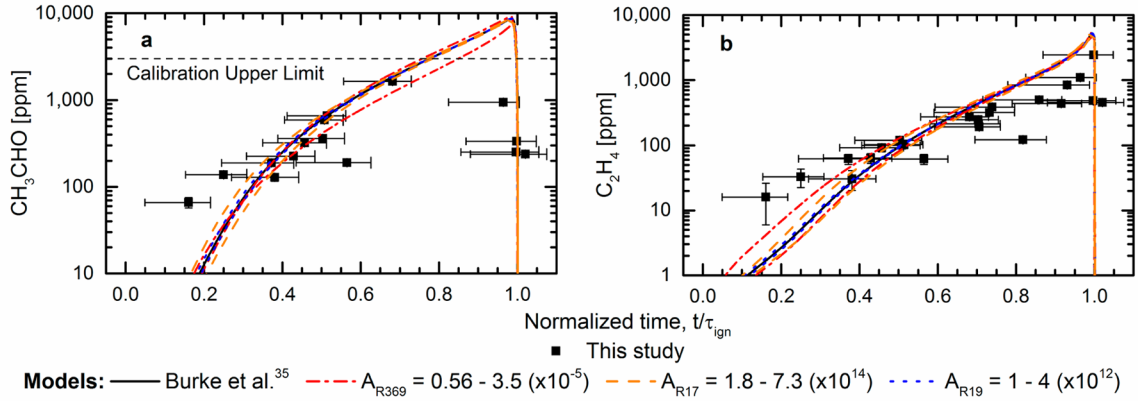

Figure 10. Measured and predicted (using the reaction mechanism by Burke et al.[35]) time histories of stable intermediate species produced during ethanol autoignition: (a) ethanal and (b) ethene. Average conditions for the sampling experiments were used for the model predictions which were P = 10.1 atm, T = 930 K, ϕ = 0.99, C_2H_5OH = 3.75%, O_2 = 11.33%, and inert/O_2 = 7.5. The effects of modifying the pre-exponential factors within the respective uncertainty limits of reactions R17, R19, and R369 are included.

were defined for each experiment as the time corresponding to one-half the area under the sampling pressure curve starting from the time the valve was triggered to the time of maximum sampling pressure. The uncertainty in sample timing was defined by the integration limits, which represented the duration of the gas sampling. The average sample duration was 2.1 ms with corresponding uncertainties of ±0.1 ms. The transport delay of ~1 ms, between the moment the sample valve opened and when the pressure in the sample volume started to increase, was accounted for to define the sample time and included in Table S.3 of the Supporting Information.

For this study, gas sampling data were acquired from 15 ignition experiments with average P_{eff} = 10.10 ± 0.26 atm, T_{eff} = 930 ± 4 K, and τ_{ign} = 11.9 ± 1.3 ms. All experiments used the same mixture composition of C_2H_5OH = 3.75%, O_2 = 11.33%, N_2 = 79.6%, and Ar = 5.31% (mole basis). Twelve species were detected and quantified using the GC/FID-TCD systems and the temperature profiles described by Wagnon et al.[41] and summarized in the Supporting Information in Table S.1. Figure 9 presents typical chromatograms corresponding to the sample 2 (red solid line) data presented in Figure 8.

The stable intermediate species measurements from the gas sampling and GC analysis are presented in Figures 10 and 11. In both figures, the temporal scales were normalized to the ignition delay time of each experiment, where t/τ_{ign} = 0 corresponds to the end of compression and t/τ_{ign} = 1 corresponds to autoignition. The data were normalized due to slight variations in the end-of-compression conditions that occurs due to the interference fit used to seat the nosecone of the sabot, which affects the compression ratio of each experiment. Both normalized and non-normalized results for the species measurements are provided in the Supporting Information in Table S.3. The symbols represent the mole fractions of the stable species in the mixture collected during each sampling interval. The horizontal error bars in Figures 10 and 11 correspond to the duration (in normalized time) of the sampling events, and vertical error bars represent the standard deviation of each mole fraction measurement as a statistical indication of the uncertainty associated with the sampling and GC measurement systems. Uncertainties in the species mole fraction measurements come from two main sources: the measurement error of the GCs and the fast-gas sampling system. A detailed description of the GC calibration process and the uncertainty assessment of the gas sampling measurements are provided in the Supporting Information. High concentrations of ethanal (over 3000 ppm) and ethanol (over 10 000 ppm) saturated the GC columns; hence, ethanal and ethanol data above their calibration limits were not included in Figures 10 and 11.

The stable species detected and measured in this study included ethanal (CH_3CHO) and ethene (C_2H_4) (presented in Figure 10), and ethanol (C_2H_5OH), methane (CH_4), ethane (C_2H_6), ethyne (C_2H_2), carbon monoxide (CO), carbon dioxide (CO_2), propane (C_3H_8), propene (C_3H_6), 1-butene (C_4H_8-1), and 1,3-butadiene (C_4H_6-1,3) (presented in Figure 11). Ethanal and ethene are early intermediates of the two main reaction pathways expected for ethanol oxidation at the conditions studied here. Both species were measured at peak levels of over 0.1% (mole basis). Both CO and CO_2, as final products of combustion, were produced at high levels (>2% mole fraction each) at times close to ignition. The experimental measurements showed ethanol was consumed relatively late in

DOI: 10.1021/acs.jpca.6b06725
J. Phys. Chem. A XXXX, XXX, XXX−XXX

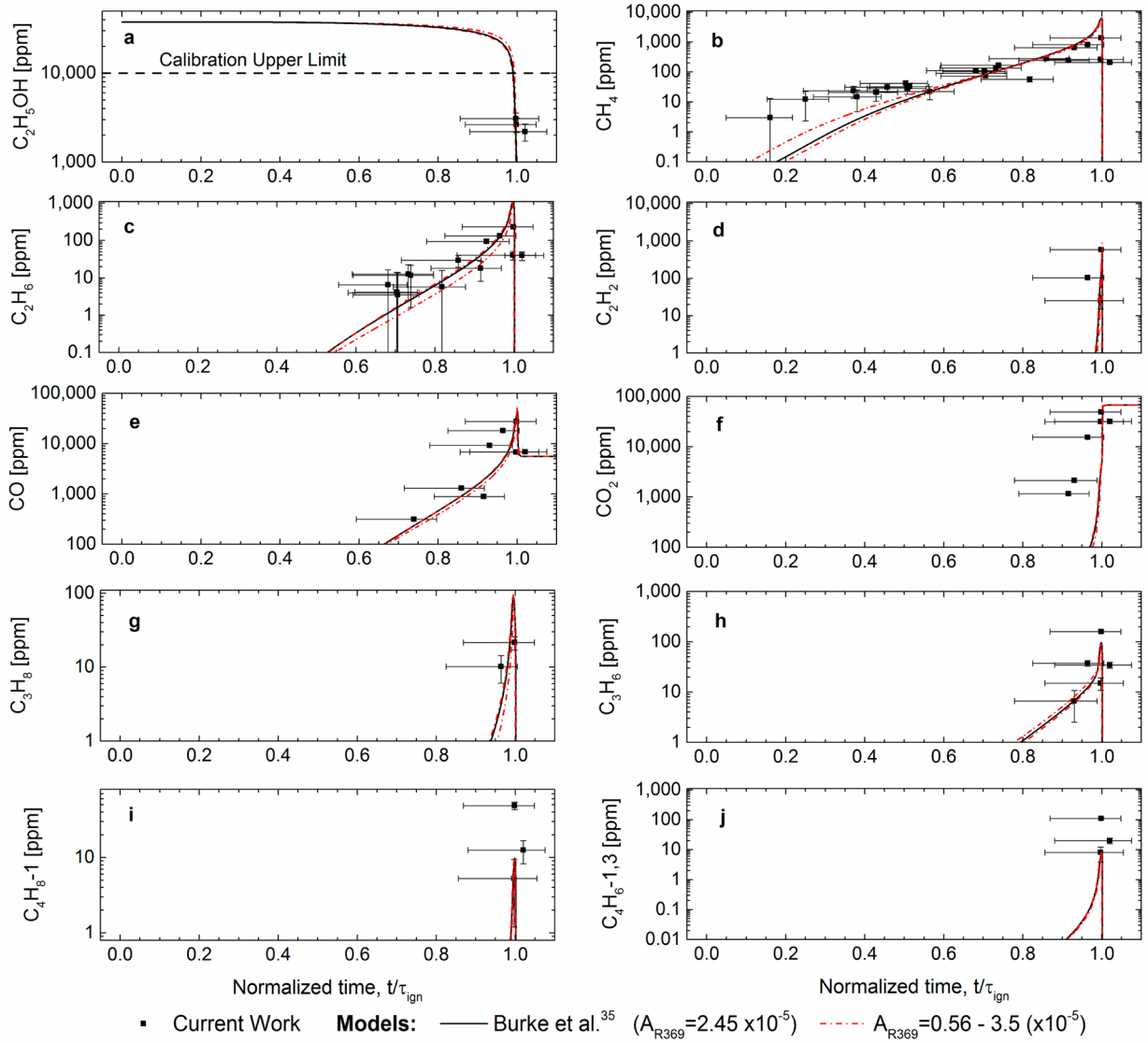

Figure 11. Measured and predicted time histories of stable intermediate species produced during ethanol autoignition: (a) ethanol, (b) methane, (c) ethane, (d) ethyne, (e) carbon monoxide, (f) carbon dioxide, (g) propane, (h) propene, (i) 1-butene, (j) 1,3-butadiene. Average conditions for the sampling experiments were used for the model predictions, which were P = 10.1 atm, T = 930 K, ϕ = 0.99, C_2H_5OH = 3.75% O_2 = 11.33%, and inert/O_2 = 7.5. The effects of modifying the pre-exponential factor within the uncertainty limits of reaction R369 are included.

the ignition process, specifically after 95% of the ignition delay time. With the exception of methane, ethane, and ethyne, the remaining species were measured at levels <∼100 ppm.

The species measurements are compared with model predictions using the mechanism by Burke et al.[35] at the average sampling conditions in Figures 10 and 11. The level of agreement between the experimental data and the model predictions was very good for most species, typically within the uncertainty of the measurements, particularly close to the time of ignition. In Figure 11a, rapid consumption of ethanol near the ignition delay time was well represented by the model even though only a few experimental data points were available for comparison. The model tended to underpredict the ethanal, ethene, and methane at earlier times, t/τ_{ign} < 0.3, which could be an indication of the model underpredicting the ethanol consumption rate at early times. The maximum values of 1-butene and 1,3-butadiene were underpredicted; however, these species were formed late in the ignition process and at relatively low quantities. Otherwise, the peak values for the other intermediate species were consistently well predicted by the Burke et al.[35] mechanism.

Again, the good level of agreement between the model predictions and the experimental data gave confidence to using the reaction mechanism by Burke et al.[35] to further interpret the experimental data via reaction path analysis. The results are presented in Figure 12 and show ∼72% of the ethanol reacted to produce ethanal as an early intermediate of the reaction sequence initiated by hydrogen abstraction by different radicals (predominantly OH and HO_2) from the α-carbon site of ethanol and completed by the low-barrier reaction of α-hydroxyethyl radical (sC_2H_4OH) and O_2.[49,50] Most of the ethanal was consumed in a series of steps to produce methanal (formaldehyde, CH_2O, not detected by the GC systems) before oxidizing to CO. The latter carbonyls (aldehydes) are a well-known concern for the use of pure ethanol or high-ethanol blends from the pollution control perspective in the transportation sector.[51] Methane (Figure 11b) and ethane (Figure 11c) were produced from branches of the main pathway when

DOI: 10.1021/acs.jpca.6b06725
J. Phys. Chem. A XXXX, XXX, XXX−XXX

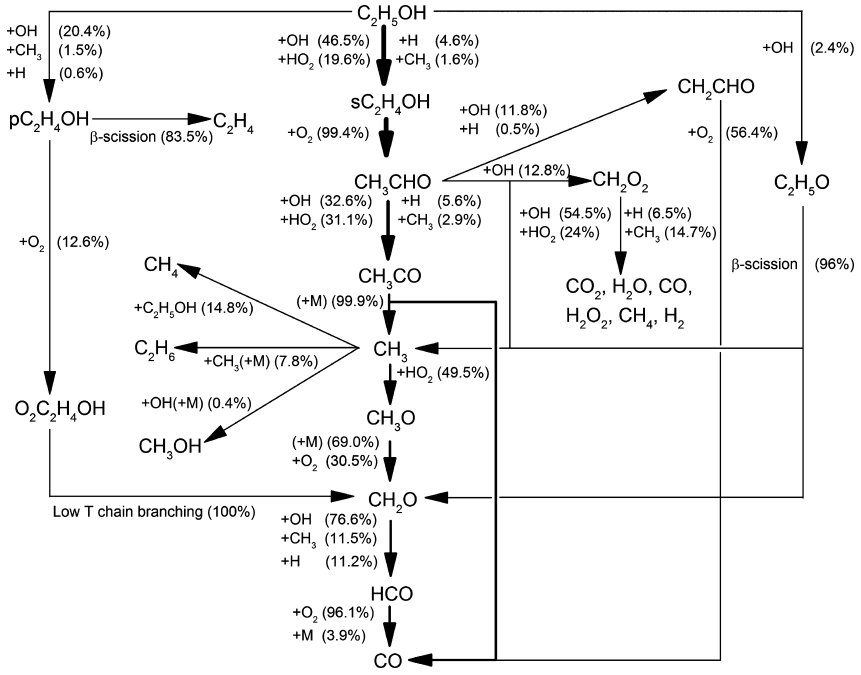

Figure 12. Schematic representation of the reaction pathway analysis for ethanol oxidation using the reaction mechanism by Burke et al.[35] for conditions of P = 10.1 atm and T = 930 K, C_2H_5OH = 3.75%, O_2 = 11.33%, N_2 = 79.6% and Ar = 5.31%, and normalized time of t/τ_{ign} = 0.9.

ethanal reacted to form methanal. Ethene was the product of the H atom abstraction reactions from the secondary or β-carbon site on ethanol followed by the β-scission reaction (Figure 12).

The sensitivity of the model predictions for the species to changes in the pre-exponential factors of reactions R17, R19, and R369 was also investigated. The A-factors for reactions R17, R19, and R369 were varied within the assigned uncertainty limits (as in Figure 7), and the results are shown in Figure 10 for ethanal and ethene. These species showed the highest sensitivity to changes in the A-factors of the three reactions. As seen in Figure 10, modifying the A-coefficients did not significantly improve agreement for ethanal, whereas the agreement with ethene was modestly improved at earlier times by reducing the A-factor for reaction R369. Figure 11 includes the results of modifying the A-factor for reaction R369 only, and the results showed negligible changes in the species predictions for all compounds.

The lack of sensitivity (using the conventional Chemkin sensitivity analysis) of the species time histories to the reactions controlling the ignition delay time or the global reactivity of the mixture at the state conditions presents a challenge and an opportunity to evaluate our understanding of reaction pathways and reaction mechanisms. The strong sensitivity of the radical pool to the reactions controlling ignition, and the corresponding sensitivity of fuel consumption to the radical pool, eclipse or dominate the system response. Alternative methods of sensitivity analysis may provide opportunity for intermediate species measurements to be used to validate and verify reaction mechanisms beyond typical comparisons, such as those made here.

The stable intermediate species reported near t/τ_{ign} = 1.00 accounted for ~92% of the carbon initially in the mixture and corresponded well with the 87% of carbon predicted by the Burke et al.[35] mechanism. In general, there was very good agreement between the experimental data and the predictions from the mechanism, i.e., within the sampling interval and measurement uncertainties. No significant reaction pathways were identified for the higher hydrocarbons from the Burke et al.[35] mechanism; however, such species may provide some insight into how reaction pathways change when ethanol is blended with gasoline and gasoline surrogates.

CONCLUSIONS

The results of the present work expand the quantitative understanding of the reactivity of ethanol at intermediate temperatures and pressures. OH sensitivity analysis identified H-abstraction from ethanol by HO_2 (reaction R369) as the primary reaction significantly affecting the global reactivity of ethanol, but changing the A-factor for reaction R369 within the uncertainty limits had small to negligible effects on predicted intermediate species. Hence, ignition delay time data, like the results of the current work, are a basis for improving the rate coefficient uncertainties for this important reaction, and the speciation data provide important new information identifying and quantifying the reaction pathways of the stable intermediate species formed during ignition. Importantly, the results include species that are critical to predicting pollutant emissions like aldehydes and soot precursor species. The combined measurements of ignition delay times and intermediate species for ethanol ignition provide vital data for developing, validating, and verifying combustion chemistry. Excellent agreement between the experimental data and the model predictions was observed in this study without modifying any of the rate coefficient data in the original reaction mechanism developed by Burke et al.[35] The results of the study provide direct evidence to support high confidence in our predictive understanding of ethanol combustion, including the detailed reaction pathways, at conditions directly relevant to modern combustion systems.

DOI: 10.1021/acs.jpca.6b06725
J. Phys. Chem. A XXXX, XXX, XXX−XXX

■ ASSOCIATED CONTENT

Supporting Information

The Supporting Information is available free of charge on the ACS Publications website at DOI: 10.1021/acs.jpca.6b06725.

Tables of the gas chromatography methods, ignition delay data and intermediate species-time histories concentrations, and a detailed description of the GC calibration method and the uncertainty analysis for stable intermediate species are provided (PDF)

■ AUTHOR INFORMATION

Corresponding Author

*M. S. Wooldridge. E-mail address: mswool@umich.edu. Tel: 734-936-0349. Fax: 734-647-3170.

Present Address

[§]Material Science Division, Lawrence Livermore National Laboratory, Livermore, California 94550, USA.

Author Contributions

The manuscript was written through contributions of all authors. All authors have approved the final version of the manuscript.

Notes

The authors declare no competing financial interest.

■ ACKNOWLEDGMENTS

The authors acknowledge the generous support of the U.S. Department of State's Fulbright Program; the Colombian Department of Science, Technology and Innovation − Colciencias; and the U.S. Department of Energy − Office of Basic Energy Sciences via Contract No. DE-SC0002645. Portions of this work related to manuscript review were performed under the auspices of the U.S. Department of Energy by Lawrence Livermore National Laboratory under Contract DE-AC52-07NA27344 through the Special Employee Strategic Mission Support program.

■ REFERENCES

(1) Baros, S. Biofuels—Ethanol and Biodiesel. *Brazil: Biofuels Annual*; USDA Foreign Agricultural Service: Washington, DC, 2015; GAIN Report No. BR15006.

(2) Sarathy, S. M.; Oßwald, P.; Hansen, N.; Kohse-Höinghaus, K. Alcohol Combustion Chemistry. *Prog. Energy Combust. Sci.* **2014**, *44*, 40−102.

(3) Mittal, G.; Burke, S. M.; Davies, V. A.; Parajuli, B.; Metcalfe, W. K.; Curran, H. J. Autoignition of Ethanol in a Rapid Compression Machine. *Combust. Flame* **2014**, *161* (5), 1164−1171.

(4) Lee, C.; Vranckx, S. On the Chemical Kinetics of Ethanol Oxidation: Shock Tube, Rapid Compression Machine and Detailed Modeling Study. *Z. Phys. Chem.* **2012**, *226*, 1−27.

(5) Storch, M.; Hinrichsen, F.; Wensing, M.; Will, S.; Zigan, L. The Effect of Ethanol Blending on Mixture Formation, Combustion and Soot Emission Studied in an Optical DISI Engine. *Appl. Energy* **2015**, *156*, 783−792.

(6) Natarajan, K.; Bhaskaran, K. A. An Experimental and Analytical Investigation of High Temperature Ignition of Ethanol. *Proc. 13th Internatinal Symp. Shock Tubes Waves* **1981**, 834−842.

(7) Dunphy, M. P.; Simmie, J. M. High-Temperature Oxidation of Ethanol: Part 1.-Ignition Delays in Shock Waves. *J. Chem. Soc., Faraday Trans.* **1991**, *87* (11), 1691−1696.

(8) Curran, H. J.; Dunphy, M. P.; Simmie, J. M.; Westbrook, C. K.; Pitz, W. J. Shock Tube Ignition of Ethanol, Isobutene and MTBE: Experiment and Modeling. *Symp. Combust., [Proc.]* **1992**, *24*, 769−776.

(9) Noorani, K. E.; Akih-Kumgeh, B.; Bergthorson, J. M. Comparative High Temperature Shock Tube Ignition of C_1−C_4 Primary Alcohols. *Energy Fuels* **2010**, *24* (11), 5834−5843.

(10) Heufer, K. A.; Olivier, H. Determination of Ignition Delay Times of Different Hydrocarbons in a New High Pressure Shock Tube. *Shock Waves* **2010**, *20* (4), 307−316.

(11) Cancino, L. R.; Fikri, M.; Oliveira, A. A. M.; Schulz, C. Measurement and Chemical Kinetics Modeling of Shock-Induced Ignition of Ethanol−Air Mixtures. *Energy Fuels* **2010**, *24* (5), 2830−2840.

(12) Norton, T.; Dryer, F. An Experimental and Modeling Study of Ethanol Oxidation Kinetics in an Atmospheric Pressure Flow Reactor. *Int. J. Chem. Kinet.* **1992**, *24*, 319−344.

(13) Alzueta, M. U.; Hernandez, J. M. Ethanol Oxidation and Its Interaction with Nitric Oxide. *Energy Fuels* **2002**, *16* (1), 166−171.

(14) Li, J.; Kazakov, A.; Dryer, F. L. Experimental and Numerical Studies of Ethanol Decomposition Reactions. *J. Phys. Chem. A* **2004**, *108*, 7671−7680.

(15) Kasper, T.; Oswald, P.; Kamphus, M.; Kohsehoinghaus, K. Ethanol Flame Structure Investigated by Molecular Beam Mass Spectrometry. *Combust. Flame* **2007**, *150* (3), 220−231.

(16) Leplat, N.; Seydi, A.; Vandooren, J. An Experimental Study of the Structure of a Stoichiometric Ethanol/Oxygen/Argon Flame. *Combust. Sci. Technol.* **2008**, *180* (3), 519−532.

(17) Haas, F. M.; Chaos, M.; Dryer, F. L. Low and Intermediate Temperature Oxidation of Ethanol and ethanol−PRF Blends: An Experimental and Modeling Study. *Combust. Flame* **2009**, *156* (12), 2346−2350.

(18) Dagaut, P.; Togbe, C. Experimental and Modeling Study of the Kinetics of Oxidation of Butanol ″n-Heptane Mixtures in a Jet-Stirred Reactor. *Energy Fuels* **2009**, *23* (7), 3527−3535.

(19) Leplat, N.; Dagaut, P.; Togbé, C.; Vandooren, J. Numerical and Experimental Study of Ethanol Combustion and Oxidation in Laminar Premixed Flames and in Jet-Stirred Reactor. *Combust. Flame* **2011**, *158* (4), 705−725.

(20) Xu, H.; Yao, C.; Yuan, T.; Zhang, K.; Guo, H. Measurements and Modeling Study of Intermediates in Ethanol and Dimethy Ether Low-Pressure Premixed Flames Using Synchrotron Photoionization. *Combust. Flame* **2011**, *158* (9), 1673−1681.

(21) Tran, L. S.; Glaude, P. A.; Battin-Leclerc, F. An Experimental Study of the Structure of Laminar Premixed Flames of Ethanol/methane/oxygen/argon. *Combust., Explos. Shock Waves* **2013**, *49* (1), 11−18.

(22) Tran, L.; Glaude, P.; Fournet, R.; Battin-Leclerc, F. Experimental and Modeling Study of Premixed Laminar Flames of Ethanol and Methane. *Energy Fuels* **2013**, *27* (4), 2226−2245.

(23) Herrmann, F.; Jochim, B.; Oßwald, P.; Cai, L.; Pitsch, H.; Kohse-Höinghaus, K. Experimental and Numerical Low-Temperature Oxidation Study of Ethanol and Dimethyl Ether. *Combust. Flame* **2014**, *161* (2), 384−397.

(24) Dunphy, M. P.; Patterson, P. M.; Simmie, J. M. High-Temperature Oxidation of Ethanol: Part 2.-Kinetic Modellig. *J. Chem. Soc., Faraday Trans.* **1991**, *87* (16), 2549−2559.

(25) Egolfopoulos, F. N.; Du, D. X.; Law, C. K. A Study on Ethanol Oxidation Kinetics in Laminar Premixed Flames, Flow Reactors, and Shock Tubes. *Symp. Combust., [Proc.]* **1992**, *24*, 833−841.

(26) Marinov, N. M. A Detailed Chemical Kinetic Model for High Temperature Ethanol Oxidation. *Int. J. Chem. Kinet.* **1999**, *31* (3), 183−220.

(27) Saxena, P.; Williams, F. A. Numerical and Experimental Studies of Ethanol Flames. *Proc. Combust. Inst.* **2007**, *31* (1), 1149−1156.

(28) Andrae, J. C. G. Development of a Detailed Kinetic Model for Gasoline Surrogate Fuels. *Fuel* **2008**, *87* (10−11), 2013−2022.

(29) Cancino, L. R.; Fikri, M.; Oliveira, A. A. M.; Schulz, C. Ignition Delay Times of Ethanol-Containing Multi-Component Gasoline Surrogates: Shock-Tube Experiments and Detailed Modeling. *Fuel* **2011**, *90* (3), 1238−1244.

(30) Metcalfe, W. K.; Burke, S. M.; Ahmed, S. S.; Curran, H. J. A Hierarchical and Comparative Kinetic Modeling Study of C_1−C_2

DOI: 10.1021/acs.jpca.6b06725
J. Phys. Chem. A XXXX, XXX, XXX−XXX

Hydrocarbon and Oxygenated Fuels. *Int. J. Chem. Kinet.* **2013**, *45* (10), 638−673.
(31) Mehl, M.; Pitz, W. J.; Westbrook, C. K.; Curran, H. J. Kinetic Modeling of Gasoline Surrogate Components and Mixtures under Engine Conditions. *Proc. Combust. Inst.* **2011**, *33* (1), 193−200.
(32) Zhong, B.-J.; Zheng, D. Chemical Kinetic Mechanism of a Three-Component Fuel Composed of Iso-Octane/ N -Heptane/ Ethanol. *Combust. Sci. Technol.* **2013**, *185* (4), 627−644.
(33) Zhong, B.-J.; Zheng, D. A Chemical Mechanism for Ignition and Oxidation of Multi-Component Gasoline Surrogate Fuels. *Fuel* **2014**, *128*, 458−466.
(34) Burke, S. M.; Metcalfe, W.; Herbinet, O.; Battin-Leclerc, F.; Haas, F. M.; Santner, J.; Dryer, F. L.; Curran, H. J. An Experimental and Modeling Study of Propene Oxidation. Part 1: Speciation Measurements in Jet-Stirred and Flow Reactors. *Combust. Flame* **2014**, *161* (11), 2765−2784.
(35) Burke, S. M.; Burke, U.; Mc Donagh, R.; Mathieu, O.; Osorio, I.; Keesee, C.; Morones, A.; Petersen, E. L.; Wang, W.; DeVerter, T. A.; et al. An Experimental and Modeling Study of Propene Oxidation. Part 2: Ignition Delay Time and Flame Speed Measurements. *Combust. Flame* **2015**, *162* (2), 296−314.
(36) Donovan, M. T.; He, X.; Zigler, B. T.; Palmer, T. R.; Wooldridge, M. S.; Atreya, A. Demonstration of a Free-Piston Rapid Compression Facility for the Study of High Temperature Combustion Phenomena. *Combust. Flame* **2004**, *137* (3), 351−365.
(37) Donovan, M.; He, X.; Zigler, B.; Palmer, T.; Walton, S.; Wooldridge, M. Experimental Investigation of Silane Combustion and Particle Nucleation Using a Rapid-Compression Facility. *Combust. Flame* **2005**, *141* (4), 360−370.
(38) Walton, S.; He, X.; Zigler, B.; Wooldridge, M.; Atreya, A. An Experimental Investigation of Iso-Octane Ignition Phenomena. *Combust. Flame* **2007**, *150* (3), 246−262.
(39) Karwat, D. M. A.; Wagnon, S. W.; Wooldridge, M. S.; Westbrook, C. K. Low-Temperature Speciation and Chemical Kinetic Studies of N-Heptane. *Combust. Flame* **2013**, *160* (12), 2693−2706.
(40) Wagnon, S. W.; Karwat, D. M. A.; Wooldridge, M. S.; Westbrook, C. K. Experimental and Modeling Study of Methyl Trans −3-Hexenoate Autoignition. *Energy Fuels* **2014**, *28* (11), 7227−7234.
(41) Wagnon, S. W.; Barraza-Botet, C. L.; Wooldridge, M. S. Effects of Bond Location on the Ignition and Reaction Pathways of Trans-Hexene Isomers. *J. Phys. Chem. A* **2015**, *119*, 7695.
(42) He, X.; Donovan, M. T.; Zigler, B. T.; Palmer, T. R.; Walton, S. M.; Wooldridge, M. S.; Atreya, A. An Experimental and Modeling Study of Iso-Octane Ignition Delay Times under Homogeneous Charge Compression Ignition Conditions. *Combust. Flame* **2005**, *142* (3), 266−275.
(43) Mansfield, A. B.; Wooldridge, M. S.; Di, H.; He, X. Low-Temperature Ignition Behavior of Iso-Octane. *Fuel* **2015**, *139*, 79−86.
(44) Karwat, D. M. A.; Wagnon, S. W.; Wooldridge, M. S.; Westbrook, C. K. On the Combustion Chemistry of N-Heptane and N-Butanol Blends. *J. Phys. Chem. A* **2012**, *116* (51), 12406−12421.
(45) Karwat, D. M. A.; Wagnon, S. W.; Teini, P. D.; Wooldridge, M. S. On the Chemical Kinetics of N-Butanol: Ignition and Speciation Studies. *J. Phys. Chem. A* **2011**, *115* (19), 4909−4921.
(46) Zhou, C.-W.; Simmie, J. M.; Curran, H. J. Rate Constants for Hydrogen Abstraction by HO_2 from N-Butanol. *Int. J. Chem. Kinet.* **2012**, *44*, 155−164.
(47) Troe, J. The Thermal Dissociation/Recombination Reaction of Hydrogen Peroxide $H_2O_2(+M) \Leftrightarrow 2OH(+M)$ III. Analysis and Representation of the Temperature and Pressure Dependence over Wide Ranges. *Combust. Flame* **2011**, *158* (4), 594−601.
(48) Hippler, H.; Troe, J.; Willner, J. Shock Wave Study of the Reaction $HO_2+HO_2 \rightarrow H_2O_2+O_2$: Confirmation of a Rate Constant Minimum near 700 K. *J. Chem. Phys.* **1990**, *93* (1990), 1755.
(49) Zádor, J.; Fernandes, R. X.; Georgievskii, Y.; Meloni, G.; Taatjes, C. A.; Miller, J. A. The Reaction of Hydroxyethyl Radicals with O_2: A Theoretical Analysis and Experimental Product Study. *Proc. Combust. Inst.* **2009**, *32* (1), 271−277.
(50) Silva, G. da; Bozzelli, J. W.; Liang, L.; Farrell, J. T. Ethanol Oxidation: Kinetics of the Alpha-Hydroxyethyl Radical + O_2 Reaction. *J. Phys. Chem. A* **2009**, *113*, 8923−8933.
(51) Poulopoulos, S. G.; Samaras, D. P.; Philippopoulos, C. J. Regulated and Unregulated Emissions from an Internal Combustion Engine Operating on Ethanol-Containing Fuels. *Atmos. Environ.* **2001**, *35* (26), 4399−4406.

DOI: 10.1021/acs.jpca.6b06725
J. Phys. Chem. A XXXX, XXX, XXX−XXX